UNIVERSITY OF CALIFORNIA SAN DIEGO

Static and Dynamic Phenomena in Strongly Correlated Magnetic Thin Films

A dissertation submitted in partial satisfaction of the
requirements for the degree

Doctor of Philosophy

in

Physics

by

Sheena K. K. Patel

Committee in charge:

Professor Eric E. Fullerton, Chair
Professor Oleg G. Shpyrko, Co-Chair
Professor Richard D. Averitt
Professor Alex Frañó
Professor Vitaliy Lomakin

2023

The dissertation of Sheena K. K. Patel is approved, and it is acceptable in quality and form for publication on microfilm and electronically.

University of California San Diego

2023

DEDICATION

To all the people who supported and encouraged me along the way,
especially the teachers.

EPIGRAPH

What I am going to tell you about is what we teach our physics students in the third or fourth year of graduate school... No, you're not going to be able to understand it... That is because I don't understand it. Nobody does.
— Richard P. Feynman

Magnetism, as you recall from physics class, is a powerful force that causes certain items to be attracted to refrigerators.
— Dave Barry

TABLE OF CONTENTS

LIST OF FIGURES

LIST OF TABLES

ACKNOWLEDGEMENTS

This section is, in some ways, the hardest of all to write. Not because I have no one to thank, but because I am acutely aware of how much my personal success has relied on the support of the people around me. I have always been surrounded by teachers, professors, mentors, colleagues, and friends who believe in me, and I would be lost without them all. I cannot name each and every one here and I fear leaving out people who deserve to be acknowledged, so I just want to start by expressing how grateful I am to everyone who has encouraged me along the way and for all of the opportunities I have had.

First and foremost, I want to thank Professor Eric Fullerton. It is difficult to find the words to express how grateful I am for all of his guidance, support, enthusiasm, humor, advice, encouragement, and kindness. I have had an incredible range of experiences as a member of his group, participating in many different types of experiments all over Europe and the United States and have learned so much from him about science and research and just about being human. I am also incredibly appreciative for his compassion and support when my personal life derailed my research life.

I also want to thank the other members of my committee. Professor Oleg Shpyrko met with me and encouraged me to come to UC San Diego for my graduate studies, has collaborated on much of my work, and is co-chair for my dissertation. I really appreciate the advice and help he has given me over the years. I am grateful to Professors Richard Averitt, Alex Frañó, and Vitaliy Lomakin for serving on my committee and providing their encouragement and guidance.

I appreciate the support of all the coauthors of my work. I have learned so much from all of my colleagues and would have been completely lost without them. Experiments conducted at national labs are often very intensive and require a team of people working around the clock, so I needed their help for experiments I led and am grateful to have participated in and learned from experiments led by others. I know that there are times when I would have been completely lost without them and our experiments would have been far less successful.

All of the members of the Fullerton research group have had such an impact on my time here, and I want to thank them all for their help and discussions over the years. A lot of advice has been passed down over the years and I hope I have been able to do the same for others. Nasim Eibagi took me under her wing in my first few months here, teaching me much of what I needed to learn in the cleanroom as well as imparting helpful advice about life during graduate school. Roopali Kukreja was so encouraging when I was feeling insecure, and has been a mentor, friend, and inspiration. Vojtěch Uhlíř, another mentor, taught me how to make epitaxial thin films through sputtering, which was a crucial part of my work, and first introduced me to the world of synchrotron experiments within a month of my arrival. So many people helped when things were broken in the lab and I was unsure of what to do or needed an extra hand, but I want to acknowledge Jeffrey Brock in particular, who always had an answer and was always willing to help. I remember many late night discussions with so many members of our group over the years, which often had nothing to do with science but were wonderful moments of humor or interest or commiseration. Everyone has helped and made an impact in so many ways big and small over the years.

My undergraduate advisors, Professors James C. Eckert and Patricia D. Sparks at Harvey Mudd College, introduced me to magnetism and research, took me to international conferences to present my work, and introduced me to Professor Fullerton during my time as an undergraduate. They have continued to be mentors and friends in the time since. I have also had the opportunity to collaborate with them and work with eleven of their undergraduate research students, who have been able to present their results at conferences. This includes Lorenzo Calvano, who came to UC San Diego to work with me directly in the lab one summer and worked with me remotely for another summer. I have enjoyed the chance to mentor these students and hope they had a positive experience of research and science.

I had the opportunity to visit l'Institut Jean Lamour in Nancy, France for several months in 2017 and 2018. I want to thank Professor Stéphane Mangin and his research group for welcoming

me and thank Juan Carlos Rojas-Sanchez and Laurent Badie for their support in the lab during my time there.

I also want to acknowledge the support of many people at UC San Diego. Iris Villanueva, Octavio Ochoa, and Marina Robenko have been so important in keeping our lab and the Center for Memory and Recording Research up and running, handling funding issues and navigating the systems for ordering equipment and shipping samples and reimbursement for travel. Staff in the Physics Department, including Sharmila Poddar, Catherine Mcconney, Hilari Ford, helped me with all the logistical issues, funding, paperwork, and confusion of various kinds over the years.

And of course I want to acknowledge the people who are a part of my life outside of research. I am thankful to my family for the ways they have supported my education over the years. I met Haley Erickson and Lydia Jahl on the first day I arrived for my undergraduate education and they continue to be amazing friends and great people. Our weekly Zoom sessions have been keeping me [somewhat] sane. When I arrived at UC San Diego, I made so many friends among my incoming class of physics graduate students and their partners, and we were able to make it through classes and the qualifying exam together. We played intramural volleyball, tennis, and flag football (and they indulged my fitting but nerdy team name idea of "Spin Up") and had a lot of game nights and gatherings and potlucks and one rather miserable, cold, rainy camping experience. Most of us have scattered across the world now, but I have enjoyed the times we have been able to meet again since. Lindsay Lowry continues to be a really encouraging and caring presence in my life even after leaving San Diego. In the last year, I have spent many evenings with Andy Leverentz and Angela Berti, having dinner, talking about the world, loving on a very floofy cat, and watching a particularly captivating show, which has been such a welcome reprieve at stressful times. I also resumed my passion for tennis last year and have made some great new friends on the court who have cheered me on as the page count of this dissertation grew. I am so grateful to have some really kind and supportive people in my life.

And a special acknowledgement should go to my cats, Roo and Sable, for their emotional

support and unconditional love. Roo supported my early graduate education by sitting on any textbooks I had open or any papers I was about to write on, which was very helpful when I was procrastinating on studying for the qualifying exam. Sable has come into my life at the end of my graduate education, providing critical support by lying on me (and sometimes on my computer) for hours on end while I write my dissertation, simultaneously providing stress relief and keeping me hostage, unable to move my arms or body away from my computer (and usually only partially blocking my view of the screen).

And finally, it is important to me to address some of the events that have occurred since the start of 2020. There are so many people who work to provide all of us access to basic necessities like food, water, shelter, health, and safety, and most of them do not get any recognition for their efforts or fancy letters after their names. I am incredibly grateful to everyone who made a difference during the pandemic and saved lives, often at great risk to themselves or their families. I also want to acknowledge all the medical professionals who have helped me and the people I love in this time: to say that the last few years have been rough would be an understatement, but I am so thankful for their work and care.

I would like to acknowledge financial support from the U.S. Department of Energy, Office of Science, Office of Basic Energy Sciences, under Contract No. DE-SC0003678 and from the National Science Foundation, Division of Materials Research (Award #2105400). I also want to thank the National Science Foundation for funding through the Graduate Research Fellowship Program, the Embassy of France in the United States for funding through the Chateaubriand Fellowship, the Katzin family and the UC San Diego Division of Graduate Education and Postdoctoral Affairs for the Katzin Prize, and the UC San Diego Physics Department for the Physics Excellence Award and Summer Research Fellowship Award.

Section 3.1.4 contains unpublished data coauthored by Sheena K. K. Patel and Eric E. Fullerton. The dissertation author was the primary investigator of this material. This work was performed in part at the San Diego Nanotechnology Infrastructure (SDNI) of UC San Diego, a member of the National Nanotechnology Coordinated Infrastructure, which is supported by the National Science Foundation (Grant ECCS-2025752).

Section 3.2, in full, contains a reprint of research published in Andrej Singer, Sheena K. K. Patel, Vojtěch Uhlíř, Roopali Kukreja, Andrew Ulvestad, Eric M. Dufresne, Alec R. Sandy, Eric E. Fullerton, and Oleg G. Shpyrko, "Phase coexistence and pinning of charge density waves by interfaces in chromium," *Phys. Rev. B*, vol. 94, p. 174110, 2016. Copyright 2016 by the American Physical Society. The dissertation author was second author and made essential contributions to this work. This research used resources of the Advanced Photon Source, a U.S. Department of Energy (DOE) Office of Science user facility operated for the DOE Office of Science by Argonne National Laboratory under Contract No. DE-AC02-06CH11357.

Section 3.3, in full, contains a reprint of research published in Andrej Singer, Sheena K. K. Patel, Roopali Kukreja, Vojtěch Uhlíř, James Wingert, Sven Festersen, Diling Zhu, James M. Glownia, Henrik T. Lemke, Silke Nelson, Michael Kozina, Kai Rossnagel, Michael Bauer, Bridget Murphy, Olaf M. Magnussen, Eric E. Fullerton, and Oleg G. Shpyrko, "Photoinduced enhancement of the charge density wave amplitude," *Phys. Rev. Lett.*, vol. 117, p. 056401, 2016. Copyright 2016 by the American Physical Society. The dissertation author was second author and made essential contributions to this work. Use of the Linac Coherent Light Source (LCLS), SLAC National Accelerator Laboratory, is supported by the U.S. Department of Energy, Office of Science, Office of Basic Energy Sciences under Contract No. DE-AC02-76SF00515.

Section 3.4, in full, is currently being prepared for submission for publication of the material coauthored by Sheena K. K. Patel, Oleg Yu. Gorobtsov, Devin Cela, Stjepan B. Hrkac, Nelson Hua, Rajasekhar Medapalli, Anatoly G. Shabalin, James Wingert, James M. Glownia, Diling Zhu, Matthieu Chollet, Oleg G. Shpyrko, Andrej Singer, and Eric E. Fullerton. The

dissertation author was the primary investigator and author of this material. Use of the Linac Coherent Light Source (LCLS), SLAC National Accelerator Laboratory, is supported by the U.S. Department of Energy, Office of Science, Office of Basic Energy Sciences under Contract No. DE-AC02-76SF00515.

Chapter 4, in part, is currently being prepared for submission for publication of the material coauthored by Sheena K. K. Patel, Stjepan B. Hrkac, Jeffrey A. Brock, Nelson Hua, Haidan Wen, Donald Walko, Oleg G. Shpyrko, and Eric E. Fullerton. The dissertation author was the primary investigator and author of this material. This research used resources of the Advanced Photon Source, a U.S. Department of Energy (DOE) Office of Science user facility operated for the DOE Office of Science by Argonne National Laboratory under Contract No. DE-AC02-06CH11357. This work was performed in part at the San Diego Nanotechnology Infrastructure (SDNI) of UC San Diego, a member of the National Nanotechnology Coordinated Infrastructure, which is supported by the National Science Foundation (Grant ECCS-2025752).

Section 5.1.2 contains unpublished data coauthored by Sheena K. K. Patel, Timothy R. Charlton, Michael R. Fitzsimmons, Tao Zou, Tao Hong, and Eric E. Fullerton. The dissertation author was the primary investigator of this material. Neutron diffraction was conducted as part of a user project at the High Flux Isotope Reactor (HFIR), which is a US Department of Energy, Office of Science User Facility at Oak Ridge National Laboratory.

Section 5.2, in part, is currently being prepared for submission for publication of the material coauthored by Aleksandr Buzdakov, Irina Dolgikh, Sheena K. K. Patel, Rajasekhar Medapalli, Km Rubi, Elvina Dilmieva, Uli Zeitler, Theo Rasing, Eric E. Fullerton, Peter C. M. Christianen, Konstantin A. Zvezdin, Anatoly K. Zvezdin, and Alexey V. Kimel. The dissertation author was the primary investigator of a portion of this material and a contributing author to the paper. High field transport measurements were conducted as part of a user project supported by the High Field Magnet Laboratory and the Foundation for Dutch Scientific Research Institutes (HFML-RU/NWO-I), members of the European Magnetic Field Laboratory (EMFL). We

acknowledge the European Synchrotron Radiation Facility (ESRF) for provision of synchrotron radiation facilities and we would like to thank Elvina Dilmieva for assistance and support in using beamline ID12 for measurements of x-ray magnetic circular dichroism. This work was performed in part at the San Diego Nanotechnology Infrastructure (SDNI) of UC San Diego, a member of the National Nanotechnology Coordinated Infrastructure, which is supported by the National Science Foundation (Grant ECCS-2025752).

Section 5.3 contains unpublished data coauthored by Sheena K. K. Patel, Jon Ander Arregi, Sunil K. Sinha, Valeria Lauter, Vojtěch Uhlíř, and Eric E. Fullerton. The dissertation author was the primary investigator of this material. Polarized neutron reflectometry was conducted as part of a user project at the Spallation Neutron Source (SNS), which is a US Department of Energy, Office of Science User Facility at Oak Ridge National Laboratory. This work was performed in part at the San Diego Nanotechnology Infrastructure (SDNI) of UC San Diego, a member of the National Nanotechnology Coordinated Infrastructure, which is supported by the National Science Foundation (Grant ECCS-2025752).

VITA

2023	Ph.D. in Physics, University of California San Diego
2016	M.S. in Physics, University of California San Diego
2010	B.S. in Physics, Harvey Mudd College *Graduated with High Distinction and Honors in Physics*

PUBLICATIONS

S. K. K. Patel, O. Yu. Gorobtsov, D. Cela, S. B. Hrkac, N. Hua, R. Medapalli, A. G. Shabalin, J. Wingert, J. M. Glownia, D. Zhu, M. Chollet, O. G. Shpyrko, A. Singer, and E. E. Fullerton. "Critical slowing of the spin and charge density wave order in thin film Cr following photoexcitation," (*In Preparation*).

S. K. K. Patel, S. B. Hrkac, N. Hua, J. A. Brock, H. Wen, D. A. Walko, O. G. Shpyrko, and E. E. Fullerton. "Time-resolved x-ray diffraction measurements of giant negative thermal expansion and magneto-volume effects in $Mn_3Cu_{1-x}A_xN$ thin films," (*In Preparation*).

N. Hua, S. K. K. Patel, R. Medapalli, A. G. Shabalin, S. B. Hrkac, J. Wingert, D. Cela, J. Ruby, J. M. Glownia, D. Zhu, M. Chollet, A. Singer, E. E. Fullerton, and O. G. Shpyrko. "Measuring electron-phonon coupling time scales in chromium by photoexcitation," (*In Preparation*).

A. Buzdakov, I. Dolgikh, S. K. K. Patel, R. Medapalli, K. Rubi, E. Dilmieva, U. Zeitler, T. Rasing, E. E. Fullerton, P. C. M. Christianen, K. A. Zvezdin, A. K. Zvezdin, and A. V. Kimel. "Phase diagrams for magnetic field and temperature-induced ferromagnetism in antiferromagnetic FeRh," (*In Preparation*).

J.-J. Song, S. K. K. Patel, R. Bhattacharya, Y. Yang, S. Pandey, X. M. Chen, M. B. Maple, E. E. Fullerton, S. Roy, C. Mazzoli, C. M. Varma, and S. K. Sinha, "Direct measurement of temporal correlations above the spin-glass transition by coherent resonant magnetic x-ray spectroscopy," (*In Preparation*).

I. A. Dolgikh, T. G. H. Blank, G. Li, K. H. Prabhakara, S. K. K. Patel, A. G. Buzdakov, R. Medapalli, E. E. Fullerton, O. V. Koplak, J. H. Mentink, K. A. Zvezdin, A. K. Zvezdin, P. C. M. Christianen, and A. V. Kimel, "Ultrafast Emergence of Ferromagnetism in Antiferromagnetic FeRh in High Magnetic Fields," (*In Preparation*).

N. Tang, W. L. N. C. Liyanage, S. A. Montoya, S. K. K. Patel, L. J. Quigley, A. J. Grutter, M. R. Fitzsimmons, S. K. Sinha, J. A. Borchers, E. E. Fullerton, L. DeBeer-Schmitt, and D. A. Gilbert, "Skyrmion-excited spin wave fractal network," to appear in *Adv. Mater.*, (2023).

N. Zhou Hagström, M. Schneider, N. Kerber, A. Yaroslavtsev, E. Burgos Parra, M. Beg, M. Lang, C. M. Günther, B. Seng, F. Kammerbauer, H. Popescu, M. Pancaldi, K. Neeraj, D. Polley, R. Jangid, S. B. Hrkac, S. K. K. Patel, S. Ovcharenko, D. Turenne, D. Ksenzov, C. Boeglin, M. Baidakova, C. von Korff Schmising, M. Borchert, B. Vodungbo, K. Chen, C. Luo, F. Radu, L. Müller, M. Martínez Flórez, A. Philippi-Kobs, M. Riepp, W. Roseker, G. Grübel, R. Carley, J. Schlappa, B. E. Van Kuiken, R. Gort, L. Mercadier, N. Agarwal, L. Le Guyader, G. Mercurio, M. Teichmann, J. T. Delitz, A. Reich, C. Broers, D. Hickin, C. Deiter, J. Moore, D. Rompotis, J. Wang, D. Kane, S. Venkatesan, J. Meier, F. Pallas, T. Jezynski, M. Lederer, D. Boukhelef, J. Szuba, K. Wrona, S. Hauf, J. Zhu, M. Bergemann, E. Kamil, T. Kluyver, R. Rosca, M. Spirzewski, M. Kuster, M. Turcato, D. Lomidze, A. Samartsev, J. Engelke, M. Porro, S. Maffessanti, K. Hansen, F. Erdinger, P. Fischer, C. Fiorini, A. Castoldi, M. Manghisoni, C. B. Wunderer, E. E. Fullerton, O. G. Shpyrko, C. Gutt, C. Sanchez-Hanke, H. A. Dürr, E. Iacocca, H. T. Nembach, M. W. Keller, J. M. Shaw, T. J. Silva, R. Kukreja, H. Fangohr, S. Eisebitt, M. Kläui, N. Jaouen, A. Scherz, S. Bonetti, and E. Jal, "Megahertz-rate ultrafast x-ray scattering and holographic imaging at the European XFEL," *J. Synchrotron Radiat.*, vol. 29, pp. 1454-1464, (2022).

D. Zusin, E. Iacocca, L. Le Guyader, A. H. Reid, W. F. Schlotter, T.-M. Liu, D. J. Higley, G. Coslovich, S. F. Wandel, P. M. Tengdin, S. K. K. Patel, A. Shabalin, N. Hua, S. B. Hrkac, H. T. Nembach, J. M. Shaw, S. A. Montoya, A. Blonsky, C. Gentry, M. A. Hoefer, M. M. Murnane, H. C. Kapteyn, E. E. Fullerton, O. G. Shpyrko, H. A. Dürr, and T. J. Silva "Ultrafast perturbation of magnetic domains by optical pumping in a ferromagnetic multilayer," *Phys. Rev. B*, vol. 106, pp. 144422, (2022).

J. Li, O. Yu. Gorobtsov, S. K. K. Patel, N. Hua, B. Gregory, A. G. Shabalin, S. Hrkac, J. Wingert, D. Cela, J. M. Glownia, M. Chollet, D. Zhu, R. Medapalli, E. E. Fullerton, O. G. Shpyrko, and A. Singer, "Phonon-assisted formation of an itinerant electronic density wave," *Commun. Phys.*, vol. 5, pp. 125, (2022).

G. Li, R. Medapalli, J. H. Mentink, R. V. Mikhaylovskiy, T. G. H. Blank, S. K. K. Patel, A. K. Zvezdin, Th. Rasing, E. E. Fullerton, and A. V. Kimel, "Ultrafast kinetics of the antiferromagnetic-ferromagnetic phase transition in FeRh," *Nat. Commun.*, vol. 13, pp. 2998, (2022).

M. Horký, J. A. Arregi, S. K. K. Patel, M. Staňo, R. Medapalli, O. Caha, L. Vojacek, M. Horák, V. Uhlíř, and E. E. Fullerton, "Controlling the metamagnetic phase transition in FeRh/MnRh superlattices and thin-film $Fe_{50-x}Mn_xRh_50$ alloys," *ACS Appl. Mater. Interfaces*, vol. 14, pp. 3568-3579, (2022).

O. Yu. Gorobtsov, L. Ponet, S. K. K. Patel, N. Hua, A. G. Shabalin, S. B. Hrkac, J. Wingert, D. Cela, J. M. Glownia, D. Zhu, R. Medapalli, M. Chollet, E. E. Fullerton, S. Artyukhin, O. G. Shpyrko, and A. Singer, "Femtosecond control of phonon dynamics near a magnetic order critical point," *Nat. Commun.*, vol. 12, p. 2865, (2021).

R. Medapalli, G. Li, S. K. K. Patel, R. V. Mikhaylovskiy, T. Rasing, A. V. Kimel, and E. E. Fullerton, "Femtosecond photocurrents at the FeRh/Pt interface," *Appl. Phys. Lett.*, vol. 117, p. 142406, (2020).

J. Wingert, A. Singer, S. K. K. Patel, R. Kukreja, M. J. Verstraete, A. H. Romero, V. Uhlíř, S. Festersen, D. Zhu, J. M. Glownia, H. T. Lemke, S. Nelson, M. Kozina, K. Rossnagel, B. M. Murphy, O. M. Magnussen, E. E. Fullerton, and O. G. Shpyrko, "Direct time-domain determination of electron-phonon coupling strengths in chromium," *Phys. Rev. B*, vol. 102, p. 041101, (2020).

S. Matzen, L. Guillemot, T. Maroutian, S. K. K. Patel, H. Wen, A. D. DiChiara, G. Agnus, O. G. Shpyrko, E. E. Fullerton, D. Ravelosona, and P. Lecoeur, "Tuning ultrafast photoinduced strain in ferroelectric-based devices," *Adv. Electron. Mater.*, vol. 5, p. 1800709, (2019).

F. Pressacco, V. Uhlíř, M. Gatti, A. Nicolaou, A. Bendounan, J. A. Arregi, S. K. K. Patel, E. E. Fullerton, D. Krizmancic, and F. Sirotti, "Laser induced phase transition in epitaxial FeRh layers studied by pump-probe valence band photoemission," *Struct. Dyn.*, vol. 5, p. 034501, (2018).

A. Singer, S. K. K. Patel, R. Kukreja, V. Uhlíř, J. Wingert, S. Festersen, D. Zhu, J. M. Glownia, H. T. Lemke, S. Nelson, M. Kozina, K. Rossnagel, M. Bauer, B. M. Murphy, O. M. Magnussen, E. E. Fullerton, and O. G. Shpyrko, "Photoinduced enhancement of the charge density wave amplitude," *Phys. Rev. Lett.*, vol. 117, p. 056401, (2016).

A. Singer, S. K. K. Patel, V. Uhlíř, R. Kukreja, A. Ulvestad, E. M. Dufresne, A. R. Sandy, E. E. Fullerton, and O. G. Shpyrko, "Phase coexistence and pinning of charge density waves by interfaces in chromium," *Phys. Rev. B*, vol. 94, p. 174110, (2016).

CONFERENCE PRESENTATIONS

"Critical slowing of the spin and charge density wave order in thin film Cr following photoexcitation"
Oral presentation
CMRR Research Review | May 25-26, 2023 | La Jolla, CA

"Photoinduced spin-density and charge-density wave dynamics in chromium"
Invited oral presentation
Magnetism and Magnetic Materials Conference | November 2-6, 2020 | Virtual

"Lattice dynamics of antiperovskite manganese nitrides exhibiting large negative and positive thermal expansion"
Oral presentation
American Physical Society March Meeting | March 2-6, 2020 | Denver, CO | (Conference canceled)

"Reestablishment of spin-density-wave magnetic order in epitaxial chromium films following photoexcitation"
Oral presentation
Magnetism and Magnetic Materials Conference | November 3-7, 2019 | Las Vegas, NV

"Reestablishment of magnetic order in epitaxial thin film Cr following photoexcitation"
Oral presentation
Joint Magnetism and Magnetic Materials - IEEE Intermag Conference | January 14-18, 2019 | Washington DC

"Recovery of antiferromagnetic order in Cr following photoexcitation"
Oral presentation
CMRR Research Review | November 1-2, 2018 | La Jolla, CA

"Charge density wave dynamics in Cr following ultrafast photoexcitation"
Oral presentation
Nanomagnetism Workshop | February 7, 2018 | Nancy, France

"Transport and x-ray pump probe studies of the charge and spin density wave in Cr"
Oral presentation
Magnetism and Magnetic Materials Conference | November 6-10, 2017 | Pittsburgh, PA

"Enhancement of charge ordering in Cr via dynamic electron-phonon interaction"
Poster
Magnetism and Magnetic Materials Conference | October 31-November 4, 2016 | New Orleans, LA

"Transport measurements of Co/Tb multilayers engineered for all-optical switching"
Poster
IEEE Intermag Conference | May 4-8, 2014 | Dresden, Germany

"Hall effect study of Co/Ni multilayers"
Poster
Magnetism and Magnetic Materials Conference | November 4-8, 2013 | Denver, CO

"Magnetotransport properties of Co-Ir synthetic ferrimagnets with perpendicular magnetic anisotropy"
Poster
Magnetism and Magnetic Materials Conference | November 4-8, 2013 | Denver, CO

"Anomalous Hall measurements of Co/Ni multilayers"
Poster
International Conference on Magnetism | July 8-13, 2012 | Busan, South Korea

"Anisotropic magnetoresistance of Co/Ni Multilayers"
Poster
International Conference on Magnetism | July 8-13, 2012 | Busan, South Korea

ABSTRACT OF THE DISSERTATION

Static and Dynamic Phenomena in Strongly Correlated Magnetic Thin Films

by

Sheena K. K. Patel

Doctor of Philosophy in Physics

University of California San Diego, 2023

Professor Eric E. Fullerton, Chair
Professor Oleg G. Shpyrko, Co-Chair

Magnetic materials have played an enormous role in the advancement of technology over the past two centuries. Much of the current understanding of magnetism, however, is limited by the complexity of the interactions between particles from which collective behavior and interesting phenomena emerge. In the regime where the miniaturization of technologies combined with ultrafast responses are desired, these phenomena can become even more obscure. Probing these systems and interactions to gain insight into the origin of these phenomena is required for both fundamental understanding and for the engineering of novel materials and devices for application. In this dissertation, we study three magnetic systems exhibiting complex phenomena

in confined geometries, mostly confining in one dimension as thin films. Elemental chromium is an antiferromagnetic metal with coupled spin density wave, charge density wave, and periodic lattice distortion. We track this ordering primarily through x-ray diffraction measurements statically, on ultrafast time scales following photoexcitation, and over longer time scales to follow the evolution and recovery to the static state. Certain antiperovskite manganese nitride compounds exhibit magnetovolume effects including negative thermal expansion tied to the transition in magnetic ordering between ferrimagnetic, antiferromagnetic, and paramagnetic phases. These magnetovolume effects are demonstrated for thin films through static x-ray diffraction measurements as well as dynamically following photoexcitation. And iron rhodium is an alloy with a room temperature transition between an antiferromagnetic phase and a ferromagnetic phase that also exhibits large magnetoresistance and magnetostructural effects. We conduct a study of its magnetic phase diagram through resistivity measurements and x-ray magnetic circular dichroism measurements at high field and with theoretical calculations. We also examine the effects of confinement in a film and in wires through polarized neutron reflectometry measurements. These experiments provide insight into the collective interactions in these materials and into the strong coupling of the charge, spin, and lattice degrees of freedom seen in each of them.

Chapter 1

Introduction

Current research in condensed matter physics is focused on understanding and manipulating strongly correlated systems. Materials with weak interactions between particles can be described well by traditional free particle models. However, in more complex materials, these correlations can no longer be neglected and interactions such as Coulombic forces between electrons must be accounted for. These interactions result in collective behavior within the system and the emergence of interesting and varied phenomena which are usually difficult to predict, understand, and control [1, 2]. There are many different types of strongly correlated systems of interest. Conventional superconductors, which are able to support dissipationless charge transport, have proven to be invaluable in technological applications and in research and are generally understood well through Bardeen-Cooper-Schreiffer (BCS) theory, but the origin of superconductivity in unconventional superconductors is far less clear [3]. Work in this field holds promise for the development and engineering of high-temperature superconductors, ideally room-temperature superconductors, which will provide a significant advantage in application. The field of spintronics was developed around the large change in electrical resistivity (~80%) between parallel and antiparallel alignments of adjacent ferromagnetic layers, a phenomenon called giant magnetoresistance [4]. Colossal magnetoresistance, in which there is a change of

multiple orders of magnitude in the resistivity of certain manganite perovskites with application of an external magnetic field, could provide the next step for increasing the density of data in magnetic hard drives and decreasing power consumption, but the search for materials which operate at a reasonable temperature range and require low applied magnetic fields has continued [4–6]. The lack of understanding of the mechanisms behind colossal magnetoresistance may be preventing the development and engineering of materials and devices that can utilize it.

In magnetic systems, a focus of this work, the interactions between electrons lead to many types of collective ordering of spins and spin textures, everything from typical ferromagnetism and antiferromagnetism to spin density waves to topological features such as skyrmions [7]. Magnetic materials are an integral component of so much of modern technology and the possibilities for developing technology are endless, from spintronics applications of smaller, faster, more efficient magnetic hard drives [8–10] to biomedical applications such as contrast material for MRIs [11, 12]. One type of magnetic ordering, antiferromagnetism, is of great interest in spintronics. Traditionally, antiferromagnets have been difficult to identify, measure, and control because they have a low net moment and are insensitive to applied fields. But these properties also make them potentially very useful for more modern experimental techniques. Their insensitivity to applied fields make them more stable and their smaller stray fields mean that there is weaker coupling between neighboring devices, allowing for greater device density. Switching with antiferromagnets would require less transfer of angular momentum to the lattice, which is a slow process, potentially boosting switching speeds into the THz regime, a significant improvement

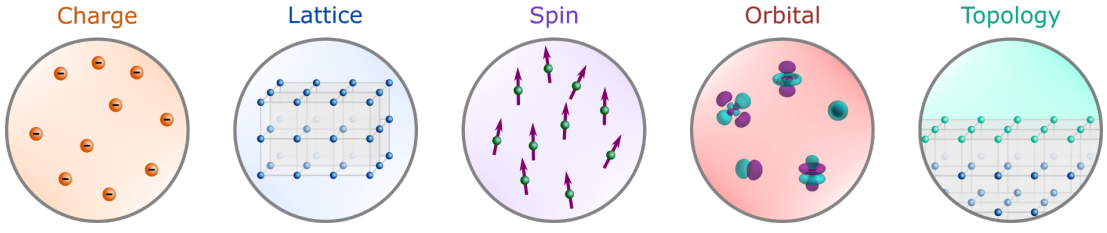

Figure 1.1: Representations of the degrees of freedom used in describing interactions and coupling in quantum materials with emergent phenomena.

over current GHz devices [13–15]. In order to actually engineer devices that can make use of these properties, however, it is necessary to gain an understanding of how antiferromagnets behave and how they can be manipulated and controlled.

Much of the experimental research in strongly correlated materials focuses on probing the interactions in these strongly correlated systems to build up an understanding of the nature of the interaction and how to influence and engineer different parameters. Broadly, these interactions are often described by the coupling of various degrees of freedom of the quantum materials, including charge, spin, lattice, orbital, and topology represented in Fig. 1.1. The probing techniques often involve application of electricity, magnetism, light, stress, or heat to provide some sort of stimulus and measure the overall system response, which provides insight into how those degrees of freedom uncouple or recouple or how they can be manipulated [1].

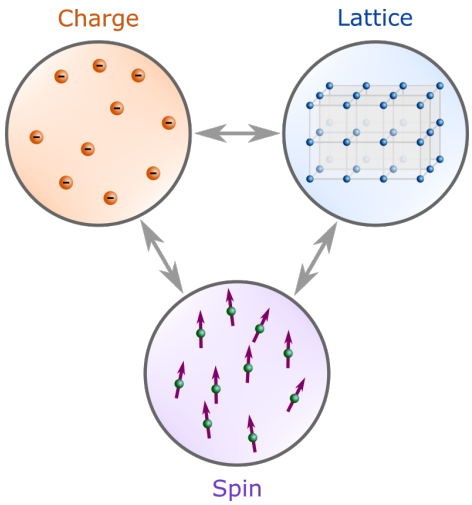

Figure 1.2: Schematic of the interacting charge, spin, and lattice degrees of freedom that are of focus in this work.

In this dissertation, we focus on three different magnetic materials or class of material that exhibit strongly correlated behavior and specifically exhibit strong coupling between charge, spin, and lattice degrees of freedom (represented schematically in Fig. 1.2): elemental chromium (Cr), antiperovskite manganese nitrides (Mn_3AN), and iron rhodium (FeRh). These materials will be studied in confined geometries, usually confined in one dimension as thin films, in which there is

a breaking of the symmetry of bulk which has implications for the correlative behavior. Thin films provide advantages in some experimental methods and for understanding how these phenomena may extend to the types of technological applications that require miniaturization. The types of experiments conducted in this work include more common techniques of magnetometry, electric transport, and simple x-ray diffraction as well as more advanced techniques such as time-resolved x-ray diffraction following laser-induced photoexcitation and polarized neutron reflectometry.

To begin with, however, this chapter introduces some of the broad concepts that are needed to understand these materials and experiments. We start with a basic introduction of current understanding of the origins of magnetism and the types of magnetic ordering that are relevant to the materials studied in this work, followed by a brief look at what the magnetic effects of confining the dimensions of the material. We also briefly introduce magnetoelectric transport and the interaction of x-rays and neutrons with matter, which are the bases for the main experimental techniques here. And finally we discuss ultrafast laser-induced spin dynamics and the three-temperature model of charge, spin, and lattice interactions.

In Chapter 2, we present the sample fabrication, characterization, and experimental methods that are relevant to this work. The fabrication methods involve sputter deposition and lithography. Characterization and experimental methods include magnetometry, electric transport, and x-ray and neutron reflectometry and diffraction. While some of these techniques were conducted in-house at UC San Diego in the Fullerton lab or at the Nano3 facility, which is part of the San Diego Nanotechnology Infrastructure (SDNI) of UC San Diego, some experiments were conducted at national laboratories and user facilities, including the Advanced Photon Source (APS) at the Argonne National Laboratory (ANL), the Linac Coherent Light Source (LCLS) at the SLAC National Accelerator Laboratory (SLAC), the High Flux Isotope Reactor (HFIR) at the Oak Ridge National Laboratory (ORNL), the High Field Magnet Laboratory (HFML), the European Synchrotron Radiation Facility (ESRF), and the Spallation Neutron Source (SNS) at the ORNL. A brief summary of these facilities and the experimental capabilities relevant to this

work are also included.

Chapter 3 focuses on measurements in thin film Cr, primarily through three experiments utilizing x-ray diffraction to measure the lattice distortion in a system that exhibits coupled charge, spin, and lattice degrees of freedom. The first experiment involves characterizing the lattice distortion and order parameter as a function of temperature, and the other two experiments observe the dynamic behavior of this ordering following ultrafast photoexcitation on two very different time scales. In the first 10 ps following photoexcitation (ultrafast time scales), we observe complex nonequilibrium behavior and demonstrate transient enhancement of the order in the system. Measurements on much longer time scales, from 10 ps to 400 ns, demonstrate a slowing down of the recovery of ground state order which demonstrates a probe of the energetic landscape through the time domain. Chapter 4 involves fabrication and characterization of thin film Mn_3AN which exhibit complex magnetovolume effects. We measure time-resolved x-ray diffraction following photoexcitation, which demonstrates the competing pressures of phononic and negative thermal expansion. And finally, Chapter 5 involves experiments of thin film iron rhodium (FeRh). We make measurements in high magnetic fields to measure the phase transition and model the system in order to understand the nature of the magnetic phase diagram and the magnetic phases. We also make polarized neutron reflectometry measurements as a probe of strain effects in order to determine the magnetic depth profile of a thin film and of patterned stripes of FeRh. We end in Chapter 6 with a brief conclusion of this work.

1.1 The Origins of Magnetism

Magnetism is not exactly a new discovery, with the earliest known references to magnetite, also known as lodestone or Fe_3O_4, in Chinese writings dating back possibly as far as 4000 B.C.E. The ancient Greeks were also fascinated by their discovery of this material that is able to attract some other materials from a distance, with evidence of its study in the 6^{th} century B.C.E. [16, 17].

Humans were able to make use of magnetism long before gaining any real insight into it, most notably for navigation with the development of the compass [17, 18]. But it has really only been for the last two centuries, once Hans-Christian Oersted made the accidental discovery in 1820 of the production of a magnetic field by a current-carrying wire, that more scientific and mathematical rigor in magnetism have been developed, beginning with more phenomenological relations of electricity and magnetism and continuing into the atomic origins of magnetism. As understanding has grown, our society has been revolutionized with magnetism-based technologies, but we have also become aware of how much more there is that remains to be explained.

We will look here at magnetism on three scales. We start with the moment of an atom and how magnetism arises from its electrons. We then look at the picture of groups of atoms which are able in limited ways to interact. And then we discuss the magnetism that comes from itinerant electrons which are unbound to atoms. These treatments will help us understand the magnetic ordering seen in materials, including the materials studied in this work.

1.1.1 The Moment of an Isolated Atom

We begin by presenting the theory of how a magnetic moment arises in a single atom. The big picture here is that the moment is primarily the result of two properties of electrons, their orbital motion and an intrinsic property called spin, and the coupling between these two properties. Most of the mathematical derivations and more detailed explanations have been omitted here, but these can be found in quantum mechanics texts or magnetism texts discussing the problem of the hydrogen atom.

Electron Orbitals

In the Bohr model of an atom, electrons are in a circular orbit around a nucleus in a Coulomb potential due to the nucleus of charge Ze where Z is the atomic number of the atom. It is assumed that each electron experiences a Coulomb potential solely from the positively-charged

nucleus and not from other electrons in the atom. This potential is

$$\varphi_e = -\frac{Ze^2}{4\pi\varepsilon_0 r},$$

where r is the distance between the nucleus and the electron and $\varepsilon_0 = 8.854 \times 10^{-12}$ F/m is the permittivity of free space. In order to solve for the allowable energies of the electron, we must start with the time-independent Schrödinger equation

$$-\frac{\hbar^2}{2m_e}\nabla^2\Psi + V(r)\Psi = E\Psi, \tag{1.1}$$

where $\hbar = \frac{h}{2\pi}$, $h = 6.626 \times 10^{-34}$ J/s is the Planck constant, and m_e is the electron mass.

Separation of variables in polar coordinates allows a simplification onf Eq. 1.1 into three ordinary differential equations, with a wave function that is a product of three functions: $\Psi(r,\theta,\phi) = R(r)\Theta(\theta)\Phi(\phi)$. The derivation of the angular component of Eq. 1.1 has several implications. First, it finds that the z component of the orbital angular momentum is quantized with

$$L_z = m_l\hbar, \tag{1.2}$$

where m_l is an integer. It also finds that the total magnitude of the orbital angular momentum is quantized with

$$|\boldsymbol{L}| = \hbar\sqrt{l(l+1)}, \tag{1.3}$$

where l is a whole number. And finally, it finds that the angular components of the wave function, denoted as $Y_{l,m_l}(\theta,\phi)$ which are called the spherical harmonics, are determined by the quantum numbers l and m_l, or by the total magnitude of the angular momentum and the magnitude in one

direction. This angular component of the wave function can be expressed as

$$Y_{l,m_l}(\theta,\phi) = \sqrt{\frac{2l+1}{4\pi}\frac{(l-m_l)!}{(l+m_l)!}} P_l^{m_l}[\cos\theta]\, e^{im_l\phi}, \tag{1.4}$$

where $P_i^j[x]$ are the generalized Legendre polynomials.

Next, we consider the radial component of the wave function. In this derivation, the solution to the angular components and the Coulomb potential are substituted into Eq. 1.1. The end result is a radial component of the wave function that looks like

$$R_{n,l}(r) = \left(\frac{2Z}{na_0}\right)^{3/2} \left(\frac{(n-l-1)!}{2n((n+l)!)}\right)^{1/2} e^{-Zr/na_0} \left(\frac{2Zr}{na_0}\right)^l F_{n-l-1}^{2l+1}\left[\frac{2Zr}{na_0}\right], \tag{1.5}$$

where $F_i^j[x]$ are the generalized Laguerre polynomials of order i, n is a natural number, and $a_0 = \frac{4\pi\varepsilon_0\hbar^2}{m_e e^2}$ is the Bohr radius.

Combining Eq. 1.4 and Eq. 1.5, the wave function for the electron in the atom is

$$\Psi_{n,l,m_l}(r,\theta,\phi) = R_{n,l}(r) Y_{l,m_l}(\theta,\phi) \tag{1.6}$$

with corresponding energies

$$E_n = -\frac{Z^2}{n^2}\left(\frac{m_e e^4}{8\varepsilon_0^2 h^2}\right). \tag{1.7}$$

So this quantum mechanical approach to the wave function, referred to as the orbital, for an electron finds quantized energy levels which depend on n where $n = 1, 2, 3, \ldots$. The principal quantum number n designates the electron shell. For an electron occupying a higher shell, its probable radial distance from the nucleus increases from the lowest energy ground state with $n = 1$. One consequence of this is increasing atom size as higher energy states are occupied.

The magnitude of the orbital angular momentum in this model is quantized and depends on l where $l = 0, 1, 2, \ldots, n-1$. The orbital angular momentum quantum number l helps determine

the shape of the orbital. These different orbital shapes have been assigned letters as label, where $l = 0$ refers to the s subshell, $l = 1$ to the p subshell, $l = 2$ to the d subshell, $l = 3$ to the f subshell, $l = 4$ to the g subshell, and continuing on in alphabetical order, skipping over j and other letters already used.

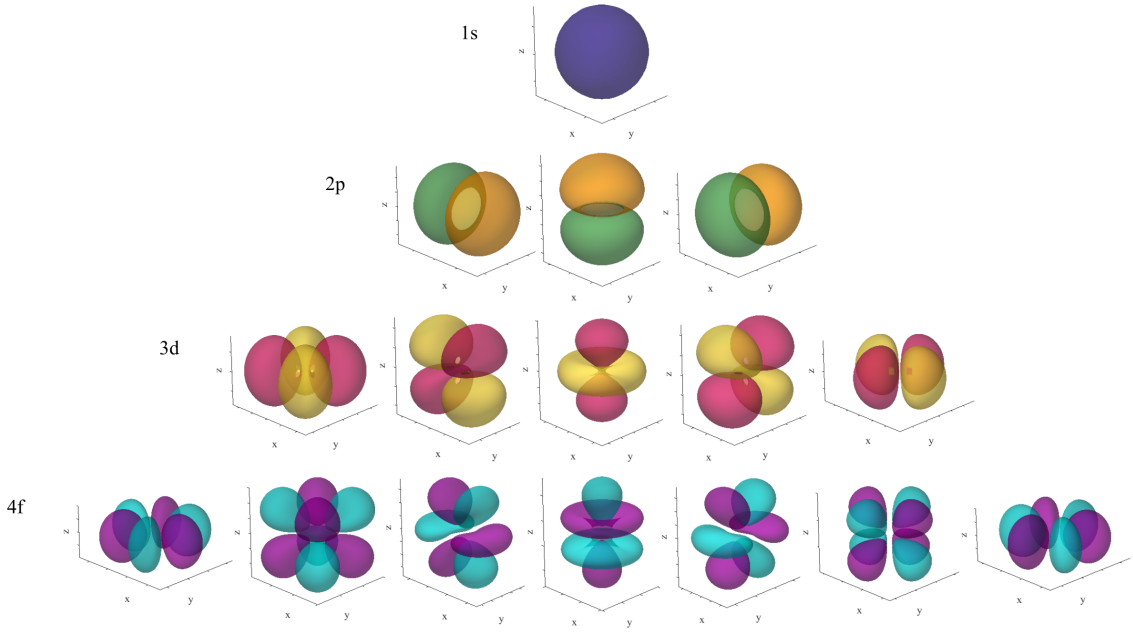

Figure 1.3: Schematic of the $1s$ ($n = 1$ and $l = 0$), $2p$ ($n = 2$ and $l = 1$), $3d$ ($n = 3$ and $l = 2$), and $4f$ ($n = 4$ and $l = 3$) orbitals of the hydrogen atom. It should be noted that these are not to scale: the most probable radial distance of the electron increases significantly with n. Figures produced with code adapted from [19]. Copyright 2011 by Peter van Alem.

And then there is a spatial quantization to the orbital angular momentum, where the projection along an axis depends on m_l where $m_l = 0, \pm 1, \pm 2, ..., \pm l$. The magnetic quantum number m_l references the orientation of the subshell, with $2l + 1$ possibilities. Fig. 1.3 shows the shapes of the $1s$ orbital, the three $2p$ orbitals, the five $3d$ orbitals, and the seven $4f$ orbitals.

All this means that for a total orbital angular momentum of $|\boldsymbol{L}| = \hbar\sqrt{l(l+1)}$, the projection along an axis z is $L_z = m_l\hbar$, with possible L_z quantized and ranging from $-l\hbar$ to $l\hbar$. For a system in the presence of a magnetic field $\boldsymbol{H}$ and with the field axis defined to be along $\hat{z}$, it is

clear that L_z will always be less than $|\boldsymbol{L}|$, meaning the orbital angular momentum can never be fully aligned to the field. Instead, precessional motion of $\boldsymbol{L}$ along $\hat{z}$ with a constant L_z is observed, which we will see has an important implication for the atom's magnetism.

Orbital Moment

Moving electric charges will generate a magnetic field: a loop of current I that encloses an area A has a magnetic moment of $\mu = IA$, with its direction determined by the right-hand rule. Stepping into a classical model of the atom, the electron in an atom is a moving electric charge which is orbiting a nucleus with speed v at a radius r. The current is the quotient of the charge -3 and the period of rotation $2\pi r/v$, so $I = -\frac{ev}{2\pi r}$. By multiplying by the area enclosed by the electron motion, the orbital moment is found to be $\boldsymbol{\mu_\ell} = -\frac{1}{2}e\boldsymbol{r} \times \boldsymbol{v}$. The orbital angular momentum of the electron can be expressed as $\boldsymbol{L} = m_e \boldsymbol{r} \times \boldsymbol{v}$, so the moment of the orbiting electron can be expressed in terms of the angular momentum as

$$\boldsymbol{\mu}_\ell = -\frac{e}{2m_e}\boldsymbol{L} = \gamma \boldsymbol{L},$$

where $\gamma = -\frac{e}{2m_e}$ is the gyromagnetic ratio. The projection of the magnetic moment in some direction, in this case the z-axis along the field, can then be expressed as $\mu_{\ell,z} = \gamma L_z$. The possible L_z are quantized as described in Eq. 1.2, which is substituted in to get

$$\mu_{\ell,z} = -\frac{e\hbar}{2m_e} m_l = -\mu_B m_l,$$

where $\mu_B = \frac{e\hbar}{2m_e} = 9.274 \times 10^{-24}$ Am^2 is called the Bohr magneton. Thus, the z-component of the orbital magnetic moment is quantized as an integral number of Bohr magnetons and it is possible to have zero orbital moment when $m_l = 0$. There is another quantity of relevance, the g-factor, which is the ratio of the moment (in units of μ_B) to the angular momentum (in units of $\hbar$). For the case of orbital moment and orbital angular momentum, the orbital g-factor is $g_\ell = 1$.

We know that there is a potential energy of a moment in an applied field, $E = -\boldsymbol{\mu} \cdot \boldsymbol{B}$. This means that in the presence of an external field, the degeneracy of electron energies for a given n is broken, the moment along the field direction is quantized and the energy levels of electrons with different m_l will split. This effect, the Zeeman effect, has been observed experimentally.

Electron Spin

Electrons have an intrinsic angular momentum called spin which adds an additional component to the moment of an electron. Descriptions of the spin angular momentum sometimes draw an analogy to a picture of a moment arising from an electron spinning on its axis, though this is not what is actually occurring. The electron spin is described in quantum mechanics and has been observed in experiments such as the Stern-Gerlach experiment, but it does not have a simple classical explanation. The spin angular momentum $\boldsymbol{S}$ is treated in much the same way as the orbital angular momentum $\boldsymbol{L}$. There is a spin angular momentum quantum number s analogous to l, though for an electron which is referred to as a spin-1/2 particle, this is fixed with $s = \frac{1}{2}$ so the magnitude of the spin angular momentum of an electron is always

$$|\boldsymbol{S}| = \hbar\sqrt{s(s+1)} = \frac{\sqrt{3}}{2}\hbar.$$

There are only two possible orientations of the spin along an axis, commonly referred to as spin-up and spin-down with spin magnetic quantum number $m_s = \pm\frac{1}{2}$:

$$S_z = m_s\hbar = \pm\frac{\hbar}{2}.$$

This quantization of the spin angular momentum has been confirmed by the Stern-Gerlach experiment.

The spin angular momentum also results in a moment, which is defined as

$$\boldsymbol{\mu}_s = -g_s \frac{e}{2m_e} \boldsymbol{S}, \tag{1.8}$$

where g_s is the spin g-factor (analogous to the orbital g-factor defined earlier). Experimentally, it has been determined that $g_s \approx 2.0023$ [20]. The spin magnetic moment is found to be

$$|\boldsymbol{\mu}_s| = g_s \frac{e\hbar}{2m_e} \sqrt{s(s+1)} \approx \sqrt{3}\mu_B,$$

and the projection of the magnetic moment in the z-direction is

$$\mu_{s,z} = -g_s \frac{e\hbar}{2m_e} m_s \approx \pm\mu_B.$$

So while an electron may or may not have an orbital moment, the implication of this result is that it always has a spin moment.

In an atom or molecule, the electrons are almost always arranged in pairs which have opposing spin orientations and thus cancel each other out. When there is an even number of electrons and they cancel completely, there is only the orbital contribution to the moment, which results in a phenomenon called diamagnetism, described more later in this chapter. For an odd number of electrons, it is not possible to cancel out the spin moment, and the result is called paramagnetism.

The Spin-Orbit Interaction Energy

The separation of the spin and orbital components of the angular momentum is complicated by the interaction between the two, called spin-orbit interaction. So far, the two have been treated independently, but in reality, the spin moment has an impact on the orbital motion and the orbital moment has an impact on the spin. Moving into the frame of reference of the electron,

the nucleus of charge Ze is orbiting around it, generating a magnetic field which interacts with the spin magnetic moment (in this frame, the electron is at rest and has no orbital moment). The magnitude of the magnetic field is $B = \mu_0 Zev/4\pi r^2$ where $\mu_0 = 1/\varepsilon_0 c^2 = 1.256 \times 10^{-6}$ N/A^2 is the permeability of free space. The energy of interaction of this magnetic field and the electron's intrinsic spin moment given in Eq. 1.8 is $E_{\text{so}} = -\boldsymbol{\mu}_s \cdot \boldsymbol{B}$, and can be approximated as

$$E_{\text{so}} \approx -\frac{\mu_0 \mu_B^2 Z^4}{\pi a_0^3 \hbar^2} \boldsymbol{L} \cdot \boldsymbol{S}. \tag{1.9}$$

The Z^4 dependence means that for lighter elements, the spin-orbit interaction is weak, but for heavier elements, it becomes strong and can result in varied magnetic phenomena such as magnetocrystalline anisotropy, anomalous and spin Hall effects, and magnetostriction.

In Eq. 1.7, the energy levels of the electron are shown to depend on the principal quantum number n. Here, these energies are modified by E_{so}, which depends on the orbital and spin angular momentum:

$$E \approx E_n + E_{\text{so}},$$

where E_n was found in Eq. 1.7 and E_{so} in Eq. 1.9. We will return later to a discussion of the spin-orbit interaction and first discuss how electrons occupy different states in the atom.

Electron Configurations in an Atom

We have described the electron orbitals with the three quantum numbers n, l, m_l. For each shell designated by the principal quantum number n, there are n subshells designated by the orbital angular momentum quantum number l. For each of these subshells, there are $2l+1$ possible orbitals, designated by the spatial quantization number m_l. One additional quantum number, the spin magnetic quantum number m_s, describes the spin state of the electron and rounds out the description of the electron's configuration in the atom.

There are two primary principles that govern electron configurations and the occupancy

of the orbitals in an atom: The Pauli exclusion principle and Hund's rules. the Pauli exclusion principle states that no two electrons can have the same set of quantum numbers n, l, m_l, m_s. This means that each orbital can have at most two electrons in it and those two electrons must have different spins. Atoms with more than two electrons can only have two electrons at the lowest energy level described by Eq. 1.7. As an example, the electron configuration of silicon (Si) can be described by $1s^2 2s^2 2p^6 3s^2 3p^2$. The lowest energy subshell, $1s$, has two electrons in it, denoted by the superscript 2. The next lowest energy subshell, $2s$, also has two electrons in it. The orbital $2p$ has three orbitals corresponding to $m_l = 0, \pm 1$, with two electrons in each for a total of six electrons. Two more electrons can occupy $3s$. And then the two additional electrons will occupy the $3p$ subshell. The Aufbau principle tells us that the electrons will fill up lower energy levels before higher ones. The order of filling given this will be $1s$, $2s$, $2p$, $3s$, $3p$, $4s$, $3d$, $4p$, $5s$, $4d$, $5p$, $6s$, $4f$, $5d$, $6p$, $7s$, $5f$, $6d$, $7p$, etc. This generally only applies for neutral atoms in their ground state and has many exceptions given the small energy gap between some levels, such as $3d$ and $4s$, and other energetic considerations to each state.

Hund's rules build on the Pauli exclusion principle to define the electron configuration of the ground state of the atom. The first of these three rules is that the energy is minimized when the total spin quantum number, which is the sum of the spin magnetic quantum numbers for each electron ($S = \sum m_{s_i}$), is maximized for the unfilled subshell. That means that each orbital in the open subshell will fill with a single electron before any of them will be filled with two. In the example of Si, above, each orbital in $1s$, $2s$, $2p$, and $3s$ contains two electrons with opposite spin. In the $3p$, subshell, however, two of the three orbitals will be occupied by one electron (as opposed to both electrons occupying a single orbital). This occurs due to Coulombic forces and screening effects. The second rule is that the total orbital angular momentum quantum number, which is the sum of the spatial quantization numbers of each electron ($L = \sum m_{l_i}$) is maximized. The classical interpretation of this is that electrons rotating in the same direction have a reduced Coulomb energy compared to those rotating in opposite directions. The third rule assists in

minimizing the spin-orbit interaction energy. It tells us that the total angular momentum quantum number J is

$$J = \begin{cases} |L-S| & \text{if the open subshell is less than half full} \\ S & \text{if the open subshell is half full} \\ |L+S| & \text{if the open subshell is more than half full} \end{cases} \tag{1.10}$$

These rules work quite well in some simpler cases but, predictably, do not always hold. Particularly when more than one atom is considered in our model, there are effects that have not been accounted for here. But this is a good starting point for determining the configuration of electrons in an atom.

Neutron and Proton Spins

A natural question at this point might be to wonder about magnetism that originates from the other subatomic particles that make up the atom. The nucleus also has an intrinsic spin, which can be treated similarly to the electron's spin. In this case, the spin angular momentum is labeled $|\boldsymbol{G}|$ and the associated quantum numbers I and m_I. The angular momentum is quantized such that

$$|\boldsymbol{G}| = \hbar\sqrt{I(I+1)},$$

where I can be an integer or half-integer (0, $\frac{1}{2}$, 1, $\frac{3}{2}$, ...). The spatial quantization allows m_I to take on values of $-I$, $-I+1$, ... $I-1$, I. The nuclear magnetic moment is expressed as

$$\boldsymbol{\mu}_N = -g_I \frac{e}{2m_p}\boldsymbol{G},$$

where m_p is the proton mass and g_I is the nuclear g-factor. Protons have $g_I = 5.586$, and neutrons have $g_I = -3.826$. The isotope of hydrogen called deuteron, which has one proton and neutron,

has $g_I = 0.857$. The magnitude of the nuclear magnetic moment is

$$|\boldsymbol{\mu}_N| = g_I \frac{e\hbar}{2m_p}\sqrt{I(I+1)} = g_I \mu_N \sqrt{I(I+1)},$$

where $\mu_N = \frac{e\hbar}{2m_p} = 5.05 \times 10^{-27}$ Am^2 is the nuclear magneton. It follows that

$$\mu_{N,z} = g_I \mu_N m_I.$$

The nuclear magneton is three orders of magnitude smaller than the Bohr magneton, so the nuclear magnetic moments are typically much weaker than the electron moments. As a result, the magnetism of an atom is dominated by the magnetism of the electrons and the nuclear contribution is usually ignored.

The Total Moment of an Atom

There are two main models of coupling used to account for the spin-orbit interaction: L-S coupling and j-j coupling. L-S coupling involves combining the orbital angular momenta of the electrons separately from the spin momenta before introducing the coupling of spin and orbit as a perturbation. This works well generally for lighter elements, but given the Z^4 term in the spin-orbit energy, it is less useful for heavier elements where the spin-orbit coupling of each electron is significant. In that case, j-j coupling provides a way of first accounting for the spin-orbit coupling of each electron and then coupling together different electrons. For many heavier materials, neither model is sufficient, but they provide some guesses.

In the case of L-S coupling, there is a net angular momentum and the magnitude of the total moment of the atom given by

$$|\boldsymbol{\mu}_{\text{atom}}| = -g_{\text{atom}} \frac{e}{2m_e} |\boldsymbol{J}| = g_{\text{atom}} \mu_B \sqrt{J(J+1)}, \tag{1.11}$$

where J was defined in Eq. 1.10 and the Landé g-factor g_{atom} [21] can be shown to be

$$g_{\text{atom}} = 1 + \frac{S(S+1) + J(J+1) - L(L+1)}{2J(J+1)}. \tag{1.12}$$

In the case of j-j coupling, the total moment of the atom is found to be

$$\boldsymbol{\mu}_{\text{atom}} = \sum \boldsymbol{\mu}_i = -\sum g_i^{\text{j-j}} \frac{e}{2m_e} \boldsymbol{j_i}, \tag{1.13}$$

where $\boldsymbol{j_i}$ are the angular momenta of each electron. In this case, there are different g-factors for electrons in different orbitals.

Experimentally, the moment of a material is sometimes expressed in units of Bohr magnetons. This gives us a measure of g_{atom} and takes on non-integral values. The measured moment for many materials is often quite different from what is predicted from this model for the atom. One consideration for some materials is the quenching of the orbital angular momentum. In a crystal lattice, outer electrons can be affected by the electric field of neighboring ions and strongly coupled to the crystal lattice (orbit-lattice coupling), reducing the influence of an applied field on the orbital motion and reducing the orbital contribution to the moment. The spins are still free to align and so the system behaves as $L = 0$ and $J = S$, which is called quenching of the orbital angular momentum. This is true in some of the $3d$ transition metals, where the electrons in these outermost partially-filled orbitals experience strong homogeneous electric fields from adjacent ions which are stronger than spin-orbit interactions. The measured atomic moments are usually close to what would be seen if $L = 0$. In the case of $4f$ lanthanides, however, L-S coupling predicts the observed atomic moment quite well. The electrons in the partially filled $4f$ subshells which are determining the magnetism of the atom are closer to the nucleus than the $5s$ and $5d$ orbitals which are filled and less subject to crystal field effects [22, 23].

So while there are exceptions to the rules and anomalous behavior in many materials, the model of the atom laid out here is a useful starting point for understanding the origin of magnetism

in different materials. However, this picture will become very complicated very quickly when looking at real systems in which there are a large collection of atoms.

1.1.2 Collections of Localized Moments

In this section, we move on from the magnetism of a single atom to the collective magnetic behavior when large groups of atoms or molecules are assembled. These localized moments sometimes interact through the exchange interaction and result in a wide range of phenomena. The broad classes of magnetic behavior that will be discussed include diamagnetism, paramagnetism, ferromagnetism, antiferromagnetism, and ferrimagnetism. This picture of moments as localized is limited, especially for metals, but it can effectively describe the magnetic ordering seen in many materials. We begin with diamagnetism, which is valid for all materials, though it is often ignored when studying other phenomena which have a much larger effect. Next, we discuss a model of paramagnetism, relevant for materials that contain atoms with a net moment. From there, we discuss the phenomenological molecular field theory to build a basis of understanding magnetic phenomena that arise in the presence of interactions between localized moments. This theory works well in some ways, despite being built on the incorrect assumption that there is a strong internal field in a material which is able to align moments over extended regions. We end with a discussion of the exchange interaction, which forms a basis for how to understand the internal field of the molecular field theory and provides a more accurate picture of the interaction of localized moments.

One thing to note at this point is the use of the term ordering, which refers to the collective behavior that that arises from interactions in these materials. A ferromagnetic material is considered to be in an ordered state when there is a tendency for spins to align, which happens at temperatures $T < T_C$, where T_C is called the Curie temperature. Above T_C, the material behaves paramagnetically and considered to be disordered. This is similar for an antiferromagnetic material below and above T_N, the Néel temperature. There are properties that are observed

or which we seek to measure which are called order parameters, which have a temperature dependence in these materials and go to zero at an order-disorder transition. An example of this is the spontaneous magnetization for a ferromagnetic material. An order parameter relevant in this dissertation will be the periodic lattice distortion in Cr, which is examined in Ch. 3.

There are some other important definitions to discuss before beginning this section. Two important quantities in magnetism are the magnetic field **H** (with units of A/m) and the magnetic induction or magnetic flux density **B** (with units of T). In free space, these quantities are linearly related by $\mathbf{B} = \mu_0 \mathbf{H}$, where $\mu_0 = 1.256 \times 10^{-6}$ N/A^2 is the permeability of free space as stated previously. But the relationship becomes more complicated when considering what happens inside of a material: the magnetic moments within the material will respond to an applied field and produce additional magnetic fields (referred to as the demagnetizing field within the material and the stray field outside of it). In this scenario, the relation of **B** and **H** is modified to

$$\mathbf{B} = \mu_0 \left(\mathbf{H} + \mathbf{M} \right),$$

where **M** is the magnetization of the material (with units of A/m), which in a uniformly magnetized material is the vector sum of all the moments in the material divided by the total volume, and note that **H** is a sum of the external contribution and the demagnetizing field.

We also can consider the magnetic susceptibility χ. In an isotropic material, the susceptibility is the dimensionless ratio of the magnetization to the applied field,

$$\chi = \frac{M}{H}, \tag{1.14}$$

which is a measure of how much a material magnetizes in response to a magnetic field. A negative susceptibility indicates an induced magnetization in the material that opposes the applied field. A positive susceptibility indicates alignment of the moments in the direction of the field and its magnitude determines the strength of the alignment, which makes it a useful description of the

magnetic behavior of a material.

Diamagnetism

Diamagnetism is an effect that arises from the precession of electronic orbits in the presence of an applied field. This precession will result in a moment that opposes the field, resulting in a negative susceptibility $\chi < 0$. This is a behavior that is exhibited by all materials, though it is sometimes dominated by other magnetic effects and ignored. Diamagnetism can be treated classically by the Langevin theory [24] or quantum mechanically to achieve the same result. Here, we will start with the Langevin theory of diamagnetism.

This picture considers an electron orbiting a nucleus with angular velocity ω. This is equivalent to a current loop and results in a magnetic moment $\boldsymbol{\mu}_{\text{orbit}} = -\frac{e}{2m_e}\boldsymbol{L}$, where $\boldsymbol{L}$ is the orbital angular momentum of the electron. In a field $\mathbf{H}$ or magnetic induction $\mathbf{B} = \mu_0\mathbf{H}$, the moment experiences a torque given by $\boldsymbol{\tau} = \boldsymbol{\mu}_{\text{orbit}} \otimes \mathbf{B} = \boldsymbol{\omega}_L \otimes \boldsymbol{L}$ where $\boldsymbol{\omega}_L = \frac{e\mu_0}{2m_e}\mathbf{H} = 2\pi f_L$ is an angular velocity and f_L is the Larmor frequency. This describes a precession and results in an induced magnetic moment $\boldsymbol{\mu}_{\text{prec},i} = -\frac{\mu_0 e^2 \mathbf{H}}{4m_e}\langle r^2_{\text{prec},i}\rangle$ where $\langle r^2_{\text{prec},i}\rangle$ is the average of the square of the radius of precession for the electron. For an atom with Z electrons in spherically symmetric orbits, the total moment becomes $\boldsymbol{\mu}_{\text{prec}} = -\frac{\mu_0 Z e^2 \mathbf{H}}{6m_e}\langle r^2\rangle$ where $\langle r^2\rangle$ is the square of the average radial distance of all the electrons in the atom. For an atomic weight A and density ρ, the magnetization due to this precession is

$$\boldsymbol{M} = -\frac{\mu_0 Z e^2}{6m_e}\frac{N_0\rho}{A}\mathbf{H}\langle r^2\rangle,$$

where $N_0 = 6.022 \times 10^{23}$ is Avogadro's number. The diamagnetic susceptibility follows:

$$\chi_{\text{dia}} = -\frac{\mu_0 Z e^2}{6m_e}\frac{N_0\rho}{A}\langle r^2\rangle.$$

Quantum mechanics is required to calculate $\langle r^2\rangle$ for the actual charge distribution of the atom.

But this result demonstrates that the susceptibility is negative, meaning the induced moment will oppose an applied field. These susceptibilities also do not have a strong dependence on temperature, which only appears weakly in $\langle r^2 \rangle$.

Electrons in closed shells in atoms are usually oriented so that there is no net moment in the atom, which means in the presence of a magnetic field, only diamagnetism will apply. This means that materials in which there are no unfilled shells will be diamagnetic. This includes the noble gases such as He, Ne, and Ar. Water and most organic materials are diamagnetic, as are some metals.

Paramagnetism

We now consider an assembled group of atoms that each have a net moment but do not interact (or at least do not interact strongly). The moments will align arbitrarily so that in the absence of an applied field, the sum of the vector moments is zero and there is no net magnetization in the material. But in the presence of an external field, the moments will tend to want to align to the field, opposed by thermal agitation of the atoms. As the field is increased, the alignment increases and there is a linear increase in the magnetization of the material, giving a constant positive susceptibility. The susceptibility decreases with temperature because of the increased thermal agitation.

As with diamagnetism, paramagnetism can be treated classically or quantum mechanically, but with slightly different results. The classical Langevin theory of paramagnetism considers the potential energy of a magnetic moment in a magnetic field:

$$E_{\mathrm{p}} = -\boldsymbol{\mu} \cdot \mathbf{B} = -\mu_0 \mu H \cos(\theta), \tag{1.15}$$

where θ is the angle between the moment and the field, which favors alignment of the moments with the field. There is also a thermal energy $k_B T$ which tends to randomize the alignment of the

moments. The distribution of moments then follow Boltzmann statistics with a probability that is proportional to $e^{\frac{-E_p}{k_B T}} = e^{\alpha \cos\theta}$ where $\alpha = \frac{\mu_0 \mu H}{k_B T}$. Considering the number density of moments that are oriented in each step of $d\theta$ sets up an integral of the magnetic moments in all orientations over all possible angles of the sphere. The resulting magnetization is

$$M = M_0 \left(\coth(\alpha) - \frac{1}{\alpha} \right) = M_0 \mathcal{L}(\alpha),$$

where M_0 is the magnetization corresponding to total alignment of the moments parallel to the field and $\mathcal{L}(\alpha)$ is the Langevin function. The Langevin function goes to 1 for large α (meaning large applied field), which implies that large fields will overcome thermal effects and saturate the magnetization (fully align the moments) in the material. For $\alpha \lesssim 0.5$, the Langevin function can be approximated as linear and the magnetization is given by $M = \frac{\mu_0 n \mu^2 H}{3 n k_B T}$ where n is the number density of the moments. This leads to the Curie law of paramagnetism,

$$\chi_{\text{para}} = \frac{\mu_0 n \mu^2}{3 k_B T} = \frac{C}{T}, \tag{1.16}$$

where $C = \frac{\mu_0 n \mu^2}{3 k_B}$ and the susceptibility of the ideal paramagnet (meaning the moments are localized and noninteracting) is inversely proportional with temperature.

The quantum treatment of paramagnetism, in which the spatial quantization of the magnetic moments is accounted for, improves the agreement between theory and experiment. In this case, the magnetization is found to be

$$M = M_0 \left[\frac{2J+1}{2J} \coth\left(\frac{\alpha(2J+1)}{2J} \right) - \frac{1}{2J} \coth\left(\frac{\alpha}{2J} \right) \right] = M_0 \mathcal{B}_J(\alpha),$$

where $\mathcal{B}_J(\alpha)$ is the Brillouin function and J is the quantum number defined in Eq. 1.10. We

substitute $M_0 = g\mu_B nJ$ where the g-factor was defined in Eq. 1.12 to get

$$M = gn\mu_B J\mathcal{B}_J(\alpha).$$

When $\alpha \ll 1$, $\mathcal{B}_J$ can be approximated by neglecting higher-order terms to get a paramagnetic susceptibility of

$$\chi_{\text{para}} = ng^2\mu_0\mu_B^2\frac{J(J+1)}{3k_BT},$$

once again noting the inverse relationship between susceptibility and temperature. As J increases, the allowed orientations begin to look continuous and $\mathcal{B}_J(\alpha) \to \mathcal{L}(\alpha)$. When $L = 0$ and the orbital moment is quenched, $J = S = \frac{1}{2}$ and $g = 2$ and it can be seen that there are only two allowable moments μ_B parallel and antiparallel to the applied field. In materials, J, L, and S are only known for isolated atoms and the susceptibility must be experimentally determined.

It can be noted that in this calculation, the diamagnetic moment which opposes the applied field has not been accounted for. The diamagnetic susceptibility is usually much smaller than the paramagnetic susceptibility, but the susceptibility of a paramagnetic material can be corrected by the diamagnetic contribution.

Molecular Field Theory

So far, the assumption has been that there is no interaction between the magnetic moments in these materials. This treatment was modified by Weiss [25] to allow for some influence of the magnetization of the surrounding material on each moment with the inclusion of an internal field $\mathbf{H}_{\text{in}}$ in the material that tends to align the spins. He supposed that this field is proportional to the magnetization $\mathbf{M}$ to a first approximation, and $\mathbf{H}$ in the paramagnetic treatment can be replaced by

$$\mathbf{H}_{\text{tot}} = \mathbf{H} + \mathbf{H}_{\text{in}} = \mathbf{H} + \lambda\mathbf{M},$$

where λ is the constant of proportionality. This is called the mean-field approximation. The calculation then proceeds similarly to attain

$$M = M_0 \mathcal{L}(\alpha) \tag{1.17}$$

with the modification of

$$\alpha = \frac{\mu_0 \mu (H + \lambda M)}{k_B T}.$$

In the case of small α, Eq. 1.17 can be simplified and related the magnetization and the field by

$$H = M \left(\frac{3 k_B T}{\mu_0 n \mu^2} - \lambda \right) \tag{1.18}$$

to get what is known as the Curie-Weiss law

$$\chi = \frac{C}{T - \theta}, \tag{1.19}$$

where $\theta = \lambda C = \frac{\mu_0 n \mu^2 \lambda}{3 k_B}$. As before, moving into the quantum mechanical regime replaces the Langevin function $\mathcal{L}(\alpha)$ in Eq. 1.17 with the Brillouin function $\mathcal{B}_J(\alpha)$.

This is applicable for paramagnetic materials which have weak interactions between moments that cannot be neglected. There is still a linear relationship between the inverse susceptibility and temperature, but it is shifted such that the divergence of the susceptibility (or where the inverse susceptibility goes to zero) occurs at $T = \theta$. This shift can take on both positive and negative values for different materials and is a measure of the strength of the interaction between moments due to its dependence on λ. One class of materials which follow the Curie-Weiss law well is salts of the transition elements. There are metals that are paramagnetic, but often this originates in the itinerant electrons and the Curie-Weiss law will not apply.

Ferromagnetism

In paramagnetic materials, the strength of the interaction between moments is quite weak. The next consideration is materials in which this interaction is not weak, which requires us to go back to the definition of α in Eq. 1.18, which includes the strength of the coupling in the numerator through λ. It is still assumed that α is small when temperature T (in the denominator) is large. In this case, the Curie-Weiss law of Eq. 1.19 applies. The critical temperature θ is called the Curie temperature and labeled T_C:

$$\chi = \frac{C}{T - T_C}. \tag{1.20}$$

This predicts that even materials with strong interactions between moments will behave paramagnetically at high temperature.

When $T < T_C$, the limit of small α which was used to simplify the Langevin or Brillouin functions is no longer valid. Now, the magnetization responds to the application of an external field, but it is also nonzero in the absence of that field. Materials that exhibit this behavior are called ferromagnets. The moments in ferromagnetic materials have a strong tendency to align parallel to one another. As a result, even in the absence of an external field, regions called domains are observed in which all the moments are aligned in one direction. In the absence of an applied field, the overall measured moment could be zero, but rather than random orientations for each moment, each domain is spontaneously magnetized in random orientations such that they sum to zero, and the material said to be demagnetized. If a field is applied, the material will be magnetized and will retain a magnetization when the field is removed. The response of the magnetization to the applied field is nonlinear and hysteretic, meaning there is a kind of memory to the ordering and the alignment of all of the domains (saturation) occurs at fields easily achievable in a lab.

The magnetization of ferromagnetic domains in the absence of an applied field is called the

spontaneous magnetization M_s, which is represented graphically later in this chapter in Fig. 1.6(a). In the molecular field model, $H = 0$ was used to determine the temperature dependence of M_s from the Langevin or Brillouin functions. At $T = T_C$, the spontaneous magnetization is zero, and it increases as temperature decreases until reaching maximum alignment M_0 at $T = 0$ K. Comparing this model to experiment, the temperature dependence of the spontaneous magnetization for Fe, Co, and Ni is predicted somewhat well by the Brillouin function with $J = \frac{1}{2}$ or $J = 1$, but with noticeable deviations [26]. The experimentally determined moments of the atoms are significantly different from what would be implied by these total angular momentum quantum numbers, suggesting that some of our assumptions must be revisited, for example, the assumption that L-S coupling is sufficient to describe the spin-orbit interaction and that the localization of the magnetic moments applies for these materials.

Antiferromagnetism

As the name would suggest, antiferromagnetism refers in a way to the opposite ordering of ferromagnetism, which is much more difficult to measure. Antiferromagnetic materials have a small positive susceptibility χ at all temperatures, like paramagnets, but with an unusual temperature dependence. They have a strong coupling of moments, like ferromagnets, but an antiparallel alignment of the moments is preferred. These materials can be thought of as having two (or more) sublattices in which the moments of each sublattice are in parallel alignment and have a spontaneous moment similar to ferromagnets, but in which the sum of the vector moments of each of the sublattices is zero.

Molecular field theory can be used again here. In this case, the assumption is that there are two sublattices which are labeled A and B. The assumption is that there is a crystal in which the nearest neighbor interactions that must be accounted for are all A-B interactions and all A-A and B-B interactions can be neglected. There are two molecular fields $H_{\mathrm{m,A}}$ and $H_{\mathrm{m,B}}$ which reflect that the moments in sublattice A experience a field due to the neighboring moments in

sublattice B and vice versa:

$$H_{\mathrm{m,A}} = -\lambda M_{\mathrm{B}}$$
$$H_{\mathrm{m,B}} = -\lambda M_{\mathrm{A}}$$

and $H_{\mathrm{tot},i} = H + H_{\mathrm{m},i}$ for each sublattice. With the assumption that the relation $\chi = C/T = M/H_{\mathrm{tot}}$ holds, which is reasonable at high temperature, this gives

$$\begin{aligned} M_{\mathrm{A}} T &= C'(H - \lambda M_{\mathrm{B}}) \\ M_{\mathrm{B}} T &= C'(H - \lambda M_{\mathrm{A}}). \end{aligned} \tag{1.21}$$

Adding these together gives

$$(M_{\mathrm{A}} + M_{\mathrm{B}})T = 2C'H - \lambda C'(M_{\mathrm{A}} + M_{\mathrm{B}}).$$

Since the total magnetization is $M = M_{\mathrm{A}} + M_{\mathrm{B}}$, the susceptibility is

$$\chi = \frac{2C'}{T + \lambda C'} = \frac{C}{T + \Theta}.$$

This looks similar to the case of the ferromagnet which is paramagnetic above its ordering temperature, following the Curie-Weiss law in Eq. 1.20. A key difference here is the difference in sign in the denominator, which reflects that when a field is applied, each sublattice is magnetized parallel to the field but there is an internal molecular field that opposes that magnetization from the other sublattice. This reduces the susceptibility from the ideal paramagnetic behavior. If the susceptibility were extrapolated the susceptibility to low temperature, the divergence would occur at a negative temperature $T = -\Theta$ (alternatively, it can be thought of as the inverse susceptibility going to zero at this negative temperature).

At an ordering temperature called the Néel temperature T_N, thermal effects are no longer strong enough to overcome the interactions between the moments, and the sublattices of the antiferromagnet spontaneously magnetize antiparallel to one another. This means the net magne-

tization is $\mathbf{M} = \mathbf{M}_\mathrm{A} + \mathbf{M}_\mathrm{B} = 0$. Just below T_N, this spontaneous magnetization is small and it can be assumed that $\mathrm{M} \propto \mathrm{H}$ is still valid, so $H = 0$ is used in Eq. 1.21 to find $M_\mathrm{A} T_N = -\lambda C' M_\mathrm{B}$. Substituting in $\mathbf{M}_\mathrm{A} = -\mathbf{M}_\mathrm{B}$, the Néel temperature is found to be $T_N = \lambda C' = \Theta$. So the susceptibility of an antiferromagnetic material in its paramagnetic phase is

$$\chi = \frac{2C'}{T + \lambda C'} = \frac{C}{T + T_N}, \tag{1.22}$$

and the temperature at which the inverse susceptibility above T_N would extrapolate to zero is $T = -T_N$.

Below T_N, the same analysis as for ferromagnetism is followed for each of the two sublattices i individually, which each exhibit spontaneous magnetization $M_{s,i}$ and approach $M_{0,i}$ at $T = 0$ K:

$$M_{s,i} = M_{0,i} \mathcal{B}_J(\alpha),$$

where

$$\alpha = \frac{\mu_0 \mu H_{\mathrm{tot},i}}{k_B T},$$

where μ is the moment of each atom, which is the same for both sublattices.

The spontaneous magnetization in the absence of an external field ($H = 0$) is

$$M_{s,i} = M_{0,i} \mathcal{B}_J\left(\frac{\mu_0 \mu \lambda M_{s,i}}{k_B T}\right).$$

Therefore, there is the same temperature dependence for the spontaneous magnetization for each sublattice, understanding that these are oriented antiparallel so they sum to zero, which will be represented graphically later in the chapter in Fig. 1.6(b). So the net magnetization of the system at any temperature in the absence of an external field is zero.

In the absence of a field, the axis of the magnetization of the sublattices (the spin axis) in a crystal will have a preferred direction based on the magnetocrystalline anisotropy. When an

external field is applied, there is a small positive susceptibility which depends on the direction of the applied field in relation to the spin axis. For a field applied perpendicular to the spin axis, the susceptibility is constant, independent of temperature. For a field applied parallel to the spin axis, the susceptibility goes to zero as temperature goes to zero. So the overall susceptibility for these materials has a peak or plateau at T_N and exhibits antiferromagnetic behavior below and paramagnetic behavior above T_N. An example representation of inverse susceptibility vs. temperature is shown later in the chapter in Fig. 1.5.

Ferrimagnetism

Ferrimagnetic materials are a little like antiferromagnetic materials in which there are two or more antiparallel sublattices, with moments within each sublattice aligned. In this case, however, the magnitudes of the magnetization of each sublattice are different, usually as a result of different magnetic species in the different sublattices. This means that ferrimagnetic materials look a little like ferromagnetic materials with spontaneous magnetization below their ordering temperature (the Curie temperature T_C), saturation of the magnetization, and hysteresis. Above their ordering temperature, they are paramagnetic.

We will once again begin with molecular field theory. As temperature increases above the Curie temperature, the measured susceptibility of ferrimagnets is asymptotic to the Curie-Weiss law of Eq. 1.22. However near the Curie temperature, it deviates from this and is better explained by considering not only interactions of moments with nearest neighbor moments of the other sublattice, but also of interactions with nearby spins in the same sublattice, meaning the molecular field describes parallel alignment of spins to neighboring spins in the same lattice and antiparallel alignment to neighboring spins in the opposite sublattice. The internal fields for sublattices A and

B then become

$$H_{\mathrm{m,A}} = -\lambda_{\mathrm{AB}} M_{\mathrm{B}} + \lambda_{\mathrm{AA}} M_{\mathrm{A}}$$

$$H_{\mathrm{m,B}} = -\lambda_{\mathrm{AB}} M_{\mathrm{A}} + \lambda_{\mathrm{BB}} M_{\mathrm{B}},$$

where it is assumed that $\lambda_{\mathrm{AB}} = \lambda_{\mathrm{BA}}$.

For $T > T_C$, the assumption is that the Curie law will with a modification accounting for the fractional volumes φ_{A} and φ_{B} of the sublattices (in the antiferromagnetic case, it was assumed that $\varphi_{\mathrm{A}} = \varphi_{\mathrm{B}} = 0.5$). This gives

$$M_{\mathrm{A}} T = C\varphi_{\mathrm{A}} H_{\mathrm{tot,A}} = C\varphi_{\mathrm{A}}(H - \lambda_{\mathrm{AB}} M_{\mathrm{B}} + \lambda_{\mathrm{AA}} M_{\mathrm{A}})$$

$$M_{\mathrm{B}} T = C\varphi_{\mathrm{B}} H_{\mathrm{tot,B}} = C\varphi_{\mathrm{B}}(H - \lambda_{\mathrm{AB}} M_{\mathrm{A}} + \lambda_{\mathrm{BB}} M_{\mathrm{B}}).$$

We define $\alpha = \lambda_{\mathrm{AA}}/\lambda_{\mathrm{AB}}$ and $\beta = \lambda_{\mathrm{BB}}/\lambda_{\mathrm{AB}}$ and sum the magnetization of the two sublattices and simplify to find the inverse susceptibility:

$$\frac{1}{\chi} = \frac{T}{C} + \frac{1}{\chi_0} - \frac{\zeta}{T - \Theta}, \tag{1.23}$$

where

$$\frac{1}{\chi_0} = \lambda_{\mathrm{AB}}(2\varphi_{\mathrm{A}}\varphi_{\mathrm{B}} - \varphi_{\mathrm{A}}^2\alpha - \varphi_{\mathrm{B}}^2\beta)$$

$$\Theta = \lambda_{\mathrm{AB}}\varphi_{\mathrm{A}}\varphi_{\mathrm{B}} C(2 + \alpha + \beta)$$

$$\zeta = \lambda_{\mathrm{AB}}^2 \varphi_{\mathrm{A}}\varphi_{\mathrm{B}} C\left[\varphi_{\mathrm{A}}(1+\alpha) - \varphi_{\mathrm{B}}(1+\beta)\right]^2.$$

When $T \to \infty$, Eq. 1.23 becomes

$$\frac{1}{\chi} = \frac{T}{C} + \frac{1}{\chi_0},$$

so the inverse susceptibility is asymptotic to a form equivalent to the Curie-Weiss law. At the

Curie temperature, the inverse susceptibility goes to zero, which allows us to solve for the Curie temperature,

$$T_C = \frac{\lambda_{AB} C}{2}\left[\varphi_A \alpha + \varphi_B \beta \sqrt{(\varphi_A \alpha - \varphi_B \beta)^2 + 4\varphi_A \varphi_B}\right].$$

The positive solutions to this require that α and β be small and negative, which implies that the A-A and B-B interactions are weakly antiparallel and the A-B interactions are strongly antiparallel.

Below the ordering temperature T_C, the antiferromagnetic derivation is followed with a modification for A-A and B-B interactions. The spontaneous magnetization for each sublattice with $H = 0$ becomes

$$M_{s,A} = M_{0,A}\mathcal{B}_J\left[\frac{\mu_0 \mu \lambda_{AB}(\alpha\varphi_A - \varphi_B)M}{k_B T}\right]$$
$$M_{s,B} = M_{0,B}\mathcal{B}_J\left[\frac{\mu_0 \mu \lambda_{AB}(\beta\varphi_B - \varphi_A)M}{k_B T}\right],$$

where $M = M_A + M_B = \varphi_A M + \varphi_B M$ is the sum of all moments on both sublattices. These are not independent quantities, implying that the magnetization of each sublattice depends on the magnetization of the other. For each sublattice, M_s increases from 0 at T_C to saturation at $T = 0$ K, but the temperature dependence of each can be different. The overall spontaneous magnetization,

$$M_s = M_{s,A} - M_{s,B},$$

could similarly simply increase with decreasing temperature or it could deviate quite dramatically. The spontaneous magnetization of some ferrimagnetic materials have a maximum at a temperature other than $T = 0$ and exhibit a spontaneous magnetization less than this as $T \to 0$. In some systems, the magnitudes of the spontaneous magnetization of one sublattice can be greater than the other at some temperatures and less at others, resulting in a compensation point at a temperature where the magnetizations of the two sublattice are equal, with spontaneous magnetization in

opposite directions above and below this point. Three representations of possible temperature dependence of the spontaneous magnetization for a ferrimagnet are shown later in the chapter in Fig. 1.6(c).

Conclusions from Molecular Field Theory

And so we have been able to broadly describe the types of magnetic behavior seen in materials with this treatment, relying on this idea of the internal molecular field to which individual moments respond, resulting in parallel or antiparallel alignment of spins. We see that ferromagnetism, antiferromagnetism, and ferrimagnetism can arise, however it is an empirical model, with no explanation of the origin of the field or prediction of the sign of the coupling between moments. We move now to a discussion of the exchange interaction, where some understanding of this can be found.

Exchange Interaction

The idea of the internal molecular field which aligns isolated moments is not real. In a classical picture, a more accurate picture of how different moments interact might be a magnetostatic coupling between moments dependent on the magnitude of their separation, but this results in forces that are three orders of magnitude too small to account for the molecular field and strength of the alignment. And so we will move into a quantum mechanical view of the interactions between moments.

In a simplified model of two hydrogen atoms each with one electron, each has a separate wave function of the electrons. When the atoms are brought into proximity, there is an exchange force that describes their interaction. If the electron spins are antiparallel, the Pauli exclusion principle applied to the system as a whole allows them to have the same energy and bonding occurs, where the wave functions combine positively and the electrons have a greater probability of localization between the nuclei, forming a stable molecule. If the electron spins are parallel,

the Pauli exclusion principle prevents the electrons from having the same energy and the wave functions will combine negatively, demonstrating that the atoms will repel one another and the electrons are distributed away from the nuclei. Considering the two lowest energy states for the electron system together, a singlet state is defined in which the two electrons have opposite spin and their wave functions add, which has an energy E_S. The other possible state, a triplet state, has a parallel alignment of the spins of the two electrons and their wave functions subtract, which has an energy E_T. When the energy of the triplet state is greater than the energy of the singlet state, the preferred orientation is an antiparallel spin alignment of the electrons. For $E_T < E_S$, the preferred orientation is for the spins of the two electrons to be parallel.

This model can be expanded past the case of hydrogen atoms. The exchange energy between atoms i and j with spin angular momenta $\mathbf{S}_i\hbar$ and $\mathbf{S}_j\hbar$ is given by

$$E_{ij}^{\text{ex}} = -2\mathcal{J}_{ij}\mathbf{S}_i \cdot \mathbf{S}_j, \tag{1.24}$$

where $\mathcal{J}_{ij}$ is the exchange integral. This exchange interaction is isotropic, depending only on the distance r_{ij} between the spins, and acts over short distances, so it is reasonable to consider it only for nearest-neighbor interactions. If $\mathcal{J}_{ij} < 0$, the exchange energy is minimized when the spins are antiparallel, which occurs for most elements. For $\mathcal{J}_{ij} > 0$, the exchange energy is minimized when the spins are parallel, which results in ferromagnetism and only occurs for a few elements. The exchange integral $\mathcal{J}_{ij}$ can then be thought of as a function of how closely the electrons and atoms can be positioned.

In the case of electrons (labeled 1 and 2) of two atoms (labeled a and b) the exchange integral is calculated from

$$\mathcal{J}_{12} = \iint \Psi_a^*(\mathbf{r}_1)\Psi_b^*(\mathbf{r}_2)\left[\frac{1}{r_{ab}} - \frac{1}{r_{a2}} - \frac{1}{r_{b1}} - \frac{1}{r_{12}}\right]\Psi_a(\mathbf{r}_1)\Psi_b(\mathbf{r}_2)d^3r_1 d^3r_2.$$

We see, then, that the sign of the exchange integral depends on the relative distances of the

electrons and atoms.

Bethe and Slater calculated $\mathcal{J}_{ij}$ for two electrons in d-orbitals as a function of r_{ab}/r_d where r_d is the radius of the d orbital. The result is known as the Bethe-Slater curve. This treatment is more phenomenological, but it correctly reproduces some important behavior seen in transition metals. For small r_{ab}/r_d, the exchange is negative. It decreases in magnitude, becomes positive, peaks, and stays positive approaching zero as $r_{ab}/r_d \to \infty$. This correctly predicts the sign of the exchange integral for the magnetic transition metals, negative for Cr and Mn and then positive for Fe, Co, and Ni (in order of increase r_{ab}/r_d. Assuming a system with ferromagnetic behavior and equating the exchange energy in Eq. 1.24 with the energy of the atom in the quantum mechanical treatment of the internal molecular field (and assuming quenching of the orbital angular momentum), $\mathcal{J}_{\text{exch}}$ can be found as

$$\mathcal{J}_{\text{exch}} = \frac{3k_B T_C}{2zS(S+1)},$$

where z is the number of nearest neighbors for each atom, which suggests that the exchange integral is proportional to T_C. For, Fe, Co, and Ni, the exchange integral is highest for Co and lowest for Ni, in agreement with their observed T_C.

The Bethe-Slater curve suggests antiferromagnetic behavior for smaller distances between atoms, ferromagnetic behavior for slightly larger distances, and no magnetic order at larger distances, which generally agrees with observations. Transition metals below this row in the periodic table have a smaller ratio r_{ab}/r_d, and ferromagnetism does not arise in any of these metals. While Mn is antiferromagnetic (with T_N below room temperature), some alloys that contain Mn have been observed to be ferromagnetic, which could be a result of the increased separation of the magnetic Mn atoms when compared to elemental Mn.

Of course this is not the whole picture for the exchange interaction in materials. There are many non-elemental ferromagnetic and antiferromagnetic compounds that would be expected to

have little magnetism if considering only r_{ab}/r_d for the transition metals. In these cases, we must revisit the electron configurations and orbitals given the bonding that occurs to understand the different types of exchange interactions and behavior such as indirect exchange interactions in which there is a mediation of the exchange between transition metal ions by oxygen ions in some oxides, for example. However we can get a sense of how the quantum mechanical treatment of the atom can give rise to collective magnetic behavior when atoms are brought into proximity, and how these exchange interactions are important in understanding and engineering materials with useful properties. We also begin to understand how the separation of atoms in a lattice can impact the magnetic behavior, which is relevant in this dissertation in which magnetostriction and magnetovolume effects are observed.

1.1.3 The Magnetism of Itinerant Electrons

These models of the atom and interactions between atoms which can be considered localized moments are sufficient for some materials, especially in a lot of nonconducting compounds. But they often fall far short in describing magnetism in metals. There are many paramagnetic metals, but their susceptibility does not follow the Curie-Weiss law as might be expected. Instead, they have a small positive susceptibility that may increase, decrease, or stay constant with temperature. There would also be many more metals with large moments and ferromagnetic ordering expected with these models. We know that the orbital angular momenta are completely or nearly completely quenched in the ferromagnetic $3d$ metals, so we would expect their atomic moments to be an integral number of Bohr magnetons, however the experimentally observed moments are $\mu_{\mathrm{Fe}} = 2.22\mu_B$, $\mu_{\mathrm{Co}} = 1.72\mu_B$, and $\mu_{\mathrm{Ni}} = 0.61\mu_B$. Relevant to this dissertation, Cr is antiferromagnetic, so we might expect to treat it as we did other antiferromagnets in the previous section, with two opposing sublattices. However the magnetic ordering in Cr is actually incommensurate, meaning there is a sinusoidal modulation of the spins that is incommensurate with the lattice, which cannot be explained with localized moment magnetism.

And so we now consider magnetic behavior that has its origins in itinerant electrons, the valence electrons which are not bound to atoms but are free to move around in metals. There are many different models and theories of itinerant magnetism, with different interactions and assumptions and modifications for each magnetic system. So this will be more of a basic introduction into paramagnetism in metals and the ferromagnetism of the $3d$ transition metals.

The Density of States

In discussing exchange, we briefly discussed a picture of two atoms, each with an electron, which interact. Here, we start with this picture, where two atoms are brought close together and bond in a way that the orbitals of each atom combine or hybridize to become molecular orbitals. Each of the energy levels of the atom, which could be identified by the quantum numbers n, l, m_l, and m_s, split into two energy levels of the molecule, which are called bonding and antibonding levels. As more atoms are added to the system, the atomic energy levels split further until there is a solid metal with atom density N in which each of the atomic energy levels has split into N levels. When N is very very large, as it will be in macroscopic systems commonly studied, these closely spaced levels appear continuous, which are called the energy band. In this regime, the density of states $g(E)$, where $g(E)dE$ is the number of states per energy per unit volume with energy E and $E+dE$, can be treated as a continuous function of energy.

In the free electron theory of metals, the valence (outermost) electrons are assumed to be itinerant electrons which are free to move throughout the metal and that their energy is entirely kinetic, ignoring the lattice potential, so they are referred to as an electron gas. In a macroscopic system of N electrons in a cube at $T = 0$ K, it is assumed that the total energy is minimized when the $N/2$ lowest energy states are occupied (by the Pauli exclusion principle, each energy state can be occupied by at most two electrons which have opposite spin), thus defining the ground state.

The energy of the highest filled levels in this ground state is

$$E_F = \frac{h^2}{2m_e}\left(\frac{3n_0}{8\pi}\right)^{2/3},$$

where n_0 is the number of electrons per unit volume. E_F is called the Fermi energy or Fermi level. The density of states is calculated to be

$$g(E) = \frac{8\pi m_e}{h^3}\sqrt{2m_e E} = \frac{3n_0}{2E_F^{3/2}}\sqrt{E},$$

and note that at the Fermi energy, $g(E_F) = \frac{3n_0}{2E_F}$. When temperature is above absolute zero, there are more higher energy level states that are filled, so the probability $f(E)$ that a state with energy E is filled is given by the Fermi-Dirac distribution:

$$f(E) = \frac{1}{e^{\frac{E-\mu}{k_B T}} + 1},$$

where μ is the temperature-dependent chemical potential. When $T \to 0$ K, $\mu = E_F$ and $f(E)$ becomes a step function equal to one for energy $E < \mu$ and zero for energy $E > \mu$. The product of the density of states $g(E)$ and the Fermi-Dirac distribution $f(E)$

$$g(E)f(E) = \frac{8\pi m_e}{h^3}\sqrt{2m_e E}\,\frac{1}{e^{\frac{E-E_F}{k_B T}} + 1}$$

gives the density of occupied states, which is a good approximation when $k_B T \ll E_F$, which is true for most metals up to their melting point.

Paramagnetism

So we have considered the ground state for this collection of electrons, in which occupied states contain two electrons of opposite spin. If a field is applied, the electron energies will be

modified by $E = \mathbf{m} \cdot \mathbf{B}$ where $\mathbf{m}$ is the moment of each spin. Considering the energies for spin-up and spin-down electrons separately, a field applied along $+\hat{z}$ will change the spin-up band by $\Delta E = -\mu_B B$ and the spin-down band by $\Delta E = \mu_B B$, which shifts the density of states. If this altered density of states is filled with electrons, the ground state energy now has more spin-up electrons than spin-down electrons. Assuming that the susceptibility of the material is small, the magnetization is

$$M = \mu_B^2 B \frac{3n_0}{2E_F}$$

and the susceptibility (called the Pauli paramagnetic susceptibility) is

$$\chi_{\text{Pauli}} = \mu_B^2 \mu_0 \frac{3n_0}{2E_F}. \tag{1.25}$$

This result is independent of temperature and much smaller than the paramagnetic susceptibility found in the Curie law (Eq. 1.16). In the molecular field theory, electrons from every atom in the material contribute a moment, whereas in this treatment, we are limited to the electrons near the Fermi level.

Ferromagnetism

The Stoner model of ferromagnetism ties together the molecular field theory of ferromagnetism with this band theory of metals. It describes how a slight magnetization of the electron gas will give rise to in an internal magnetic field $H = \lambda M$. This further magnetizes the gas, increasing the internal field, etc. The energies associated with both of these processes can be equated to find that spontaneous magnetization will occur when

$$\mu_0 q \mu_B^2 g(E_F) = U g(E_F) > 1,$$

which is the product of the density of states $g(E_F)$ at the Fermi level and a Coulomb potential energy U that is based in interatomic exchange interactions. This means that ferromagnetism can be predicted in materials when there is a large density of states at the Fermi level and/or when the interatomic Coulomb interactions are strong. This model correctly predicts that ferromagnetism arises only in Fe, Co, and Ni and suggests that some other elements including Pt and Pd come close to achieving ferromagnetic order. A calculation of the susceptibility in this model gives

$$\chi = \frac{\chi_{\text{Pauli}}}{1 - U g(E_F)}, \tag{1.26}$$

which describes an enhancement of the Pauli paramagnetic susceptibility of Eq. 1.25 by the Stoner factor, even in metals that do not spontaneously magnetize.

Further refining this picture for the 3d transition metals and their alloys involves looking at the splitting and occupation of the 3d and 4s bands. The 4s electrons are the valence electrons that are completely delocalized while the 3d electrons determine the magnetism, but the energy bands overlap, so it is not straightforward to understand how these bands are filled or how are electrons separated into them. This allows for estimations of magnetic moments that are a non-integer number of Bohr magnetons and does fairly well in describing these metals and alloys. Slater [27] and Pauling [28] developed an approximation of how the alloying will affect the atomic moments, which has led to the Slater-Pauling curve, which illustrates this dependence for different 3d alloys.

This treatment is, of course, incomplete, having made some assumptions that turn out to not be true, such as discounting the effects of crystal structure or hybridization resulting in a change in the band structure when alloying. It has not accounted for alloys with materials outside of the 3d elements, where ferromagnetic ordering can also be seen. And then there is magnetism in rare earth metals, which can be described by what is known as the RKKY interaction. Various models involving itinerant electrons are used in describing the magnetism of different materials. But from this treatment, it is seen that magnetism can arise non-locally and depends greatly on

band structure and Fermi levels.

Notes on Itinerant Magnetism in Cr

We may also ask about other magnetic behavior, antiferromagnetism or ferrimagnetism, which are relevant to materials in this dissertation. Theories describing itinerant antiferromagnetism exist [29, 30], which we will not get into here. But we note that itinerant antiferromagnetism can look quite different from localized antiferromagnetism. In this treatment of the localized antiferromagnet, we had two sublattices which, in the absence of a field, had equal and opposite spontaneous magnetization. Adjacent moments in that model were antiparallel, so there is a periodicity to the reversal of moment that is associated with (or commensurate to) the lattice. But there also exist materials in which the antiferromagnetism is incommensurate with the lattice, in which the periodicity of the modulation of moments is independent of the lattice spacing. This is suggestive of magnetism of non-localized origin.

Cr is considered the archetypal itinerant antiferromagnet, and it contains this incommensurate antiferromagnetic ordering, known also as a spin density wave. We will discuss the spin density wave in Cr in Chapter 3, but note here that the origin of the spin density wave lies in the structure of the Fermi surface [31, 32]. In this system, the magnetism of itinerant electrons drives a periodic distortion of the lattice, called a strain wave, which also results in a modulation of the charges, called a charge density wave [32, 33]. It is possible that the charge density wave is enhanced by a modulation of the conduction charges not bound to the lattice sites [32, 34]. So this is a material in which atomic moments, interacting localized moments, and itinerant contributions to the ordering must all be considered, resulting in complex behavior that couples spins, charges, and lattice. Understanding these contributions and their coupling from first principles is difficult to say the least, and so we seek to observe the behavior that results to form a basis for understanding of the system.

1.2 Magnetic Ordering in Materials

We will turn now from a more rigorous discussion of the origins of magnetism to an overview of the types of ordering that result. Fig. 1.4 shows a schematic of a classical treatment of the five types of magnetism discussed with representations of the localized moments. The first is diamagnetism, which is seen in all materials, but is usually dominated by other magnetic behavior in materials that have a net atomic moment. In the absence of a field, diamagnetic atoms have no net moment. When a field is applied, they acquire a small moment due to the precession of the electron orbits which opposes the field. The second type of magnetism is paramagnetism, in which individual atoms have a net atomic moment which are randomly oriented. When a field is applied, these moments experience a torque which tends to want to align them in the direction of the field opposed by thermal effects which randomize the alignment, and so the spins will rotate in the direction of the field to an extent that depends on the field and temperature. Diamagnetism and paramagnetism are generally referred to as disordered or nonmagnetic states.

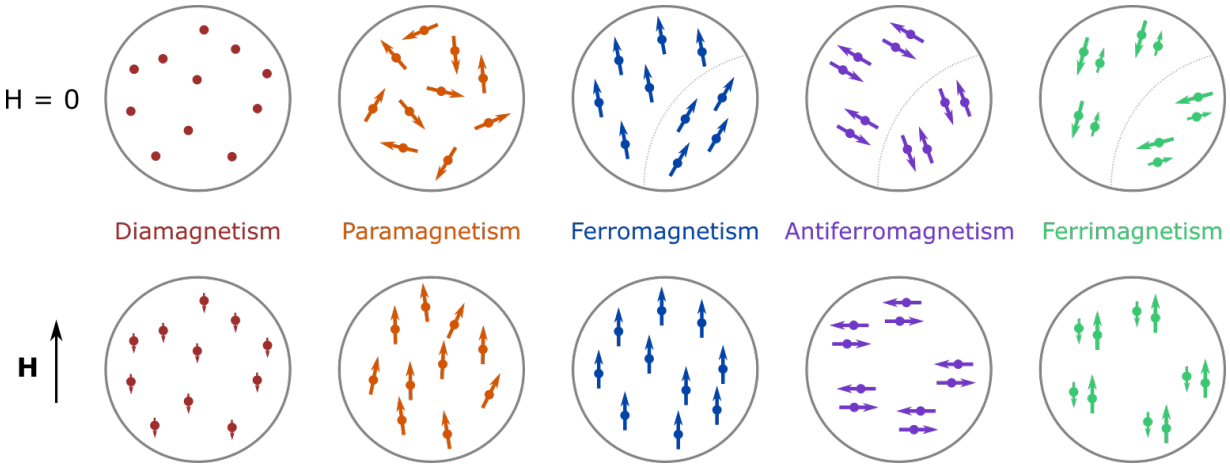

Figure 1.4: Schematic of localized atomic moments in five types of magnetism (diamagnetism, paramagnetism, ferromagnetism, antiferromagnetism, and ferrimagnetism) in zero field (top) and with an applied field (bottom). Diamagnetism and paramagnetism are considered disordered states, and ferromagnetism, antiferromagnetism, and ferrimagnetism are considered to be types of magnetic ordering. The dotted lines indicate a domain boundary. More details are included in the text.

The three types of magnetism that are discussed which result in magnetic ordering are

ferromagnetism, antiferromagnetism, and ferrimagnetism. In these phenomena, there are strong interactions between the atomic moments. In a ferromagnet, adjacent spins tend to want to align in the same direction. In the absence of a field, there are different regions called domains (with the domain boundary indicated by the dotted lines in Fig. 1.4) in which all the moments will be aligned parallel to one another. The magnetizations of different domains may be randomly oriented for a demagnetized ferromagnet, resulting in zero net magnetization for a macroscopic system. But with application of a field, the system will magnetize, and those domains will align to the field, resulting in a large magnetization. In an antiferromagnet, adjacent spins tend to want to be antiparallel. We can think of two sublattices in these materials, each of which will spontaneously magnetize like a ferromagnet, but which perfectly oppose one another. The application of a field may favor a specific orientation, usually with the magnetization of both sublattices perpendicular to the field. A ferrimagnet is a hybrid or combination of a ferromagnet and an antiferromagnet. Atomic moments tend to prefer to align antiparallel to adjacent spins and can be thought of as separate sublattices with opposite magnetization as with an antiferromagnet, but the magnetic species on the two sublattices differ and each will have a spontaneous magnetization with a different temperature dependence. The result is a nonzero spontaneous magnetization and some properties in common with ferromagnets.

One measure of magnetism that we have discussed is the magnetic susceptibility, defined in Eq. 1.14 as a measure of how much a material magnetizes in response to a magnetic field and reproduced here:

$$\chi = \frac{M}{H}.$$

In considering the temperature dependence of the susceptibility, it is useful to recall Eq. 1.19, the Curie-Weiss law reproduced below, which estimates the temperature dependence of the susceptibility for some materials with localized moments:

$$\chi = \frac{C}{T - \theta}.$$

This is applicable for paramagnetism of localized moments. The ideal paramagnet (with no interaction between moments) has $\theta = 0$. The Curie-Weiss law applies for a ferromagnet above its ordering temperature, the Curie temperature T_C, with $\theta = T_C$. And it applies for an antiferromagnet above its ordering temperature, the Néel temperature T_N, with $\theta = -T_N$. Below T_N, the susceptibility generally stays constant or decreases. The susceptibility of a ferrimagnet above its ordering temperature is asymptotic with a line that follows the Curie-Weiss law, but differs near T_C, as described by Eq. 1.23. The inverse susceptibilities for a diamagnet, an ideal paramagnet, a ferromagnet above T_C, an antiferromagnet above T_N, and a ferrimagnet above T_C are shown in Fig. 1.5. Deviations from this occur, especially in metals when we must consider the magnetism of itinerant electrons. For example, we described a treatment of the Pauli paramagnetic susceptibility in Eq. 1.25 to be independent of temperature, and allowed for some interactions which enhances the susceptibility in Eq. 1.26.

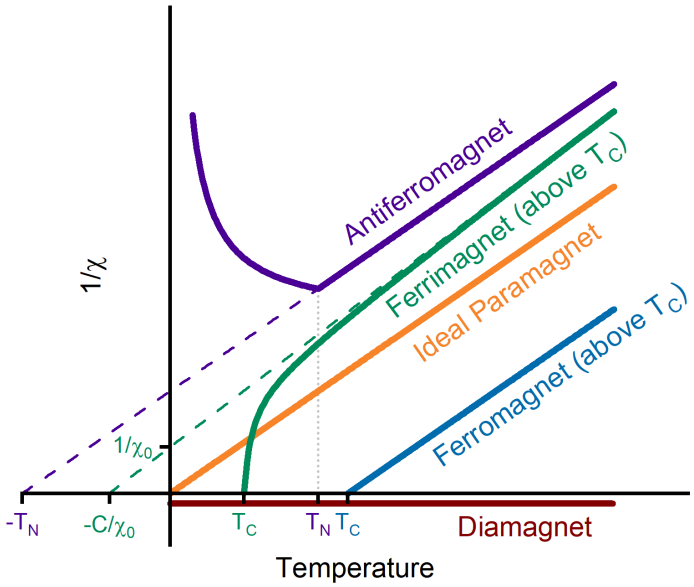

Figure 1.5: Representations of the inverse of susceptibility predicted by molecular field theory of a diamagnet, paramagnet, ferromagnet above T_C, antiferromagnet above T_N, and ferrimagnet above T_C.

The susceptibility of diamagnetic materials is generally $\chi_{\text{dia}} < -10^{-5}$ while for paramag-

netic materials, it is generally χ_{para} ~$10^{-5} - 10^{-3}$. In ferromagnets, susceptibilities tend to be in the range χ_{ferro} ~$10 - 10^{4}$.

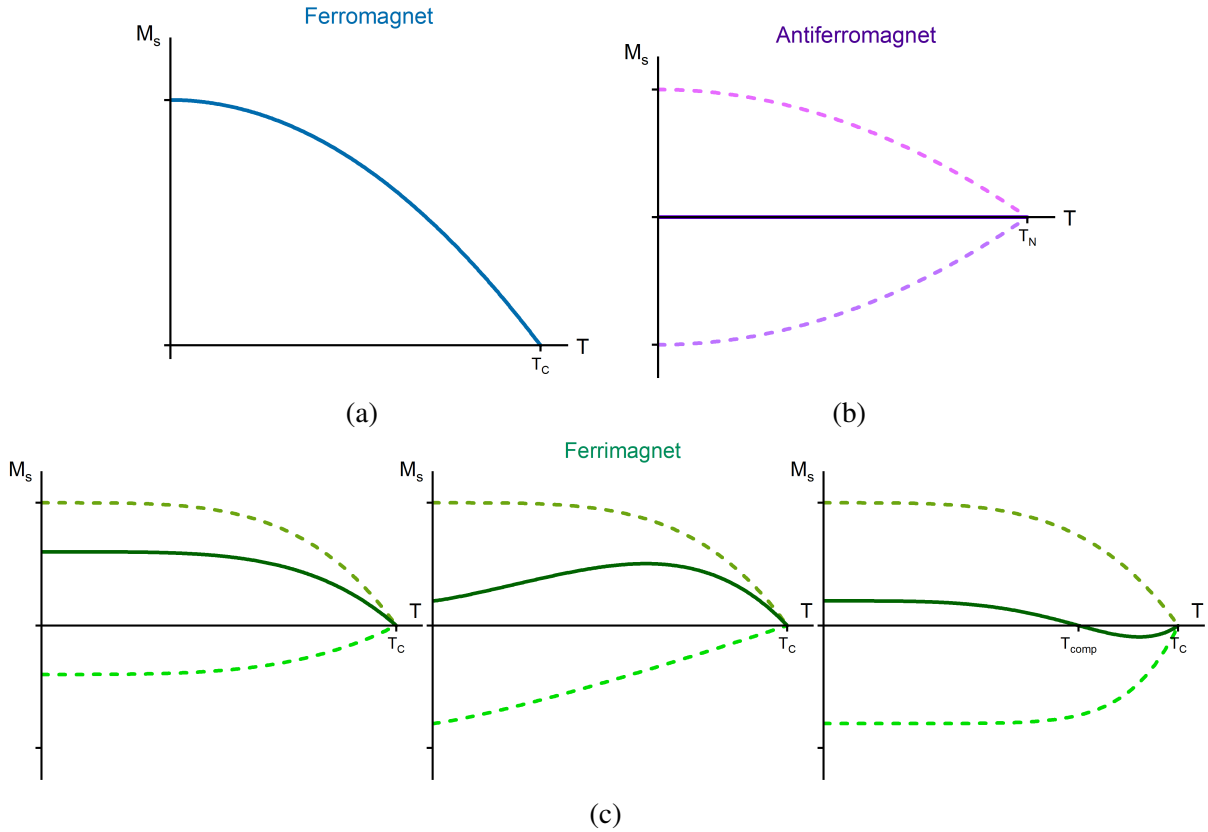

Figure 1.6: Representations of the spontaneous magnetization of each sublattice (dashed lines) and the system as a whole (solid lines) for (a) a ferromagnet, (b) an antiferromagnet, and (c) ferrimagnets. For a ferromagnet with $T < T_C$, all moments in a domain spontaneously magnetize in the same direction. For an antiferromagnet, there are two sublattices (of the same magnetic species) which each spontaneously magnetize below T_N in opposite orientations, giving a net magnetization of zero of the entire system. Ferrimagnets have two sublattices formed of different magnetic species which spontaneously magnetize in opposite orientations with different magnitudes and often with different temperature dependence, which can result in complex temperature dependence of the magnetization of the whole system.

Below their ordering temperatures, we see that localized moments in ferromagnets, antiferromagnets, and ferrimagnets will prefer to align in certain ways, even in the absence of a field. Fig. 1.6 presents the expected spontaneous magnetization in these materials. For a ferromagnet, all the moments in each domain will align in the same direction. The spontaneous magnetization shown in Fig. 1.6(a) increases as temperature decreases from the Curie temperature

to $T = 0$ K, where all moments are perfectly aligned in the direction of the field and the maximum possible magnetization of the system is achieved. For an antiferromagnet, we have two sublattices which contain the same magnetic species. Each sublattice has a similar spontaneous magnetization to the ferromagnet, but oriented in opposite directions such that their sum, the total magnetization of the system, is zero, as depicted in Fig. 1.6(b). The ferrimagnet also has two sublattices, but they contain different magnetic species, which have different temperature dependence of their spontaneous magnetization and different atomic moments. This gives rise to varied temperature dependence of the system as a whole, with three possibilities shown in Fig. 1.6(c). In some ferrimagnets, the net magnetization looks similar to the ferromagnet. But sometimes they have very different temperature dependence and the maximum magnetization occurs at a temperature above absolute zero. In other ferrimagnets, the temperature dependence and atomic moments are such that there is a compensation point at which the net magnetization is zero, and the spontaneous magnetization above and below the compensation point is oriented in opposite directions.

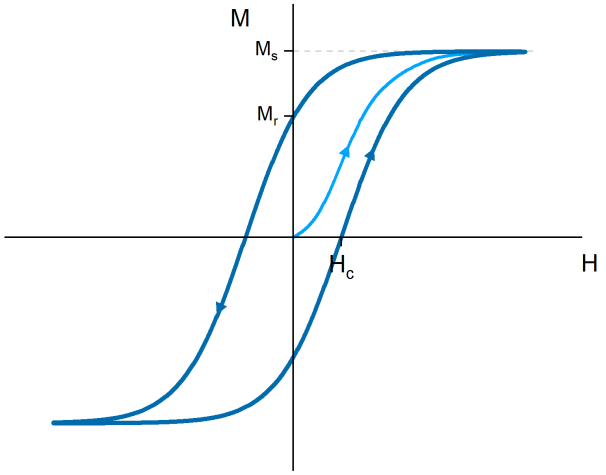

Figure 1.7: Representation of a magnetic hysteresis curve for a ferromagnet or ferrimagnet. At some temperature, the material will spontaneously magnetize. In the absence of a field for a demagnetized sample, each domain will be randomly oriented and the net magnetization will be zero. With application of a field, the domains will align and the magnetization of the system will be maximized at the saturation magnetization M_s, as shown by the light blue curve. The remanent magnetization M_r reflects the magnetization retained by the system if the field is removed after it is saturated. The coercive field H_c reflects the field that must be applied in opposition of the magnetization at which the net magnetization goes to zero.

Fig. 1.7 shows a M-H hysteresis curve for a ferromagnet or ferrimagnet. In the absence of an applied field, domains in a demagnetized field will spontaneously magnetize in orientations that sum to zero. As a field is applied, the domains will tend to align to the field until all are saturated in the direction of the field and the saturation magnetization of the system equals the spontaneous magnetization M_s. If the field is removed, the system will retain some of the alignment and the remaining magnetization is called the remanent magnetization M_r. A coercive field H_c opposing the magnetization is required to bring the net magnetization to zero.

In this work, we consider magnetism in solid materials with crystalline structure. So a natural question is what magnetic ordering looks like in a crystal. Fig. 1.8 shows a few of the many possibilities for a cubic crystal with one magnetic species. Fig. 1.8(b) shows an example of ferromagnetism, where atomic moments within a domain are all aligned in the same direction, with magnetocrystalline anisotropy that often prefers alignment along one of the three cubic axes $\langle 100 \rangle$. In an antiferromagnet, there are two equivalent sublattices with equal and opposite moments. The other types of ordering shown in Fig. 1.8 are all possible antiferromagnetic configurations. The A-type ordering shown has a parallel alignment of moments within the (001) plane with alternating orientation of the planes. C-type ordering, on the other hand, has a parallel alignment of moments within the (110) planes. G-type ordering is a type of ordering we will see for a material relevant to this work, FeRh, in its antiferromagnetic phase. The type of magnetic ordering can be determined by neutron diffraction, where the symmetry of the ordering can give rise to certain magnetic peaks. These magnetic configurations are of course far from adequate in explaining all magnetic behavior seen in all materials. An alternate ordering antiferromagnetic ordering of spins in a body-centered cubic lattice is shown in Fig. 1.9(a).

The direction of the moments has a preference in most materials. When a field is applied to an antiferromagnet, the energy of the state with the spin axis perpendicular to the field is generally lower than the energy of the state with parallel alignment. The magnetocrystalline anisotropy, however, sets a preferential axis of alignment of the spins with an energy associated

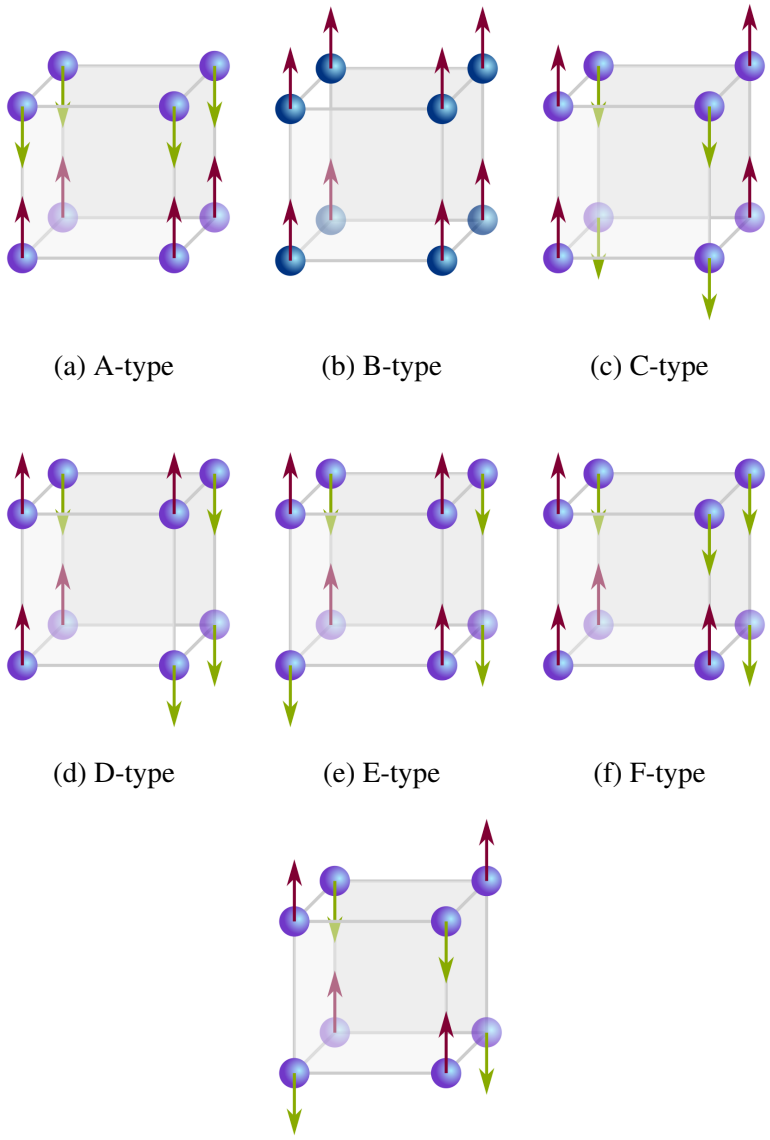

(a) A-type (b) B-type (c) C-type

(d) D-type (e) E-type (f) F-type

(g) G-type

Figure 1.8: Representations of possible ferromagnetic and antiferromagnetic ordering of moments in a cubic lattice, where all atomic moments have the same magnitude but can be oriented parallel or antiparallel with one another.

with moving the spin axis away from this easy axis. In a material with weak magnetocrystalline anisotropy, a large enough field applied parallel to the spin axis can suddenly rotate the magnetization of the sublattices from parallel to perpendicular to the field, in what is called a spin-flop transition. In a material with strong magnetocrystalline anisotropy, the spins of the antiparallel

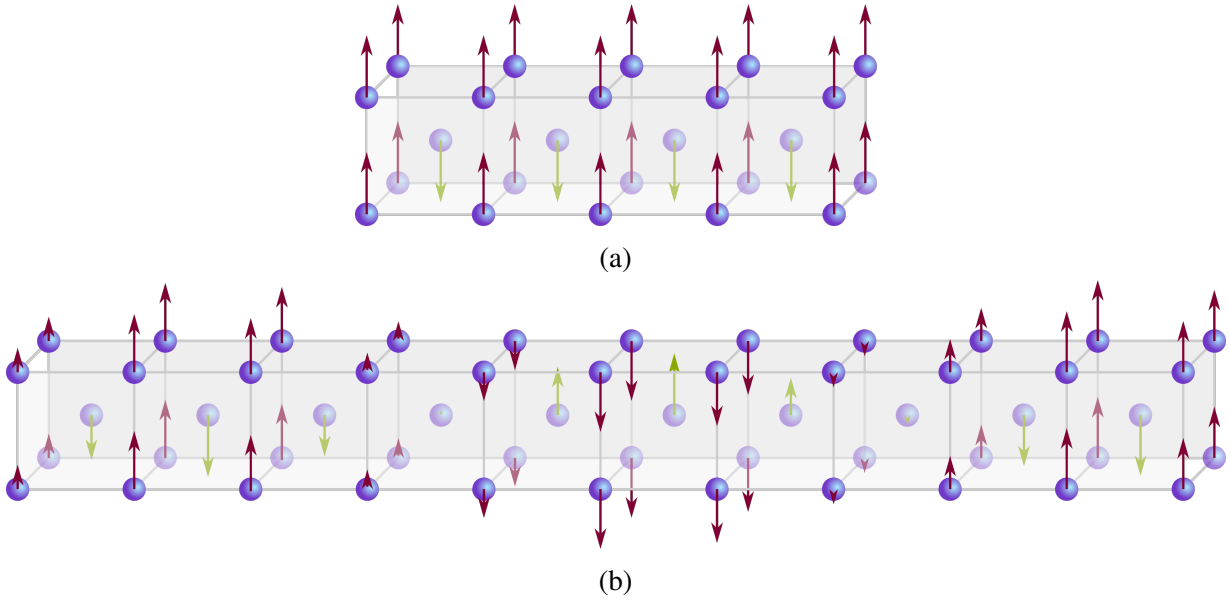

Figure 1.9: Representations of (a) commensurate and (b) incommensurate antiferromagnetic ordering of moments in a body-centered cubic lattice.

sublattice can suddenly flip so all moments are parallel to the field like in a ferromagnet, which is called a spin-flip transition. Alternatively, in materials with a very strong magnetocrystalline anisotropy, perpendicular spin directions may be forbidden and a large enough field can result in a metamagnetic transition in which the antiparallel spins reorient parallel to the field and the material becomes ferromagnetic.

The magnetic ordering in materials is often described with these kinds of localized atomic moments. But we previously discussed how itinerant electrons also contribute to the magnetism, especially in metals. We mentioned that Cr has a spin density wave, a type of antiferromagnetic ordering that is incommensurate to the lattice, as a result of itinerant electrons. This kind of spin density wave is depicted in Fig. 1.9(b), with what appears as a modulation of the atomic moments. In fact, antiferromagnetic ordering in general can be thought of as a periodic modulation of the spins in a material. In the commensurate case of Fig. 1.9(a), the period of this modulation is a multiple of or a rational fraction of the lattice constant. But in the incommensurate case, the periodicity of the modulation is not directly related to the lattice constant and we suspect that

itinerant magnetism may play a significant role.

1.3 Confined Geometries

As we seek to miniaturize our technology, it is important to understand how materials exhibiting complex phenomena behave in confined geometries. By this, we mean restricting the length of a material in one or more dimensions, usually on sub-μm scales, which can no longer be treated as infinite. Nanomagnetism is a field that seeks to understand the magnetism arising in and manipulated by nanostructured systems. We also find that, in some cases, nanoscale systems provide an advantage in modern experimental techniques: for example, a thin film can be uniformly photoexcited with an optical laser where a macroscopic system would be severely limited by the penetration depth at those frequencies.

1.3.1 Thin Films

Confinement in one dimension usually refers to thin films, in which surfaces and interfaces will play an important role. The extreme limit of this is in systems that are one or a few atomic layers thick, which are considered two-dimensional systems. In a single monolayer of a magnetic material, there are fewer neighboring atoms with which to interact, and we may start to observe more isolated atomic behavior rather than interactions. As an example, we can consider Fe. The isolated Fe atom has an electron configuration $1s^2 2s^2 2p^6 3s^2 3p^6 3d^6 4s^2$, where the open subshell is the $3d$ shell with 6 electrons. The orbital angular momentum is nearly completely quenched and there are 4 unpaired electrons, so our prediction is for an Fe atom to have a moment of $\mu_{\text{Fe,pred}} = 4\mu_B$. The experimentally determined moment of bulk body-centered cubic Fe is $\mu_{\text{Fe,exp}} = 2.2\mu_B$, a result of itinerant behavior. A monolayer of Fe reduces the number of neighboring atoms with which each atom interacts from eight and so we might expect the magnetization to be enhanced in this two-dimensional system. Theoretical models have predicted

a monolayer to have moment $\mu = 3.10\mu_B$. A monolayer on MgO (001) with which there would be little hybridization of electron orbitals is predicted to have moment $\mu = 3.07\mu_B$ and two layers on MgO (001) to have moment $\mu = 2.96\mu_B$ [35]. It is difficult in practice to actually grow a continuous perfect monolayer of material and experimental realities like oxidation come into play. But some studies have shown enhancement of the moment in ultrathin Fe layers at interfaces with MgO [36, 37]. The isolated Cr atom should have an atomic moment even larger than that of Fe, but the observed moment is $\mu_{\mathrm{Cr,exp}} = 0.59\mu_B$. However significant enhancement of the Cr moment is predicted [38] and observed [39] at some interfaces, which can also be attributed to a higher density of states at the Fermi level.

Most of the work in this dissertation involves thin films of a single material, roughly 30 nm in thickness, which is on the order of 100 unit cells. The isolation of atoms will not come into play here, where most of the atoms are still subject to short-range exchange interactions. But it turns out that the interfaces can play an important role in the magnetic behavior in these films, as we will later discuss for Cr and FeRh.

An experimental reality of thin films is that they cannot be freestanding, but must be grown on a surface. This interface with the substrate is hugely significant in the material properties. Atoms in the substrate will hybridize to some extent with atoms of the film and interface magnetic properties may arise. The surface will partly determine the crystal structure of the material, providing a template on which atoms of the film will land and start to build up. This means that different crystal orientations for growth can be preferred depending on the substrate surface, or even result in a crystal structure different from what is seen in bulk. One of the significant effects at the substrate-film interface is strain. A film which grows in the structure that is preferred in bulk will still have a mismatch of lattice parameter at this interface, bringing atoms closer together with compressive strain or further apart with tensile strain. This effect will influence deeper layers in the material, which means this can influence a significant portion of a thin film. In discussing exchange interactions, we briefly touched on how the spacing of atoms can influence

the parallel or antiparallel alignment of spins and the strength of the exchange forces, and so it is not unreasonable to assume that these strained layers will have an impact on the magnetism of the film.

Another consideration would be the surface interface. Oxidation of films will significantly change the material and material properties, so often we have a capping layer that does not oxidize to protect the film. There can be some strain at this interface, though this is usually less of a concern than the substrate interface. But this also introduces another material which will interact with the film to some extent, which is not necessarily a defect. Interface effects give rise to many phenomena that are useful in technologies and devices and are an important area of research.

We have previously mentioned the idea of magnetocrystalline anisotropy leading to a preferred orientation of the spins in materials. Surfaces and interfaces in films will break the symmetry seen in bulk and have an influence on the anisotropy. Again, this is very important in technology, for instance in engineering a device in which we want an on-off switch of the magnetization state versus one in which we want a continuous encoding of states. Anisotropy effects are seen most obviously in very thin ferromagnetic thin films, which can be classified as perpendicular (with preferred orientation of the magnetization out-of-plane) or longitudinal (with preferred orientation in-plane). In a material with correlated magnetic behavior, the interface effects and anisotropy can have implications for the magnetic behavior throughout the film.

1.3.2 Confinement in Two or Three Dimensions

Confinement in two dimensions refers to very thin wires or stripes. Some measurements of wires where the width is several μm or more will essentially be measuring a thin film (it is confined in one dimension to a thin film but can still be treated as macroscopic in the wire width and length directions). But as this wire width is decreased, the material properties can be altered and new effects may emerge or new methods of understanding properties can be accessed. We include a few limited studies of systems that can be considered to be confined in two dimensions.

It is also possible to confine further in three dimensions and study nanoparticles, which is not in the scope of this work.

1.4 Magnetoelectric Transport

We turn now from the origins and types of magnetism to some of the effects of coupling of magnetism with charge and lattice and techniques which can be used to study and probe magnetism. The first is magnetoelectric transport, which implies a coupling of spins and charges. The magnetism in materials arises primarily from electrons, including the itinerant electrons which are also responsible for electrical conduction, so it is not surprising that magnetism can influence electrical conduction. These magnetoresistive phenomena have been critical in the development of much of our modern technology.

We can start with some basics of electric transport in a metal in the free electron model. In this model, electrons in zero applied electric field are traveling around in all directions in a metal at the Fermi velocity (which is very fast, at around $v_F = 0.01c$) such that the net movement of electrons is zero. When an electric field E is applied, the Fermi surface in momentum space is shifted by a very small amount in the direction of the electric field and the electrons move in the field direction at the drift velocity (which is around ten orders of magnitude slower than the Fermi velocity). Each electron experiences a force due to the electric field and drift in that direction until they are scattered, which happens on a characteristic time τ_σ. The characteristic distance that an electron travels in the time τ_σ between collisions is called the mean free path $\lambda = v_F \tau_\sigma$.

Ohm's law gives us a way to relate the current density $\mathbf{j}$ in the presence of an electric field $\mathbf{E}$:

$$\mathbf{j} = \sigma \mathbf{E} = \frac{\mathbf{E}}{\rho},$$

where σ is the electrical conductivity of the material and is the inverse of its electrical resistivity

ρ. We find that the conductivity of a material is

$$\sigma = \frac{ne^2\tau_\sigma}{m^*},$$

where n is the number density of electrons and m^* is the effective mass for the electrons, which depends on the electronic band structure. The conductivity and resistivity in materials are actually tensors which sometimes reduce to a scalar, reflecting different scattering in different directions in a crystal. Experimentally, we usually measure the resistance R of a wire in units of Ω, which is related to the resistivity by $\rho = RA/l$ where l is the length of the wire and it has a uniform cross-sectional area A. The resistivity, which is the inverse of the conductivity, is inversely proportional to the scattering time τ_σ and the mean free path λ and so it is a reflection of the amount of scattering that occurs.

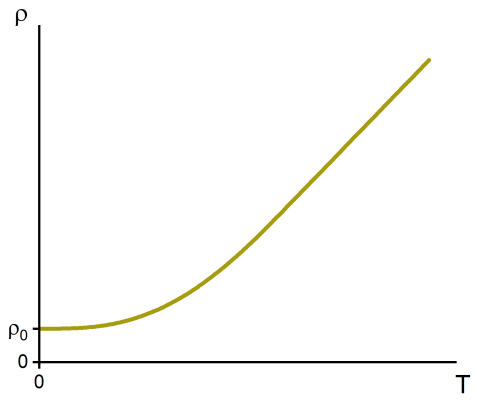

Figure 1.10: Model of the temperature dependence of the resistivity of a metal, which can be approximated as linear at high temperature and plateaus at low temperature to the residual resistivity ρ_0 due to scattering from defects.

In metals, scattering occurs from deviations from a perfectly periodic lattice, which is due to defects (such as impurities or grain boundaries) and phonons (lattice vibrations). This introduces an obvious temperature dependence into the resistivity, as phonons will increase with temperature. The resistivity of a metal at high temperature is dominated by electron-

phonon interactions and is usually linear with temperature to a first approximation. At very low temperatures, the phonon modes are frozen and the scattering is due primarily to the defects, which results in a plateau of the resistivity to ρ_0, the residual resistivity. A representation of the temperature dependence of the resistivity for a metal is shown in Fig. 1.10. The residual resistivity ratio $\frac{\rho(300K)}{\rho_0}$ is used as a measure of the purity and quality of a metallic sample.

Changes in a material's resistance due to magnetic effects is called magnetoresistance. If a magnetic field is applied to a moving charge, we know that the charge will experience a force in a direction determined by the cross product of its velocity and **B**, which will influence the motion of the electrons. The mean free path in the direction of the current will be reduced, increasing the resistivity. This is the ordinary or Lorentz magnetoresistance. It is dependent on the band structure which influences scattering, but can be approximated in a metal in low magnetic fields as a change in resistivity that is quadratic in B and linear in the carrier mobility and is a small effect in metals, around 1% in a 1 T field. It is interesting to note that the perpendicular deflection of charges in the presence of a field will also result in a transverse voltage, which is called the Hall effect.

There are other magnetoresistive effects that have been fundamental in technologies, such as in magnetic hard drive technology. Anisotropic magnetoresistance (AMR) arises from the spin-orbit interaction in magnetic materials and depends on the angle between the applied current and the magnetization, resulting in resistivity changes of around 1-5% in ferromagnetic metals. Giant magnetoresistance (GMR) is an effect in devices that have multiple ferromagnetic layers in which the resistance of a parallel alignment of the magnetization of the layers is lower than an antiparallel alignment, which is a quantum mechanical effect typically up to 80% that has to do with the differential scattering rates of spin-up and spin-down electrons in a magnetized layer. And colossal magnetoresistance (CMR), briefly described at the beginning of this chapter as an area of significant interest in spintronics, can result in orders of magnitude changes in the resistivity of materials.

What we conclude from the existence of these types of magnetoresistance is that magnetic fields and the magnetization of a material has an impact on its resistance, and spin and charge are interrelated degrees of freedom. Spin-up and spin-down conduction electrons will have different scattering cross-sections in a magnetized lattice. This means that a material that undergoes a phase transition, for example from ferromagnetic to paramagnetic at the Curie temperature or from antiferromagnetic to paramagnetic at the Néel temperature, might experience changes in scattering which results in some kind of anomaly, such as a drop or jump in the resistivity. When other methods of determining magnetic ordering are unavailable, anomalies in the resistivity provide a clue that a material may have a phase transition at a certain temperature. This was true for Cr, for which the anomaly was noted in 1932 by Bridgman [40]. Néel suggested that Cr may be antiferromagnetic in 1936 [41], but it was not until 1959 that the antiferromagnetic order was confirmed through neutron diffraction [42, 43].

1.5 The Interaction of X-Rays with Matter

X-rays were first discovered by Wilhelm Conrad Röntgen in 1985 [44] and have become an incredibly consequential in our world. The most well-known application is in medicine, with x-rays used for imaging of the human body and diagnosis of various conditions. But x-rays are also used in research in many different scientific fields, from determining material structures and correlations in materials science to studying protein structure and folding in biology. In this dissertation, x-ray diffraction is used extensively, both in simple characterizations of the crystal structure of films and as a central component to studying specific phenomena in the materials. What follows here is a brief discussion of the interaction of x-rays with matter and how this is useful in studying materials.

Electromagnetic radiation is broken into different categories, such as visible, radio, or microwave, based on its wavelength and energy. The wavelength λ and energy $\mathcal{E}$ of radiation can

be related by

$$\mathcal{E} = \frac{hc}{\lambda},$$

where $h = 6.626 \times 10^{-34}$ m^{2}kg/s is Planck's constant and $c = 2.9979 \times 10^8$ m/s is the speed of light. X-rays are the category of electromagnetic radiation with wavelength in the range of around 10 pm to 10 nm or energy in the range around 100 eV to 100 keV. These wavelengths of radiation are useful in resolving features on the order of Å or nm, such as the spacing of atoms in a crystal lattice or the bond length of molecules. X-rays can be further split into soft x-rays, with an energy of less than about 5 keV, and hard x-rays, with an energy greater. Hard x-rays are able to penetrate deeply into a material, which allows for a kind of imaging of the internal structure of a material.

Classically, electromagnetic radiation is viewed as a wave, with the linearly polarized x-ray propagating with wavevector $\mathbf{k}$ with oscillating perpendicular electric field $\mathbf{E}$ and magnetic field $\mathbf{H}$ such that $\mathbf{k}\cdot\mathbf{E} = \mathbf{k}\cdot\mathbf{H} = \mathbf{E}\cdot\mathbf{H} = 0$. The electric field for this wave is

$$\mathbf{E}(\mathbf{r},t) = E_0\, e^{i(\mathbf{k}\cdot\mathbf{r}-\omega t)}\,\hat{\boldsymbol{\varepsilon}}.$$

Quantum mechanically, radiation is thought of as photons with energy $\mathcal{E} = \hbar\omega$ and momentum $\mathbf{p} = \hbar\mathbf{k}$. Considering both the particle and the wave nature of electrons is useful in understanding the interaction of x-rays with matter.

There are two ways that x-rays interact with matter: scattering and absorption. Scattering processes involve some kind of deflection of an x-ray in an interaction with an atom. Absorption is a process in which the x-ray is absorbed by the atom, exciting an electron into an unoccupied higher energy level or ejecting it from the atom completely. Most of the x-ray measurements in this dissertation are of x-ray diffraction from crystals which can be explained well with the explanation of x-ray scattering that will come next, which begins with Thomson scattering from a free electron and extends that to an atom and a collection of atoms in a crystal. There are other types and models of scattering which are not discussed here. A brief introduction of x-ray

absorption is also included.

1.5.1 X-Ray Diffraction from a Crystal

There are a few terms that are helpful to define first to understand scattering. A scattering cross section σ is a measure of how likely a material is to interact with and scatter an incident photon. It can be thought of as an effective area, with larger cross section increasing the probability of scattering, and has units of area. The differential cross section $\frac{d\sigma}{d\Omega}$, then, is the likelihood of scattering into a particular direction and can be used to understand the spatial distribution of scattering. For electromagnetic radiation, the wavevector $\mathbf{k}$ has a magnitude $k = \frac{2\pi}{\lambda}$ and is oriented in the direction of propagation of the wave. Here we will write the wavevector of the incident x-ray as $\mathbf{k}$ and the wavevector of the scattered x-ray as $\mathbf{k}'$. The quantity $\mathbf{Q} = \mathbf{k} - \mathbf{k}'$ is called the scattering vector or the wavevector transfer.

In a classical description of x-ray scattering from a free electron, the electric field of an incident x-ray causes an electron to vibrate and radiate a scattered x-ray as a result of that motion. This process, called Thomson scattering, is elastic, meaning that the scattered x-ray has the same energy as the incident x-ray and $|\mathbf{k}| = |\mathbf{k}'|$. It is also coherent, meaning the phase of the scattered x-ray is not random (for the case of scattering off an electron, the scattered wave will acquire a phase change of $\pi/2$). The incident x-ray has an electric field given by $\mathbf{E}_{\text{in}} = E_{\text{in}}\hat{\varepsilon}$. When the x-ray interacts with an electron, the electron will oscillate in position and radiate a spherical wave with $\mathbf{E}_{\text{rad}} = \frac{1}{r}e^{ikr}\hat{\varepsilon}'$. A derivation of the differential cross section gives

$$\left(\frac{d\sigma}{d\Omega}\right)_{\text{Thomson}} = r_0^2 |\hat{\varepsilon}\cdot\hat{\varepsilon}'|^2 = P(\theta),$$

where 2θ is the angle between the incident x-ray and the scattered x-ray, $P(\theta)$ is the polarization

factor for scattering, and the Thomson scattering length r_0 is

$$r_0 = \frac{e^2}{4\pi\varepsilon_0 mc^2} = 2.82 \times 10^{-15} \text{ fm}.$$

The Thomson scattering length is also thought of as the classical electron radius, which is more of a metaphor as we consider the electron to be a point particle. If the incident x-rays are unpolarized, meaning the electric field of incident X-rays are oriented in random directions perpendicular to its direction of propagation, the polarization factor is $P(\theta) = \frac{1}{2}\left(1 + \cos^2 2\theta\right)$. If the incident x-rays are linearly polarized, $P(\theta) = 1$ when the scattering plane is perpendicular to both the incident x-ray plane of polarization and the incident x-ray direction of propagation and $P(\theta) = \cos^2 2\theta$ when the scattering plane is in the plane of polarization of the incident x-rays. The cross section for scattering can be found by integrating over all possible scattering angles, which gives

$$\sigma_{\text{Thomson}} = \frac{8\pi r_0^2}{3} = 6.65 \times 10^{-25} \text{ cm}^2 = 0.665 \text{ barn}.$$

This cross section is not dependent on the energy of the x-rays: it simply suggests that all radiation will scatter in this way. It is based, however, on the assumption that we have a free electron rather than one bound to an atom, which is not always true. It is a good approximation for high-energy radiation such as x-rays, except near the resonant energies at which electrons bound to atoms can be excited to higher states and resonant scattering or x-ray absorption must be considered, which is outside the scope of this dissertation.

We can refine this model by considering x-ray interaction with an atom that has Z electrons distributed around its nucleus with density $\rho(\mathbf{r})$. We must consider x-rays scattering elastically over this entire electron cloud, in which the path length of individual x-rays is different, resulting in a phase difference, and so the scattered x-rays will interfere. Fig. 1.11 shows two possible scattering events with incident x-ray wavevector $\mathbf{k}$, one at the origin and one at a position $\mathbf{r}$ relative to the origin. The scattering vector $\mathbf{Q}$ is the same for these two events, but the path length

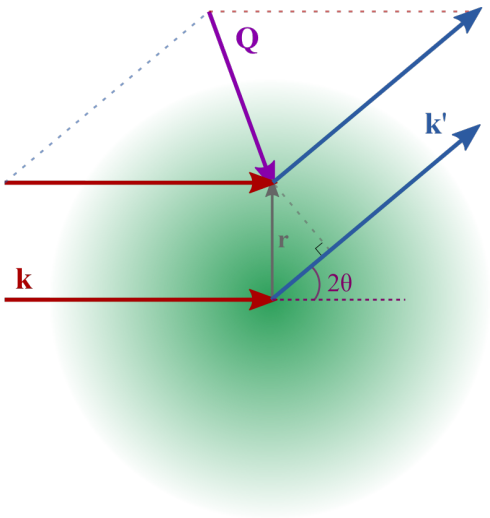

Figure 1.11: Schematic of the scattering of two x-rays from an atom with an electron distribution indicated by the orange circle. The incident wavevectors $\mathbf{k}$ (red arrows) and scattered wavevectors $\mathbf{k}'$ (blue arrows) have scattering vector $\mathbf{Q} = \mathbf{k} - \mathbf{k}'$. The scattering events in this schematic occur at the origin and at a position $\mathbf{r}$, resulting in a phase difference of the scattered wavevector given by $\Delta\phi(\mathbf{r}) = \mathbf{k}\cdot\mathbf{r} - \mathbf{k}'\cdot\mathbf{r} = \mathbf{Q}\cdot\mathbf{r}$.

differs. The resulting phase difference between the two events is $\Delta\phi(\mathbf{r}) = \mathbf{k}\cdot\mathbf{r} - \mathbf{k}'\cdot\mathbf{r} = \mathbf{Q}\cdot\mathbf{r}$. The scattering length here becomes

$$-r_0 f^0(\mathbf{Q}) = -r_0 \int \rho(\mathbf{r}) e^{i\mathbf{Q}\cdot\mathbf{r}} d\mathbf{r}, \tag{1.27}$$

where $f^0(\mathbf{Q})$ is called the atomic form factor or the atomic scattering factor and is the scattering amplitude of radiation from a single atom. The intensity of scattering, then, is proportional to $|f^0(\mathbf{Q})|^2$. In the limit $\mathbf{Q} \to 0$, where the incident and scattered wavevector would be equal and parallel, there would essentially be no phase difference between the scattered x-rays and $f^0(0) = Z$. The form of the integral of Eq. 1.27 is just a Fourier transform, and so the scattering from an atom can be thought of as a Fourier transform of its electron distribution. In this treatment, we have assumed that the scattering events look like scattering from free electrons and neglected to consider a few effects, including x-ray absorption and how the binding of electrons to the atom influences its response to the x-ray's electric field. These effects result in dispersion corrections

to the form factor that have both **Q**-dependence and energy dependence. Without discussing these further, we will simply write the form factor here as $f(\mathbf{Q})$, understanding its limitations in describing the true scattering.

Experimentally, we are of course always considering more than one atom in scattering. So we can consider scattering from a group of atoms, like the atoms making up a molecule or the atoms in the unit cell of a crystal. Since we are looking at crystals in this work, we will continue with notation and descriptions relevant to this. X-rays interact with each atom in the unit cell, so we can sum up the scattering from each atom individually in a sense. However there will again be a phase difference introduced into the scattering due to the different positions of the atoms. So we must consider that each atom has position $\mathbf{r}_j$ and form factor $f_j(\mathbf{Q})$, to find the unit cell structure factor:

$$F_{\text{cell}}(\mathbf{Q}) = \sum_j f_j(\mathbf{Q}) e^{i\mathbf{Q}\cdot\mathbf{r}_j}. \tag{1.28}$$

The scattering from crystals that we measure in this dissertation involves scattering from a large number of these unit cells, which are arranged periodically into a crystal lattice. The scattering from each unit cell will contribute according to Eq. 1.28, but there will be a phase difference associated with different positions of the unit cells. Now we consider unit cells with position $\mathbf{R}_n$, each containing atoms with position $\mathbf{r}_j$ relative to the unit cell position, so that the position of any given atom can be described as $\mathbf{R}_n + \mathbf{r}_j$. The scattering amplitude for the crystal is

$$F_{\text{crystal}}(\mathbf{Q}) = F_{\text{cell}}(\mathbf{Q}) \sum_n e^{i\mathbf{Q}\cdot\mathbf{R}_n} = \sum_j f_j(\mathbf{Q}) e^{i\mathbf{Q}\cdot\mathbf{r}_j} \sum_n e^{i\mathbf{Q}\cdot\mathbf{R}_n} \tag{1.29}$$

and reflects that the scattering depends on both the scattering from individual atoms as well as placement of those atoms in the lattice.

To better understand what is seen in crystal diffraction, Fig. 1.12 shows two possible elastic scattering events from a simple cubic crystal lattice with spacing d and incident and scattered x-rays at angles θ as shown. The phase difference between the scattered x-rays due

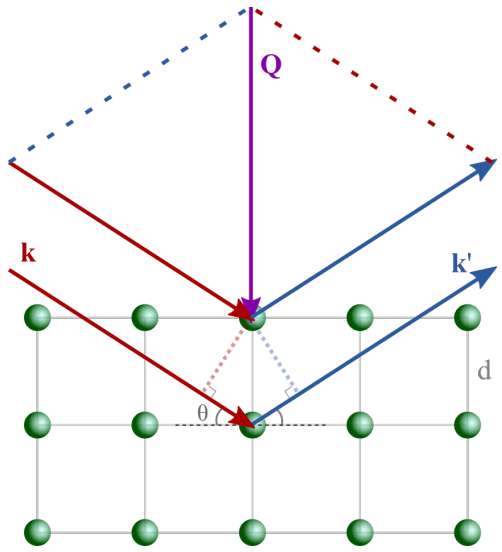

Figure 1.12: Schematic of the scattering of two x-rays from a crystal lattice. The incident wavevectors $\mathbf{k}$ (red arrows) and scattered wavevectors $\mathbf{k}'$ (blue arrows) have scattering vector $\mathbf{Q} = \mathbf{k} - \mathbf{k}'$. The phase difference of the scattered x-ray is determined by the lattice spacing and the angle of the incident and scattered x-rays.

to the separation of the atoms is a result in a path difference $2d\sin\theta$. The scattered waves will interfere, with the path difference and wave energy determining whether there is constructive or destructive interference. The scattered intensity is maximized for the Bragg condition:

$$n\lambda = 2d\sin\theta, \tag{1.30}$$

where n is an integer and λ is the wavelength of the radiation. And so if the x-ray scattering were conducted as a function of θ, for example, there would be certain angles at which the scattered intensity would greatly increase, and the location of those peaks give structural information about the crystal lattice. From the scattering amplitude for the crystal in Eq. 1.29, we see that the scattering intensity is quite low everywhere except when the condition $\mathbf{Q}\cdot\mathbf{R}_n = 2\pi z$ where z is an integer is met. For a periodic arrangement of the unit cells in a crystal, we use this property as the basis for crystal diffraction.

Eq. 1.29 implies the scattering from a crystal is a Fourier transform of the crystal structure.

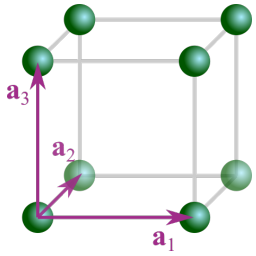

Figure 1.13: Schematic of the lattice basis vectors $(\mathbf{a}_1, \mathbf{a}_2, \mathbf{a}_3)$ for a cubic lattice.

It is useful to introduce reciprocal space (or momentum space or k-space), which is the Fourier transform of the real space or Euclidean space. A crystal structure is defined in real space with lattice basis vectors $\mathbf{a}_i$ as shown in Fig. 1.13. Each unit cell in the crystal is located at $\mathbf{R}_n = \sum_i n_i \mathbf{a}_i$ where n_i are integers. The reciprocal basis vectors are defined as

$$\mathbf{a}_i^* = 2\pi \frac{\mathbf{a}_j \times \mathbf{a}_k}{\mathbf{a}_i \cdot (\mathbf{a}_j \times \mathbf{a}_k)}$$

and follow the property $\mathbf{a}_i \cdot \mathbf{a}_j^* = 2\pi\delta_{ij}$. The reciprocal space vector corresponding to $\mathbf{R}_n$ is $\mathbf{G}_m = \sum_i m_i \mathbf{a}_i^*$ where m_i are integers and sometimes written as the Miller indices h, k, and l. Since $\mathbf{G}_m \cdot \mathbf{R}_n = 2\pi z$ where z is an integer, the diffraction condition is met at reciprocal lattice vectors $\mathbf{G}_m$.

A lattice plane in a crystal is referred to (hkl) and defined as the plane connecting the points $\mathbf{a}_1/h$, $\mathbf{a}_2/k$, and $\mathbf{a}_3/l$. If any of the indices is negative, we indicate that by a bar over that index. Fig. 1.14 gives some examples of lattice planes and their corresponding Miller indices. These lattice planes are equally spaced by d_{hkl}, and for a lattice in which we have orthogonal basis vectors $\mathbf{a}_i$, this spacing is given by

$$\frac{1}{d_{hkl}^2} = \frac{h^2}{a_1^2} + \frac{k^2}{a_2^2} + \frac{l^2}{a_3^2}.$$

In a cubic lattice, we can refer to a set of planes that are related by symmetry as $\{hkl\}$. So for example, $\{100\}$ refers to the planes (100), (010), (001), $(\bar{1}00)$, $(0\bar{1}0)$, and $(00\bar{1})$. A direction or

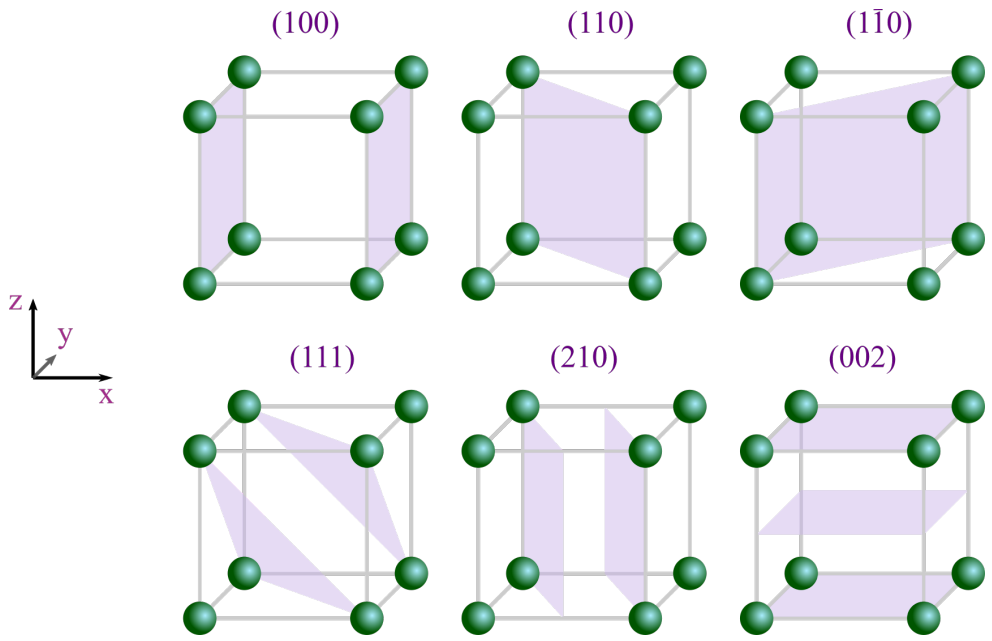

Figure 1.14: Example lattice planes in a cubic crystal identified by Miller indices.

vector in the crystal $U\mathbf{a}_1 + V\mathbf{a}_2 + W\mathbf{a}_3$ is commonly referred to as $[UVW]$, and the equivalent vectors by symmetry as $\langle UVW \rangle$.

Given all this, we can measure the scattering of a crystal with the appropriate x-ray energy and observe specific diffraction peaks. The location of these peaks, also called reflections, will give us information about the lattice spacing. So far, we have stuck to the simple case of a cubic crystal. However many materials have different structures which sometimes restrict which lattice planes will result in diffraction peaks and which will destructively interfere and be forbidden, and there are rules for h, k, l corresponding to the diffraction condition. This allows us to make determinations of the orientation of atoms within each unit cell. And so far, all calculations have assumed a perfect crystal, but real crystals have imperfections, especially when we consider thin films of materials. One example of this is mosaicity in a crystal, which we describe as many small blocks of perfect crystals which are in slight misalignment with one another. When scattering from such a crystal, the angles of incidence and scattering will be slightly different from different blocks, resulting in a broadening of the diffraction peak. It is possible to measure the width of

peaks to get an idea of the mosaic spread in a crystal.

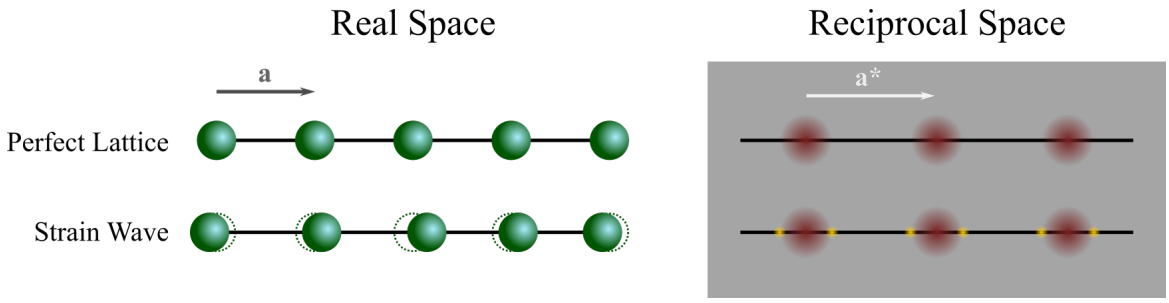

Figure 1.15: Real space and reciprocal space depictions of x-ray diffraction from a one-dimensional perfect lattice and strain wave.

One thing to note of importance to this work is the possibility of additional periodicities in systems resulting in stronger diffraction. We see this in Cr, which has a periodic lattice distortion (or strain wave) and charge density wave. Simplified real and reciprocal space depictions of a one-dimensional perfect lattice and a one-dimensional lattice that has a strain wave are in Fig. 1.15. For the perfect lattice, we have the Bragg peaks as discussed. The strain wave adds in an additional periodic lattice distortion, which will of course show up in a Fourier transform of the lattice. In the case of a strain wave that is incommensurate with the lattice (has a period that is not a rational fraction or multiple of the lattice spacing), the strain wave shows up as satellite peaks around the Bragg peaks as shown.

X-ray diffraction measurements in this work are made on thin films, which provides additional complexity to the calculations. We have assumed essentially infinite lattice planes, each giving a different phase to the scattered x-ray which results in constructive or destructive interference. For a thin film, there are a finite number of lattice planes from which to scatter. When the diffraction condition is met at the Bragg peak, total constructive interference can occur as expected. But elsewhere, there is incomplete destructive interference. If the film is of high crystal quality, with smooth interfaces and high uniformity of the crystal structure throughout, the incomplete destructive interference will result in oscillations around the Bragg peak which are called Laue oscillations or Laue fringes. The period of these oscillations gives a measure of the

number of unit cells that are diffracting coherently, which is a measure of the thickness of the film.

All this provides a good basis for understanding crystal diffraction in this work. Some of the shortcomings were already pointed out: that it neglects to consider absorption energies and it assumes the energy of the radiation is high enough to treat the electrons as free. It also makes a kinematical approximation, in which we assume a weak interaction of the x-rays with the lattice and do not have to account for multiple scattering events, which is a good approximation for imperfect crystals and scattering from thin films, so we will not consider the alternative, the dynamical diffraction. This treatment has also assumed elastic scattering, in which the incident x-ray and scattered x-ray have the same energy. Rayleigh scattering will refine this to account for electrons bound to an atom and an x-ray energy that is not high enough to approximate them as unbound. Compton scattering is a type of inelastic scattering in which we can consider x-rays as quantum mechanical particles which collide with electrons, transferring some energy to the electron, and then the scattered x-ray will have a reduced energy. This is not a significant quantity in the experiments conducted here, but becomes more important for higher energy scattering experiments.

1.5.2 X-Ray Reflectivity

X-ray diffraction in the previous section required understanding the interaction of x-rays with electrons in atoms in a crystal lattice. But there is another phenomenon associated with electromagnetic waves passing through different materials: refraction. This is commonly associated with visible light bending when it goes through glass or water, for instance. But of course it occurs with x-rays also. In the treatment of x-ray diffraction, one of the assumptions made is the Born approximation, that x-rays are very weakly scattered in the material. At small incident angles, where we measure reflectivity, this approximation is no longer valid. In thin films, x-ray reflectivity is a way of measuring a depth profile of the electronic distribution.

For visible light, most materials have an index of refraction greater than 1, but with x-rays, we have indices less than 1. Following Snell's law, this implies that there is an angle, the critical angle θ_c, below which x-rays will be totally reflected at the surface of a material. The index of refraction when considering x-rays can be expressed as

$$n = 1 - \frac{\lambda^2 \rho_{\text{at}} f^0(0) r_0}{2\pi} + i\frac{\mu\lambda}{4\pi} = 1 - \delta + i\beta, \tag{1.31}$$

where ρ_{at} is the atomic number density and μ is the absorption coefficient, the inverse of the characteristic length of attenuation of intensity in the material. In solids, δ is on the order of 10^{-5} and $\beta \ll \delta$. Following the same geometry as for diffraction in Fig. 1.12, x-ray reflectivity is involves measuring scattering at low angles θ. Using Snell's law, the critical angle can be found by evaluating

$$1 - \delta = \cos\theta_c \approx 1 - \frac{\theta_c^2}{2} \quad \longrightarrow \quad \theta_c \approx \sqrt{2\delta}. \tag{1.32}$$

The conclusion from this is that θ_c provides a measure of the atomic density of the material being studied. Fig. 1.16 demonstrates this with simulated reflectivities for films of Pt, FeRh, and Cr on MgO substrates with other parameters held constant (film thicknesses of 30 nm, substrate interface roughness of 0.6 nm, and surface roughness of 0.3 nm), with the intensity on a log scale. The critical angle, where the intensity of reflection drops dramatically, clearly decreases as the film density decreases, which is consistent with what is expected from Eq. 1.31 and Eq. 1.32.

For $\theta > \theta_c$, scattering intensity will decrease quickly by orders of magnitude. However there is information that can be understood about a material in how the intensity decreases, particularly in measuring film thicknesses of roughly 20-40 nm and in evaluating the quality of surfaces and interfaces. There are, of course, rigorous derivations and theories in explaining x-ray reflectivity. Since x-ray reflectivity is used mainly in characterizing films rather than as a central component of experiments in this work, those are not included here. However, we will qualitatively discuss the topic for thin films relevant to this dissertation.

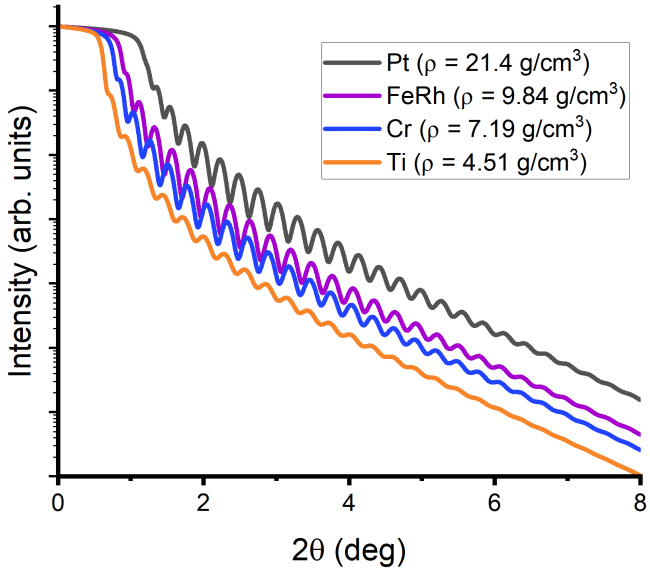

Figure 1.16: Simulated x-ray reflectivity for 30 nm films of Pt, FeRh, and Cr on MgO substrates with substrate interface roughness 0.6 nm and surface roughness 0.3 nm. Simulations created using the reflectivity modeling software *GenX* [45].

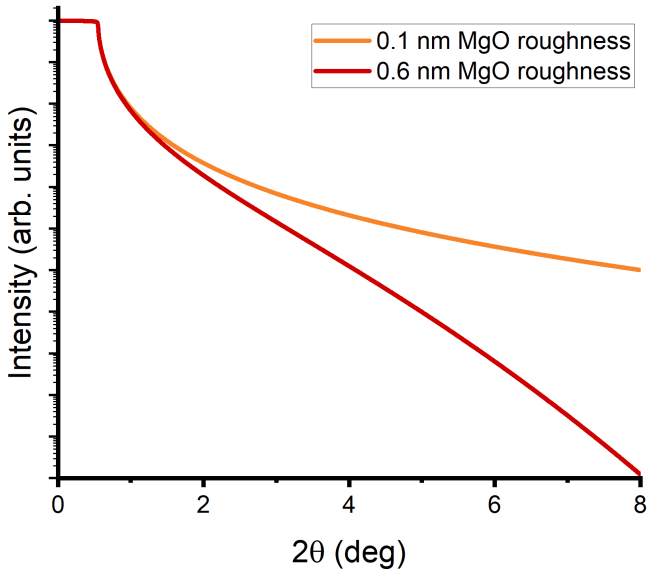

Figure 1.17: Simulated x-ray reflectivity for MgO substrates with roughness 0.1 nm and 0.6 nm. Simulations created using the reflectivity modeling software *GenX* [45].

Fig. 1.17 shows simulated x-ray reflectivity for two MgO substrates with different roughness. Both show identical critical angles, which is expected since the material, and therefore the densities, are the same. However the intensity of scattering from the substrate with greater roughness drops off faster, with the scattering intensity over five orders of magnitude smaller at $2\theta = 8$ deg (the x-ray energy used is 8.04 keV). A rough surface can be thought of as a lot of small surfaces that are not perfectly parallel. Incident x-rays will then elastically scatter into slightly different angles. For an incident x-ray angle θ, then, the scattered intensity at an exact scattered x-ray angle θ will be reduced. We call the case where the angle of incidence and angle of reflection or angle of scattering are equal specular reflection. When the angle of reflection is different, it is considered off-specular reflection. Off-specular reflection is significant when there are structural periodicities to the material. Roughness can be thought of as like this, and will result in diffuse off-specular reflection.

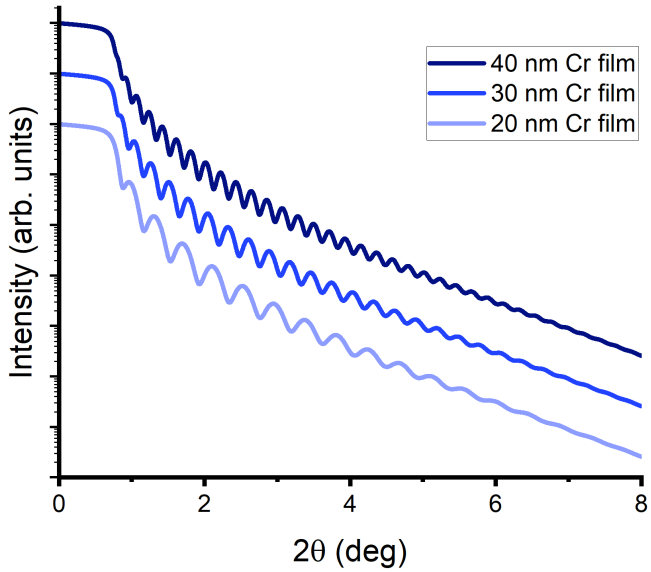

Figure 1.18: Simulated x-ray reflectivity for 40 nm, 30 nm, and 20 nm films of Cr on MgO substrates with substrate interface roughness 0.6 nm and surface roughness 0.3 nm. Simulations created using the reflectivity modeling software *GenX* [45].

When a film is deposited on top of a substrate, the reflectivity exhibits oscillations known

as Kiessig fringes [46], shown in Fig. 1.16 and Fig. 1.18. These fringes come from interference of the x-rays that are scattered from both interfaces of the film. This picture is analogous to the one shown in Fig. 1.12 with interference of x-rays scattering from atoms in a crystal lattice with a well-defined lattice spacing, but in this case, the relevant distance is the distance between the interfaces (the thickness of the film). We can use the Bragg condition of Eq. 1.30 to understand the origin of these oscillations and find that the minima of the oscillations occur at θ_{min} given by

$$\theta_{\text{min}}^2 \approx n^2 \left(\frac{\lambda}{2d}\right)^2 + 2\delta,$$

where n is an integer and d is the thickness of the film. So then the positions of the minima can be used to find the film thickness. In Fig. 1.18, it is shown that the period of oscillation decreases as the film thickness increases. The amplitude of the oscillation is influenced by the contrast of densities between the film and the substrate, which can be seen in Fig. 1.16 for films of different densities on MgO (with density 3.58 g/cm^3).

The roughness of the film that is deposited on the substrate also impacts the reflectivity. The film roughness can be thought of similarly to the substrate roughness, with bits of surface that are not perfectly in alignment. The roughness of different interfaces cannot be separated perfectly, but it is understood that increased roughness will reduce the scattering intensity overall. It also impacts the Kiessig fringes, resulting in a faster decay of the oscillation with imperfect interfaces of the film. This is demonstrated in Fig. 1.19 for Cr films with roughness 0.3 nm and 1.5 nm.

And so an x-ray reflectivity measurement of thin films allows for an analysis of some of the film properties. The densities of the materials influence the critical angle and their relative intensities influence the amplitude of oscillation. The period of the oscillation is determined by the film thickness. The decay of the intensity and of the oscillations is determined by the roughness at each interface and surface. This qualitative analysis is sufficient to understand the x-ray reflectivity presented in this dissertation.

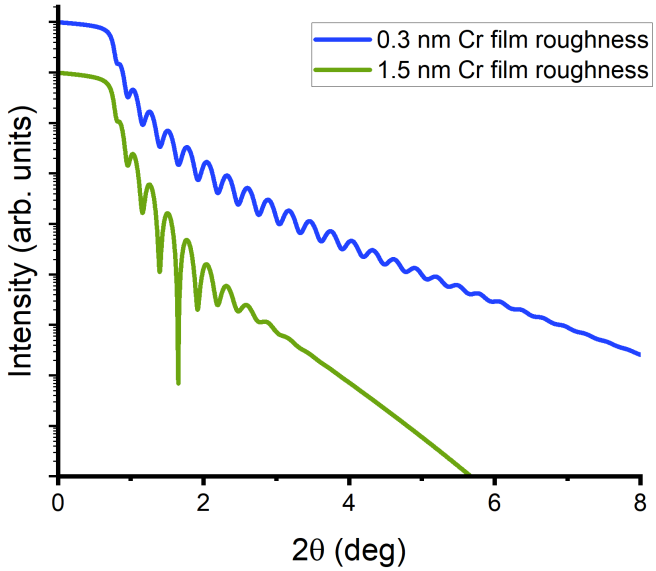

Figure 1.19: Simulated x-ray reflectivity for 30 nm films of Cr on MgO substrates with substrate interface roughness 0.6 nm and surface roughness 0.3 nm and 1.5 nm. Simulations created using the reflectivity modeling software *GenX* [45].

1.5.3 X-Ray Absorption

X-ray absorption or photoelectric absorption is a process by which energy from an incident x-ray is transferred to an electron, and the electron is expelled from the atom. Fig. 1.20 shows a schematic of the energy required to expel each core electron. For a measurement of absorption vs. x-ray energy, there are sharp discontinuities at certain energies, referred to as absorption edges, where the x-rays at that energy or higher are able to transfer enough energy to expel a specific electron. The edge corresponding to the $1s$ electrons (in the K shell where $n = 1$) is referred to as the K edge. For the electrons in the L shell with $n = 2$, the edge is referred to as the L_1 edge for $2s$ electrons and L_2 or L_3 edges for $2p$ electrons.

When an electron is expelled from the atom, there is a hole created in that shell which is filled either through fluorescence or through the Auger effect. In fluorescence, an electron in an outer shell fills the hole, emitting a photon with an energy given by the difference in the binding

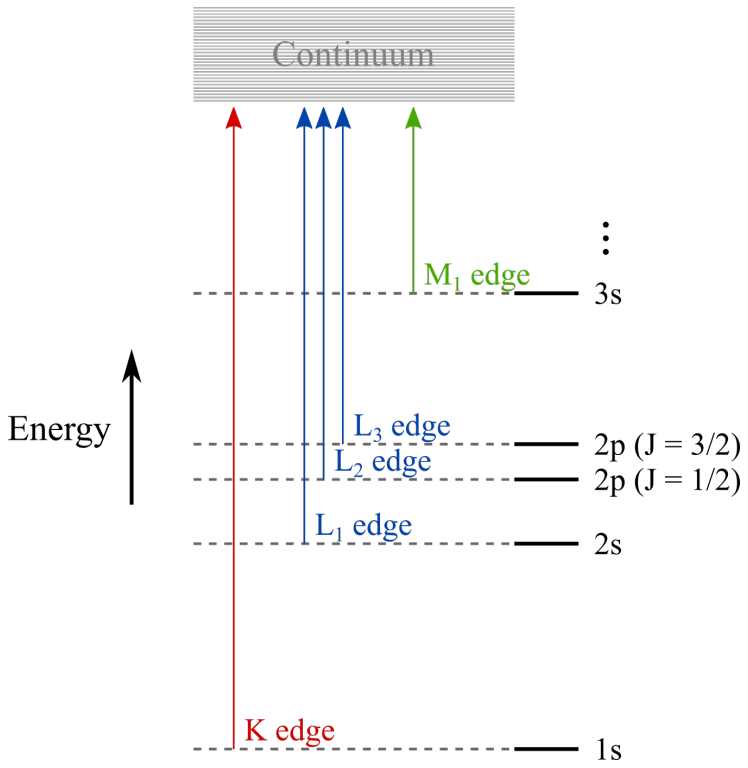

Figure 1.20: Schematic of the core electron energy levels of an atom and the energy required to excite and expel an electron from each energy level. These energies are referred to as absorption edges, where there is a discontinuous rise in absorption measured as a function of incident x-ray energy corresponding to the absorption of the photon and ejection of the electron.

energies of the two states. For an electron that drops from the L shell to the K shell, the emitted radiation is referred to as Kα. For an electron that drops from the M shell (with $n = 3$) to the K shell, the emitted radiation is referred to as Kβ. Alternatively, the hole in the shell can be filled with Auger electron emission, in which an electron drops into the hole from a higher energy state and the energy is transferred to an outer electron which is expelled from the atom. Usually this is also accompanied by an emitted photon since the energy differences are not exact.

X-Ray Magnetic Circular Dichroism (XMCD)

The interaction of x-rays and matter so far has considered only the electric field of the x-rays and electron charge. But the x-ray's magnetic field also interacts with the electrons, giving rise to terms in the scattering cross section which are sensitive to spin and orbital moments. For

scattering from a single electron, the ratio of the intensities of magnetic and charge scattering [47] is

$$\frac{I_{\text{magn}}}{I_{\text{charge}}} = \left(\frac{\hbar\omega}{mc^2}\right)^2,$$

which is on the order of 10^{-4} for the relevant x-ray energies. In an atom where most of the electrons are paired, only a few of the electrons will contribute to magnetic scattering, and this ratio for scattering from atoms can be depressed by around two orders of magnitude. So generally, the magnetic scattering is neglected from these treatments. There are certain scenarios when magnetism-sensitive scattering and absorption are non-negligible and very useful. These are outside the scope of this work except for the case of x-ray magnetic circular dichroism, which is measured in Section 5.2.

Circularly polarized light is light in which the electric field of the radiation has a constant magnitude and is rotating in the plane normal to the direction of propagation of the wave. This radiation has a spin angular momentum in the direction of propagation given by $+\hbar$ (right-circularly polarized) or $-\hbar$ (left-circularly polarized). Conservation of angular momentum will forbid the absorption of this light for certain transitions depending on the polarization of the incident light which gives rise to differences in the absorption spectra of left- and right-circularly polarized x-rays, which is called XMCD. This is a very sensitive technique, able to detect moments on the order of 10^{-3} μ_B/atom, and allows for the separation of the spin and orbital contributions to the moment. These differences are measured at energies near the absorption edges, giving element-specific information, which is very useful in alloys and materials with multiple species of atoms.

1.6 The Interaction of Neutrons with Matter

Neutron science is another useful area of research, especially in studying magnetic ordering in materials. Neutron techniques such as neutron diffraction can be analogous in some

ways to x-ray science, but there are some important differences which make each of them useful in different scenarios.

Neutrons have mass $m_n = 1.675 \times 10^{-27}$ kg, no charge, and are spin-1/2 particles with magnetic moment $\mu_n = -1.913\mu_N = -0.0010\mu_B$. The quantum mechanical wave-particle duality gives a description of the neutron as a wave, or matter wave, with an energy $\mathcal{E}$, de Broglie wavelength λ, and wavevector $\mathbf{k}$, which give momentum

$$p = \frac{h}{\lambda} = \hbar k$$

and non-relativistic neutron energy

$$\mathcal{E} = \frac{p^2}{2m_n} = \frac{\hbar^2 k^2}{2m_n}.$$

If a neutron reaches thermal equilibrium with a material near room temperature at $T = 300$ K, its average kinetic energy is $E \sim k_B T = 4.1 \times 10^{-21}$ J $= 26$ meV, which corresponds to $\lambda \sim 1.8 \times 10^{-10}$ m. This is on the order of the distance between atoms in materials, which means that neutrons, like x-rays, are useful for resolving atomic-scale features. Neutrons are broadly categorized as cold with energies of 0.1-10 meV (and temperature 1-120 K and wavelength 0.4-3 nm), thermal with energies 5-100 meV (and temperature 60-1000 K and wavelength 0.1-0.4 nm), or hot with energies 100-500 meV (and temperature 1000-6000 K and wavelength 0.04-0.1 nm).

When describing the interaction of x-rays with matter, the primary mode of scattering is charge scattering, in which the x-rays interact with electrons electromagnetically. Neutrons, on the other hand, are electrically neutral. This means that there are two dominant modes of scattering that are considered. First, their neutral charge means that they are not screened by the electrons surrounding the nucleus and, for an atom with no net moment, will scatter only from the atomic nucleus. The second mode of scattering is for the case when an atom does have a net moment, in which case the small magnetic moment of the neutron interacts with the electronic magnetization.

These two contributions are referred to as nuclear scattering and magnetic scattering.

Nuclear scattering occurs via the strong nuclear force, which is very strong but short range, on the order of 10^{-15} m. Since the separation of atoms is on the order of 10^{-10} m, the nuclear scattering cross section is very small and neutrons are able to penetrate deeply in to a material, typically on the order of cm compared to hundreds of nm to hundreds of μm for x-rays. This is useful for evaluating bulk effects rather than being sensitive to surface conditions (except in the case of reflectometry). But this also makes the measurement of thin films more difficult, since a higher flux of neutrons would be required to achieve a strong signal. Light elements (such as hydrogen) with low atomic number Z have a lower probability of interaction with x-rays than high-Z materials do because there are fewer electrons to interact with. Neutrons, however, interact with the nuclei and there is no simple relation of the cross section on Z, with different scattering lengths for different elements and isotopes. Some lighter elements have strong neutron scattering cross sections and make this a more useful technique in their study. Neutrons also generally deposit very little energy in a sample and so it is a non-destructive technique suitable for studying soft matter as well as hard matter.

The magnetic scattering of neutrons comes from the magnetic potential

$$V_m = -\boldsymbol{\mu} \cdot \mathbf{B},$$

which describes the interaction of the neutron magnetic moment with the magnetic field from the unpaired electrons in the atoms, including the field from their orbital and spin moments. It is useful to note that the orientation of the moments in the sample relative to the neutron moment has an impact on the potential (that this is not a central potential) and that the magnetic interactions are longer range. This results in a more complex expression of the magnetic cross section which ends up being on the order of the nuclear cross section. There is a property of neutron magnetic scattering called spin flip which is used in some techniques. For neutrons polarized in a field

direction along the z-axis, an interaction with a moment along $\hat{x}$ or $\hat{y}$ will cause the neutron's spin to flip (from spin-up to spin-down or vice versa) while an interaction with a moment along $\hat{z}$ will not. All of these properties of magnetic neutron scattering make it very powerful in determining the ordering, magnitude, and direction of magnetic moments in a material.

There are several disadvantages of neutron science as compared to x-ray science. Traditionally, neutrons have been produced in nuclear reactors that are optimized for research work, which is an obvious barrier to their establishment. More recently, spallation sources have been developed, which can provide more intense pulsed neutron beams, but the relatively weak beams given the low scattering cross sections means that neutron flux is often a limiting factor in experiments and some x-ray techniques (such as time-resolved scattering) that are implemented at modern synchrotron and x-ray free electron facilities are more difficult to realize with neutrons. But the strength of the magnetic scattering makes it continue to be crucial in studies of magnetic materials.

As with x-rays, neutrons can also interact with matter through absorption. This could occur by the absorption of the neutron into the nucleus, which is an excited state which will relax with the emission of a gamma ray. This will vary between elements and isotopes and depend on the neutron energy. For the work in this dissertation, it is negligible compared to scattering and will be neglected, however there are cases when resonant behavior occurs and must be taken into account or becomes the dominant interaction.

1.6.1 Neutron Diffraction from a Magnetic Crystal

One of the most common neutron scattering techniques is neutron diffraction. For this, the nuclear and magnetic scattering will be considered separately. For a neutron plane wave with wavevector $\mathbf{k}$ incident on an isolated bound nucleus, the scattered wave function is spherically symmetric and given by

$$\psi(\mathbf{r}) = -\frac{b}{r} A e^{ikr},$$

where r is the radial distance from the center of the nucleus and b is the bound nuclear scattering length, which varies depending on the element and isotope and can be positive, negative, or complex, indicating that the phase may change during the scattering event. There is considerable variation in the value of b as a function of Z. This can be extended to a system of bound nuclei labeled j each with bound nuclear scattering length b_j and position $\mathbf{r}_j$. Using the definition of the scattering vector $\mathbf{Q} = \mathbf{k} - \mathbf{k}'$ (as with x-rays), the neutron intensity at a detector is given by

$$I_{\text{nuc}}(\mathbf{Q}) = \left| \sum_j b_j e^{i\mathbf{Q}\cdot\mathbf{r}_j} \right|^2 .$$

As before in the case of x-rays, considering elastic scattering and ordering of the atoms into a crystal simplifies this picture considerably. The intensity of the nuclear scattering of unpolarized neutrons becomes

$$I_{\text{nuc}} = \left| \sum_j b_j e^{2\pi i(hx_j + ky_j + lz_j)} \right|^2 , \tag{1.33}$$

where $\mathbf{r_j} = x_j\hat{x} + y_j\hat{y} + z_j\hat{z}$ and h, k, and l refer to the Miller indices introduced with x-ray diffraction. This nuclear scattering of neutrons is analogous to the scattering of x-rays, with the diffraction giving a Fourier transform of the nuclear distribution of the crystal, which should look like the Fourier transform of the electron distribution in x-ray scattering. There are peaks in the diffraction that correspond to lattice planes and specific reflections, allowing the arrangement of atoms in the crystal to be determined.

However neutrons have an additional contribution to the scattering from the magnetic interactions. The magnetic scattering cross section is far less straightforward since the interaction of the spins is not a central potential, and the derivation will not be reproduced here. But the magnetic scattering cross section is comparable in strength to the nuclear scattering cross section and is proportional to the square of the magnetic form factor, which is a Fourier transform of the spin distribution in real space. It also has a dependence on the relative orientation of the spin, and can vanish for certain orientations of the neutron spin and $\mathbf{Q}$.

For elastic scattering of unpolarized neutrons from a crystal, the intensity of magnetic scattering is

$$I_{\text{magn}} = \left| \sum_j q_j p_j e^{2\pi i(hx_j + ky_j + lz_j)} \right|^2, \tag{1.34}$$

where p_j is the magnetic scattering length and q_j is the magnetic interaction vector where

$$\mathbf{q} = \hat{\mathbf{n}}(\hat{\mathbf{n}} \cdot \hat{\mathbf{m}}) - \hat{\mathbf{m}},$$

and $\hat{\mathbf{n}}$ and $\hat{\mathbf{m}}$ are unit vectors normal to the scattering plane and parallel to the moment of the atom that the neutron is scattering from, respectively.

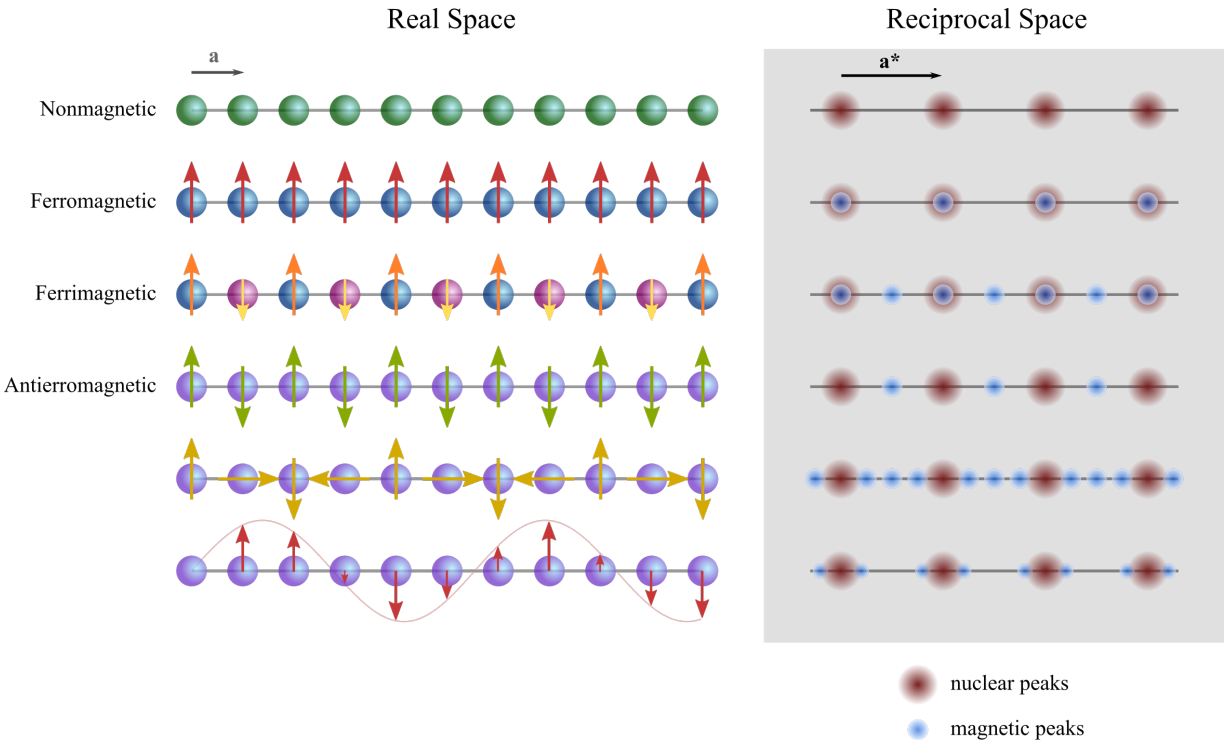

Figure 1.21: Real space and reciprocal space depictions of the diffraction of unpolarized neutrons from a one-dimensional perfect lattice for several possible types of magnetic ordering. In reciprocal space, a nonmagnetic lattice has only nuclear scattering peaks at integer indices. A ferromagnetic lattice has magnetic peaks superimposed on the nuclear peaks. A ferrimagnetic lattices has magnetic peaks superimposed on the nuclear peaks as well as at half-integer indices. Antiferromagnetic lattices can vary, with the three possibilities shown demonstrating magnetic peaks at half-integer indices, at every quarter index except at the integer indices, or as satellite peaks around the nuclear peaks.

The total scattering intensity of unpolarized neutrons from a magnetic crystal is simply the sum of the nuclear component from Eq. 1.34 and magnetic component from Eq. 1.33:

$$I = I_{\text{nuc}} + I_{\text{magn}}.$$

This is depicted in Fig. 1.21 for a one-dimensional lattice exhibiting some common types of magnetic ordering. For nonmagnetic atoms, only nuclear peaks are observed in diffraction at integer indices. For a ferromagnetic lattice, the magnetic scattering contributes additional intensity at the same nuclear peak locations. A ferrimagnetic lattice will have magnetic scattering at both integer and half-integer indices. The simplest antiferromagnetic lattice, with alternating antiparallel spins, will have magnetic scattering only at the half-integer indices. For the antiferromagnetic lattice that is incommensurate, with a period that is not a rational fraction or multiple of the lattice spacing, the observed magnetic scattering occurs as satellite peaks around the nuclear peaks.

For a polarized neutron beam, the nuclear and magnetic components will not simply add. The polarization of neutrons that scatter magnetically may change and the scattered neutrons may interfere. But unpolarized neutron diffraction is sufficient to determine the direction of the magnetic moments of atoms in the crystal, which makes this a very useful technique in magnetism.

1.6.2 Polarized Neutron Reflectometry

Polarized neutron reflectometry is an incredibly useful measurement of thin magnetic systems. Reflectometry refers to a similar geometry as diffraction, but with small angles of incidence and reflection, where the Born approximation that neutrons are weakly scattered in the material is no longer valid. Specular neutron reflectometry or reflectivity is the elastic scattering case of neutron reflectometry, analogous to x-ray reflectivity, and because of the nuclear scattering of neutrons, unpolarized neutron reflectometry provides a structural depth profile of the system.

For the inelastic case, what is called off-specular reflectometry or diffuse scattering, there is significant scattering in the case of structural periodicities in the material such as interfacial roughness or patterned structures. But neutrons can also scatter magnetically, and reflectometry can be conducted with polarized neutrons to achieve a magnetic depth profile from reflectivity and determine the presence of magnetic periodicities such as domains from off-specular reflection.

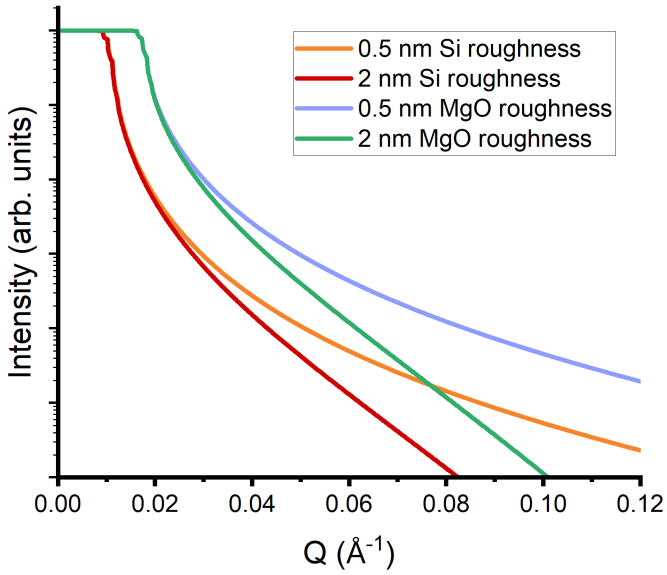

Figure 1.22: Simulated neutron reflectivity for Si and MgO substrates with roughness 0.5 nm and 2 nm. Simulations created using the reflectivity modeling software *GenX* [45].

Fig. 1.22 shows simulated neutron reflectivity for a Si substrate with 0.5 nm roughness and an MgO substrate with 0.5 nm and 2 nm roughness. As with x-ray reflectivity, the critical angle (or critical wavevector transfer) changes depending on the material that is being scattered from and the roughness influences how quickly the scattering intensity drops off. The expression for the critical wavevector transfer is

$$Q_c = \sqrt{16\pi\rho_b},$$

where ρ_b is the nuclear scattering length density (nSLD) given by

$$\rho_b = \sum_j b_j n_j,$$

where n_j is the number of nuclei per unit volume and b_j is the scattering length of nucleus j as previously discussed. The index of refraction can be shown to be

$$n = \sqrt{1 - \frac{\lambda^2 \rho_b}{\pi}} \approx 1 - \frac{\lambda^2 \rho_b}{2\pi},$$

where λ is the neutron wavelength. This demonstrates that the index of refraction is less than 1. The reflectivity from a material with a characteristic length scale of roughness σ can be shown to be

$$R \approx \left(\frac{16\pi^2 \rho_b^2}{Q^4} \right) e^{-q_z^2 \sigma^2},$$

which demonstrates that for a perfectly smooth interface, the reflectivity will go as Q^{-4} and increasing roughness results in a faster drop-off in reflected intensity. The nature of the rough interfaces is not so important in the specular reflectivity, but it does change where the neutron intensity is lost to. For a diffuse interface, those neutrons are transmitted and add to the transmitted beam. For a rough interface, the neutrons are scattered into different angles and contribute to off-specular scattering.

If the material is magnetized, the magnetic scattering must also be accounted for. For polarized neutrons, the index of refraction is modified to

$$n_\pm \approx 1 - \frac{\lambda^2 (\rho_b \pm \rho_p)}{2\pi},$$

where ρ_p is the magnetic scattering length density (mSLD) and gives a measure of the magnitude of the moments in the sample. A schematic of a polarized neutron reflectivity measurement is shown in Fig. 1.23. The neutrons that scatter from this sample are sensitive to the component of

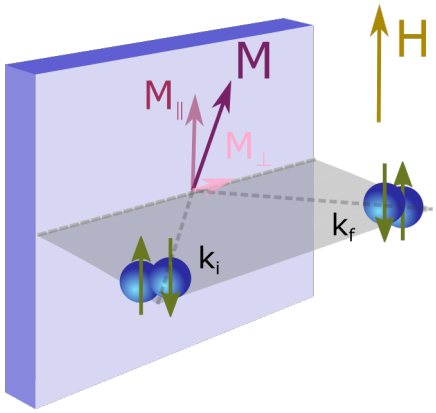

Figure 1.23: Schematic of a polarized neutron reflectivity measurement. Neutrons of spin up or spin down are incident on a film with in-plane magnetization **M** in the presence of a magnetic field parallel or antiparallel to the neutron spin and in the film plane. Reflected neutrons can either remain unchanged or flip.

the magnetization that is in-plane. If the magnetization is parallel to the field and the neutron spin axis, there will be only non-spin-flip scattering (all spin-up neutrons will remain spin-up when scattered and vice versa). If there is a perpendicular component to the magnetization, there will be some spin-flip scattering.

In Fig. 1.24, neutron reflectivities are simulated for an Fe substrate. A nonmagnetic substrate has the reflectivity shown in green. For a substrate that is magnetized entirely in the parallel orientation, the critical wavevector transfer of spin-up and spin-down neutrons will differ as shown in blue and red, respectively. Fig. 1.25(a) shows the simulated neutron reflectivities for two 50 nm FeRh films on an MgO substrate. In green is the case of nuclear scattering only for a nonmagnetic film. If the film is magnetized in the parallel orientation, the non-spin-flip reflectivities will be as shown in blue and red. The resulting depth profile of the scattering length densities are shown in Fig. 1.25(b). The nSLD of MgO is higher than for FeRh, which is demonstrated in gold by the increase in nSLD below the film. Above the film, the nSLD is zero as expected. Both interfaces with the film have roughness so the nSLD has a continuous profile between the layers. The mSLD is zero for the nonmagnetic film (green) and constant at 0.3 fm/Å^3 for the magnetic film.

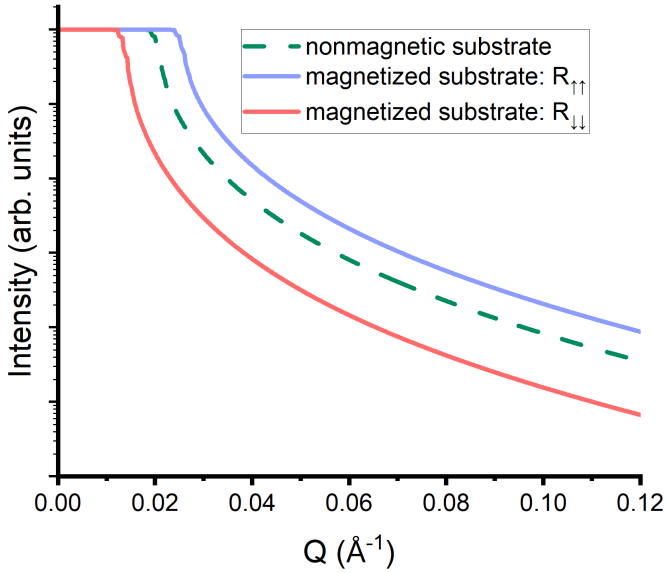

Figure 1.24: Simulated neutron reflectivity for Fe substrates with roughness 0.5 nm and magnetic scattering length density 0 and 0.2 fm/Å^3. For the magnetized substrate, the reflectivity of polarized neutrons (red and blue solid lines) differs from the nuclear reflectivity of a nonmagnetic substrate (green dashed line) as shown. Simulations created using the reflectivity modeling software *GenX* [45].

Fig. 1.26 shows two examples where the magnetization is not completely parallel to the field axis. In Fig. 1.26(a), the non-spin-flip and spin-flip reflectivities are shown for a 50 nm film with constant magnetization oriented 10 deg from the field axis. There are parallel and perpendicular components to the mSLD as shown in Fig. 1.26(b). In Fig. 1.26(d), a second possibility is shown, with a constant total magnetization in the film, but a 5 nm layer of the FeRh at the substrate interface that has magnetization directed 45 deg from the field axis while the rest of the film has magnetization directed 10 deg from the field axis. The resulting non-spin-flip and spin-flip reflectivities are shown in Fig. 1.26(c).

Measurements of the polarized neutron reflectivities can be fit to determine the nSLD and mSLD depth profile. Unfortunately, solutions are not unique [48], but with an understanding of what is reasonable and expected in a material, this technique can be used successfully to understand magnetic effects in thin films. In Section 5.3, the magnetic depth profile of an FeRh

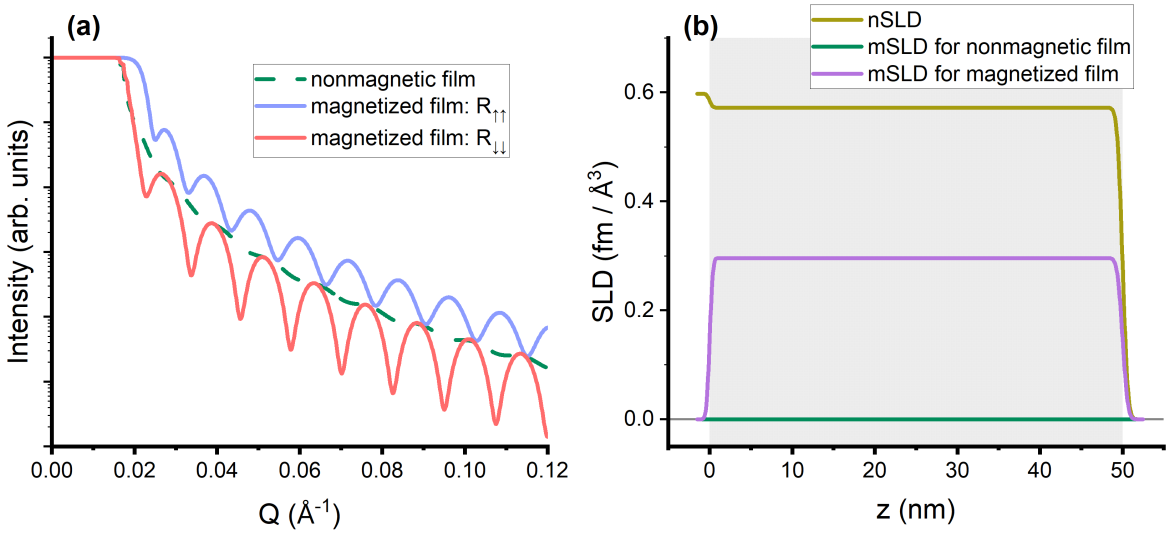

Figure 1.25: Simulated neutron reflectivity for two 50 nm FeRh films on MgO with magnetic scattering length density (mSLD) 0 and 0.3 fm/Å^3. The substrate roughness is 0.3 nm and the film roughness 0.5 nm. (a) The reflectivity of the nonmagnetic film (green dashed line) reflects nuclear scattering only. For the magnetized film, there is strong magnetic scattering and differences are seen in the reflectivity of spin-up neutrons (blue solid line) and spin-down neutrons (red solid line). (b) The nuclear scattering length density (nSLD) (gold line) shows a constant density throughout the depth of the film, with the interface and substrate roughness resulting in a continuous change at both interfaces. The mSLD for each film reflects that there is zero magnetic scattering for the nonmagnetic film (green line) and nonzero constant magnetic scattering for the magnetized film (purple line). Simulations created using the reflectivity modeling software *GenX* [45].

film is found for several field and temperature conditions, demonstrating interface effects. Off-specular scattering is a more recent area of study, requiring a high intensity of neutrons for useful statistics. It will not be discussed further here, but is an area of future study for this work.

1.7 Ultrafast Laser-Induced Dynamics

The discussion of magnetism so far in this chapter has been largely an exploration of magnetic moments and their interactions in static equilibrium. But magnetization dynamics, how moments reorient and how domains expand or contract or move, is of crucial importance in applications such as spintronics, where speed, minimization of energy usage, and miniaturization

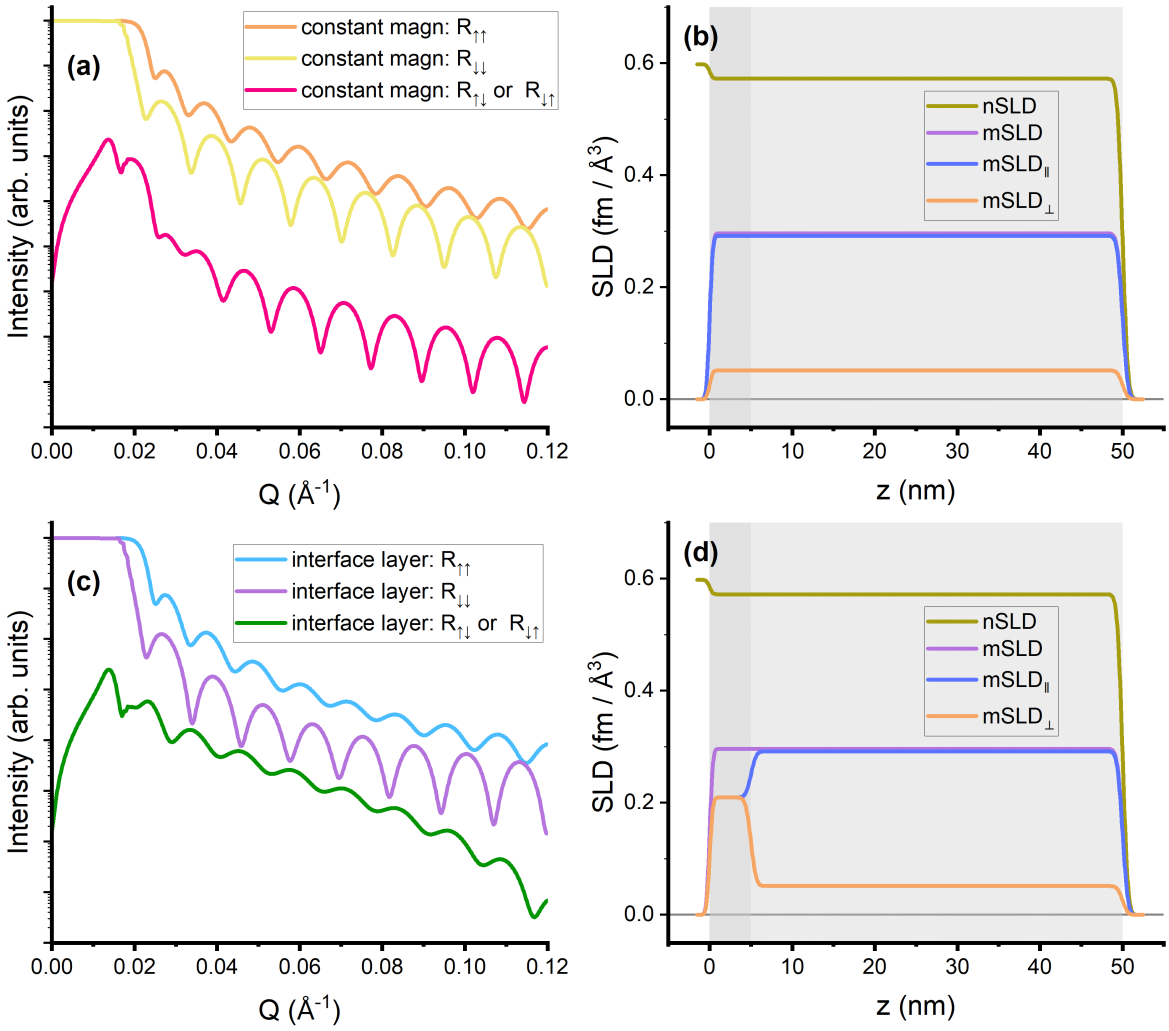

Figure 1.26: Simulated neutron reflectivity for two 50 nm FeRh films with magnetic scattering length density (mSLD) 0.3 fm/Å^3 with different orientations of the magnetization. The data in (a) and (b) is for a film that has magnetization directed in-plane 10 deg from the neutron polarization axis, resulting in (a) both non-spin-flip and spin-flip reflectivity and (b) mSLD contributions both parallel to the neutron polarization axis and perpendicular to the neutron polarization axis that is constant through the depth of the film. The data in (c) and (d) is for a film that has a 5 nm interface layer with magnetization directed in-plane 45 deg from the neutron polarization axis. The rest of this film has magnetization directed in-plane 10 deg from the neutron polarization axis. The result is (c) reduced non-spin-flip reflectivity and increased spin-flip reflectivity. (d) The mSLD reflects the greater perpendicular component for the interfacial layer compared to the rest of the film. Simulations created using the reflectivity modeling software *GenX* [45].

are required. As previously discussed, strongly correlated systems are described by the interactions of the degrees of freedom shown in Fig. 1.1. Different experimental techniques exploit the coupling to measure magnetic properties, such as measuring how changes in the movement of charges is used to determine magnetic ordering, or to alter the magnetic properties, such as inducing strain to shift or change a magnetic transition. These degrees of freedom can be thought of as separate reservoirs which interact, exchanging energy and angular momentum. The time scales for these interactions set the limits for how quickly technology can operate. Current magnetic devices rely largely on the precession of spins to induce magnetization reversal, a process which is limited to 1 ps to 1 ns time scales. But it is possible to influence the spins in different ways, indirectly through interactions with other degrees of freedom, which can occur on much faster time scales, such as the spin-orbit interaction, which occurs on time scales of 100 fs to 1 ps. Measuring these interactions on these time scales provides fundamental insight into the nature of the coupling of these degrees of freedom as well as of effects such as the exchange interaction which are not well understood. It is also critical to determining future advancement of technology. There are many different experimental techniques that have been developed to observe and probe and manipulate dynamic behavior in these systems, and the one that is used in this work is laser-induced dynamics.

Ultrafast magnetization dynamics were first reported in 1996, with 60 fs laser pulses resulting in the demagnetization of a Ni film within 1 ps measured by a time-resolved magneto-optical Kerr effect signal [49]. The three-temperature model, suggested in [50] and applied to the demagnetization seen in the magnetic films since, has provided a phenomenological blueprint to understand this behavior. In this model, the charge, spin, and lattice degrees of freedom are considered as separate but interacting reservoirs, shown schematically in Fig. 1.2. Each of them has an effective temperature T_j and heat capacity C_j where $j = e$ for the charge system, $j = s$ for the spin system, and $j = l$ for the lattice system. The strength of the interaction of the reservoirs is described by coupling constants G_{ij}. A laser pulse $P(t)$ provides a stimulus to this system

experienced by the electrons which respond to the optical frequencies within 1 fs, absorbing and scattering the incident photons and creating an excited state with electron-hole pairs or hot electrons. The temporal evolution of the system is described by the coupled differential equations

$$\begin{aligned} C_e\frac{dT_e}{dt} &= -G_{el}(T_e - T_l) - G_{es}(T_e - T_s) + P(t) \\ C_s\frac{dT_s}{dt} &= -G_{es}(T_s - T_e) - G_{sl}(T_s - T_l) \\ C_l\frac{dT_l}{dt} &= -G_{el}(T_l - T_e) - G_{sl}(T_l - T_s) \end{aligned} \tag{1.35}$$

and is shown for a metal with strong spin coupling in Fig. 1.27. The transfer of energy from the charge system to the spin system occurs on time scales of 100 fs, resulting in the demagnetization that has been observed in various magnetic films. The transfer of energy to the lattice system is slower, on the order of 1 ps. The exact time scales will differ based on the specific system and the strength of the interactions, but this demonstrates a unique method of manipulating that magnetism of the system that can occur on far faster time scales than existing techniques.

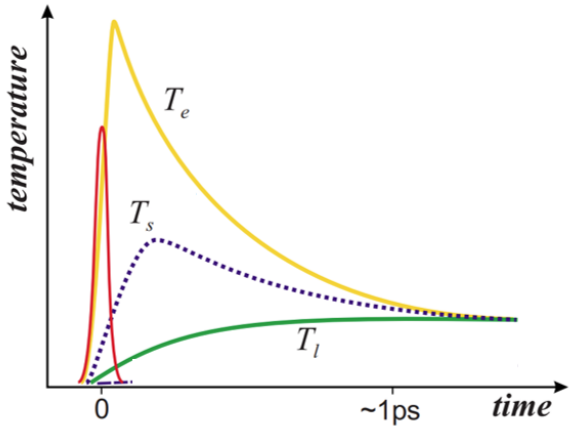

Figure 1.27: Model of the temporal evolution of the charge (yellow line), spin (purple dashed line), and lattice (green line) temperatures following an optical laser pulse (red line) for a metal with strong spin coupling based on the three-temperature model. Figure reproduced with permission from [51]. Copyright 2016 by the American Physical Society.

A schematic representation of the ultrafast laser-induced experiment is shown in Fig. 1.28. The optical laser pulse excites the charge system, which transfers energy to the spin and lattice

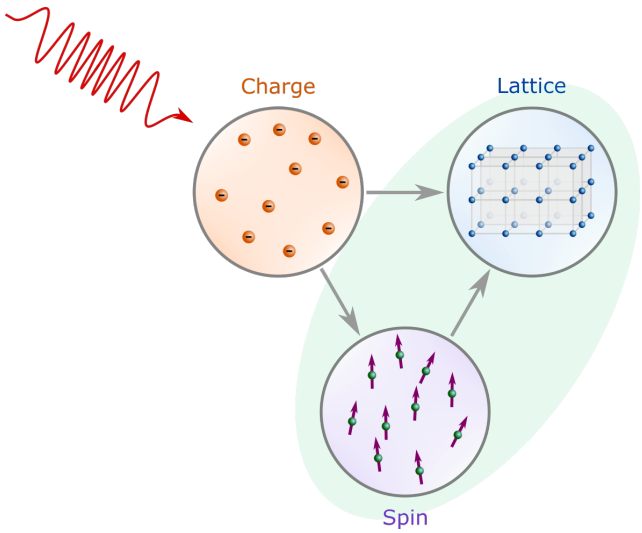

Figure 1.28: Schematic of the energy transfer in materials exhibiting coupled charge, spin, and lattice degrees of freedom following a laser pulse. The electron system is excited very quickly and transfers energy to the spin and lattice system on different time scales, resulting in an uncoupling of the degrees of freedom and a three-temperature model of their evolution. It is possible to probe the system in different ways on ultrafast time scales and watch the uncoupling and recoupling.

systems. The result is that these three systems are temporarily out-of-equilibrium and are able to evolve separately for a time. And the time required for them to recouple will differ. So a probe that is able to watch the evolution of spins or the lattice, for example, can observe non-equilibrium transient states that cannot be accessed on longer time scales and separate out the coupling of the degrees of freedom that occur on different time scales.

This is relevant in this dissertation in the ultrafast pump-probe experiment on thin film Cr presented in Section 3.3. The laser pulse uncouples the charge, spin, and lattice systems and the lattice responds: the static periodic modulation that was stabilized by the magnetic ordering becomes a dynamic coherent phonon, measured with time-resolved x-ray diffraction. Transient enhancement of the ordering can be observed with low laser fluence as a result of the quick recoupling of the spin and lattice before the phonon mode is damped out. Understanding these dynamics and the coupling could provide insight into the fundamental nature of the interaction and how to this can be exploited in systems to manipulate the order.

Chapter 2

Fabrication and Experimental Methods

2.1 Introduction

The fabrication, characterization, and experimental processes used in this work are presented in this chapter. There are numerous methods of thin film fabrication, including magnetron sputtering, chemical vapor deposition, molecular beam epitaxy, ion beam assisted deposition, atomic layer deposition, and electroplating. The first of these, sputtering, is advantageous in part for its scalability and preexisting use in industry, such as in fabricating components of hard drives, and for the wide range of materials that can be fabricated. Magnetron sputtering was used for deposition of all films discussed here and will be explored in Section 2.2. For some experiments, the films grown through sputtering must be patterned into microstructures or nanostructures. This was done primarily through two methods of lithography described in Section 2.3: UV photolithography for structures on the order of 1 μm and electron beam lithography for structures on the order of 10 nm to 100 nm.

Subsequent sections in this chapter present the various methods of film characterization and experimental techniques used in this work and crucial in the study of magnetic and strongly correlated materials. Magnetometry and electric transport are used characterize the quality and

material properties of the films and can be helpful in determining some of the mechanisms behind transitions and other phenomena that are studied. X-ray diffraction is a very powerful technique, especially given the brilliance of x-rays available at sources such as synchrotrons and free electron lasers and integral to much of the work in this dissertation. Neutron diffraction and reflectometry are very useful in the study of magnetic materials and have been used in this work to characterize and understand the magnetism in a system.

2.2 Sputter Deposition

Sputtering is a method of physical vapor deposition that is commonly used for the growth of thin films. One or more high purity discs of material called targets are bombarded by high energy ions, and atoms of the desired material are ejected, collecting on a substrate surface, as shown in Fig. 2.1. This process begins when a voltage is applied between the substrate (anode) and target (cathode) in the presence of a regulated low pressure inert gas, usually argon (Ar). Free electrons accelerate away from the cathode in the resulting electric field and collide with Ar atoms to create Ar ions

$$e^- + \mathrm{Ar} \rightarrow 2e^- + \mathrm{Ar}^+$$

which accelerate towards the cathode target. When an Ar ion bombards the target with kinetic energy greater than the binding energy of the target material, an atom of the desired material and some electrons are expelled from the target. The atom travels towards the chamber walls, sample holder, and substrate, resulting in film growth. The electrons accelerate away from the target, but magnets that are place below the target as shown in Fig. 2.2 produce a magnetic field that results in helical motion and confinement of the electrons above the target surface. These electrons will ionize additional Ar atoms and the process will avalanche and ignite a plasma near the target surface. The use of a magnetic field in this way during sputtering is referred to as magnetron sputtering and significantly increases the material deposition rate.

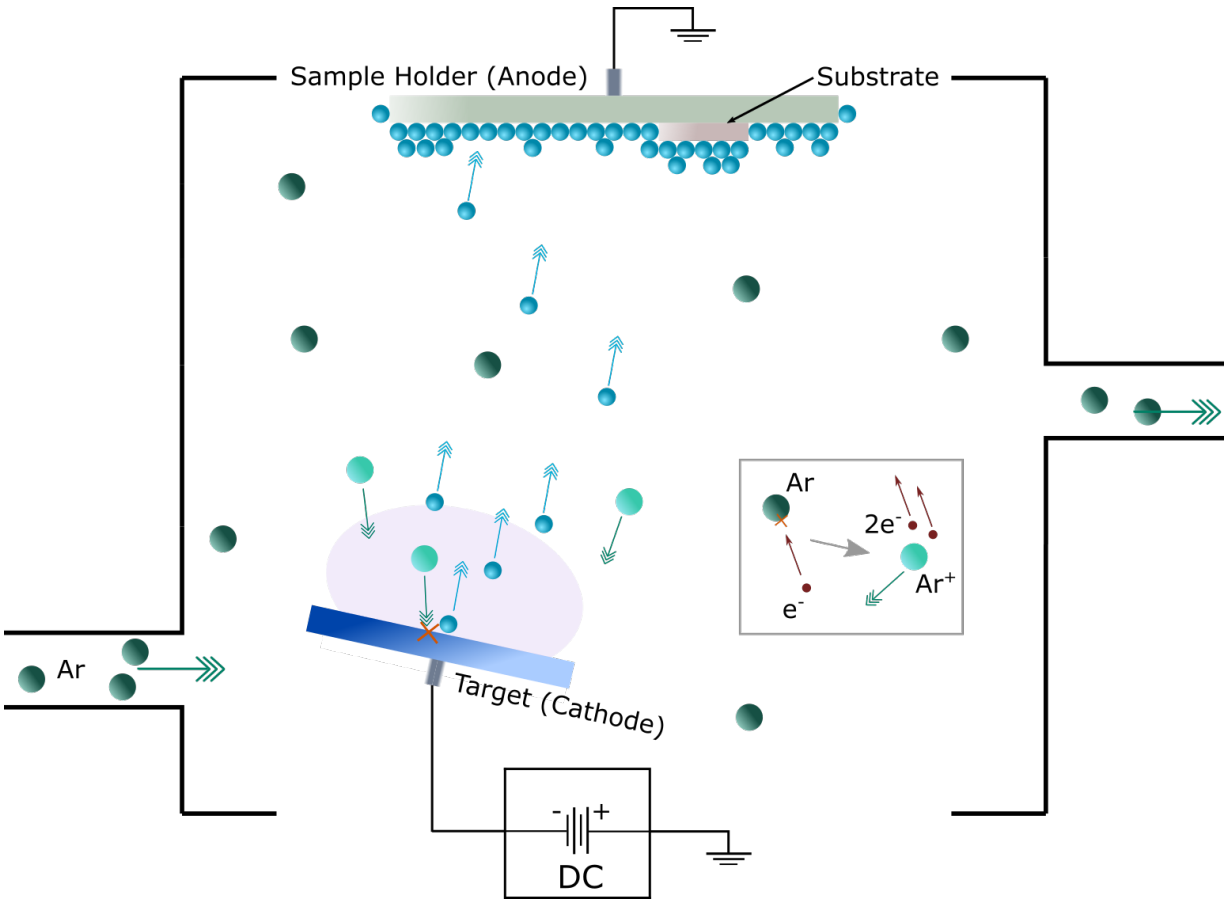

Figure 2.1: Schematic of the sputtering process. An inert gas, usually Ar, is introduced into the deposition chamber. An electric field is applied between the substrate (anode) and target (cathode). Free electrons accelerate away from the cathode, colliding with and ionizing Ar atoms, as depicted in the inset gray box. The Ar ions accelerate towards and bombard the target, ejecting atoms of the desired material, which collects on and around the substrate surface.

2.2.1 Sputtering System

All samples presented in this work were grown in an ATC Orion sputtering system by AJA International in the Fullerton lab at UC San Diego, shown in Fig. 2.3(a). High vacuum is required in the deposition chamber, on the left, to prevent sample contamination. A turbomolecular pump in the system achieves typical base vacuum pressures on the order of 10^{-9} Torr. The system has two mass flow controllers for introducing process gases into the chamber during sputtering: one for Ar, the inert process gas, and the other can be used for O_2, N_2, or other reactive process gases required for material growth (see Section 2.2.3). Higher Ar pressure allows for more collisions

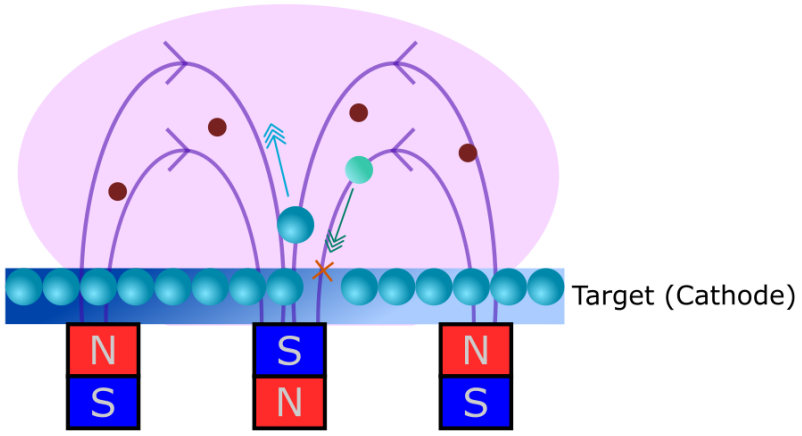

Figure 2.2: Schematic of the orientation of the magnets below a target and the magnetic field above it while sputtering. Magnets are placed below the target such that the magnetic field will trap free electrons near the target surface, allowing for more ionization of Ar atoms and the generation of a plasma. This increases the bombardment of the target by high-energy Ar ions and therefore results in higher rates of deposition.

with atoms in the chamber, reducing their energy before they land on the substrate surface. This results in less surface diffusion, producing films with greater surface roughness [52–54]. For this work, smoothness of interfaces and surfaces was desired, so relatively low Ar pressures of 2.5 mTorr to 3.5 mTorr were used.

There are eight sputter guns contained in the bottom of the deposition chamber. These are arranged confocally with the seven outer guns angled slightly towards the center of the chamber and one gun in the center. Each gun can hold a cylindrical material target that is 2 inches in diameter and up to 1/4 inch thick. A plasma is ignited just above the target surface and a shutter above the gun is opened to allow atoms to escape and reach the substrate. Fig. 2.3(b) shows the eight guns at the bottom of the deposition chamber and an open shutter above a Pt material target in one of the guns. Each gun can be powered with a 500 W DC power source or a 300 W RF power source. DC power is preferred when depositing materials that are electrically conductive, as the deposition rate is much higher. DC sputtering was used to grow all samples for this work. Deposition rates are material-dependent and will generally vary linearly with the applied power across the relevant range of power used for growth (25 W to 200 W). Typical rates for metals are

(a) (b)

(c) (d)

Figure 2.3: Pictures of the AJA International ATC Orion sputtering tool in the Fullerton lab at UC San Diego that was used for growth of most of the samples in this work. (a) The deposition chamber is on the left, with the load lock and arm for sample loading extending out to the right. The power supplies, control boxes, and computer with software Phase II-J, a LabView-based control program, are on the right. (b) A top-down view of the eight sputter guns inside the deposition chamber. The shutter above one gun is open, showing the surface of a Pt material target. (c) A bottom-up view of a sample holder loaded in the chamber. There is a 5 mm $\times$ 5 mm substrate clamped to the sample holder by a mask. (d) A view into the chamber during deposition at high temperature. During deposition, a plasma is established and stabilized and the shutter is opened, allowing ejected material (in this picture Pt) from the target to reach the sample holder that is suspended above the guns. The light above the sample holder is from the heat lamps, heating the sample holder for high temperature deposition.

0.5 Å/s to 1.5 Å/s at 100 W at a working distance (the distance between the target and substrate) of about 20-25 cm.

Substrates are attached to inconel sample holders, introduced into the deposition chamber through the load lock, and suspended from the top of the chamber. A bottom-up view of a sample holder with a substrate clamped to it with a mask and screws is shown in Fig. 2.3(c). Sample holders rotate during the deposition, allowing for more uniformity of deposition across the sample surface. Heating of substrates is achieved by quartz lamps. Fig. 2.3(d) shows a view into the chamber while the quartz lamps are on, directly above the sample holder, with plasma established in one gun above a Pt target and the shutter open, allowing for deposition. The sputtering systems used for growing materials in this work are designed to achieve temperatures of up to 850 °C, though, due to the placement of the thermocouple on the quartz plate above the sample holder and the configuration of the sample holder, the actual substrate temperature is likely 50 °C to 100 °C lower than that. Growth temperatures mentioned in this work are the temperatures that are measured at the thermocouple location.

2.2.2 Sputtering Alloys

There are two methods of sputtering alloys. The first is to sputter from a single gun with a material target composed of the desired alloy. This was how the FeRh (roughly 50% atomic percent iron and 50% atomic percent rhodium) films presented in Chapter 5 were grown. Using a single target is simpler, as it does not require a precise calibration rate of multiple materials to grow samples, but it does not allow for changes in alloy composition of the samples.

Using a single target is complicated in situations where compositional precision is required because of differences in the physical transport of atoms of different elements from the target to the sample and diffusion on the sample. Different elements have different mass, so there will be a disparity in the rates at which they will be ejected from the material target surface, the impact of collisions with gas molecules as they travel, and how likely they are to stick to the sample surface (sticking coefficient), all of which will result in a film that has a different composition from the target used for sputtering. Some of these effects can be minimized by sputtering in lower

Ar pressures (to minimize the collisions of atoms with gas molecules) and in alloys of materials with similar weight, but film composition will differ from target composition [55, 56].

The second method of sputtering alloys, one which avoids some of the uncertainty in composition of the previous method, is to cosputter multiple materials in different guns simultaneously. This is the method used to deposit the antiperovskite films presented in Chapter 4. To achieve the correct stoichiometry, deposition rates must be found for each of the material targets under the same process conditions (Ar sputter pressure, temperature, radial positioning of the substrate on the sample holder) so that the ratio of the required power applied to each target can be calculated.

2.2.3 Reactive Sputtering

In reactive sputtering, sputtering takes place with the additional presence of a reactive gas such as oxygen (O_2) or nitrogen (N_2). The gas combines with sputtered atoms to form new compounds, depicted in Fig. 2.4. This is one method of sputtering oxide or nitride films, including the Antiperovskite manganese nitrides discussed in Chapter 4.

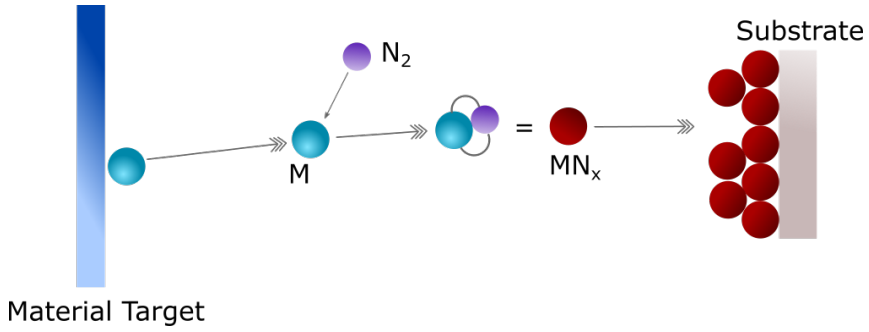

Figure 2.4: Schematic of sputtering with reactive gases. A material, usually some metal M, is ejected from a target. When a reactive gas such as N_2 or O_2 is introduced, it can bond with the metal and form a new compound, MN_x or MO_x.

Reactive sputtering requires consideration of the flow of reactive gas into the chamber. Too much of the gas can result in the formation of the compound material on the material target surface, which will significantly slow the deposition. The partial pressure of N_2 during deposition

of the nitride samples in this work was approximately 0.4 mTorr.

2.2.4 Epitaxial Growth

Sputtering is primarily used for polycrystalline film growth but epitaxial growth is also possible. All of the studies conducted in this work require epitaxial films. There are several parameters that must be tuned for each material to achieve this. The first consideration is the substrate material and orientation. Epitaxial growth usually requires a single crystal substrate with lattice spacing that aligns with the optimal material parameters in some way. Fig. 2.5 shows how epitaxial FeRh, which has a bulk lattice parameter of 2.985 Å, can be grown on MgO (001) and Al_2O_3 (0001). In Fig. 2.5(a), FeRh (001) is shown to grow directly on MgO (001), which has a bulk lattice parameter of 4.212 Å, with an in-plane rotation of 45 degrees. Fig. 2.5(b) shows how FeRh (001) grows on top of an epitaxial layer of W (001) on MgO (001) results in a similar orientation of FeRh growth, but with different strain at the interface. And Fig. 2.5(c) shows the growth of FeRh (111) atop a single crystal sapphire substrate [57]. Lattice matching substrate properties with the deposited material properties in this way provides a template for epitaxial growth.

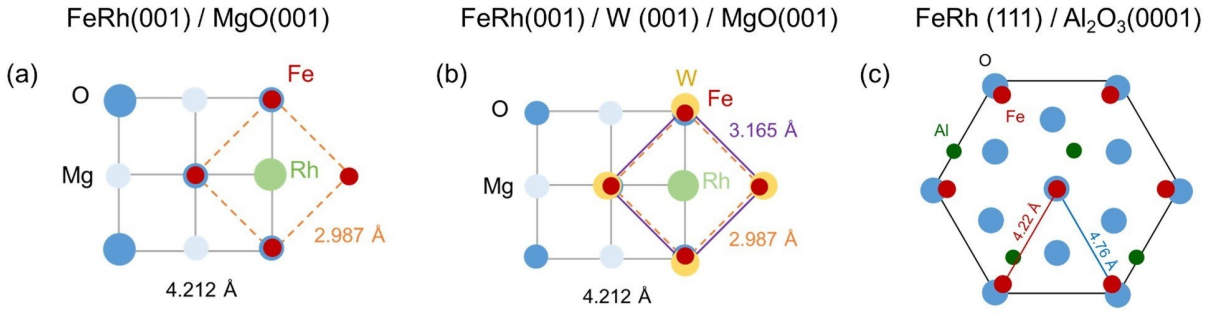

Figure 2.5: Schematic of the lattice matching of FeRh grown on MgO or Al_2O_3, demonstrating the growth of FeRh in different orientations on different substrates: (a) FeRh (001) grown on MgO (001), (b) FeRh (001) grown on W (001) / MgO (001), and (c) FeRh (111) grown on Al_2O_3 (0001). Figure reproduced with permission from [57]. Copyright 2020 by the American Physical Society.

Additional considerations in epitaxial growth of thin films by sputter deposition is growth

of the films at high temperature and post-growth annealing. At room temperature, sputtered atoms will land on the substrate surface and transfer momentum, allowing for some mobility of the particles at the surface of the film during the growth process. When heated during depositions or afterwards (post-annealing), these particles have additional kinetic energy and mobility and will more easily find an energetically-preferred lattice arrangement. The higher the temperature, the more energy and sometimes, the better the crystal quality of the films. However, there are consequences to heating that may reduce the quality of the film. One is unwanted diffusion of materials. Atoms from the substrate can diffuse into the film. Atoms of an alloy may diffuse such that one of the materials collects at the substrate interface or at the surface rather than arranging in the desired crystalline configuration. Atoms such as oxygen or nitrogen could diffuse to the surface and escape as gas, altering the overall composition of the material. So achieving the desired material composition and epitaxy requires tuning of sample growth parameters including substrate heating.

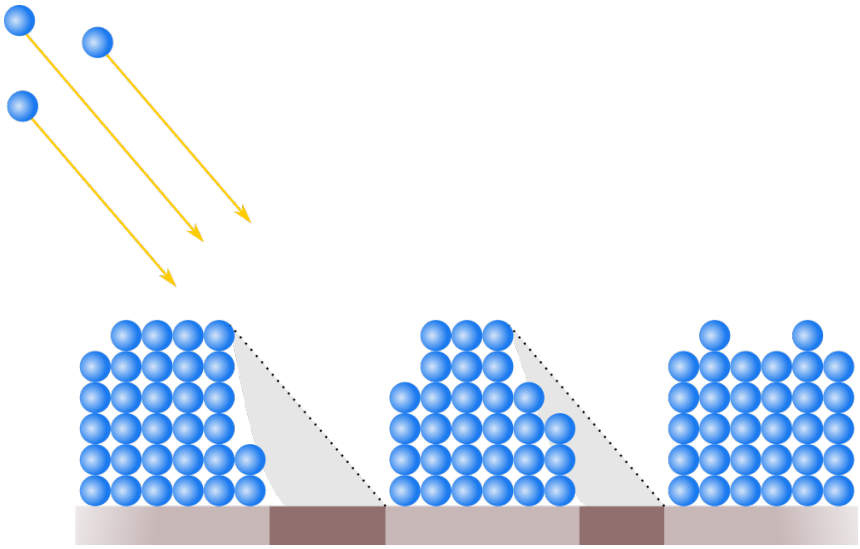

Figure 2.6: Schematic of a shading effect during sputtering resulting in islands or holes instead of smooth films. When material clusters discretely on the substrate, the footprint of those clusters may result in a shading effect where some areas of the substrate are inaccessible to newly deposited material.

Another consequence of heating a substrate too much during sample growth is the possi-

bility of island formation. Because the atoms landing on the substrate have high mobility, they may move and collect in certain locations rather than forming a smooth layer across the entire substrate. As these collections grow taller, there is a shading effect demonstrated in Fig. 2.6 which prevents sputtered atoms from reaching the empty spaces on the substrate. This can result in holes or islands rather than thin films. So higher temperatures may achieve better crystallinity but prevent the growth of continuous films. For some materials, such as FeRh on a MgO substrate, it is beneficial to start the growth at lower temperatures to wet the substrate, or create a smooth layer as a starting point to encourage smooth adhesion of sputtered atoms to the entire area of the sample, and then increase temperature while the film is grown to improve crystallinity. Fig. 2.7 presents SEM images of three Cr and FeRh films. The Cr films are Fig. 2.7(a) grown starting at 400 °C for 1.5 min followed by 6.5 min growth while increasing temperature to 800 °C which has grown in islands, Fig. 2.7(b) grown at 700 °C for 8 min which shows the presence of holes, and Fig. 2.7(c) grown at 500 °C for 8 min which is a smooth film, as desired. The FeRh film shown in Fig. 2.7(d) demonstrates a very clear effect, with large aggregated sections of material rather than a continuous film.

For growth of epitaxial Cr (001), presented in Chapter 3, the best films were achieved on MgO (001) at growth temperatures of 500 °C with post-annealing at 800 °C for 1 hr. The Mn_3AN films in Chapter 4 were grown on MgO (001) at 600 °C with no post-annealing. FeRh films in Chapter 5 were grown on MgO (001) and other chamber conditions impacted the quality of growth. Typically, optimal growth occurred with deposition starting between 300 °C and 450 °C and then ramped up to 600 to 800 °C during growth. They were post-annealed at 700 to 800 °C for 45 min.

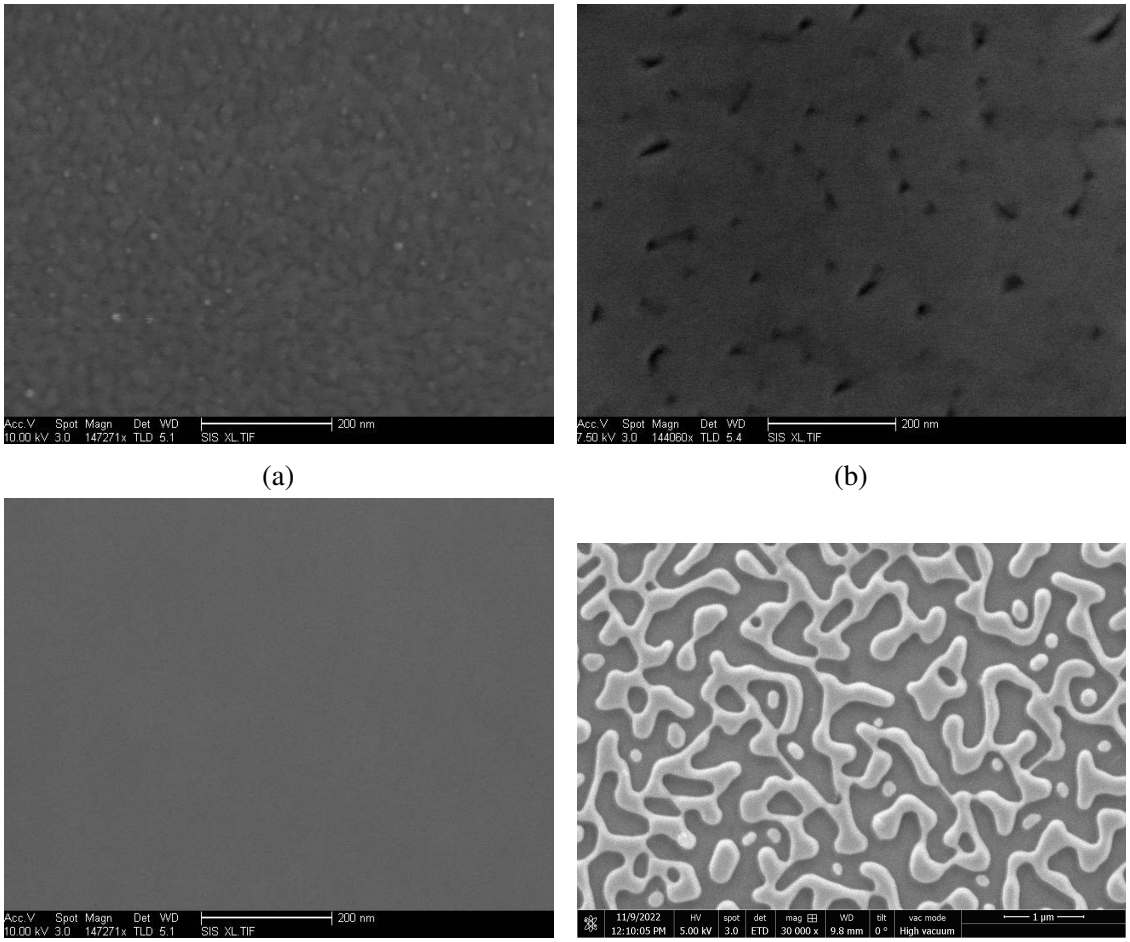

Figure 2.7: SEM images of Cr and FeRh films showing the formation of islands and holes vs. a continuous film: (a) Cr film grown at 100 W starting at 400 °C for 1.5 min followed by 6.5 min of continued growth while increasing temperature to 800 °C. (b) Cr film grown at 100 W at 700 °C for 8 min. (c) Cr film grown at 100 W at 500 °C for 8 min. (d) FeRh film grown at 25 W at 450 °C for 3 min followed by 25 min of continued growth while increasing temperature to 800 °C. At higher temperatures, the substrate surface may not wet completely during growth, resulting in a shading effect and holes or islands rather than continuous films.

2.3 Lithography

Some measurements and experiments require some sort of nano- or micro-structure rather than a continuous film. Structures such as wires in this work were fabricated through lithography from thin films that were grown by sputtering. Lithography is a process in which selective areas of a substrate or sample are covered by a protective material, a polymer called a resist, followed

by an etch or deposition process, which results in patterned features rather than a continuous film. For samples that required patterning in this work, this involved lithography after depositing a continuous thin film and etching of areas not protected by the resist. The basic steps involved are summarized in Fig. 2.8. Initially, the films have been deposited by sputtering and the sample is cleaned. The liquid resist is then spin coated to a thin continuous layer over the film. This resist, called a negative resist, is selectively exposed to radiation in certain areas. In the areas of exposure, the crosslinking between molecules increases (for a positive resist, it would decrease). The sample is then immersed in a developer which dissolves the areas of low crosslinking, leaving behind a pattern of resist on top of the continuous film. The sample is then etched (see Section 2.3.2), so the film material is removed and the substrate is exposed in all the areas not protected by the resist. Once the resist is dissolved, what remains is the desired pattern or structure on the substrate.

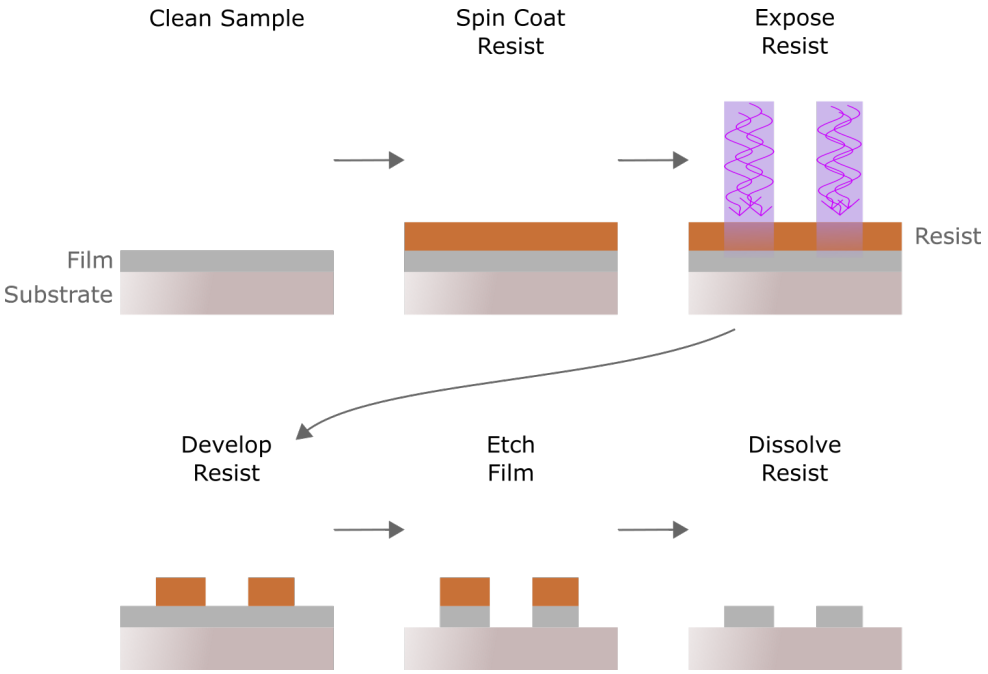

Figure 2.8: Steps of the UV photolithography process with negative resist. Initially, samples consist of a substrate and a continuous film. A polymer negative resist is deposited on top of the film by spin coating. The resist is then exposed to UV radiation in some pattern, which results in an increase in the crosslinking properties of the exposed parts of the resist. The sample is then immersed in a development solution which dissolves the areas that have not been exposed to radiation. The regions of the film that are not covered by resist are etched and the resist is dissolved, leaving the desired patterns of material on the substrate.

There are two types of lithography used for samples in this work, UV photolithography and electron beam lithography. Photolithography is the preferred method for features larger than 1 μm and electron beam lithography for structures on the order of 10-100 nm, since the resolution of a given method of lithography is determined by the diffraction limit of the radiation and the resist used in the process.

2.3.1 UV Photolithography

UV photolithography uses UV light, in this case 365 nm wavelength, as the method of exposure of patterns. As a result, the smallest resolvable features are roughly 1 μm. There are different methods of selectively exposing certain areas of the films. The one used here, which is highly scalable, is with use of a photomask. A photomask is a large glass (or some material transparent to the relevant wavelength light) plate that has the desired pattern features printed on top with an opaque material, often Cr. During the lithography process, the surface of the film with the photoresist layer is pressed into contact with the photomask and exposed to UV light.

The specific process used for most photolithography conducted in this work is as follows. To begin, samples are cleaned in acetone with sonication for at least five minutes. They are then rinsed with isopropyl alcohol, dried using compressed high-purity nitrogen, and baked briefly on a hot plate at 100 or 150 °C to remove any moisture. A photoresist, either the positive photoresist Clariant AZ 1518 or the negative photoresist Futurrex NR9-1500-PY, is spin coated onto the film to achieve a uniform 1 μm to 2 μm layer and the sample is then transferred to a hot plate for a soft bake. Exposure occurs in a Karl Suss MA6 Mask Aligner, which brings the sample into direct contact with a mask and exposes it to UV light from a mercury light for a specified amount of time. The samples are once again transferred to a hot plate for a post-exposure bake if necessary for the chosen resist. The development of the photoresist occurs with light agitation in a developer solution and is followed by a deionized water rinse and drying with compressed high-purity nitrogen. The specific parameters required for two photoresists is given in Table 2.1.

Table 2.1: Process parameters for the UV photolithography process for two photoresists used in this work. Clariant AZ 1518 is a positive photoresist, meaning areas that are exposed to UV light can be more easily dissolved. Futurrex NR9-1500-PY is a negative photoresist, meaning areas that are exposed to UV light are polymerized or crosslinked and will less easily dissolve.

Photoresist	Clariant AZ 1518 (positive)	Futurrex NR9-1500-PY (negative)
Spin Coat	5000 rpm for 40 s	4500 rpm for 30 s
Soft Bake	100 °C hot plate for 65 s	150 °C hot plate for 2 min
Exposure	direct contact with mask for 8 s	direct contact with mask for 11 s
Post-Exposure Bake	none	100 °C hot plate for 2 min
Development	Clariant AZ 300 MIF for 40 s	Futurrex RD6 for 11 s
Film Etch	depends on film material	depends on film material
Resist Removal	acetone for 5 min	acetone for 5 min

At this point in the process, the features that are desired are patterned above the continuous film. The unexposed areas can be etched (see Section 2.3.2). Finally, the sample is cleaned in acetone with sonication for 5 minutes or until all of the photoresist has been dissolved from the sample.

Rather than beginning with a continuous film and etching away sections of a film, it is possible to create a pattern on a substrate with photoresist, deposit a film, and dissolve the photoresist to remove just the areas of the film that are above the photoresist. This process is called liftoff. Liftoff is not possible for creating the wires and structures in this work because the deposition requires a clean, smooth, and crystalline surface for epitaxial film growth. The presence of contaminants from the above process and the resist features will prevent good epitaxy in films. Depositions are also usually done at high temperatures which would burn the resist and contaminate the deposition chamber. However a second UV photolithography process involving liftoff was used to deposit Au contacts to wires grown for electric transport measurements to provide an optimal surface for wirebonding. Fig. 2.9 shows an optical microscope image of a sample patterned for transport measurements into a Hall cross, which allows for current flow along a 5 μm wide wire and provides contacts to points along the wire which can be used for

longitudinal and transverse voltage measurements, which are used to measure magnetoresistance and Hall resistance. This sample was grown as a continuous film by sputtering and then patterned by UV lithography and dry etching (see Section 2.3.2). A second UV lithography process was conducted to deposit Au contacts using liftoff.

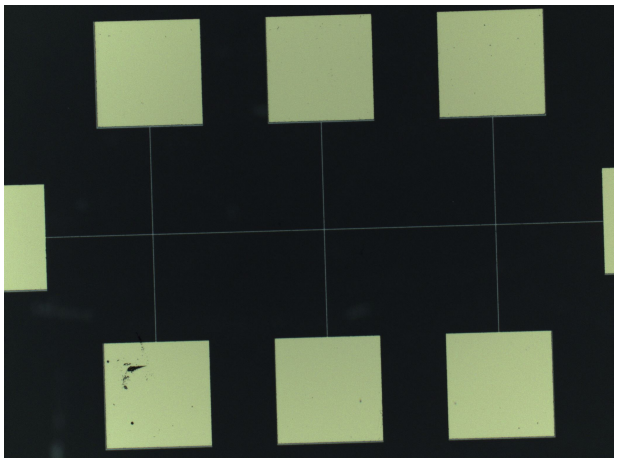

Figure 2.9: Optical microscope image of a Hall cross patterned by UV lithography from a continuous film of Dy. The film was grown by sputtering. The Hall cross pattern with 5 μm wide wires and 0.5 mm by 0.5 mm contact pads was formed on top of the film with a layer of photoresist by UV lithography. This was followed by a dry etch process to remove all areas of the film except those protected by the photoresist, which was subsequently dissolved from the sample. A second lithography process was then undertaken using a liftoff process in order to deposit a thick (several hundreds of nm) layer of Au on top of the contact pads for ease of wirebonding for magnetotransport measurements.

2.3.2 Dry Etching

The process of removing material from a substrate is called etching. Wet etching uses a liquid chemical as the etchant to dissolve or chemically alter and remove exposed surfaces. It is easier as it requires no specialized equipment, only the chemical and a working surface, but the etching often occurs isotropically, so it is difficult to get the straight edges desired for devices and often impossible to get nanometer scale structures if using for the lithography processes relevant for this work. Dry etching, or plasma etching, removes material from the sample through ion bombardment. It is more expensive but allows for more well-defined features.

The methods of dry etching relevant to this work are sputter etching and plasma etching, which can be combined in reaction ion etching (RIE). Sputter etching works identically to sputter deposition including using an inert gas such as Ar, but in this case, the sample is the cathode and is bombarded by ions rather than a material target. Plasma etching is more of a chemical process where various gases, when ionized and used to bombard the sample material, react chemically to form a new gaseous material that escapes from the sample. RIE combines these processes, so samples are bombarded with ionized gases which both eject atoms and chemically etch the material.

Table 2.2: Process parameters for the etch processes used to pattern films in this work.

Etch process	**Ar sputter etch**	**Cr etch**	**O_2 plasma etch**
RF Bias	200 W	60 W	100 W
Gas Flow Rate [sccm]	Ar: 40	O_2: 3 Cl_2: 50	O_2: 50
Pressure [mTorr]	20	200	50
Approximate etch rate [nm/min]	FeRh: 3.2 Mn_3AN: 1.6	Cr: 2.9	

Most of the etching of samples in this work was done in the Nano3 cleanroom facility, part of the San Diego Nanotechnology Infrastructure (SDNI) of UC San Diego, in an Oxford Plasmalab 80 Plus RIE. Mn_3AN and FeRh films were etched using an Ar sputter etch process. Cr films were etched by RIE with the etchants being Cl_2 and O_2 (the chemical material formed in the chemical process during bombardment is CrO_2Cl_2). The other etch process used in this work was an oxygen plasma etch to remove PMMA resist during electron beam lithography (see Section 2.3.3). A summary of these processes and the approximate etch rates is given in Table 2.2.

2.3.3 Electron Beam Lithography

Photolithography cannot be used to resolve structures much smaller than 1 μm. Electron beam lithography (or e-beam lithography) can be used to pattern nanostructures. The process is very similar to photolithography, but the method of exposure is a focused electron beam that scans a pattern into an electron-sensitive resist. This process is much slower than the quick exposure of the masked sample in photolithography since it depends on the beam spot size and the rate of scanning, but, depending on the e-beam writer and the resist used, it can create features down to around 10 nm in scale. Fig. 2.10 demonstrates features as small as 74 nm patterned from a thin film of Cr by e-beam lithography at the Nano3 cleanroom facility at UC San Diego. It also requires more intensive and expensive equipment, so it is not easily scalable for industry applications. However, it is useful for studying nanoscale effects and interactions in materials.

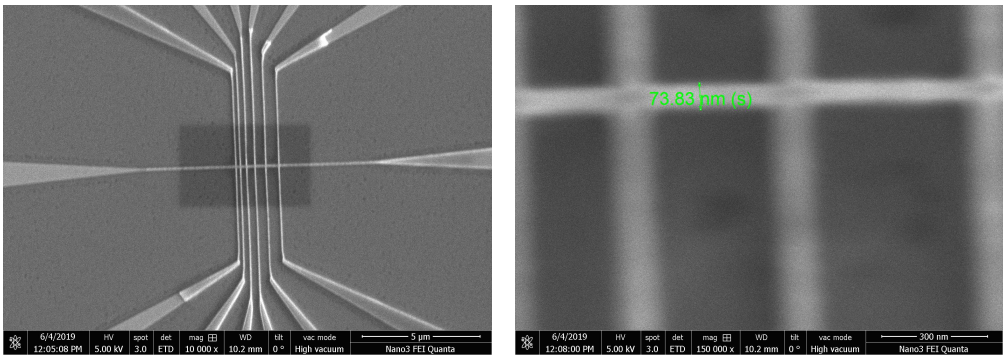

Figure 2.10: SEM images of a 74 nm wide Cr wire patterned by e-beam lithography. The wire has several intersecting wires that can be used to make contact for voltage measurements. There is some PMMA/HSQ resist that has not been removed from some of the features here.

The e-beam lithography process looks very similar to the UV lithography process. One key difference is that a different resist must be used, one whose solubility is changed by an electron beam rather than by UV radiation. Hydrogen silsesquioxane (HSQ) is a resin that acts as a negative resist in this setting. It has been shown to achieve sub-10 nm wide lines [58], so it is a good candidate for the fabrication of nanowires in this work. However, the removal of HSQ is difficult in the final step after etching the films, so this process involves the use of an

underlayer of polymethyl methacrylate (PMMA), which is a polymer material, and dissolves well in acetone. PMMA can also be a positive resist for e-beam lithography, but in this case, the PMMA has less exposure to the electron beam and is not soluble in the solution that is used to develop the HSQ. So the combination of the high-resolution negative resist properties of HSQ and the ease of removal of PMMA has been shown to be advantageous in e-beam lithography [59]. Another benefit of this process is that HSQ adheres better to PMMA than to some materials, such as the Cr films with a thin native oxide layer on top, so the HSQ patterns were less likely to wash away in the developer. After development, the PMMA is removed from exposed areas by oxygen plasma etching prior to the film etch process.

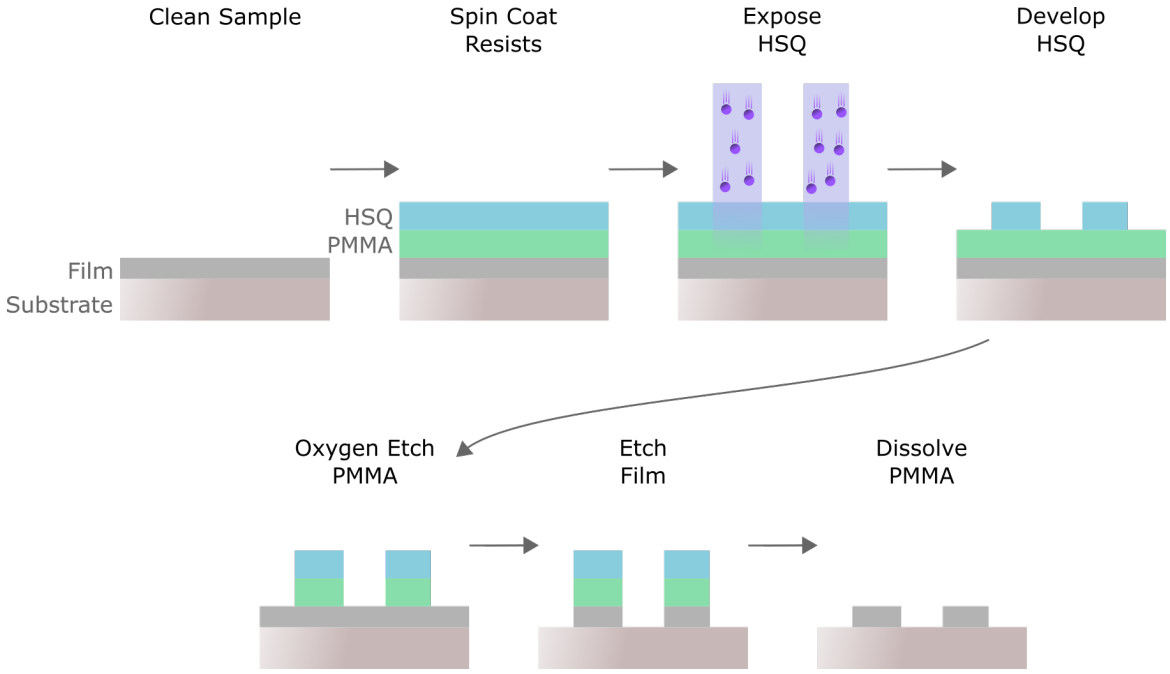

Figure 2.11: Steps of the e-beam lithography process. Initially, samples consist of a substrate and a continuous film. A layer of PMMA resist and then a layer of HSQ resist are spin coated onto the sample. The HSQ is then exposed to an electron beam in some pattern, which results in an increase in crosslinking in the exposed parts of the resist. The sample is then immersed in a developer which dissolves the areas that have not been exposed to the electron beam. The sample undergoes oxygen plasma etching, which removes exposed areas of PMMA. Then the exposed areas of the film are etched. Finally, the films is put in acetone, which will dissolve the PMMA and remove all resist from the samples, leaving only the desired patterns of material on the substrate.

The e-beam lithography process is laid out in Fig. 2.11 and Table 2.3. The sample is cleaned in acetone with sonication for at least five minutes, rinsed with isopropyl alcohol, dried using compressed high-purity nitrogen, and baked on a hot plate at 100 or 150 °C for at least 2 min to remove any moisture. The first resist, MicroChem PMMA A3, is spin coated at 6000 rpm for 1 min, and the sample is transferred to a hot plate to bake at 180 °C for 1 min. Next, the second resist, Dow Corning XR 1541 6%, which consists of a HSQ resin in a carrier solvent of methylisobutyl-ketone (MIBK), is spin coated at 5000 rpm for 1 min. The sample is baked again on a hot plate at 120 °C for 2 min. Exposure is done in a Vistec EBPG 5200 in the Nano3 cleanroom facility at UC San Diego. The electron beam scans the desired pattern, delivering an optimized dose (in this work, 850 μC/cm^2 to 950 μC/cm^2). Following exposure, the sample is developed in Clariant AZ 300 MIF for 60 s and rinsed in deionized water for 60 s.

Table 2.3: Process parameters for the electron beam lithography process used in this work.

Spin Coat MicroChem PMMA A3 Resist	6000 rpm for 1 min
Bake	180 °C hot plate for 1 min
Spin Coat Dow Corning XR 1541 6% Resist	5000 rpm for 1 min
Bake	120 °C hot plate for 2 min
Exposure	electron beam dose of 850-950 μC/cm^2
Development	Clariant AZ 300 MIF for 60 s
PMMA Etch	100 W plasma etch in 50 mTorr O_2 for 50 s
Film Etch	depends on film material
Resist Removal	acetone for 3-5 hr

After development, the desired pattern of HSQ has been written onto the film. However there is still the layer of PMMA which is covering the entire area of the film. PMMA can be removed by dry etching with an oxygen plasma. Then the film is exposed and etched. After etching, the remaining PMMA/HSQ atop the features is removed by immersing the sample in acetone and sonicating for 3-5 hr.

The e-beam lithography process does not allow for the entire pattern to be exposed at

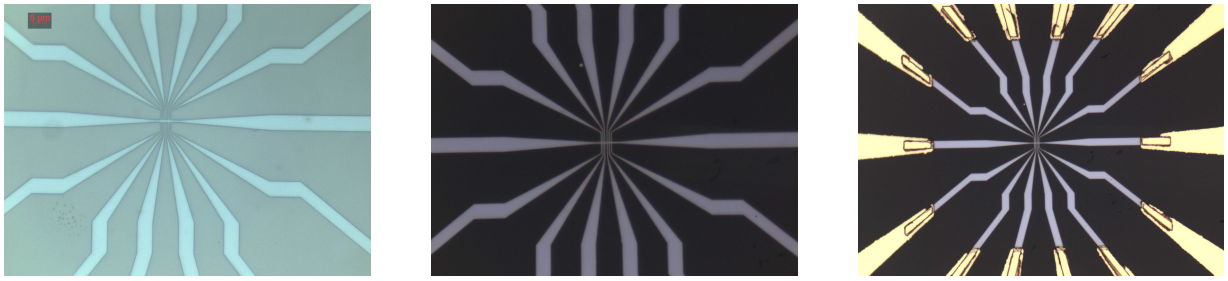

(a) (b) (c)

Figure 2.12: Microscope images of an 800 nm Cr wire fabricated by e-beam lithography: (a) the continuous Cr film and pattern of HSQ resist after development but before etching, (b) the patterned Cr wire after e-beam lithography and etching, (c) the patterned Cr wire after UV photolithography and deposition of Au contacts for electric transport measurements. The magnification of (a) and (b) is twice the magnification of (c).

the same time, as can be done with the photomask in UV lithography: it must be written into the resist with a finite beam spot size and current. This, along with the extra time required for establishment of vacuum and alignment of the sample, means this is a much slower process than photolithography. So the nanowires in this work were fabricated with e-beam lithography first and then Au contacts to the wires were deposited using the liftoff method of UV photolithography. An example of this is shown for an 800 nm Cr nanowire in Fig. 2.12. Fig. 2.12(a) shows the sample after development but before etching, when there is a continuous Cr film and a continuous layer of PMMA but the remaining HSQ shows the nanowire pattern. Fig. 2.12(b) shows the same wire after the e-beam lithography process is complete, with just patterned Cr on the MgO substrate. After this, Au contacts to the Cr features were fabricated using UV photolithography with liftoff, as seen in Fig. 2.12(c).

2.4 Magnetometry Measurements

There are many techniques for measuring the volume or surface magnetization of a sample. In this work, the volume magnetization of different samples is an important measure of the quality of samples or the magnetic phase that the samples are in. The technique used most often in this

work to quantify a sample's magnetization is vibrating sample magnetometry (VSM), which is capable of measuring the volume magnetization of a material with relatively small moments, down to roughly 1.0×10^{-7} emu, to a high degree of accuracy. This is required for thin film work in which the measurements are often conducted on small amounts of material with small magnetic moment. The measurement of magnetic moment in some samples, those of Chapter 4, requires even greater sensitivity, so VSM is used in conjunction with a Superconducting Quantum Interference Device (SQUID) sensor to measure signals down to about 1.0×10^{-8} emu.

2.4.1 Vibrating Sample Magnetometry (VSM)

The VSM device was developed and published in 1959 by Simon Foner at MIT's Lincoln Laboratory [60] and patented in the 1960s [61, 62]. A VSM exploits Faraday's law of induction, which states that a changing magnetic field will induce an electromotive force (emf) in a closed circuit:

$$\varepsilon = -\frac{d}{dt}\Phi_M = -\frac{d}{dt}\iint \mathbf{B}(t) \cdot d\mathbf{A}$$

where ε is the induced emf, Φ_M is the magnetic flux through the circuit, $d\mathbf{A}$ is an element of the surface defined by the circuit, and $\mathbf{B}(t)$ is the magnetic field through that element. It follows that if a material that has a non-zero magnetization is moved near a loop of wire, there will be a detectable current that flows through the wire, giving a measure of the change in flux.

A VSM is designed to vibrate a uniformly magnetized sample, as the name suggests. One possible setup is shown in Fig. 2.13, with the sample vibrating perpendicular to the plane of a coil of wire, referred to as a pickup coil, which experiences a changing magnetic field. The configuration of pickup coils can vary widely, but two coils aligned like this is common in VSM systems. Assuming the direction of vibration to be $\hat{z}$, the emf is

$$\varepsilon = -\left(\frac{d\Phi_M}{dz}\right)\left(\frac{dz}{dt}\right).$$

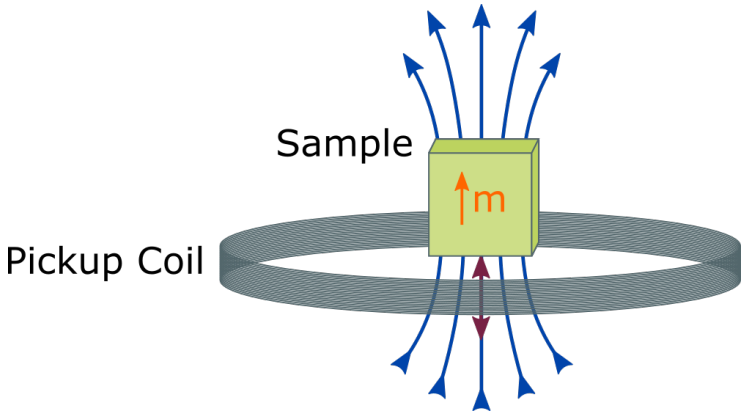

Figure 2.13: Schematic demonstrating the motion of a magnetized sample oscillating near a pickup coil.

Because the sample position is oscillating with frequency f and amplitude A_0, the induced voltage in the coil will be sinusoidal. For this configuration, the induced voltage in the coil is

$$V_{\text{coil}} \propto 2\pi f m A_0 \sin(2\pi f t),$$

where m is the magnetic moment of the sample. So, after conducting a calibration to get the coil voltage for a known reference (such as a magnetized ferromagnetic sample of known quantity), the voltage in the coil can be used to determine the magnetic moment parallel to the direction of vibration for other samples.

2.4.2 Superconducting Quantum Interference Device (SQUID)

A SQUID consists of a superconducting ring with two narrow insulating gaps called Josephson junctions, as shown in Fig. 2.14. In the absence of a changing magnetic field, current will flow equally across the two sides of the ring, tunneling across the Josephson junctions. However, in the presence of a changing magnetic flux through the ring, Faraday's Law applies and there's an induced current around the ring. The result is an increase in current across one side of the ring and decrease across the other side. As a magnetic field is linearly increased, a

voltage measurement across the device will oscillate due to the properties of current flow and the quantization of magnetic flux through a superconducting ring. Each full wavelength of voltage oscillation corresponds to a change of one flux quantum ($h/2e = 2.07 \times 10^{-15}$ Tm^2) through the ring. This provides a far more sensitive detector of changing magnetic fields than the traditional pickup coils used for VSM measurements.

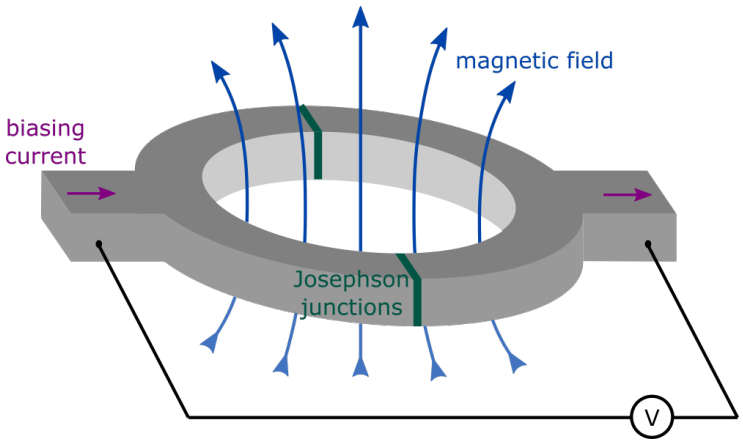

Figure 2.14: Schematic of a superconducting quantum interference device, which consists of narrow insulating gaps, Josephson junctions, separating both sides of a superconducting ring and allows for very sensitive measurements of change in magnetic flux.

2.4.3 Magnetometry Measurement Systems

There are three measurement systems at UC San Diego on which magnetometry measurements were conducted. These include a Quantum Design VersaLab Measurement System (VersaLab) and a Quantum Design Physical Property Measurement System (PPMS) in Professor Eric Fullerton's lab and a Quantum Design Magnetic Properties Measurement System (MPMS) in Professor Jeffrey Rinehart's lab. All are capable of multiple types of measurements. All three systems provide a sample environment with controllable temperature and applied field, easily allowing for measurements of moment vs. applied field at a fixed temperature and moment vs. temperature at a fixed field. This applied field is static during measurement of the moment, so it will not alter the moment measured for VSM- or SQUID-based measurements.

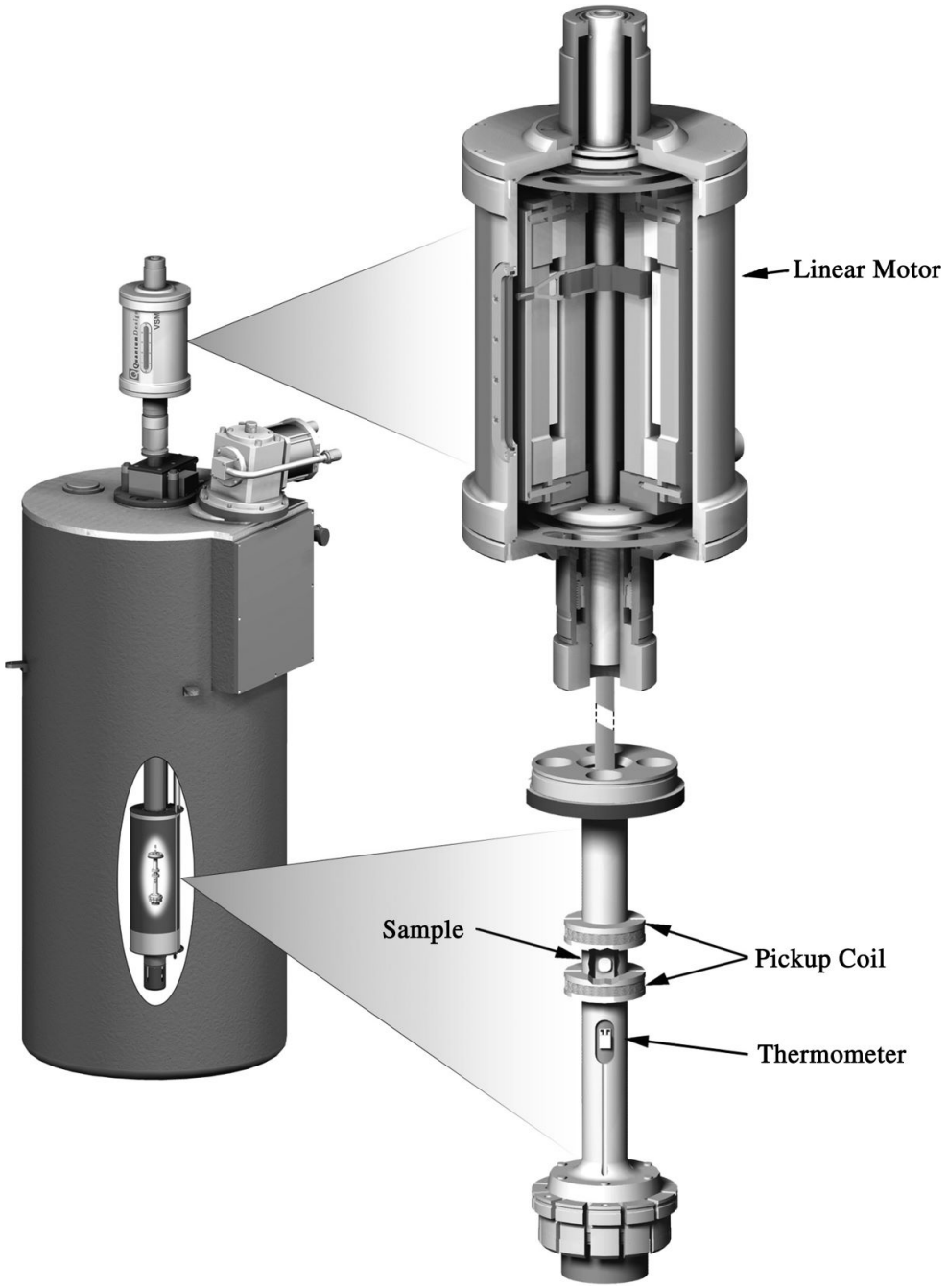

Figure 2.15: Components of a Quantum Design Vibrating Sample Magnetometer. The VSM option for Quantum Design systems consists of a linear motor that a sample rod. A sample is attached to the rod and oscillates between two pickup coils. Figure reproduced with permission from [63]. Copyright 2009 by John Wiley & Sons, Inc.

The Quantum Design VSM option, shown in Fig. 2.15, is used in conjunction with the PPMS and the VersaLab. It consists primarily of the VSM head (which contains the linear motor),

a sample rod, and a coilset (which contains two pickup coils and a thermometer). The oscillation amplitude can be adjusted from 0.1 mm to 5 mm and the frequencies from 1 Hz to 60 Hz. For all VSM measurements in this work, a typical oscillation amplitude of 2 mm and frequency of 40 Hz were chosen. There are two coilsets that can be used, a standard bore coilset with diameter 6.3 mm and coil separation 9 mm and a large bore coilset with diameter 12 mm and coil separation 12.2 mm. Typically, the standard bore can measure moments down to around 6×10^{-7} emu and the large bore can measure to roughly 1.5×10^{-6} emu [64, 65].

The fields and temperatures that can be achieved for measurements differ depending on whether the VSM is installed on the PPMS or the VersaLab. The PPMS contains a longitudinal solenoid magnet. It allows for measurements in fields up to ± 9 T and a sample temperature range of 1.8 K to 400 K [66]. The VersaLab has a conduction-cooled superconducting magnet and can achieve fields up to ± 3 T and has a temperature range of 50 K to 400 K [67]. There is an additional option, the VSM Oven option, which facilitates measurements in the range 300 K to 1000 K and has a noise floor about an order of magnitude higher than previously stated for the traditional VSM measurements [68].

The MPMS uses a SQUID sensor with the VSM option to vibrate a sample and measure smaller moments with less noise than possible in the PPMS or VersaLab. It can measure moments down to about 5×10^{-8} emu with a sample temperature range of 1.8-400 K and in fields up to ± 7 T [69]. While VSM measurements in the PPMS or VersaLab may be sensitive enough for ferromagnetic films, measurements of moment of antiferromagnetic or ferrimagnetic films may be better conducted in a MPMS.

VSM and SQUID measurements of low moment materials are complicated in practice by the presence of a background signal. The sample holder that a given sample is attached to will contribute a moment to the measurement in the presence of a magnetic field, as will the substrate if applicable. The sample holder and substrate are usually diamagnetic or paramagnetic, meaning they have a small susceptibility and the measured moment will vary linearly with magnetic field

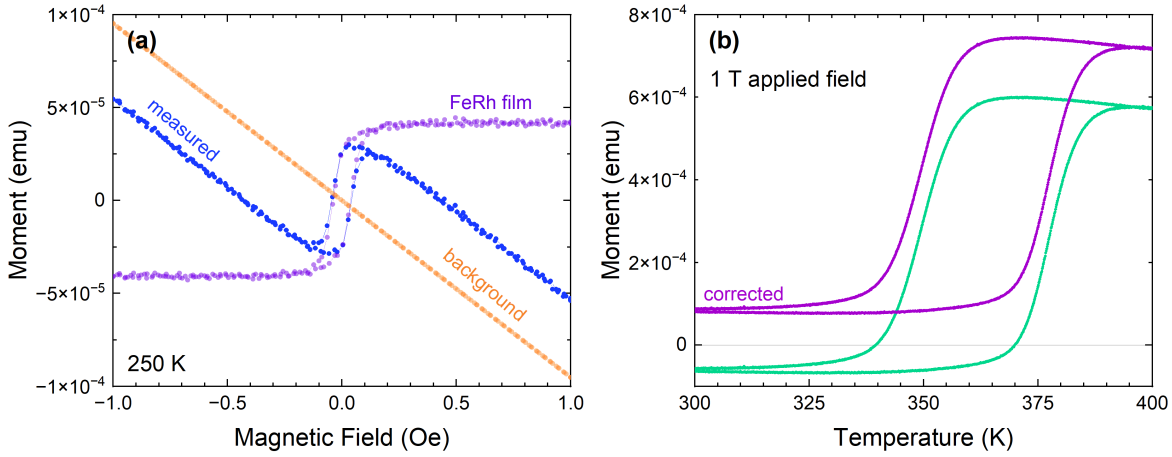

Figure 2.16: Correction of a VSM measurement of a 28.5 nm FeRh film on a MgO (001) substrate by subtraction of the diamagnetic background. (a) The measured signal of moment vs. magnetic field at 250 K is shown in blue. The non-ferromagnetic susceptibility (primarily the sample holder and substrate) is found by fitting the high or low field measurements to a straight line with slope shown in orange. The ferromagnetic signal shown in purple is found by subtracting this background from the measured moment. (b) The measured moment vs. temperature for the same sample is shown in green. The background signal varies some with temperature in the range 250-400 K, but this is assumed to be negligible for the purposes of this work. The purple data shows the moment vs. temperature with the diamagnetic moment found from (a) subtracted out, demonstrating a high temperature high moment regime and a low temperature low (and positive) moment regime for the FeRh film.

and may have a known or measurable temperature dependence. So this signal could be subtracted from the measured signal. An example of this is shown in Fig. 2.16 for a 28.5 nm FeRh film grown on MgO (001) and capped with 1 nm Si_3N_4. Fig. 2.16(a) shows the moment vs. magnetic field for this film at 250 K in blue. There is a hysteretic region around zero field and negative susceptibility regions at low and high field. This can be broken into a ferromagnetic signal and a negatively sloped linear signal. The linear fit to low and high field regions is shown in orange and primarily comes from the diamagnetic background (sample holder and substrate). Subtracting this from the measured data leave the purple data points, which is assumed to be a ferromagnetic signal coming from the FeRh film.

The moment vs. temperature measurement for this sample is given in green in Fig. 2.16(b) and includes the contribution from the FeRh film as well as the sample holder and substrate. The

susceptibility of the background will vary some with temperature, but in the temperature range of 250-300 K and at 1 T applied field, this is assumed to be negligible compared to the change in ferromagnetic signal in the film. So the moment vs. temperature contribution from just the FeRh film is found by subtracting the background moment at 1 T and 250 K and shown in purple. The FeRh film has a large positive moment at high temperature and exhibits a hysteretic transition to a low temperature state with low but positive moment. This behavior will be discussed in Chapter 5.

2.5 Magnetoresistance Measurements

Magnetoresistance measurements are made in a wide variety of conditions depending on the material and property being studied. For the work here, control of sample temperature and applied external field were required. Most transport measurements were made at UC San Diego in the PPMS or VersaLab systems that were introduced in Section 2.4.3. One experiment was conducted at the High Field Magnet Laboratory (HFML) located in Nijmegen, Netherlands.

The simplest measurement of resistance in a material is to have two points of contact and either apply a small voltage and measure the current flow or apply a small current and measure the voltage. The resistance can be determined by Ohm's law, $V = IR$ where V is the applied voltage, I is the current, and R is the resistance. One problem with this measurement is that the measured resistance includes contributions from the wire and the points of contact, as shown in Fig. 2.17. For this reason, we use four-probe measurements of resistance, where current flows between two points of contact in the sample and the voltage is measured between two different points. This eliminates some noise and makes it easier to measure subtle magnetoresistive effects.

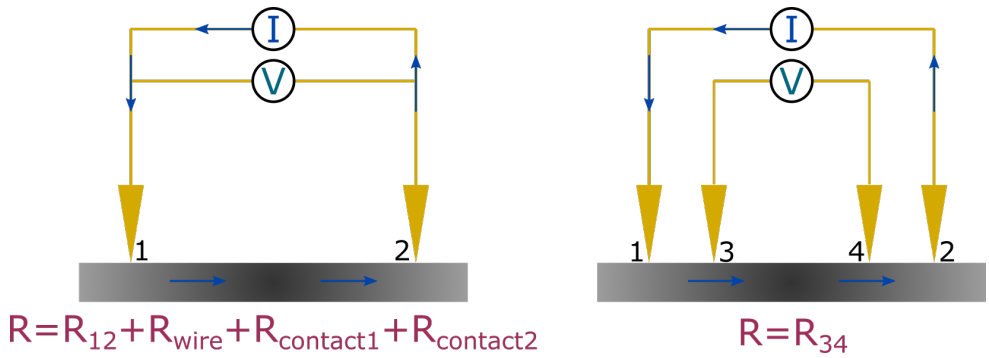

Figure 2.17: Representation of two-probe vs. four-probe resistance measurements. With a four-probe measurement, the measured voltage or resistance does not include contributions from the wire and points of contact, allowing for a more precise measurement of sample resistance.

2.5.1 Measurement Systems

In-House Transport Measurement Systems

There are two measurement systems at UC San Diego used for transport measurements in this work. These are the PPMS and the VersaLab. As stated in Section 2.4.3, the PPMS is capable of measurements in fields up to ± 9 T and temperatures of 1.8 K to 400 K [66]. The Versalab can make transport measurements in fields up to ± 3 T and temperatures of 50 K to 400 K [67]. Most measurements relevant to this work were made in the PPMS, where the DC resistance option can measure resistances of 10 $\mu\Omega$ to 5 MΩ [66].

Measurements in High Fields at the High Field Magnet Laboratory (HFML)

One experiment, presented in Section 5.2, involved measurements conducted at the High Field Magnet Laboratory (HFML). HFML is a part of the European Magnetic Field Laboratory, which is focused on promoting the study of science in high magnetic fields. HFML conducts various types of research requiring very high magnetic fields and currently can achieve fields up to 37.5 T. The work done for this dissertation was conducted in Cell 5, shown in Fig. 2.18, with a Bitter magnet that can produce fields up to ± 33 T. The temperature range achievable within the sample chamber was 4.6 K to 280 K. Transport measurements were made using a lock-in

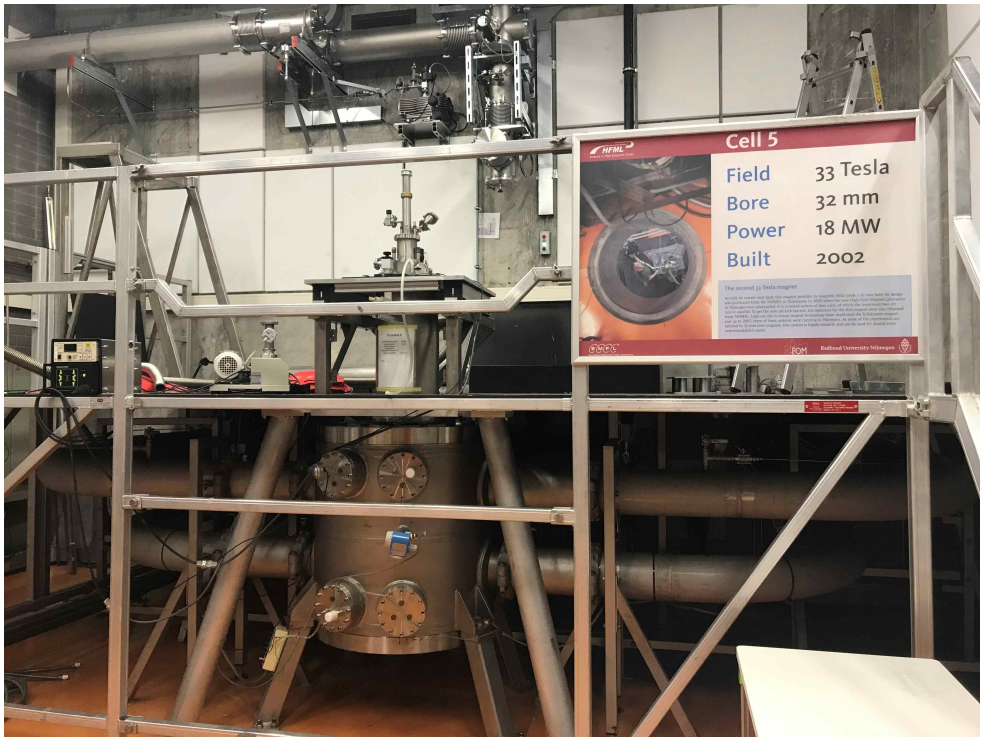

Figure 2.18: Picture of Cell 5 at the High Field Magnet Laboratory.

amplifier with an applied AC current of 275 nA.

2.6 Measurements Involving X-Rays

In Section 1.5, the interaction of x-rays with matter was introduced. The broad categories of x-ray techniques relevant to this dissertation are x-ray diffraction, x-ray reflectivity, and x-ray magnetic circular dichroism (XMCD). Here, we will discuss the experimental aspects of these measurements, including the equipment or facilities required for the production of x-rays.

2.6.1 X-Ray Techniques

X-Ray Diffraction

In this work, x-ray diffraction is used extensively to determine crystal structure of thin films. While the specifics of the x-ray sources and detectors are different depending on the experiment and facility, there are some basics of the measurement that are universal. Fig. 2.19 shows the basic experimental setup of most diffraction measurements. In order to measure diffraction from a film, we need some kind of x-ray source with a focused monochromatic x-ray beam directed at the film with incident angle ω with respect to the surface. An x-ray detector measures the intensity of x-rays at an angle 2θ with respect to the x-ray source.

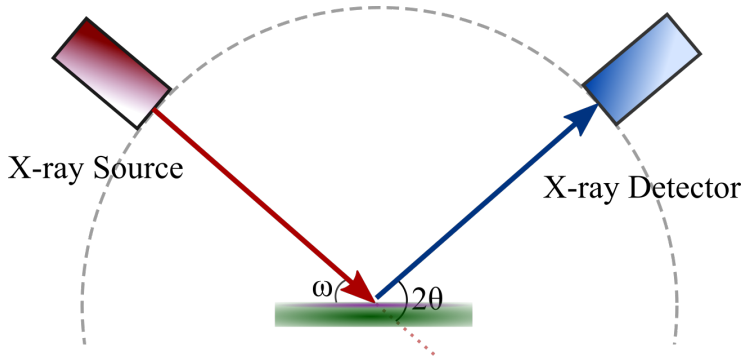

Figure 2.19: Schematic of the experimental setup of an x-ray diffraction measurement. X-rays from a source are directed at a sample with incident angle ω with respect to the sample surface. The intensity of x-rays that are scattered at an angle 2θ with respect to the incident angle are measured as a function of ω and/or 2θ.

There are several types of scans that are measured in this geometry. The most common x-ray diffraction measurement is the coupled scan or a θ-2θ scan, where the source and detector move simultaneously so that $\omega = \theta$. This gives equal angles of incidence and scattering relative to the sample plane and corresponds to the example shown in Fig. 1.12. Coupled scans are plotted as intensity vs. 2θ, and exhibit peaks that correspond to diffraction from specific planes of the film according to Bragg's law in Eq. 1.30. Another useful scan is the rocking curve, where the detector is set at the angle 2θ at which a specific reflection occurs and a scan of intensity vs.

angle ω is conducted. A perfect crystal will have a very sharp peak, but defects such as mosaicity, strain, dislocations, curvature, and inhomogeneity will result in a broadening of the rocking curve. The width of the peak, usually given as the full width at half of the maximum intensity (FWHM), is then a measure of the crystalline quality of the film.

The geometry shown in Fig. 2.19 implies an out-of-plane measurement of the x-ray diffraction, which will limit available reflections to those from planes parallel to the film surface. In-plane measurements are also possible, though more difficult for thin films due to the small footprint of the x-ray beam on the sample. The idea is the same, with the sample rotated in a way that ω refers to the angle between the x-ray beam and the relevant lattice plane.

We include time-resolved measurements of x-ray diffraction in this work. The principle is the same: measurements of specific reflections are used to get information about the crystal structure. However we assume that the crystal structure is changing as a function of time following a stimulus. This requires a sort of instantaneous diffraction measurement at different times to study the evolution of the structure. In practice, instantaneous measurements are of course not possible, so pulses of x-rays are used and give a sort of time average of the structural evolution over the pulse width in time. The facilities and brilliance available at synchrotron and x-ray free electron sources make these measurements possible.

X-Ray Reflectivity

An x-ray reflectivity measurement is conducted in the same way as an x-ray diffraction measurement, but at small angles of incidence and scattering, sometimes referred to as grazing incidence. A coupled scan plotted as intensity (on a log scale) vs. 2θ shows how the scattering intensity evolves above the critical angle, giving information in films about the densities of the materials, the relative densities of the materials, the film thicknesses, and the roughness of each interface.

X-Ray Magnetic Circular Dichroism (XMCD)

Measurements of x-ray magnetic circular dichroism (XMCD) can be carried out in a few geometries. The basic experimental setup involves left- or right-circularly polarized x-rays incident on a sample in a magnetic field. The intensity of x-rays incident on and fluoresced from or transmitted through a magnetized sample is recorded as a function of energy, giving a measure of the absorption coefficient for that polarization. Differences between the absorption between the two polarizations near absorption edges allows for measurement of the orbital and spin moments of specific atoms.

2.6.2 X-Ray Sources

A crucial part in setting up these experiments is the nature of the x-rays that are used in the measurement. In discussing the scattering of x-rays from a crystal, we required each x-ray to be of a particular energy and incident at the same angle. The polarization of the x-rays influences the measured intensity and can be a critical factor of some measurements. And often the most important factor is the intensity of the incident beam, when reflections or features in the diffraction that we seek to resolve are very small and require a very high flux of x-rays. Here we will discuss the x-ray tube, the source that is common in laboratories and very useful in studying static crystal ordering, particularly in large crystals. Then we will talk briefly about synchrotron and x-ray free electron laser facilities, which provide orders of magnitude improvement in x-ray intensities and coherence and allow for more complicated techniques such as time-resolved diffraction measurements.

The X-Ray Tube

The x-ray tube is the simplest of x-ray sources, exploiting the emission of radiation that occurs when a charged particle rapidly decelerates. It is essentially a vacuum tube that contains

a cathode and an anode. When a very high voltage is applied, often on the order of 50 kV, the cathode emits electrons which accelerate through the tube towards the anode. These electrons impact the anode, and some of the kinetic energy they lose during this collision is emitted incoherently in all directions as radiation called braking radiation or bremsstrahlung (and the rest is lost as heat).

The spectrum of emitted radiation from an x-ray tube depends on the anode material and the voltage applied and will be a continuous spectrum over a fairly broad range of wavelengths. When the voltage is high enough, this spectrum will contain sharp peaks in intensity called characteristic lines at wavelengths specific to the anode material. This comes from electrons in inner shells of atoms being ejected during the electron bombardment and the emission of radiation when an electron in an outer energy level transitions to the vacant lower energy level. The lines are identified by the energy transition that they correspond to. The three strongest lines are the $K\alpha_1$, $K\alpha_2$, and $K\beta$ lines, and sometimes the $K\alpha_1$ and $K\alpha_2$ lines cannot be resolved and are referred to as $K\alpha$. $K\alpha$ refers to a transition from an L shell with principal quantum number $n = 2$ to a K shell where $n = 1$. $K\beta$ refers to a transition from an M shell where $n = 3$ to a K shell. With a high enough voltage, the intensity of these lines will increase and the radiation from the x-ray tube will be dominated by the characteristic energies. Filters can be used to reduce the intensity of unwanted peaks so that one energy in particular can be used for measurements. An example of this is for a copper anode, where the intensity of the $K\alpha$ and $K\beta$ lines are quite strong. A piece of nickel foil can be used as a filter to significantly attenuate the $K\beta$ radiation. The resulting spectrum of energies from the x-ray tube is not perfectly monochromatic, which is reflected in x-ray diffraction measurements with added intensities (diffuse from the overall continuous spectrum or localized to specific angles from the other characteristic lines) at unexpected angles, but the overall diffraction is dominated by the scattering with a single energy.

(a) (b)

Figure 2.20: Picture of the Rigaku SmartLab X-ray Diffractometer in the Center for Memory and Recording Research Materials Characterization Facility, part of the San Diego Nanotechnology Infrastructure at UC San Diego.

Rigaku SmartLab X-Ray Diffractometer

Laboratory x-ray diffraction and reflectivity measurements included in this work to characterize crystal ordering and film properties (thicknesses, roughness) were made on one of three Rigaku SmartLab X-ray Diffractometer systems. They have a Cu anode, so the dominant x-ray energy is 8.04 keV (or wavelength 0.15406 nm). Both out-of-plane and in-plane diffraction measurements are possible.

In this work, most of the room temperature x-ray characterization of films occurred on the diffractometer shown in Fig. 2.20, located in the Center for Memory and Recording Research Materials Characterization Facility, which is part of the San Diego Nanotechnology Infrastructure at UC San Diego. Static x-ray diffraction as a function of temperature was measured using similar diffractometers with temperature stages in Professor Oleg Shpyrko's lab at UC San Diego in Chapter 4 or in Professor Vojtěch Uhlíř's lab at CEITEC – Brno University of Technology in

Chapter 5.

X-Ray Synchrotron Sources

Laboratory x-ray sources are good enough for some basic measurements of crystal structure, but their relatively low intensity incoherent x-ray beams that are non-monochromatic are inadequate for many experimental techniques. So other sources of x-rays have been developed to provide opportunities for these experiments to be conducted. One such category is the synchrotron light source, which has provided a huge advancement in research. Synchrotron radiation is the radiation emitted by a charged particle traveling at relativistic speeds that accelerates perpendicular to its velocity. The most obvious example of this kind of perpendicular acceleration would be that of an electron traveling in a magnetic field. Synchrotron light sources use magnetic fields to curve the path of relativistic electrons, resulting in a cone of emitted x-ray radiation tangential to the electron path.

A simple schematic of synchrotron facilities is shown in Fig. 2.21. The source of the electrons is often an electron gun, which consists of an electrode that releases electrons through thermionic emission when heated. Bursts or bunches of these electrons are accelerated into a linear accelerator (LINAC), where a series of radio cavities accelerate the electrons to relativistic speeds with energies on the order of hundreds of MeV. From here, they are injected into the booster ring with additional radio cavities to increase their energy to the order of several GeV. These electrons are injected into the main storage ring, with attention paid to the timing to ensure equally spaced electron bunches within it. The storage ring usually consists of a series of straight segments and turns. The straight segments contain insertion devices called wigglers or undulators (shown schematically in Fig. 2.22), alternating dipole magnets that result in a sinusoidal electron path and the emission of x-ray radiation with much greater intensity than what is achievable with a simple circular path of the electrons. The turns are achieved with bending magnets to redirect the electron path. The storage ring will also contain a radio cavity to boost the electron energy

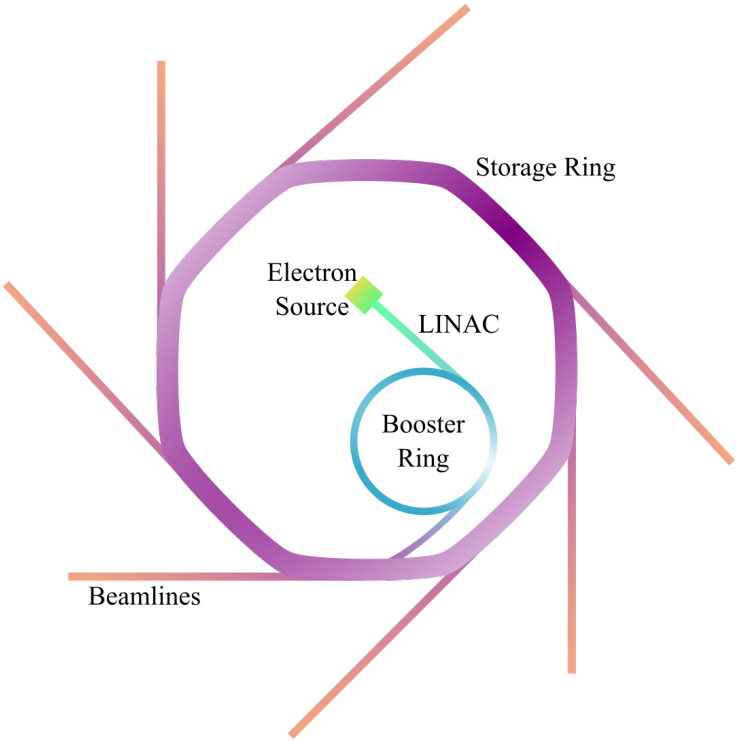

Figure 2.21: Simple schematic of an x-ray synchrotron facility. Electrons are produced in the electron source, directed in bunches or bursts to a linear accelerator (LINAC) to accelerate them to hundreds of MeV, injected into a booster ring to accelerate them additionally to energies of several GeV, and then injected into the main storage ring. In the storage ring, they travel through a series of insertion devices (where they emit high intensity x-ray radiation which are directed to beamlines) and bending magnets to turn their path.

(which has been reduced due to the emitted radiation) with each rotation. At the end of each straight segment in the storage ring is a beamline that uses the x-ray radiation produced in the storage ring for various experimental techniques.

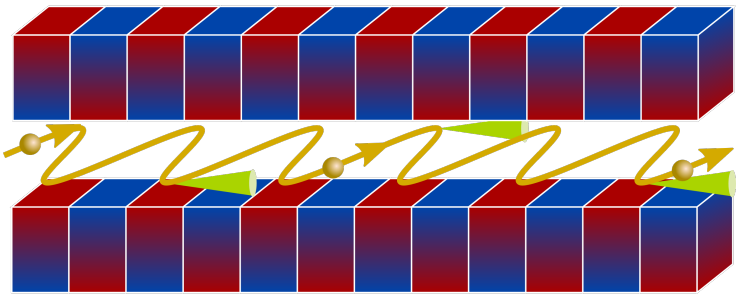

Figure 2.22: Schematic of the electron path and x-ray emission through an undulator or wiggler. A structure of alternating dipole magnets bend the path of the electrons and result in radiation emitted in cones as shown.

Because the electrons are grouped into bunches, the x-ray radiation at beamlines arrives in discrete equally-spaced pulses, which allows for time-resolved techniques, such as pump-probe experiments. In these experiments, a sample is pumped, meaning it is excited or stimulated in some way, such as with an optical pulse, and then the response is probed at various times after the pump, for example with x-ray diffraction. The energy spectrum and intensity of the x-rays emitted from the electrons can be manipulated by the nature of the insertion devices. Wigglers are designed for a large amplitude oscillation of the electron's path and radiate a higher intensity of photons with a broader range of energies and the radiation is incoherent. Undulators have a smaller amplitude oscillation, resulting in a much lower total flux but at a single frequency with a more focused and coherent beam. The total length of wigglers and undulators that are used in synchrotrons is on the order of several m, with an alternating dipole magnet period on the order of several cm.

Some of the properties of the radiation from different x-ray sources that are compared include the number of photons produced per second and the cross-sectional area, angular divergence, and bandwidth of the beam. The brightness or brilliance is used to compare these products, defined as the number of photons per second per cross sectional area per solid angle per bandwidth, usually reported with units $\left[\frac{\text{photons}}{s(\text{mrad})^2(\text{mm})^2(0.1\%\text{ bandwidth})}\right]$, which reflects the desire for a focused, monochromatic, high-intensity coherent beam. The best third-generation synchrotron light sources have brilliance ten orders of magnitude higher than the best laboratory-based sources, allowing for much more sensitive x-ray measurements. These facilities are very expensive and intensive to build and maintain, but their usefulness in advancing scientific research is massive.

The Advanced Photon Source (APS)

Argonne National Laboratory (ANL) in Lemont, IL is funded by Department of Energy (DOE) and contains many different laboratories and facilities conducting a wide range of scientific research. One of these facilities is the Advanced Photon Source (APS), which is a

third-generation x-ray synchrotron facility with electron energy in the storage ring at the APS is 7 GeV, allowing for hard x-ray measurements. The maximum brightness at the APS is on the order of 10^{19} photons/s/(mrad)^2/(mm)^2/(0.1% bandwidth). It is split up into 35 sectors, each containing at least two beamlines, set up for a wide range of different experimental techniques. As of the publication of this work, the APS is undergoing an upgrade that promises an improvement in brightness and coherence of the x-rays by over three orders of magnitude as well as the development of additional beamlines [70, 71].

In Chapter 4, x-ray diffraction measurements of thin film Mn_3AN made at instrument 7-ID-C at the APS are shown. Beamline 7-ID is set up for time-resolved x-ray scattering and spectroscopy. Hutch 7-ID-C has a few fs laser excitation sources available to conduct laser-pump x-ray diffraction probe measurements [72]. X-ray diffraction measurements of thin film Cr made at instrument 8-ID-E, which is dedicated to grazing incidence x-ray scattering, are presented in Section 3.2 [73].

The European Synchrotron Radiation Facility (ESRF)

The European Synchrotron Radiation Facility (ESRF) is a hard x-ray synchrotron facility in Grenoble, France that is a collaboration of over 20 countries, with most of their operating budget coming from European countries. It has a maximum brightness on the order of 10^{21} photons/s/(mrad)^2/(mm)^2/(0.1% bandwidth) and over 40 beamlines set up for different experiments [74]. Beamline ID12 is set up for x-ray absorption and spectroscopy measurements with x-ray energy range of 2-20 keV and polarization controlled by a helical undulator [75]. In Section 5.2, XMCD measurements from the Rh L_2 and L_3 edge in thin film FeRh that were made at beamline ID12 at different applied fields and temperatures are shown.

X-Ray Free Electron Lasers

X-ray synchrotron sources were and continue to be very powerful in experimental research, with x-ray intensities high enough for most current techniques and a broad range of experiments that can be simultaneously conducted at each facility. But x-ray free electron lasers are part of the next generation of light source, with significant improvements on some aspects of the x-ray beam that allow for the development of new techniques and more sensitive measurements.

One of the limitations of the x-rays in most synchrotron-based experiments is the incoherence of the beam. For an electron passing through an undulator, the x-rays it emits during each oscillation are in phase or coherent and will constructively interfere. But the x-rays emitted from different electrons are incoherent, and so the x-ray beam used for measurements is incoherent. The mechanism for creating a coherent beam is to change the nature of the electron bunches. Rather than a random position of electrons within the bunch, electrons at x-ray free electron lasers are spatially ordered into micro-bunches of N electrons that are each confined to a space much shorter than the x-ray wavelength and have separation equal to the x-ray wavelength, which results in coherent x-ray emission from all electrons in the bunch and an enhancement in the brilliance of the beam by N^2.

This micro-bunching of the electrons can be achieved by lengthening the wigglers or undulators that the relativistic electrons pass through. Initially, a bunch of electrons with no spatial ordering will emit radiation as described earlier, in a cone in the forward direction incoherently. The radiation field increases from zero at the undulator entrance as these x-rays are emitted. Eventually, with a high enough electron density, the electrons begin to respond to the radiation field from other electrons, which is modulated by the x-ray wavelength, and start to modulate into bunches with separation equal to the wavelength. This reinforces itself, with the radiation field increasing rapidly, a process called self-amplified stimulated emission (SASE). This process is represented schematically in Fig. 2.23(b). An x-ray free electron laser is defined as using SASE to form a highly coherent brilliant x-ray beam.

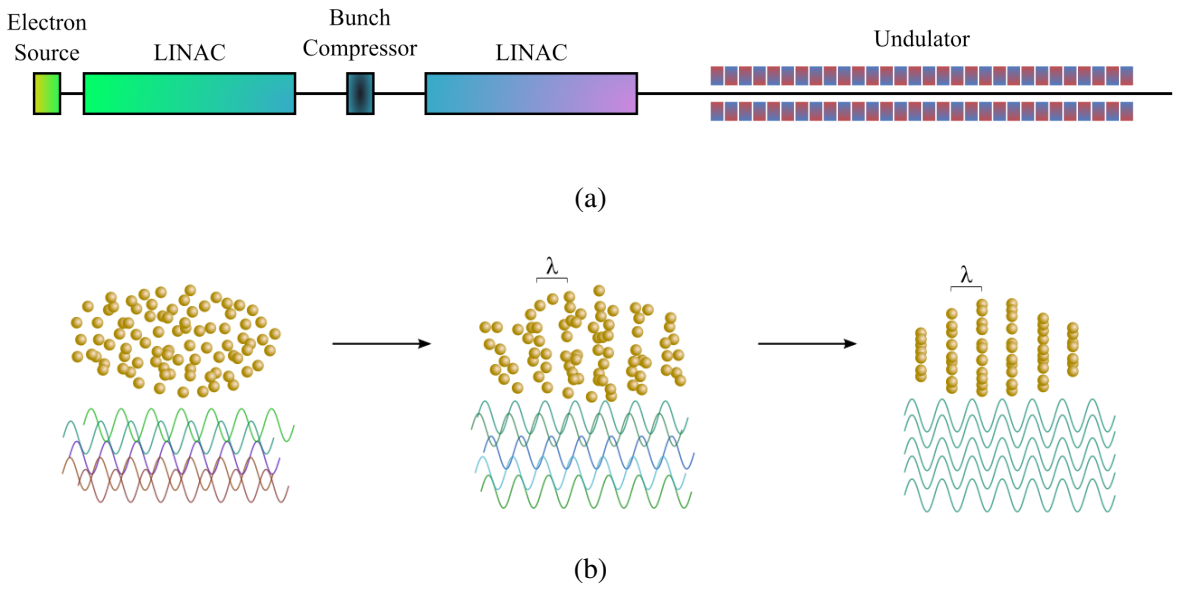

Figure 2.23: Schematic of an x-ray free electron laser. (a) Electrons are produced in an electron source and accelerated to relativistic speeds in high density bunches. These bunches enter a very long undulator where (b) the electrons emit radiation as they follow an oscillating path and begin to modulate in position as the radiation field grows until they are compressed into microbunches with spacing equal to the x-ray wavelength. The resulting x-ray beam is coherent.

The basic components of an x-ray free electron laser are shown in Fig. 2.23(a). As with a synchrotron, electrons are produced in a source and accelerated to relativistic speeds in a linear accelerator. A series of linear accelerators and bunch compressors bring the electrons to the desired energy and bunch density, with a bunch width on the order of tens of fs compared to a synchrotron bunch width on the order of 100 ps. The electrons then enter an undulator with length on the order of several hundreds of m, where their path oscillates and they emit radiation. As the radiation field grows, the electrons modulate as described previously. The brilliance of x-ray free electron sources is usually ten or more orders of magnitude greater than the brilliance of synchrotrons, and the beam is more focused spatially and temporally and of much narrower bandwidth.

The Linac Coherent Light Source (LCLS)

The SLAC National Accelerator Laboratory (SLAC) in Stanford, CA is funded by the DOE and with research focused primarily on x-ray research in condensed matter physics, chemistry, and biology as well as some work in particle physics and cosmology. It is home to a synchrotron, the Stanford Synchrotron Light Source (SSRL) as well as an x-ray free electron laser, the Linac Coherent Light Source (LCLS). The LCLS became the first operational x-ray free electron laser in the world in 2009, with peak brilliance over ten orders of magnitude stronger than that of most synchrotron sources, on the order of 10^{32} photons/s/(mrad)^2/(mm)^2/(0.1% bandwidth), and an x-ray pulse repetition rate of 120 Hz. The LCLS is currently finishing up an upgrade which will provide some huge advances, including tunable repetition rates of up to one million Hz, increase the available energy range, and implementation of a new superconducting linear accelerator [76]. The average brightness of the beam is expected to increase by around four orders of magnitude.

There are seven instruments set up for different experimental techniques and capabilities at the LCLS. The instrument used for measurements in this dissertation in Chapter 3 is the XPP instrument, which stands for x-ray pump probe. At XPP, samples are excited with ultrafast optical laser pulses and probed with x-ray pulses, allowing for time-resolved measurements of the response of the system to the laser pulse. Because of the ultrashort laser and x-ray pulses, these measurements can be ultrafast, with resolution on the order of 50 fs [77]. These ultrafast measurements allow for measurement of transient nonequilibrium behavior and the separation of coupled degrees of freedom which evolve on different ultrafast time scales.

2.7 Measurements Involving Neutrons

In Section 1.6, the interaction of neutrons with matter was introduced. In this dissertation, the neutron scattering techniques that are used are neutron diffraction and neutron reflectometry. In this section, the experimental aspects of these techniques are discussed along with the two

relevant types of neutron sources.

2.7.1 Neutron Techniques

Neutron Diffraction

The experimental setup of neutron diffraction is very similar to x-ray diffraction, with the basic idea of incident and reflected beams shown in Fig. 1.12. Neutrons scatter from nuclei while x-rays scatter from electrons, but since most of the electrons are bound to the nuclei, the Fourier transform of the atomic and electron distribution will be comparable, and the nuclear diffraction peaks from unpolarized neutrons can correspond to x-ray diffraction peaks. The magnetic scattering can be used to determine the ordering and orientation of atomic moments, with a simple schematic shown in Fig. 1.21.

In practice, the neutron diffraction measurement may look a little different than the x-ray diffraction measurement. One common technique of measuring neutron diffraction with neutrons is triple-axis spectrometry. This technique fundamentally involves three steps. First, a collimated neutron beam is scattered from a single-crystal monochromator, which results in the selection of a single neutron energy, which can be tuned by monochromator material and angle of scattering. This is necessary because of the wide spectrum of neutron energies emerging from a neutron source. This monochromatic neutron beam is then scattered from the sample of interest, where the neutron energy may or may not change. An analyzer crystal is used to select specific neutron energies for detection, and those neutrons will be scattered and reach a detector. The result is a probe of the energy transfer of a material, allowing for both elastic and inelastic scattering measurements.

The neutron diffraction measurement in this work is shown in Fig. 5.4, for the (½ ½ ½) diffraction peak of an FeRh film, corresponding to $h = \frac{1}{2}$, $k = \frac{1}{2}$, and $l = \frac{1}{2}$. The absence of scattered neutron intensity at 426 K and increasing intensity of the peak while cooling to 293 K is

indicative of a magnetic transition to a G-type antiferromagnetic phase (see Fig. 1.8(g)) during cooling.

Polarized Neutron Reflectometry

The basic setup of a neutron reflectometry measurement is similar to neutron diffraction, but with small incident and reflected angles. One of the major differences for polarized neutron reflectometry is the requirement for a polarized beam and analysis of the polarization of the scattered neutrons. The neutron beam coming from a neutron source is unpolarized, meaning it has a mix of spin-up and spin-down neutrons. This beam can be polarized with a polarizing filter, in which ^{3}He nuclei preferentially absorb neutrons with one polarization state over the other, polarizing mirrors which use the different critical angles of reflection for spin-up and spin-down neutrons to reflect one and transmit the other, or polarizing crystals, which have equal nSLD and mSLD, resulting in reflection of neutrons with one orientation and transmission of the other. Following this step, the neutron beam will be polarized in one direction. An experiment will require measurements of both spin-up polarized neutrons and spin-down polarized neutrons, so a flipper is required that can be inserted into the beam to reverse the polarization of the beam. There are various types of flippers, most of which use Larmor precession to reverse the spins of the neutrons. At this point, the neutron beam interacts with the sample and some neutrons are reflected. Since spin-flip and non-spin-flip scattering are both possible, there needs to be a method of detecting only the neutrons of a specific spin orientation, so a second flipper and an analyzer (essentially another polarizer) are available in the scattered beam path before neutrons reach the detector. The four reflectivities, $\mathscr{R}^{\pm\pm}$, can be measured with four separate measurements, detecting spin-up or spin-down neutrons reflected from the sample with a spin-up or spin-down incident beam. It is useful to note that a magnetic field is required throughout this beam path to maintain the neutron spin quantization axis. It is also impossible to achieve a fully polarized beam, so the polarization ratio can be measured and accounted for in the reflectivity or fitting.

Off-specular reflectometry is very low intensity, but can be measured with higher intensity neutron sources. Often these measurements are made using a time-of-flight method from a pulsed source introduced in Section 1.6. This requires precise timing of the neutrons incident on the sample and when they arrive at the detector.

2.7.2 Neutron Sources

The production of neutrons and the neutron beam is a crucial part of neutron scattering or absorption experiments. These particles are bound in the nucleus of atoms, so neutron sources are designed around nuclear reactions which can release them. There are a few different types of sources, but the two that are in the scope of this work which provide high enough neutron flux for more useful science are the reactor source and the spallation source.

Reactor Source

The most common type of high-flux neutron scattering facility is the reactor source, which uses a process called nuclear fission to produce neutrons. In neutron-induced fission, a heavy nucleus absorbs a neutron and then splits into multiple lighter nuclei, releasing multiple neutrons. The reason this can occur is the tendency for the ratio of neutrons (N) to protons (Z) to increase as Z increases in stable isotopes of elements. If a heavy nucleus splits apart into two lighter nuclei, the most stable configuration will release excess neutrons. This is demonstrated in Fig. 2.24 for a neutron absorbed into ^{235}U, which becomes an unstable ^{236} nucleus. There are many possible fission products, but the one shown here is the formation of a ^{141}Ba nucleus and a ^{92}Kr nucleus and the release of three neutrons and energy.

A reactor is usually arranged in a core so that the neutrons produced from a fission reaction will continue to collide with other nuclei, resulting in additional fission reactions in a chain reaction. In a research reactor, the primary goal is the production of neutrons (as opposed to a nuclear power reactor, for example, in which the goal is the production of energy). The

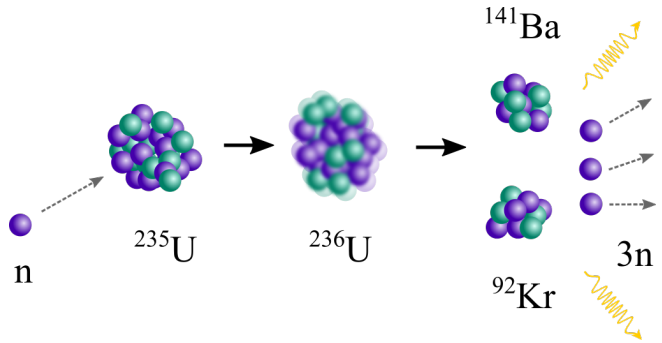

Figure 2.24: Schematic of a possible neutron-induced fission reaction. A neutron is absorbed by ^{235}U, forming a ^{236}U nucleus. This nucleus is unstable and breaks apart into smaller nuclei, in this case ^{141}Ba and ^{92}Kr, releasing neutrons and energy.

neutrons that escape from the core are directed through a moderator, in which the neutrons collide repeatedly with the moderator material (examples include liquid water, deuterium, or graphite) and come to thermal equilibrium, essentially slowing them to the desired energies. The resulting energy distribution is Maxwellian with mean kinetic energy is given by the temperature of the moderator. From here, neutrons are guided away from the core in beam tubes towards instruments used for experiments. The beam coming from reactors is steady-state, meaning there is a constant and consistent flow of neutrons.

The High Flux Isotope Reactor (HFIR)

Oak Ridge National Laboratory (ORNL) in Oak Ridge, TN is DOE-funded and conducts a wide range of science and engineering research and has several user facilities including two neutron source facilities. The High Flux Isotope Reactor (HFIR) is a nuclear research reactor at the ORNL dedicated to neutron scattering research with thermal and cold neutrons. The reactor fuel is highly-enriched (93%) ^{235}U, cooled by light water. There are four horizontal beam tubes that guide neutrons to the various instruments. Three of these are designed for thermal neutrons moderated by light water, and one is designed for cold neutrons and moderated by liquid hydrogen at 17 K [78]. There are two to four instruments associated with each beam tube set up for several types of scattering measurements.

One of the most common neutron scattering experiments is triple-axis spectrometry, described earlier for neutron diffraction. The HFIR has several triple-axis spectrometers. In Section 5.1.2, the neutron diffraction measurement shown was made at instrument CTAX CG-4C, a cold neutron triple-axis spectrometer.

Spallation Sources

The second method of neutron production is spallation. Spallation is a process where a particle or projectile impacts a target, resulting in the ejection or evaporation of materials and particles. In the case of nuclear spallation, usually there is a high-energy beam of protons that bombards a target of heavy nuclei such as W, Hg, or Pb. As shown in Fig. 2.25, the proton enters the nucleus, creating an excited nucleus which is short-lived, decaying into lighter nuclei, neutrons, and other particles. Often this reaction will produce 20-30 neutrons per heavy nucleus.

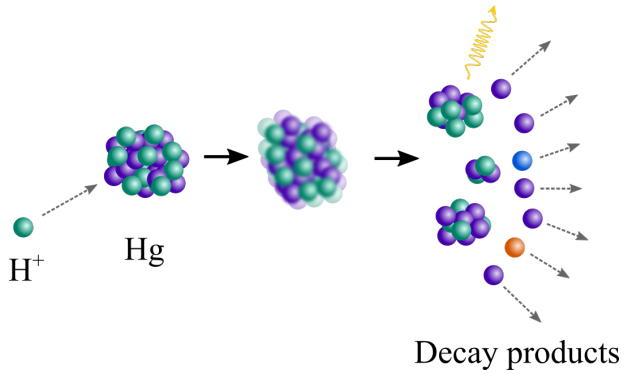

Figure 2.25: Schematic of a nuclear spallation reaction. A proton is absorbed by a heavy nucleus such as Hg, forming an unstable excited nucleus, which breaks apart into various decay products, including 20-30 neutrons.

The first step of spallation in a spallation source requires the production of a high-energy proton beam, usually pulsed. This is done with a proton accelerator, analogous to the electron accelerator used in x-ray sources. This focused proton beam is directed to the target composed of heavy nuclei where spallation takes place. The neutrons produced from spallation have an energy around 20-30 MeV and are directed through a moderator to cool them to the desired energies

before being used for experiments. The neutron pulses have frequencies of around 10-60 Hz depending on the design of the source. This pulsed nature of the beam is useful for making time-of-flight measurements. As with the reactor source, the neutrons have a spectrum of energies when they exit the moderator, and so the higher energy neutrons will travel faster and arrive at a detector sooner than the lower energy neutrons. Their flight time over this distance is therefore a measurement of their energy, and an experiment can make use of all the neutrons in the beam to simultaneously measure scattering of neutrons of different energies rather than needing to select a single neutron energy, reducing the usable flux for the experiment. Rather than a diffraction or reflectivity measurement in which the angle of the detector is changed relative to the incident neutron beam, this measures the diffraction intensity as a function of wavelength at a fixed angle to find the Bragg condition.

Spallation sources have some obvious advantages over reactor sources, starting with the elimination of the need for radioactive materials and the criticality of the nuclear chain reaction. The energy requirements of a spallation source are also lower than for a reactor source. It is, however, far more expensive than a reactor source.

The Spallation Neutron Source (SNS)

The Spallation Neutron Source (SNS) is the second neutron source at the ORNL. At the SNS, the process begins with an ion source that produces negatively charged hydrogen ions (H^-), or protons, which are then formed into a pulsed 60 Hz beam and accelerated to energies of 2.5 MeV. These ion beam pulses are injected into a linear accelerator, which accelerates them to an energy of around 1 GeV. The beam is delivered through a diamond stripper foil that strips the electrons from the ions to produce protons that circulate in a proton accumulator ring. Here, the bunches are sharpened so they are more intense and shorter in duration (less than a millionth of a second). The proton bunches leave the ring and bombard a target composed of 50 tons of liquid mercury encased in steel. Mercury atoms are excited by protons and then spall

20-30 high-energy neutrons per nucleus. The neutrons are sent through a moderator of water for experiments involving thermal neutrons or liquid hydrogen at 20 K for experiments requiring cold neutrons before delivering to the various instruments [79].

There are many instruments at the SNS that are set up for different experiments requiring those neutron pulses. The instrument that was used in this is BL-4A MAGREF, which is a magnetism reflectometer. This instrument makes time-of-flight measurements of specular and off-specular reflection as well as grazing incidence small angle scattering. There are supermirror polarizers either in reflection or transmission used to polarize the beam and the analyzer can be done with another supermirror or a ^{3}He filter. The sample environment can be manipulated with applied electric or magnetic field, temperature, pressure, stress, and light [80]. In Section 5.3, measurements of polarized neutron reflectometry of a thin film and of stripes of FeRh with changes in temperature and magnetic field are presented.

Chapter 3

Thin Film Chromium (Cr)

3.1 Introduction

As discussed briefly in Chapter 1, antiferromagnetic materials have been of increasing interest recently in areas such as spintronics [15]. Some of the difficulty in measuring and understanding their properties has been due to their net zero moment, which prevents study by common magnetic techniques like magnetometry and makes them insensitive to externally applied fields [81–83]. But these properties are advantageous in introducing additional stability to a system due to that insensitivity and allowing for increased device density because of their low stray fields. And the most encouraging aspect of antiferromagnetic integration into devices is in providing the potential for THz electrical write speeds, possible because there is no transfer of angular momentum to the lattice, which is a slow process [84].

Elemental chromium (Cr) is a useful system to study because exhibits an itinerant antiferromagnetic ordering. Neutron diffraction and electric transport techniques have provided a great deal of insight into its equilibrium magnetic properties. But in this work, we are able to explore this further by measuring the distortion of the lattice, which is stabilized by the magnetism, through x-ray diffraction conducted both statically and dynamically following perturbation in two

time regimes. These measurements were carried out at the Advanced Photon Source (APS) at the Argonne National Laboratory (ANL) and at the Linac Coherent Light Source (LCLS) at the SLAC National Accelerator Laboratory (SLAC).

3.1.1 Properties of Bulk Cr

The first evidence of a phase transition in body-centered cubic (BCC) Cr with (001) lattice spacing of 0.2884 nm at room temperature was presented by Bridgman in 1932, noting an anomaly in the electrical resistivity as a function of temperature that was not typical of metals and exhibited a dependence on pressure [40]. In 1936, Néel first suggested that Cr may be antiferromagnetic [41]. This was confirmed in 1959 with neutron diffraction studies of appearance of magnetic satellite peaks (0,0,1$\pm\delta$) around the (001) forbidden reflection below the Néel temperature of 311 K [42, 43], which is consistent with an incommensurate spin density wave (SDW) as depicted in Fig. 3.1.

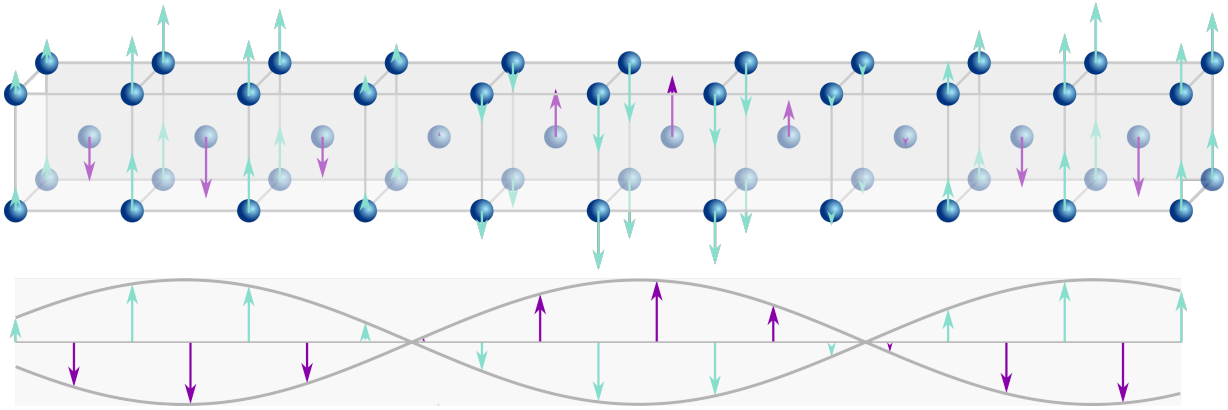

Figure 3.1: Body-centered cubic crystal structure of Cr with a transverse spin density wave (SDW) and a schematic representation of the SDW. Purple arrows indicate moments for body-centered atoms and light blue arrows indicate moments for atoms on the vertices of the unit cell. This depiction is not to scale: the wavelength or period of the spin density wave in bulk is usually ~21-28 unit cells.

As discussed in Section 1.2 and shown in Fig. 1.9(b), an incommensurate SDW is a type of antiferromagnetic ordering in which the periodicity of the spin modulation is not a multiple

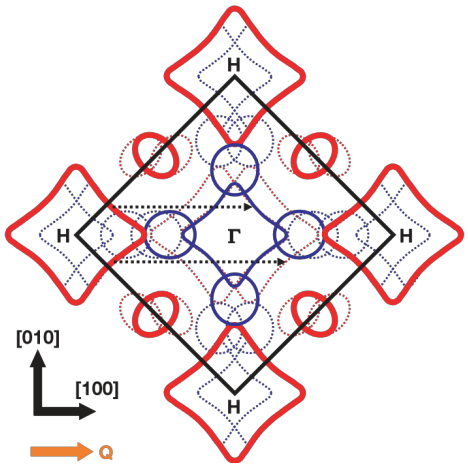

Figure 3.2: Fermi surface nesting in Cr. The solid black line shows the boundary of the first Brillouin zone. The electron octahedra (solid blue lines) are slightly smaller than the hole octahedra (solid red lines). Translations of the Fermi surface (dotted red and blue lines) by the nesting wavevectors $\mathbf{Q} = \frac{2\pi}{a}(1 \pm \delta)$ (dashed black arrows) demonstrate the conditions for electron-hole pairing. Figure reproduced with permission from [85]. Copyright 2008 by Springer Nature.

or rational fraction of the lattice constant. For a BCC crystal like Cr, the nearest neighbor moments (one on the vertex and one in the body of the cubic cell) are antiparallel with unequal moments. The amplitude of the spin modulation is approximately 0.62 μ_B with spins $\mathbf{S}$ and SDW propagation wavevector $\mathbf{Q}$ preferentially oriented along the cubic $\langle 100 \rangle$ directions [33]. The origin of the SDW in Cr was suggested in 1969 to be a result of imperfect nesting of the Fermi surface [31, 85], shown in Fig. 3.2 (reproduced from [85]). The electron and hole octahedra differ in size slightly, so electron-hole pairing occurs with translations by the nesting wavevectors $\mathbf{Q} = \frac{2\pi}{a}(1 \pm \delta)$. This gives a periodicity in the spin modulation that slightly deviates from the lattice parameter a [31, 33, 85, 86].

There is also a modulation in the lattice and in the density of itinerant and ionic charges resulting in a periodic lattice distortion (or strain wave) and a charge density wave (CDW) that appear as a second harmonic of and are stabilized by the SDW [33, 87]. The periodic lattice distortion along with the spin modulation are represented in Fig. 3.3. The CDW and lattice distortion have half the period of the SDW with minima in the lattice spacing (more densely

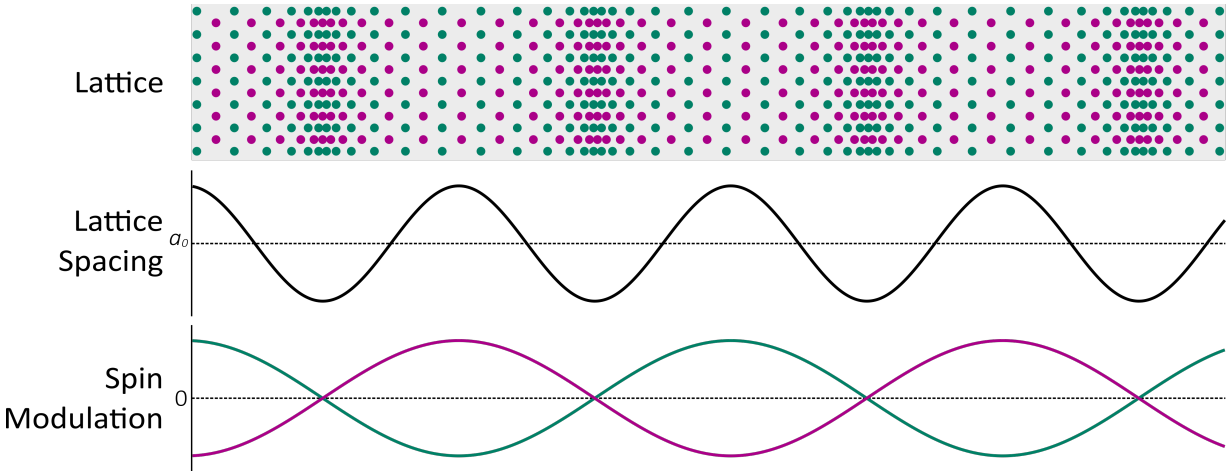

Figure 3.3: Schematic of the periodic lattice distortion in Cr, with (top) a schematic real space representation of the atomic positions in Cr in the presence of the spin density wave and charge density wave (note that the periodic distortion has been exaggerated). The (middle) lattice spacing and (bottom) spin modulation as a function of atomic position.

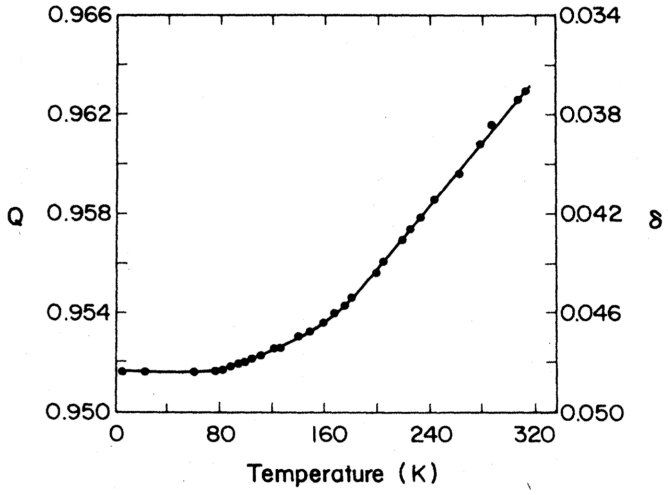

Figure 3.4: The spin density wave wavevector Q in bulk Cr as a function of temperature in units of $2\pi/a$, where $\mathbf{Q} = \frac{2\pi}{a}(1 \pm \delta)$. Figure reproduced with permission from [33]. Copyright 1988 by the American Physical Society.

packed atoms) aligning to nodes in the SDW and maxima in the lattice spacing to antinodes in the SDW [33, 87, 88].

In bulk Cr, the SDW wavevector varies continuously with temperature as shown in Fig. 3.4,

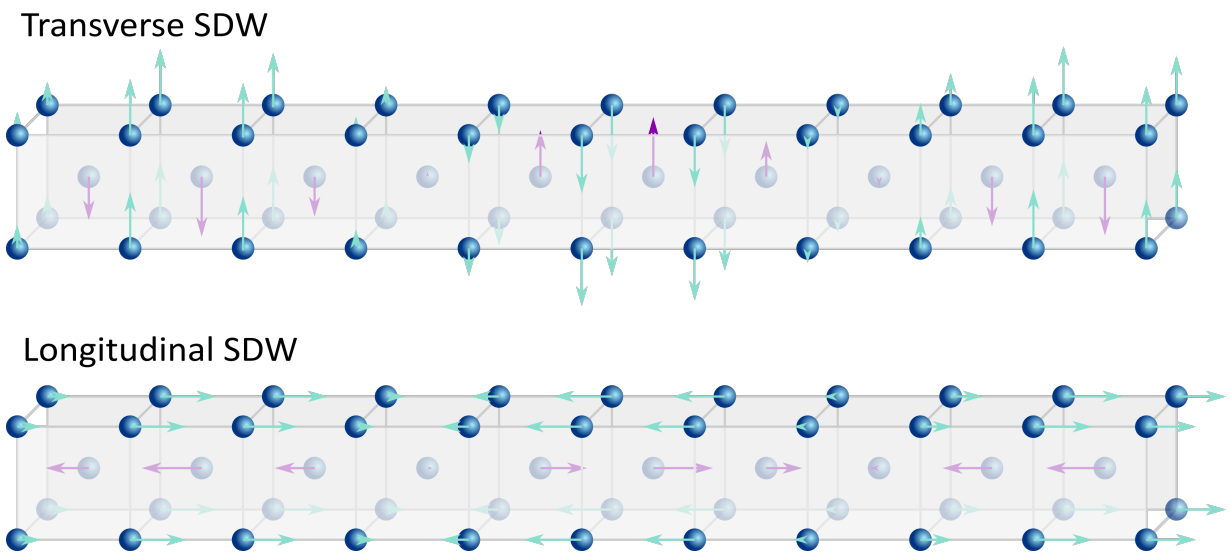

Figure 3.5: Transverse and longitudinal spin density waves (SDW) represented with atomic moments on a Cr crystal lattice. A transverse SDW has $\mathbf{S} \perp \mathbf{Q}$ and a longitudinal SDW has $\mathbf{S} \parallel \mathbf{Q}$, for spins $\mathbf{S}$ and SDW propagation wavevector $\mathbf{Q}$.

reproduced from [33]. This gives a period of the SDW ranging from about 21 unit cells (around 6 nm) at 78 K to about 28 unit cells (around 8 nm) near T_N [89]. There is a transition in bulk Cr at $T_{\mathrm{SF}} = 123$ K, called the spin-flip transition, where the polarization of the SDW changes between the two configurations shown in Fig. 3.5. Above T_{SF}, the SDW is transversely polarized, with spins perpendicular to the direction of propagation of the SDW ($\mathbf{S} \perp \mathbf{Q}$), and below T_{SF}, it is longitudinally polarized, with spins parallel to the direction of propagation of the SDW ($\mathbf{S} \parallel \mathbf{Q}$) [33, 89].

In a bulk crystal, the three $\langle 100 \rangle$ directions are equivalent, so there is no preferred direction of propagation of the SDW. Below the Néel temperature, a crystal will break into domains with length scales on the order of 1-30 μm. In each of these domains, the SDW, CDW, and strain wave are oriented along one of the $\langle 100 \rangle$ directions. Below T_{SF}, this gives three possible domain orientations. Above T_{SF}, there are six possible, with spin along either perpendicular $\langle 100 \rangle$ direction [87, 90]. In reciprocal space, the SDW and CDW appear as peaks around the forbidden (100) reflections and the (200) Bragg reflections, respectively. This is shown in Fig. 3.6 along the H reciprocal axis. Domains with wavevector propagation along the H axis contribute to

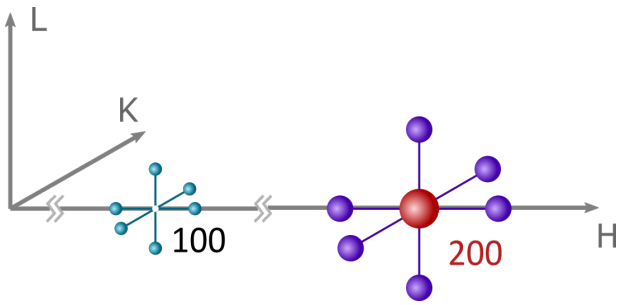

Figure 3.6: Reciprocal space representation of the spin density wave (SDW) and charge density wave (CDW) peaks around the (100) and (200) reflections in bulk Cr. The SDW peaks (blue) appear around the forbidden (100) reflection and the CDW peaks (purple) appear around the (200) Bragg reflection (red). Similar peaks are seen along the *K* and *L* axes and around other reflections.

peaks at $(1 \pm \delta, 0, 0)$ and $(2 \pm 2\delta, 0, 0)$. Those with wavevector propagation along *K* contribute to peaks at $(1, \pm\delta, 0)$ and $(2, \pm 2\delta, 0)$ and along *L* contribute to peaks at $(1, 0, \pm\delta)$ and $(2, 0, \pm 2\delta)$. Similarly, peaks will appear around (010), (020), (001), and (002) along the *K* and *L* axes and around other reflections [33, 87]. The appearance of these peaks allows for measurements of the SDW and CDW in Cr through diffraction measurements. The SDW satellite peaks are most easily measured through neutron diffraction since neutrons have strong magnetic scattering. The CDW satellite peaks, however, can be measured by x-ray diffraction, which provides opportunities for more interesting measurements such as time-resolved diffraction due to the higher x-ray intensity and experimental flexibility availability at synchrotrons and free-electron lasers. Because the magnetism stabilizes the CDW in Cr, measurements of the CDW satellite peaks provide an indirect measurement of the magnetic ordering.

3.1.2 Properties of Thin Film Cr

As with bulk Cr, thin films exhibit antiferromagnetic ordering and coupled SDW, CDW, and periodic lattice distortion. The Néel temperature in Cr films is lowered from the bulk value of 311 K to around 290 K and is a broader transition [86, 91, 92]. There are other important differences that appear as a result of the finite dimension of the system with broken symmetry

normal to the film surface and interfacial interactions, which include pinning of the Cr moment at the interfaces and quantization of the SDW, as well as the possibility for commensurate ordering.

Some of the earliest studies of Cr films looked at the magnetic behavior of layers of ferromagnetic Fe (001) which sandwiched the Cr films, because of the difficulty in directly measuring antiferromagnets as opposed to well-established methods of measuring ferromagnets. Along an interface between Cr (001) and Fe (001), the exchange coupling results in a maximized Cr moment antiparallel to the Fe moments. If the two Fe layers are allowed to rotate so their moments are either parallel (configuration F with $\vec{\mu}_{\mathrm{Fe},1} = \vec{\mu}_{\mathrm{Fe},2}$) or antiparallel (configuration A with $\vec{\mu}_{\mathrm{Fe},1} = -\vec{\mu}_{\mathrm{Fe},2}$), interesting behavior that was dependent on the thickness of the Cr layer (or the number of monolayers N) was observed [93, 94] and explained theoretically [95, 96]. For an odd number of Cr monolayers between the Fe layers up to $N = 23$, the stable configuration for the Fe layer moments was F. For an even number up to $N = 24$, the stable configuration was A. For $25 < N < 44$, there was a phase slip, where the stable configuration for odd N was A and for even N was F. Then again, for $45 < N < 64$, the phase changed again, back to configuration F for odd N and configuration A for even N. The exact number of monolayers where the slip occurs differed between the experimental observations and theoretical calculations, but the theoretical model explains well what is happening. For $N \leq 24$, the Cr film exhibits a commensurate antiferromagnetic structure, antiparallel spins with equal magnitude, and an odd number of layers results in the same direction moment for both interfacial layers, stabilizing configuration F in the Fe layers. For $N > 24$, the antiferromagnetic ordering becomes incommensurate, and there is a SDW like the one seen in bulk. The moments are still pinned at both interfaces, so there is a quantization to the SDW. When $25 < N < 44$, there is one node, meaning half a wavelength of the SDW between the interfaces, and now an odd number of layers results in opposing moment directions at the interfaces, stabilizing configuration A. For the next range of monolayers, there are two nodes of the SDW, a full wavelength, and the phase switches again. So the SDW ordering in these films is pinned at the interfaces so there is a quantized periodicity to the SDW, and the

direction normal to the film is the preferred direction of propagation for the SDW.

In the case where the two Fe layers have fixed configuration, either F or A, increasing the number of monolayers results in alternating between an incommensurate and commensurate SDW, with the same phase slip boundaries described above [95, 97]. When the Cr film is bound on either side by materials that are not ferromagnetic, the boundary conditions for the SDW may be different and impurities play a significant role in pinning of the SDW or CDW [98–100]. A vacuum interface or free Cr surface may result an antinode at the Cr interface, with no preferred spin direction [101]. This is also expected for interfaces with noble metals, including Au, Ag, Pt, Pd, and Cu, where there is weak hybridization between Cr and the nonmagnetic material [33, 102, 103]. For an interface with Mo, which has strong interface hybridization with Cr, there is a node with no Cr moment at the interface [104]. The SDW order in each of these cases is directed normal to the surface and can be commensurate at some smaller thicknesses or incommensurate with nodes and antinodes, depending on the film thickness and boundary conditions. Experimentally, interface roughness, alloying, strain, and other imperfections in the interface play a role in altering the boundary conditions of the SDW, such as by changing the Néel transition or shifting the node/antinode location away from the interfaces or destroying the surface state to create a node rather than antinode [102].

For a given film geometry with fairly smooth non-magnetic interfaces, the SDW order can be predicted fairly accurately given the boundary conditions and thickness of the film, and the boundary conditions should be constant with temperature. The SDW wavevector is always directed normal to the film surface. For very thin films, with $N \lesssim 20$, the magnetic order in the Cr film usually becomes commensurate. As the thickness increases, the ordering will become incommensurate and nodes will appear such that the boundary pinning is satisfied and the SDW wavevector is similar to the bulk Cr wavevector. Experiments have also shown that there is no spin-flip transition in films: the spins are directed in the plane of the film, along either (100) or (010) in each domain.

In bulk, we saw the continuous variation of the SDW wavevector, reproduced from [33] in Fig. 3.4, however in films, the quantization results in a mostly temperature-independent wavevector close to the bulk value [102]. However, as temperature is changed for a single film, there may be a reorientation of the SDW such that an additional node is added or removed and the number of wavelengths or periods of the SDW between the interfaces changes to achieve a wavevector closer to the preferred bulk value while still satisfying the boundary pinning, with a period in the range 5.9 nm to 8.0 nm [85, 91].

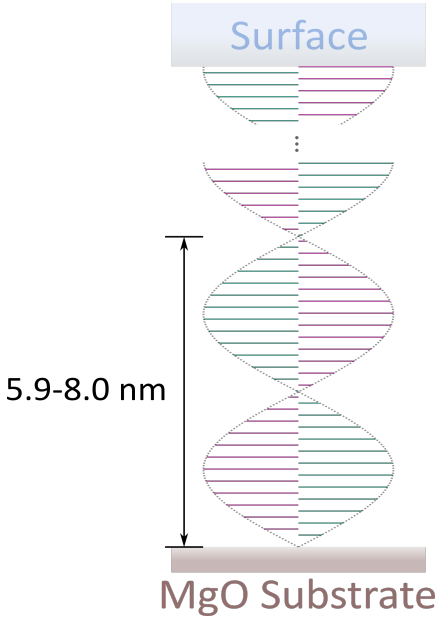

Figure 3.7: Schematic of the spin density wave (SDW) for a Cr film grown on a MgO (001) substrate. Pink and green spins differentiate between atoms at the vertices of the unit cell and body-centered atoms. The SDW in this example is pinned so there is a node at the substrate interface and an antinode at the Pt interface. The SDW in films is quantized such that the period of the SDW ranges from 5.9 nm to 8.0 nm.

In this work, we will be looking at Cr films grown on MgO (001) substrates, with a thin native oxide at the surface. Previous work has found that there are a quantized number of SDW/CDW periods in such films [86, 105]. This is represented in Fig. 3.7 with a node at the MgO substrate interface and an antinode at the surface. The pink and green spins differentiate between atoms at the vertices of the unit cell and body-centered atoms. The SDW is oriented

normal to the film surface with spins in-plane. With these boundary conditions, there are a half integer number of CDW periods in the film (and the number of SDW periods is half that) such that the wavelength of the SDW is between 5.9 nm and 8.0 nm. The work in Section 3.2 shows that the actual phase is slightly greater than π (where a phase of π would indicate a half-integer number of CDW periods) and the pinning at the substrate interface is close to an antinode.

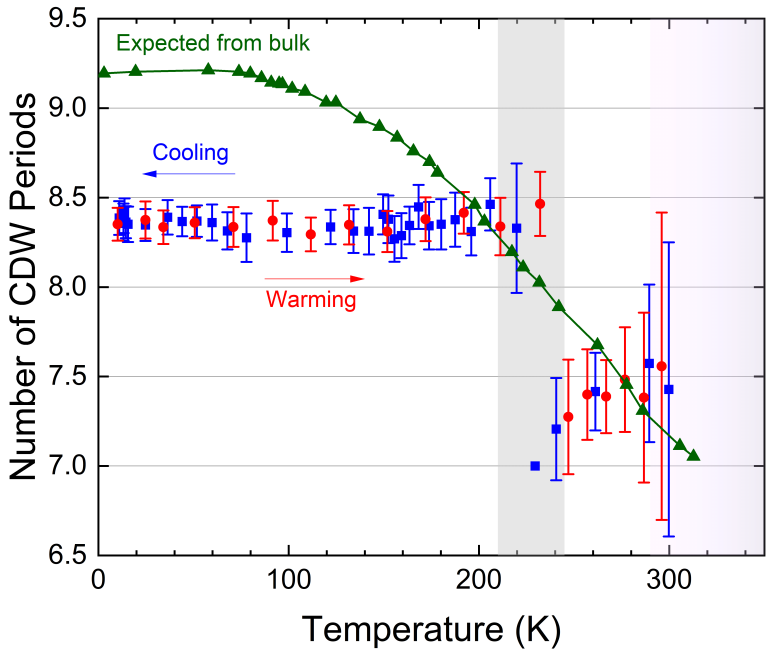

Figure 3.8: Number of charge density wave (CDW) periods in a 28 nm Cr film as a function of temperature. Blue squares are found during cooling the film and red circles during warming. Green triangles are the expected number of CDW periods calculated from the bulk spin density wave (SDW) wavevector, taken from data in [33]. The gray shaded region indicates the transition region in the film, where the SDW reorients. The pink shaded region is above the Néel temperature at 290 K. Bulk data adapted with permission from [33]. Copyright 1988 by the American Physical Society.

The number of CDW periods for a 28 nm Cr film grown on MgO (001) is shown in Fig. 3.8 during cooling (blue squares) and warming (red circles). The green triangles are the number of periods that would be expected in the film given the bulk wavevector from [33] with no boundary pinning. Just below the Néel transition, where the expectation would be 7.25-7.75 CDW

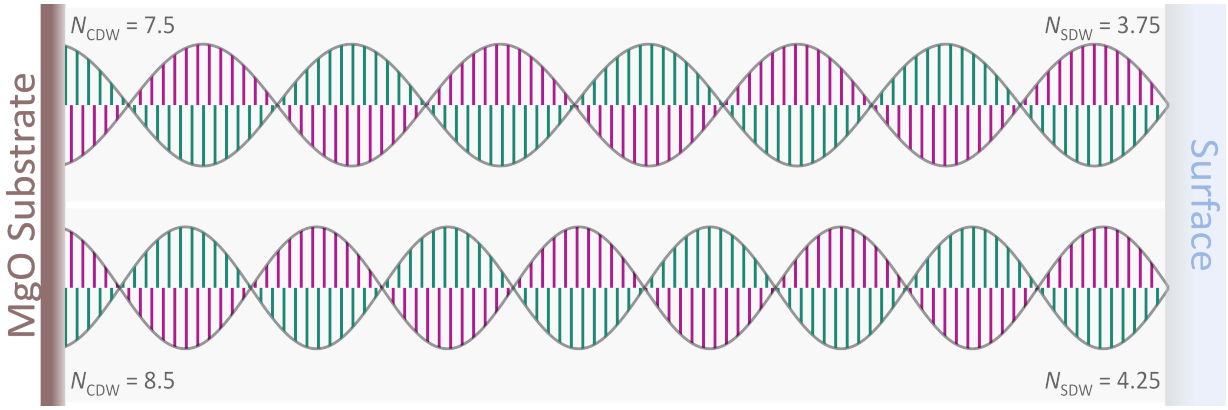

Figure 3.9: Schematic of two possible spin orientations for a 28 nm Cr thin film with boundary pinning such that there is a node at the substrate interface and an antinode at the surface and a half-integer number of charge density wave periods in the film. Pink lines refer to the spin at the vertices of the unit cells and green lines to the spin at the center of the unit cell. At low temperatures, the film is in the configuration with $N_{CDW} = 8.5$, but at higher temperatures, it switches to a state with $N_{CDW} = 7.5$.

periods, the boundary pinning in the film results in 7.5 CDW periods (or 3.75 SDW periods). As temperature is decreased further, a shorter wavelength of the SDW/CDW results in a hysteretic transition in the gray shaded region where the expectation would be 7.75-8.25 CDW periods. Below 210 K, there are 8.5 CDW periods (or 4.25 SDW periods) in the film. The expected number of periods from bulk plateaus at almost 9.25 CDW periods, so we might expect to be in a transition region to 9.5 CDW periods, but that does not appear for this film, possibly due to strain and disorder at the substrate interface. Therefore, for this film, boundary pinning is strong and the SDW wavevector is temperature-independent above and below the reorientation region. It is useful to note for Section 3.4 that near the Néel temperature, the expected wavevector leads to an expectation of 7.25 CDW periods, and following the pattern, one might expect that we are approaching a transition region to a state where domains with 6.5 CDW periods could exist. This is not easily measured in the static x-ray diffraction measurements made in Section 3.2, but we will show evidence of it in nonequilibrium measurements. Fig. 3.9 depicts the two possible configurations in the film from the static measurements, with the low temperature state with 8.5 CDW periods on top, and the higher temperature state with 7.5 CDW periods below. The

boundary conditions at the substrate interface and surface remain the same, but there is an extra node for the case with 8.5 CDW periods. The pink lines refer to the spin at the vertex of the unit cells and the green lines to the spin at the center of the unit cell. We will see an effect of the reorientation in transport measurements of a thin films in Section 3.1.4 and discuss it further through x-ray diffraction measurements of this film in Section 3.2 and Section 3.4.

A consequence of the out-of-plane propagation of the SDW is that in films, only two of the six domain configurations seen in bulk will contribute to the SDW and CDW peaks in reciprocal space, which will change what can be measured with diffraction techniques. Along the *L* axis (out-of-plane), there will be peaks at $(0,0,1\pm\delta)$ and $(0,0,2\pm2\delta)$, but not at $(\pm\delta,0,1)$, $(\pm2\delta,0,2)$, $(0,\pm\delta,1)$, or $(0,\pm2\delta,2)$. This is represented for the CDW peaks $(0,0,2\pm2\delta)$ around the (002) Bragg peak in Fig. 3.14(a) and will be discussed further in Section 3.2.

3.1.3 Growth of Cr Films

Growth of Cr films with SDW ordering is achievable through high temperature sputtering from a high purity (>99.99%) Cr target. In this work, films were sputtered at 2.5 mTorr Ar onto MgO (001) substrates with a substrate heating temperature of 500 °C followed by post-annealing at 800 °C for 1 hr. No capping layer was deposited, and the Cr films form a passive oxide layer at their surface when exposed to air. Growth at higher temperatures achieves better crystal quality (lower mosaic spread), however it also leads to the formation of holes or islands rather than a continuous film. This was described in Section 2.2.4 and shown in Fig. 2.7.

In Fig. 3.10, we present in-house x-ray diffraction characterization of a 28 nm Cr film, the film used for experiments in Sections 3.2, 3.3, and 3.4. Fig. 3.10(a) shows the out-of-plane θ-2θ scan, with the MgO (002), MgO (004), and Cr (002) peaks labeled. This demonstrates that the film grows in the (001) orientation on top of the MgO (001) substrates. In Fig. 3.10(b), the rocking curve for the Cr (002) peak has a FWHM of 0.4467 ± 0.0007 deg. From reflectivity measurements (Fig. 3.10(c), we find the film thickness to be 28 nm with a native oxide layer

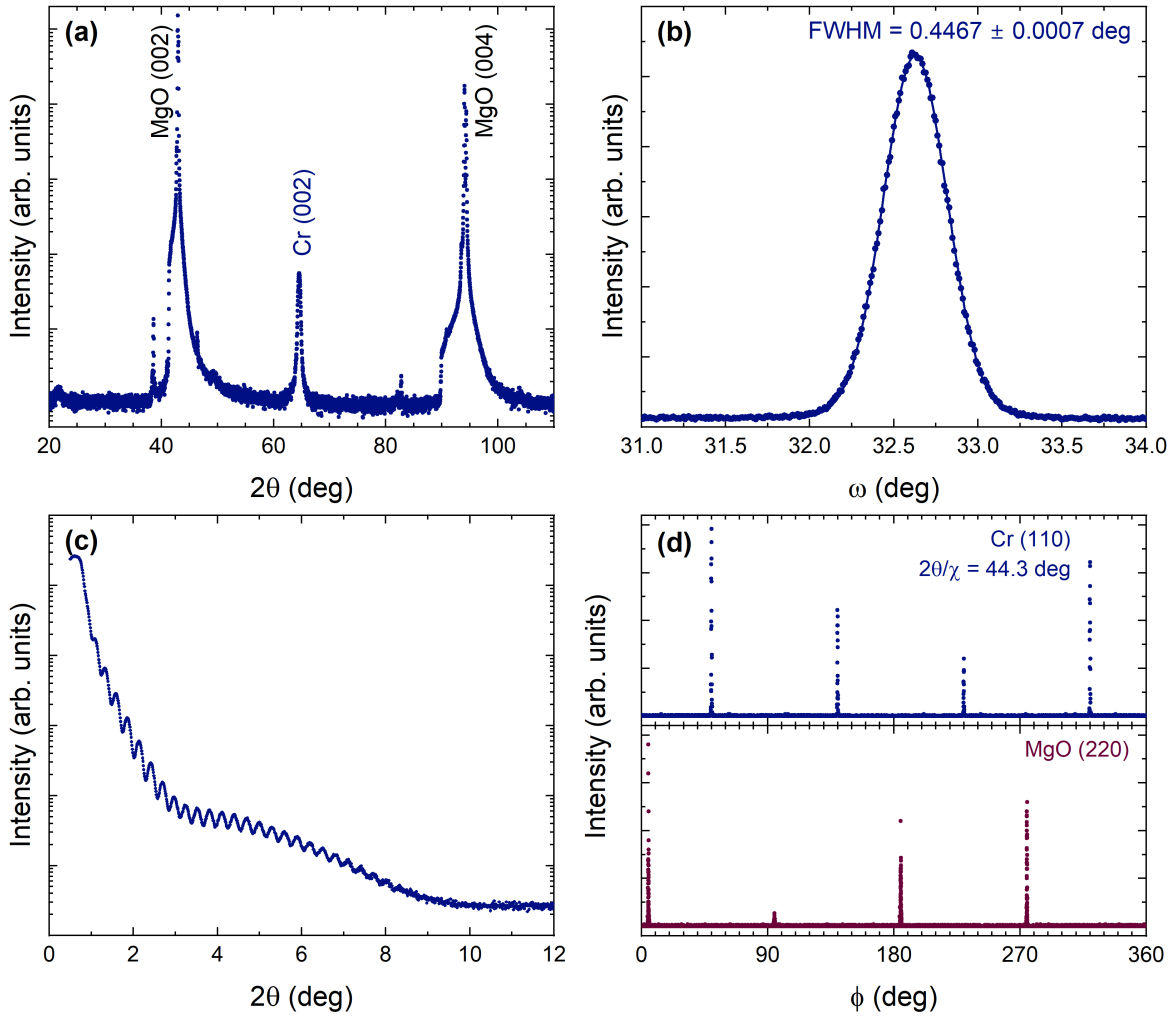

Figure 3.10: Out-of-plane x-ray characterization of a 28 nm Cr film grown on MgO (001). (a) Out-of-plane θ-2θ scan showing the Cr (002) peak, the MgO (002) peak, and the MgO (004) peak. (b) Rocking curve of the Cr (002) peak at $2\theta = 64.6$ deg. The solid line shows a Gaussian fit to the data. (c) X-ray reflectivity used to measure the film thickness and confirm smooth interfaces. (d) Phi scans of the Cr (110) peak and the MgO (220) peak, demonstrating a 45 deg rotation of the Cr unit cell with respect to the MgO unit cell. Measurements were made with Cu Kα radiation.

of about 2 nm. A 45 deg shift in the phi scans of the MgO (220) peak and Cr (110) peak in Fig. 3.10(d) demonstrate that the Cr film grows with a 45 deg in-plane rotation on the MgO substrate, so the [100] direction in Cr corresponds to the [110] direction in MgO.

In the next section, we present some electric transport measurements of wires. These wires were fabricated from continuous films grown by UV photolithography (see Section 2.3.1) and electron beam lithography (see Section 2.3.3) and included a reactive ion etching step as described in Section 2.3.2. All subsequent work in this chapter involves x-ray diffraction measurements on a single continuous Cr film that is 28 nm in thickness, the same film that was measured in Fig. 3.8 and Fig. 3.10.

3.1.4 Electric Transport Measurements

Electric transport measurements in bulk Cr were the first indication that there may be some kind of phase transition. The resistivity as a function of temperature follows metallic behavior, but with an anomaly: a sharp drop of a few % with increasing temperature at the Néel transition [33, 40]. The increase in resistance as the SDW order forms is attributed to energy gaps opening with the Fermi surface nesting [33, 106]. This carries over into resistivity measurements of thin films, however the magnitude of the anomaly at the Néel temperature is smaller and broader [85, 107], indicative of a broader Néel transition.

Fig. 3.11(a) shows a resistivity measurement from a 30 nm Cr film that was patterned through UV photolithography into a 50 μm-wide wire. Resistivity was measured at temperature increments of 2 K during warming and cooling with a wait time of 2 min at each temperature. The overall behavior is metallic, roughly linear down to 100 K. However there is a small deviation from this around 290 K. The anomaly is better seen in the derivative of the resistivity in Fig. 3.11(b), with a local minimum that indicates the Néel temperature. In thicker films and bulk Cr, this minimum is sharper and narrower, while for thinner films, it is wider, indicative of the broader Néel transition in films [85]. There is another effect that can be seen here, in the green shaded region, where there is a small hysteresis in the resistivity that can be seen as the peaks in the derivative at 224 K while warming (red points) and at 174 K while cooling (blue points). This is the hysteretic region in which a SDW node is added or removed and the SDW and CDW in the

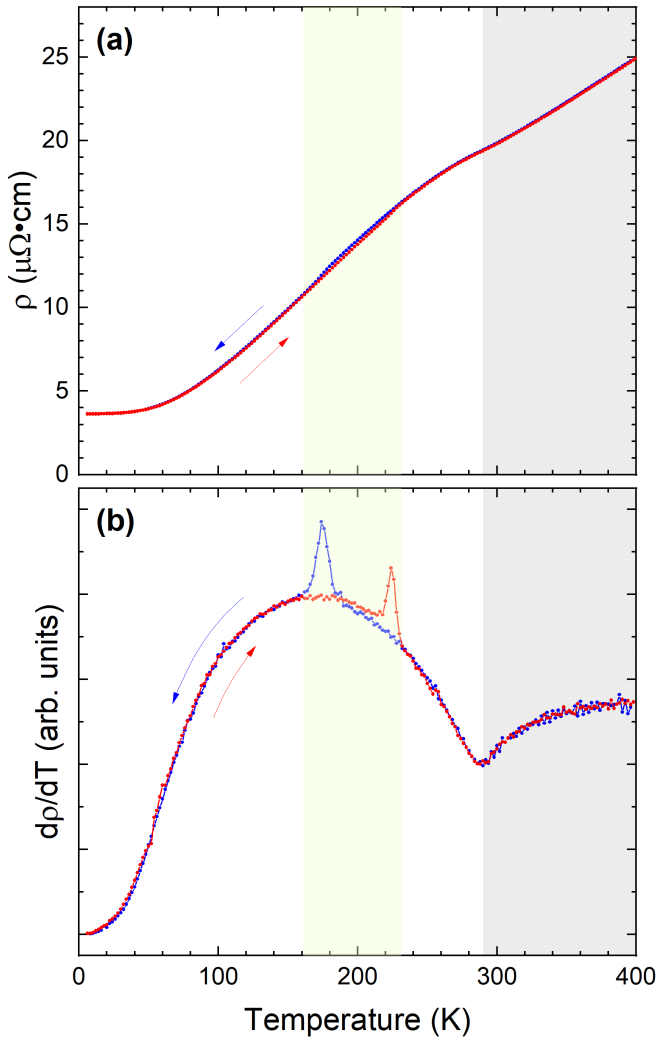

Figure 3.11: (a) Resistivity measurements of a 50 μm-wide wire fabricated from a 30 nm thick Cr film. (b) The derivative of the resistivity measurements in (a), from which the N'eel temperature can be identified by the local minimum and the spin density wave (SDW) reorientation can be identified by the hysteretic peaks. Blue data points are taken during cooling and red data points during warming. The gray shaded area above 290 K is above the Néel transition in the paramagnetic phase. The green shaded region is the hysteretic region of SDW reorientation in which an additional node appears or an existing one disappears. Measurements were taken with a wait time of 2 min at temperature increments of 2 K.

film reorient.

A width of 50 μm is still considered quite wide, so this wire is representative of resistivity

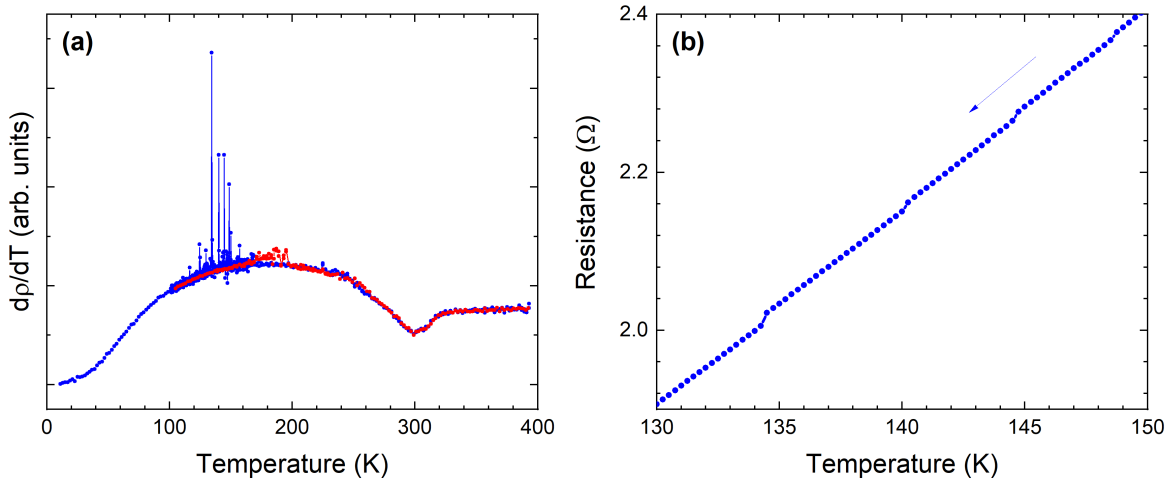

Figure 3.12: Transport measurements of an 800 nm-wide wire fabricated from a 30 nm thick Cr film. (a) The derivative of the resistivity, with blue data points taken during cooling and red during warming. Measurements were initially taken with a wait time of 2 min at temperature increments of 2 K. Additional measurements during cooling from 170 K to 100 K at increments of 0.25 K with a wait time of 30 s are also included. (b) The resistance in increments of 0.25 K is shown during cooling from 150 K to 130 K, demonstrating discrete anomalies in the resistance.

measurements from continuous films, with confinement in one dimension normal to the film surface. A question arises of what may happen in Cr if we further confine in a second dimension. To this end, we fabricated an 800 nm-wide wire from a 30 nm-thick film by electron beam lithography and measured resistivity, as shown in Fig. 3.12. Initial measurements were made at temperature increments of 2 K with a wait time of 2 min during warming and cooling. Additional measurements during cooling from 170 K to 100 K in increments of 0.25 K with a wait time of 30 s were made. The derivative of the resistivity from these measurements is shown in Fig. 3.12(a). The overall behavior is similar to films and bulk. The Néel temperature for this wire is about 300 K, still less than the bulk value but higher than measured in films. Fig. 3.13 shows the derivative of the resistivity around the Néel transition during warming for both wires from Fig. 3.11 and Fig. 3.12(a). We see more clearly here that the narrower wire has a higher Néel temperature and also possibly a narrower Néel transition. It would be worth further measurements of narrower wires to confirm this behavior.

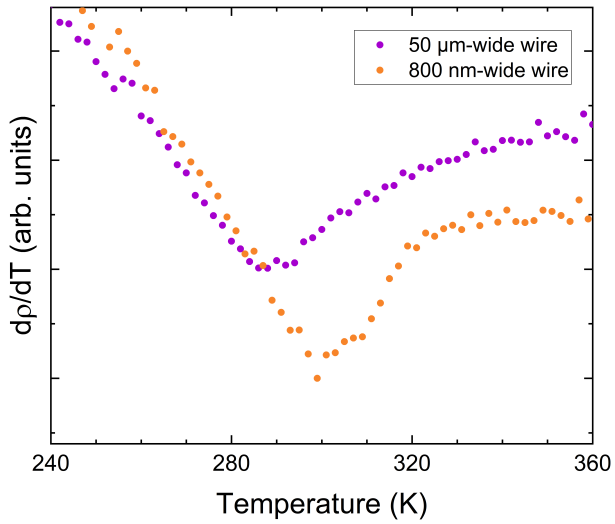

Figure 3.13: Derivative of the resistivity near the Néel transition for Cr wires of width 50 μm (purple) and 800 nm (orange).

The second important feature in Fig. 3.12(a) is the hysteretic transition that indicates a reorientation of the SDW to add or remove a node. With a wider wire, we saw smooth peaks in the derivative, indicating a smooth kink in the resistivity. For this 800 nm wide wire, there are discrete steps shown zoomed in for the cooling curve in Fig. 3.12(b). Each discrete step is indicative of a domain switching, and we are able to resolve individual domains switching at slightly different temperatures as we have confined to on the order of the domain size in two dimensions. This supports the theory that the reorientation of spins is a first order phase transition with the coexistence of domains with two different periodicities and identical boundary pinning at the interfaces in both phases (see also Section 3.2 rather than a continuous evolution between the two states. Further work with narrower wires will help to confirm this result and to better examine the Néel transition.

3.2 X-Ray Diffraction Measurements of the Charge Density Wave Phase and Pinning

In Cr, the CDW can be measured in x-ray diffraction experiments: the reciprocal space contains not only Bragg peaks but also satellites due to the periodic lattice distortion associated with the CDW, schematically represented in Fig. 3.14(a). In relatively thick samples, only the intensity and position of the satellites can be measured to determine the amplitude and period of the CDW, while the phase of the CDW is lost [102]. For thin films (~30 nm), however, interference between the Laue oscillations and satellites allows an efficient determination of the CDW phase [105]. Here we take advantage of the brightness of synchrotron radiation and use this interference to study the amplitude, period, and phase of the CDW in a Cr thin film as a function of temperature upon cooling and heating in the range between 10 K and 300 K.

We performed in-house x-ray diffraction characterization shown in Fig. 3.14(b) of a Cr film deposited onto a MgO (001) substrate at room temperature. The x-ray reflectivity curve revealed a film thickness of about 28 nm and the presence of the passive surface oxide layer (~2 nm thick). An azimuthal scan around the (011) peak confirmed the epitaxial growth of the Cr film on MgO (see left inset of Fig. 3.14(b)). A Gaussian fit to the θ-2θ scan of the (011) peak (see right inset of Fig. 3.14(b)) revealed a mosaic spread in the sample plane with a typical domain size of about 25 nm. This inhomogeneity likely appears due to a small mismatch between the in-plane MgO and Cr lattices. The interatomic spacing of the (011) planes of MgO is 3.4% larger than the interatomic spacing of (001) planes of Cr, presumably inducing defects in Cr every 30 unit cells on average (~10 nm).

Temperature-dependent x-ray diffraction studies were performed at beamline 8 ID-E of the Advanced Photon Source at the Argonne National Laboratory. A photon energy of 7.35 keV was selected by a silicon (111) double crystal monochromator. The sample was mounted inside a He flow cryostat [87], x-rays were scattered vertically, and the diffracted radiation was recorded by a

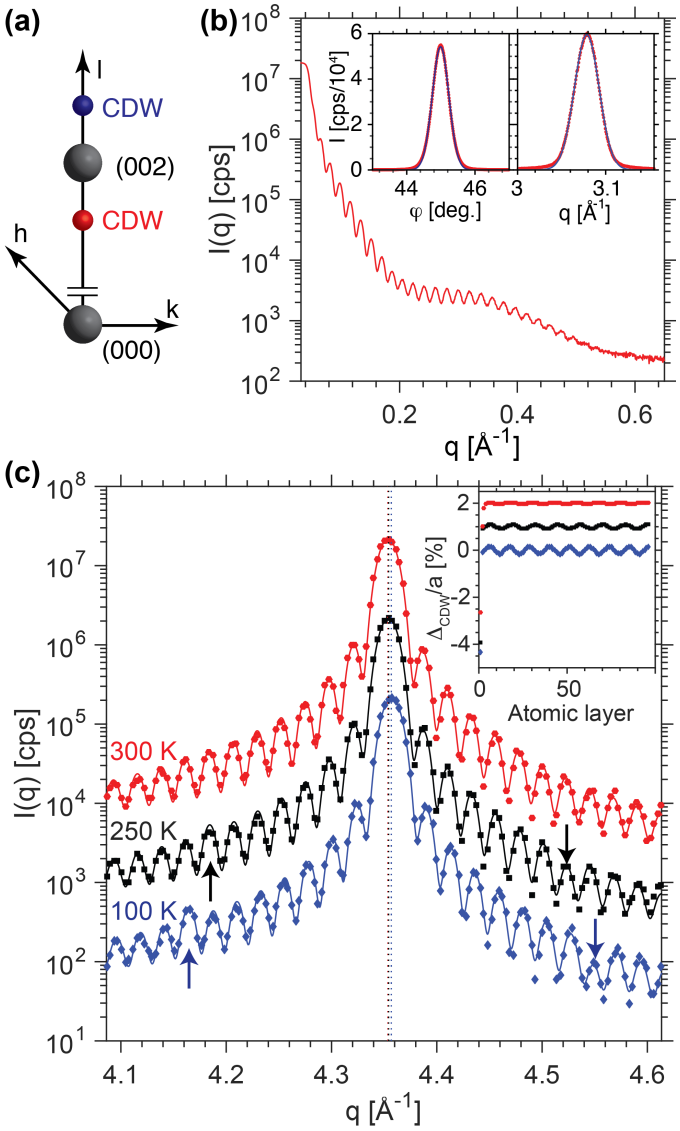

Figure 3.14: X-ray diffraction characterization of a 28 nm Cr thin film. (a) Sketch of the reciprocal space around the (002) diffraction peak of Cr in the presence of a charge density wave. (b) X-ray reflectivity measurement of the Cr thin film with Cu K-α radiation. (Left inset) The φ rotation scan and (right inset) θ-2θ scan of the (011) peak (out-of-plane). In both insets, red dots show the data, and blue solid lines show Gaussian fits used to determine the peak widths. (c) θ-2θ scans around the (002) peak recorded with synchrotron radiation at room temperature (red hexagons), 250 K (black squares), and 100 K (blue diamonds). Solid lines show theoretical fits to the data, and vertical dashed lines show the center of the Bragg peak. Inset: The corresponding lattice distortion or displacement. The curves are shifted vertically for better visibility.

scintillator detector with a vertical slit (1 mrad in angular size) placed in front of the detector to increase angular resolution. Repeated θ-2θ scans around the out-of-plane (002) Bragg peak were collected for different temperatures ranging from 10 K to 300 K, while the film was continuously cooled or heated with rates between 2 K/min and 4 K/min.

Shown in red in Fig. 3.14(c) is a scan recorded at a film temperature of 300 K. The high visibility of the Laue fringes due to the finite sample thickness demonstrates excellent crystal quality and uniform thickness over large sample areas (beam size of several hundreds of microns). When cooling below 300 K, the Bragg peak shifts to higher angles due to contraction of the lattice as expected. But it also shows additional features: satellite peaks formed due to the presence of a CDW. The CDW does not lead to an increase in the diffracted intensity at both satellite positions [33, 102, 108]. Instead, the intensity is enhanced for the low-q peak and suppressed for the high-q peak due to constructive and destructive interference [105, 109]. We discuss the constructive and destructive interference more in the next section. Noticeably, at 250 K the interference occurs on fringe number 7, while at 100 K the interference occurs on fringe 8 (see Fig. 3.14(c)), which indicates that the CDW periodicity shifts to a smaller period at lower temperature.

To get quantitative information from the x-ray data, we modeled it with the following expression:

$$I(q) = |F_{\mathrm{FILM}}(q) + F_{\mathrm{SUB}}(q)|^2, \tag{3.1}$$

where F_{FILM} and F_{SUB} are the fields scattered by the Cr film and the MgO substrate, respectively, and q is the momentum transfer along the [001] direction in the reciprocal space. The field scattered by the Cr film was calculated as a one-dimensional numeric summation over the atomic planes normal to q [110]:

$$F_{\mathrm{FILM}} = f_{\mathrm{Cr}} \sum_{j=0}^{N-1} \exp(-iqz_j)$$

positioned at

$$z_j = z_{0,j} + \Delta_{\mathrm{ST},j} + \Delta_{\mathrm{CDW},j}, \tag{3.2}$$

where N is the number of atomic layers, f_{Cr} is the scattering power per unit area of an atomic plane of Cr, $z_{0,j} = a_0 \cdot j$ is the undistorted position of the j^{th} plane, a_0 is the average lattice parameter, and $\Delta_{\mathrm{ST},j} = a_1 \cdot \exp(-j/b)$ is the displacement at the substrate interface, which was modeled to relax exponentially with amplitude a_1 and relaxation distance b [111]. The periodic lattice distortion due to the CDW is described by the last term in Eq. 3.2,

$$\Delta_{\mathrm{CDW,j}} = a_2 \cdot \cos(z_{0,j} \cdot Q + a_4),$$

where a_2 is the amplitude, $Q = 2\pi \cdot a_3/[a_0(N-1)]$, a_3 is the number of periods of the CDW in the film, and a_4 is the phase of the CDW relative to the substrate interface. The field scattered by the substrate is given by

$$F_{\mathrm{SUB}} = f_{\mathrm{MgO}} \frac{1}{1 - e^{iqd_{\mathrm{MgO}}}},$$

where d_{MgO} is the MgO (002) lattice spacing and f_{MgO} is the scattering power per unit area of an atomic plane of MgO [112]. The finite experimental resolution was taken into account by summation of intensities from Eq. 3.1 with slightly different momentum transfers $q' = q(1+\varepsilon)$, weighted by a Gaussian function $e^{-\varepsilon^2/[2*dE^2]}$, with ε having 30 points between $\pm 3dE$. The surface roughness σ was included by multiplying the scattered intensity by $e^{-(q-q_{002})^2\sigma^2}$, where $q_{002} = 4\pi/a_0$ is the position of the Bragg peak [113].

The following fitting procedure was employed. First, the number of atomic layers N of Cr was calculated from the fringe spacing. Second, the strain relaxation parameter b, surface roughness σ, and bandwidth dE were determined from the data at 300 K. These were found to be $N = 96$, $b = 0.64$, $\sigma = 3.2$ Å^{-1}, and $dE = 7.4 \cdot 10^{-4}$. Finally, the five remaining fit parameters were found at different film temperatures while fixing N, b, σ, and dE: the average lattice constant a_0, displacement of the Cr layer at the substrate interface a_1, amplitude a_2, number of periods a_3, and phase a_4 of CDW. The peak is asymmetric, the low-q tail having about twice higher intensity than the high-q tail. We attribute this asymmetry to strain at the film-substrate interface, and the

strain term $\Delta_{ST,j}$ in Eq. 3.2 is considered to be essential to reproduce the asymmetry of the x-ray data. The maximum displacement field obtained from the fit at 300 K is about 4% of the Cr unit cell size. The exceptionally large strain presumably occurs due to the large difference between the (001) lattice spacing of MgO (0.41 nm) and Cr (0.288 nm).

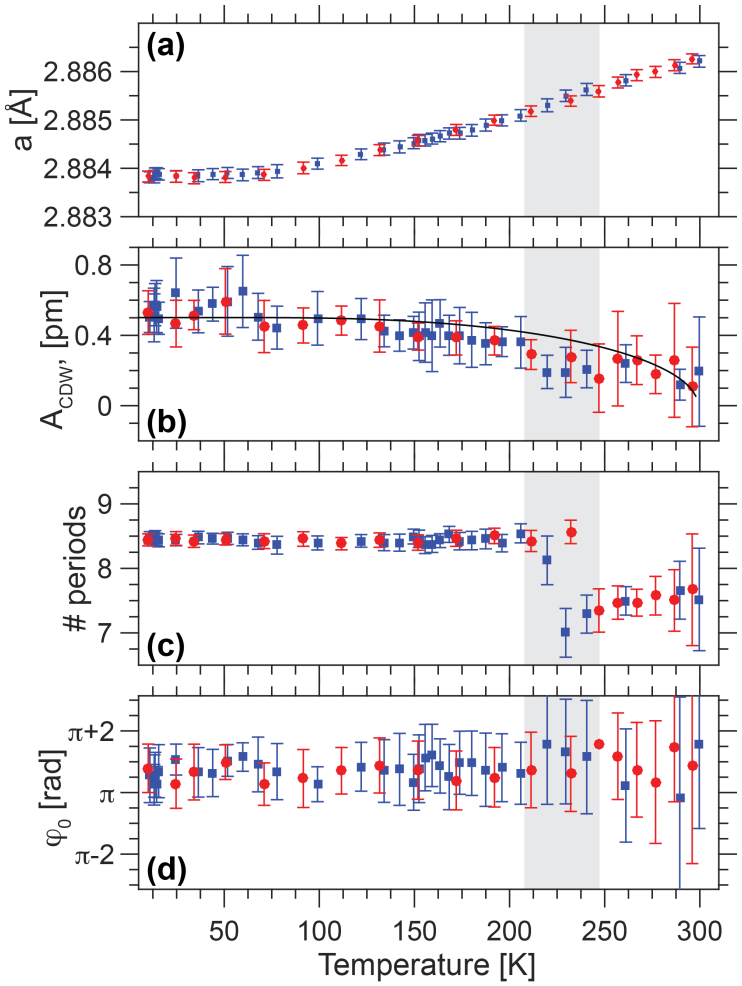

Figure 3.15: Fitting results of the charge density wave (CDW) peak data for a 28 nm Cr film at different temperatures. (a) The average lattice parameter, (b) amplitude, (c) number of periods, and (d) phase of the CDW. The black line in (b) shows a calculation of the CDW amplitude within the BCS theory based on the maximum observed CDW amplitude and a Néel temperature of 290 K. Uncertainties show 95% confidence intervals, and the error metric $\chi^2 = [\log_{10}(I_{th}) - \log_{10}(I_{exp})]^2/N$, where summation over the fitted points N was used for fitting. The gray shaded area represents the transition region between fringe 7 and fringe 8.

Typical fits to the data are shown in Fig. 3.14(c), in excellent agreement with the ex-

periment over three orders of magnitude in intensity, and correctly reproducing the data at the positions of the CDW satellites. The displacement determined from the fit, displayed in the inset of Fig. 3.14(c), shows both negative displacement at the interface and periodic modulations. The data at 100 K is consistent with a CDW having 8.5 periods in the film, while at 250 K, 7.5 periods are observed with reduced CDW amplitude. The CDW amplitude is negligible at 300 K. Presented in Fig. 3.15 are the determined fit parameters from the x-ray data recorded upon cooling (blue symbols) and heating (red symbols). The average lattice constant in Fig. 3.15(a) is in agreement with the thermal expansion coefficient of Cr reported in the literature [105, 114]. It is also identical for both cooling and heating, demonstrating that although we measured the data while the sample was continuously cooled/heated, the temperature transport from the cryostat to the sample can be considered rapid compared with the measurement time and the cooling/heating rate. The displacement of the first layer is constant around 4% to the precision of the measurement and is not shown here. Fig.3.15(b) displays the amplitude of the CDW, which agrees well with the description using the Bardeen-Cooper-Schrieffer (BCS) theory [115, 116] everywhere, except for the transition region (gray shaded area), where the used fit with only one CDW periodicity underestimates the CDW contribution.

The period of the CDW and its phase are presented in Figs. 3.15(c) and 3.15(d). As already anticipated from the inspection of the x-ray data, we observe two distinct temperature regions with $N_{\mathrm{CDW}} = 7.5$ periods and $N_{\mathrm{CDW}} = 8.5$ periods, suggesting strong pinning at the film boundaries. The number of CDW nodes displays hysteretic behavior, as expected from previous measurements in confined geometries [85, 86, 91, 105]. The phase is constant to experimental accuracy and is slightly larger than π, indicating that the node and antinode of the CDW are not exactly aligned at the MgO interface and the surface. The constant phase indicates identical pinning conditions for different temperatures and different periodicities of the CDW. For all temperatures, our data is consistent with negative displacement and tensile strain due to the CDW at the substrate interface.

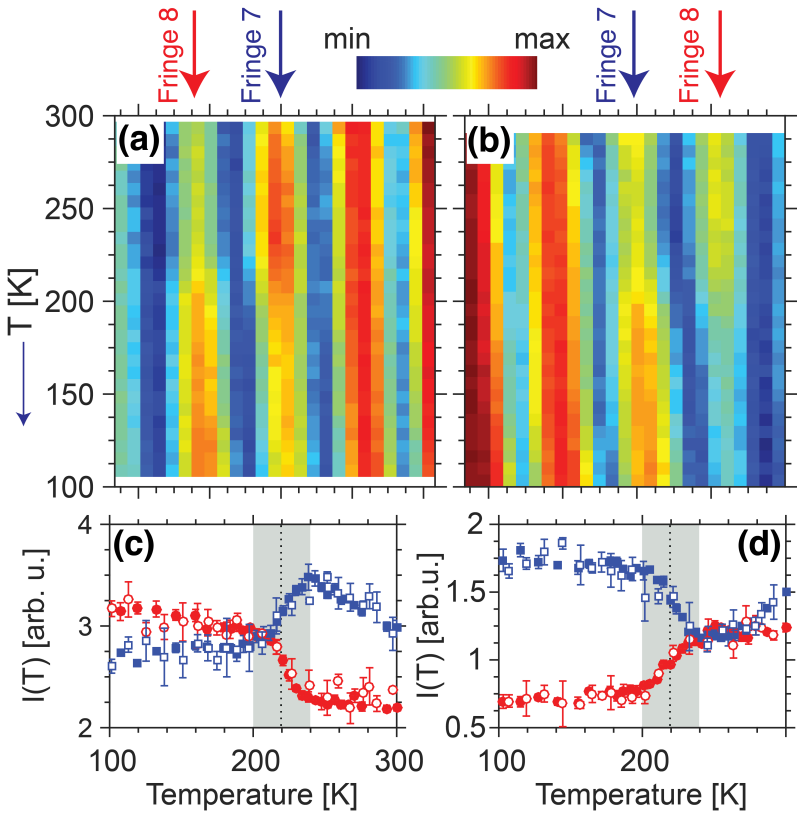

Figure 3.16: X-ray diffraction intensities of fringe 7 and fringe 8 during cooling. (a) Low-q and (b) high-q x-ray diffraction intensity with respect to the Bragg peak are shown. Fringes as counted from the Bragg peak are indicated (see Fig. 3.14(c)). The intensities are shown on a logarithmic scale. The intensity of fringe 7 (blue squares) and 8 (red circles) are found for (c) low-q and (d) high-q. Filled symbols show data collected with a cooling or warming rate of 2 K/min and open symbols with a rate of 4 K/min. The gray shaded area represents the transition region between fringe 7 and fringe 8 and is approximately 30 K wide.

To get further insights into the transition between the phases of different CDW periodicities, we performed an additional measurement. We cooled the film at a similar rate (2 K/min) but now only recorded scans around the satellite peaks (3 fringes) on both sides of the Bragg peak, shown in Figs. 3.16(a) and 3.16(b). As expected, upon cooling a slight shift of the fringes to higher q is observed, while fringe 7 at high temperatures and fringe 8 at low temperatures show the signature of the CDW. The limited q-range made fitting the data to Eq. 3.1 impossible. Instead, the intensities, $I_7(T)$, of the 7^{th} and, $I_8(T)$, of the 8^{th} fringes were found by approximating the five central data points of the respective fringe with a Gaussian, presented in Figs. 3.16(c) and 3.16(d).

We first describe the data at low q from Figs. 3.16(a) and 3.16(c). Upon cooling, we observe an approximately linear increase of $I_7(T)$, which shows that the CDW forms with $N_P = 7.5$ periods at the Néel transition and its amplitude grows with subsequent cooling. Below 240 K, $I_7(T)$ begins to drop quickly, while $I_8(T)$ rises as the temperature decreases. At 210 K through cooling, the temperature dependencies of the intensities decrease abruptly, with $I_8(T)$ greater than $I_7(T)$. The high-q data in Figs. 3.16(b) and 3.16(d) shows similar behavior for $I_7(T)$ and $I_8(T)$; however, the slopes of the curves are reversed due to destructive interference, as compared with constructive interference at low-q. We repeated the measurement with a cooling and warming rate of 4 K/min and found that it agrees well with the data collected at a rate of 2 K/min, demonstrating that the phase transition is not limited by the rate of temperature change in our experiment.

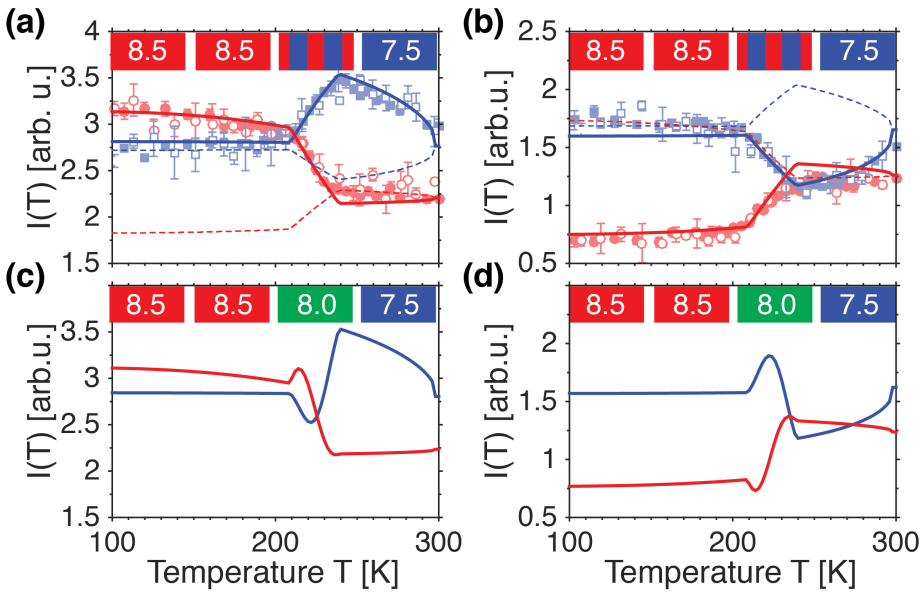

Figure 3.17: Simulated x-ray diffraction intensities for fringe 7 and 8 assuming (a), (b) abrupt and (c), (d) continuous phase transition between charge density wave phases with 7.5 and 8.5 periods. Calculations with a phase offset of $a_4 = 3.8$ rad (solid lines), and $3.8 + \pi/2$ rad (dashed lines) are shown. The data from Figs. 3.16(c) and 3.16(d) are shown by shaded symbols for comparison. Blue lines show intensity of fringe 7 and red lines shown intensity of fringe 8. Simulations at (a), (c) low-q and (b), (d) high-q are shown. The insets show schematically the composition of the phases.

To get a deeper insight into the phase coexistence during the transition between CDW with

different periods, we made the following model calculations (see Fig. 3.17). First, we simulated two distinct phases containing different numbers of periods $N_{\mathrm{CDW}} = 7.5$ and $N_{\mathrm{CDW}} = 8.5$ with a volume fraction of α and $(1-\alpha)$, respectively. We used $\alpha = 0$ for a temperature range between 100 and 210 K, $\alpha = 1$ from 240 to 300 K, and linearly interpolated α in the transition region. The temperature dependent amplitude of the CDW was determined in the framework of the BCS theory. The intensities $I_7(T)$ and $I_8(T)$ calculated using Eq. 3.1 are shown in Figs. 3.16(a) and 3.16(b) for different phases of the CDW. A comparison between the data and simulation (see solid lines for simulation and shaded symbols for the data in Figs. 3.17(a) and 3.17(b)) shows exemplary agreement, demonstrating that this simple model captures the essence of the physical processes involved in the phase transition. The best agreement is observed for a phase of $a_4 = \pi + 0.7$ and $a_1 = 0.025$, comparable to the values determined in the fits to the data (see Fig. 3.15(d)). The sensitivity of the presented method to the phase of the CDW is demonstrated by another calculation with the phase $a_4 = \pi + 0.7 + \pi/2$ (see dashed line in Figs. 3.17(a) and 3.17(b)), which clearly disagrees with the data. A similar calculation assuming a continuous phase transition, where the periodicity changes continuously from $N_{\mathrm{CDW}} = 7.5$ to $N_{\mathrm{CDW}} = 8.5$ via $N_{\mathrm{CDW}} = 7.5 \cdot \alpha + 8.5 \cdot (1-\alpha)$, is also shown in Figs. 3.17(c) and 3.17(d). This calculation does not reproduce the experimental observation, rendering this interpretation incomplete.

In conclusion, we have used x-ray diffraction to study pinning of the CDWs by interfaces in Cr as a function of temperature. The interference between the CDW peaks and Laue fringes allows us to determine not only the amplitude and the period of the CDW but also its phase on the interfaces. This phase provides insight into to the pinning of the CDW by the interfaces. Above the Néel transition, the data indicates tensile strain at the substrate interface (negative displacement as compared with the strain-free lattice). Below the Néel transition the CDW also has a negative displacement at the substrate interface, which suggests that the tensile strain at the interface pins the CDW. The temperature scans show that the CDW has a half-integer number of periods in the film at all temperatures. During cooling, the number of periods jumps from

7.5 above 240 K to 8.5 below 210 K. Upon heating, the transition occurs at higher temperatures, revealing a thermal hysteresis. Model simulations confirm a first order phase transition with a transition region of 30 K, the coexistence of distinct phases containing either 8.5 or 7.5 periods, and identical pinning conditions at the film interfaces for both phases. This work opens up ways to explore the phase coexistence of CDW and SDW in thin films. We anticipate this technique to be applicable to study other phenomena; for example, the phase of phonons in confined geometries. The apparent pinning of the CDW by interface strain promises advanced control of the spatial distribution of the structural order parameter in other correlated electron systems.

3.3 Ultrafast Photoinduced Enhancement of the Charge Density Wave Amplitude

We have discussed the origin of SDW and CDW order in Cr and thoroughly characterized the equilibrium CDW through x-ray diffraction measurements. Further studies of the coupling between various degrees of freedom that drives the formation of complex order can be done with dynamic measurements, perturbing a system in some way and measuring the response to further elucidate the origin of complex phenomena or study transient nonequilibrium states that may emerge. For example, studies suggest that spin order can be generated in iron pnictides in response to excitation of a coherent phonon [117], charge localization can be photoinduced in charge order systems [118], the superconducting order parameter in cuprates can be enhanced via suppression of the competing charge order or the transient redistribution of superconducting coherence [119–121], and hidden electronic states can be dynamically accessed [122–125]. Here we conduct an ultrafast time-resolved x-ray diffraction study of the CDW order in a Cr film following photoexcitation and demonstrate a dramatic transient enhancement of the CDW amplitude in elemental Cr following photoexcitation. This is remarkable, because external excitation typically creates disorder, reduces the order parameter, and raises the symmetry [126–

129]. We attribute the enhancement of the CDW amplitude to the dynamic electron-phonon interaction and experimentally discern multiple time scales, thus revealing the underlying physics.

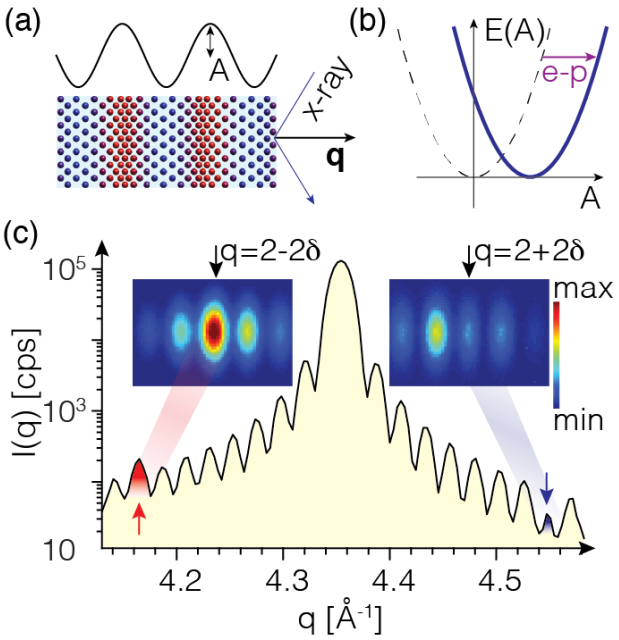

Figure 3.18: Static x-ray diffraction data from a 28 nm Cr film. (a) Schematic real space representation of the atomic positions in Cr in the presence of a charge density wave (CDW). The corresponding charge density modulation with the CDW amplitude A and the scattering geometry are also shown. (b) The potential energy surface for the CDW amplitude A. In the low-temperature ground state, the potential energy surface is shifted towards a nonvanishing value due to the electron-phonon (ep) coupling. (c) X-ray diffraction from a Cr thin film recorded with synchrotron radiation around the (002) Bragg peak (in photons per second) measured at a film temperature of 115 K. The intensity is increased (reduced) at the positions of the CDW satellites for low (high) q values (indicated by arrows). Insets: Diffraction patterns (linear scale) collected with the x-ray free-electron laser at two different momentum transfers $q = 2 - 2\delta$ and $q = 2 + 2\delta$ in the ground state, corresponding to different incident angles of x-rays.

The system studied in this work is a crystalline Cr film, which is antiferromagnetic and exhibits an incommensurate spin-density wave (SDW) below the Néel temperature $T_N = 290 \pm 5$ K, as shown in the previous section. It also forms an incommensurate CDW, appearing as the second harmonic of the fundamental SDW ordering [33]. In Fig. 3.18(a), we show the real space representation of the atomic positions in Cr in the presence of the CDW. The CDW amplitude, A is a measure of the charge density modulation. Fig. 3.18(b) shows the potential energy surface for the CDW, which is nonzero due to electron-phonon coupling. The amplitude

of the CDW can be directly measured by x-ray diffraction as the intensity of the corresponding satellite peaks. X-rays are mostly sensitive to the core electrons, and the quantity we observe in our experiment is the elastic component of the CDW (periodic lattice distortion). Static x-ray data are presented in Fig. 3.18(c) and reveal that the CDW has a wavevector normal to the film surface, is pinned by the film surfaces, and is quantized with 8.5 periods in the film, as expected from earlier studies [33, 91, 102], including the work in the previous section.

In the previous section, we measured the satellite peaks and saw constructive interference at low q and destructive interference at high q. It can be readily shown [33] that in the presence of a CDW the positions of the atomic planes r_n normal to the CDW wavevector can be written as

$$r_n = a_0 \cdot n + A\cos(2\delta\, a_0\, n - \phi_0),$$

where n is an integer, A is the CDW amplitude, 2δ is the scattering vector corresponding to the CDW periodicity, a_0 is the lattice parameter, and ϕ_0 is the relative phase of the CDW modulation with respect to the substrate interface. In an x-ray experiment with a momentum transfer q normal to the planes r_n, the scattered intensity can be written as [105]

$$I(q) = I_N\Bigg(|f(q)|^2 + qA\sin(\alpha)\Big[f(q)f(q-2\delta) - f(q)f(q+2\delta)\Big] + \frac{(qA)^2}{4}\Big[f(q-2\delta)^2 + f(q+2\delta)^2\Big]\Bigg), \quad (3.3)$$

where q is the momentum transfer, I_N is a normalization constant, $f(q) = \frac{\sin(qaN)}{sin(qa)}$, N is the number of atomic layers in the film, and $\alpha = N_{\mathrm{CDW}} \cdot \pi - \phi_0$, with N_{CDW} being the number of CDW periods in the film. In our system, ϕ_0~π and we are working at a temperature where $N_{\mathrm{CDW}} = 8.5$. For bulk, only the first and the last terms are typically observed since $f(q)$ is extremely sharp and there is enhance intensity at the satellite peaks. Here, $f(q)$ is relatively broad due to the small thickness of the film, so the last term can be neglected, and the second term, which describes the

interference, dominates. Eq. 3.3 shows that the measured intensity is enhanced or reduced in the presence of the CDW, identically opposite on both satellites $q \pm 2\delta$ around the Bragg peak, and that the amplitude A of the CDW is directly proportional to the intensity of the interference terms, as discussed in the main text.

Thus in this work, we see that the satellite peaks form constructive and destructive x-ray interference with the Laue oscillations, which leads to an increase of the scattered intensity at (0, 0, 2-2δ) or decrease at (0, 0, 2+2δ) [23, 105, 130], where 2δ is the momentum transfer of the CDW. We used short optical laser pulses to excite ultrafast dynamics in the Cr thin film, and the time-dependent CDW amplitude was monitored via ultrafast x-ray diffraction (insets in Fig. 3.18(c)).

The experiment was conducted at the XPP instrument of the x-ray free-electron laser at the Linac Coherent Light Source (LCLS) facility [131, 132] in the stroboscopic mode. The x-ray photon energy was 8.9 keV (0.14 nm), selected by the (111) diffraction of a diamond crystal. X-ray diffraction in the vicinity of the out of plane (002) Bragg peak ($2\theta = 60$ deg) from each 15 fs pulse was recorded by an area detector (CS140k) with a repetition rate of 120 Hz. Due to the mosaic spread of the crystal in the film plane, a number of Laue oscillations are observed on the area detector simultaneously. About 100 pulses were recorded for each time delay (50 fs steps in the time traces). For every time delay separately, the intensity was corrected for dark noise and normalized by the intensity measured in the region of the area detector where Laue oscillations were absent. The sample was excited by 800 nm optical, p-polarized laser pulses of duration 40 fs propagating approximately collinearly with the x-ray pulses. The final temporal resolution was estimated at 80 fs. The spot sizes (full width at half maximum) of the optical and x-ray pulses were 0.46 mm (H) x 0.56 mm (V) and 0.2 mm (H) x 0.2 mm (V), respectively. Measurements were made at an initial sample temperature of 115 K.

The time-dependent x-ray diffraction signal of the CDW satellite peak at $q = 2 - 2\delta$ is shown in Fig. 3.19 and reveals oscillations following photoexcitation (see Supplemental Material

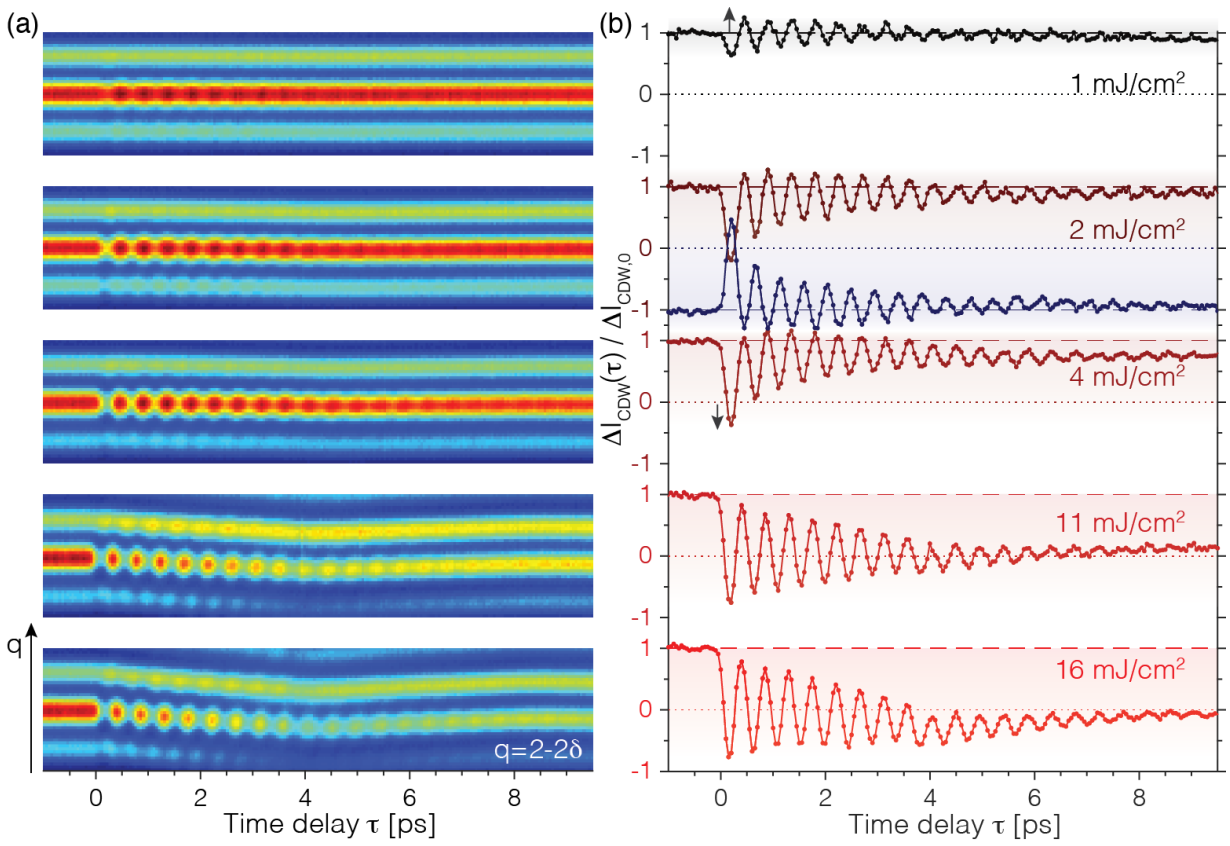

Figure 3.19: Time-resolved x-ray diffraction data of fringe 7 and 8 and the charge density wave (CDW) in a 28 nm Cr film. (a) Time dependence of the intensity in the vicinity of the CDW satellite at $q = 2 - 2\delta$ (see Fig. 3.18) for a series of pump fluences (incident, p polarization). (b) The black and red lines show the normalized transient intensity difference $|I_{\mathrm{CDW}}(\tau) - I_{\mathrm{RT}}|/|I_{\mathrm{CDW},0} - I_{\mathrm{RT}}|$ at $q = 2 - 2\delta$, where I_{CDW} is the data in (a), I_{RT} was measured at room temperature above T_N without CDW, and $I_{\mathrm{CDW},0}$ was measured in the low-temperature ground state. The intensity difference rises above its initial value of one for low fluences and drops below zero as the fluence increases (indicated by arrows). The blue line shows ΔI_{CDW} at $q = 2 + 2\delta$ for a fluence of 2 mJ/cm^2 and starts at -1 due to destructive interference.

of [109] for movies). The remarkable quality of the data allows unambiguous detection of four different time scales. The main oscillation has a period of 453 ± 1 fs and is damped with a time constant of 3.0 ± 0.5 ps so that about 20 oscillations are observed. In Fig. 3.19(b), we see that for low pump fluences the mean of the oscillation increases rapidly in less than 0.5 ps, whereas for higher fluences it remains fixed at zero. The CDW diffraction signal after significant damping of the oscillation (10 ps) decreases with pump fluence and reaches zero at 11 mJ/cm^2. At $q = 2 + 2\delta$, an identically opposite behavior occurs due to destructive interference shown in Fig. 3.19(b) at a

fluence of 2 mJ/cm^2 and in Supplemental Material of [109] for the other fluences. A positional shift of the Laue oscillations is observed for high fluences in Fig. 3.19(a) and shows a period of 8 ps. This shift is initiated by the temperature increase of the lattice and is used to calibrate the film temperature (see Supplemental Material of [109]).

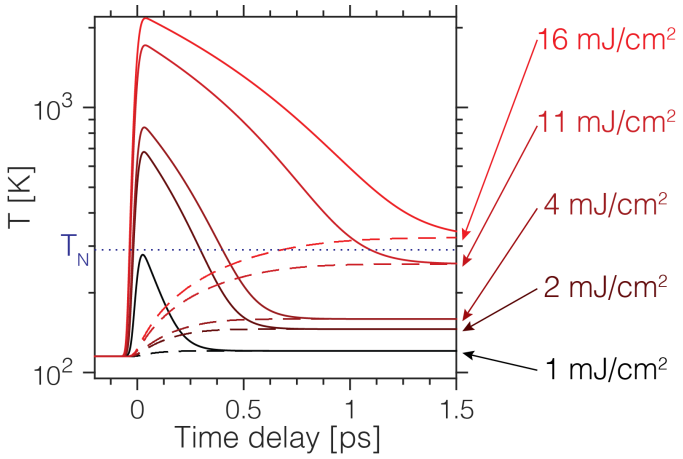

Figure 3.20: Carrier (solid lines) and lattice (dashed lines) temperatures following photoexcitation, calculated within the two-temperature model with parameters identical to [105].

We have simulated the electron T_e and lattice T_l temperatures by solving the coupled differential equations within the two-temperature model [105, 133]:

$$C_e(T_e)\frac{dT_e}{dt} = -G(T_e - T_l) + S(t)$$

$$C_l(T_l)\frac{dT_l}{dt} = G(T_e - T_l),$$

where $G = 4.6 \times 10^{11}$ W/(cm^{3}K) is the electron-phonon coupling constant [134, 135], $C_e = \gamma T_e$ with $\gamma = 211$ J/(m^{3}K) is the electron heat capacity [135], C_l is the lattice heat capacity, which was calculated within the Debye approximation [23], t denotes time, and $S(t)$ is the IR laser excitation, which was simulated as a Gaussian with 40 fs FWHM with a height adjusted to yield the final film temperature. This temperature was calculated by comparing the transient Bragg peak position after 100 ps with the thermal expansion coefficient (measured on the same sample).

The inability of the film to expand laterally was accounted for by correcting the observed lattice expansion in the pump probe experiment by $1+2\nu_P$, where $\nu_P = 0.29$ is the Poisson ratio. At 250 K the CDW with the initial periodicity vanishes for temperatures lower than T_N, and a CDW with a different periodicity emerges. The sample is optically thin and homogeneously heated, thus the heat transport during the calculated time period can be neglected [134].

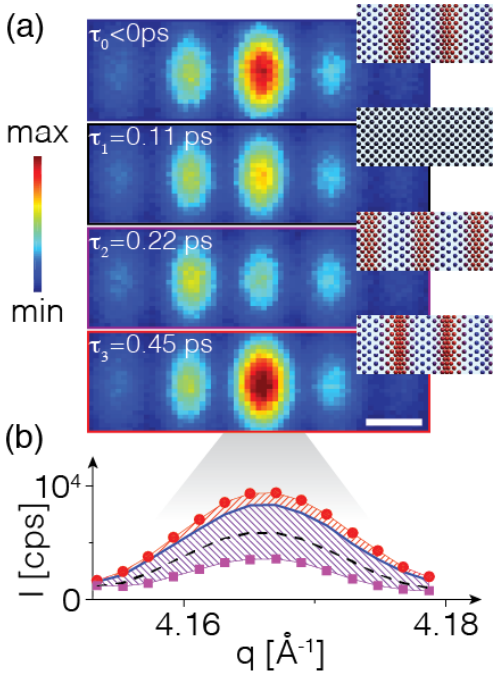

Figure 3.21: Interpretation of the time-resolved x-ray diffraction data around $q = 2-2\delta$ for a 28 nm Cr film. (a) Data and (b) the integral along the vertical direction in photons per second recorded at time delays τ_0 before 0 ps (blue solid line), $\tau_1 = 0.11$ ps (black dashed line, 5 mJ/cm^2), $\tau_2 = 0.22$ ps (magenta squares, 5 mJ/cm^2), and $\tau_3 = 0.45$ ps (red circles, 1 mJ/cm^2). The time delays represent significant instants in the first period of the oscillation in Fig. 3.19. Insets in (a): Schematic representations of the charge density modulation that are consistent with the x-ray data for different time delays. The charge density at τ_1 is similar to the room temperature case, where no charge density wave is present. The scale bar in (a) shows 0.025 Å^{-1}.

It is interesting to look at the physical processes occurring on very short time scales. The x-ray data measured at specific time delays and fluences within the first 0.5 ps are presented in Fig. 3.21, and the respective time-dependent CDW is schematically depicted in the insets in Fig. 3.21(a). In the low-temperature equilibrium state (negative time delay), the x-ray data are consistent with the presence of a static CDW at both interfaces [105]. At a time delay of

0.11 ps after photoexcitation, the dynamic x-ray data are in agreement with static x-ray data recorded above the Néel temperature T_N and show an undistorted lattice with no CDW present. At 0.22 ps, we observed a reversal of the CDW amplitude, as revealed by the change of sign of the interference term in the diffraction signal. The nodes and antinodes of the CDW are at the same location, however, the amplitude is inverted. The most striking observation of our study is the transient enhancement of the CDW amplitude at a time delay of 0.45 ps following moderate laser excitation, seen in Figs. 3.19(b) and 3.21. The transient enhancement is oscillatory and occurs up to a time delay of 4 ps.

The fluence dependence of the pump-probe data reveals that the CDW amplitude is enhanced by about 30% above the maximum value in equilibrium at a fluence of 1 mJ/cm^2, shown in Figs. 3.22(a) and 3.22(c). The experimental observation of the CDW amplitude enhancement was recorded in several independent measurements: the time traces for different fluences (Fig. 3.19), the fluence dependence of the dynamic CDW amplitude (Figs. 3.22(a)-(c)), and in the measurements of both satellite peaks at $q = 2-2\delta$ and $q = 2+2\delta$ (see Supplemental Material of [109]). To exclude the possibility of exciting a broad phonon spectrum [136, 137], we measured the transient signal at multiple q values (see Supplemental Material of [109]). Only at the position of the satellite peak do we see an oscillation of the scattering intensity. This demonstrates that for low fluences no significantly excited lattice vibrations occur, apart from the CDW, and that the enhancement of the CDW amplitude is due to the preexisting CDW in the film.

In order to understand the system response, we fit the transient CDW amplitude $A(\tau)$ to the following equation based on the theory of displacive excitation of coherent phonons [138–140]:

$$A(\tau) = A_F + B\cos\left(2\pi\frac{\tau-\tau_0}{t_P}\right)\cdot\exp\left(-\frac{\tau-\tau_0}{t_D}\right) - C\exp\left(-\frac{\tau-\tau_0}{t_{\text{ep}}}\right), \tag{3.4}$$

where A_F is the final amplitude of the CDW at 10 ps and B is the amplitude, t_P the period, and t_D the damping time of the oscillation. The parameter τ_0 is the offset of the oscillation, $C = A_F - A_1$

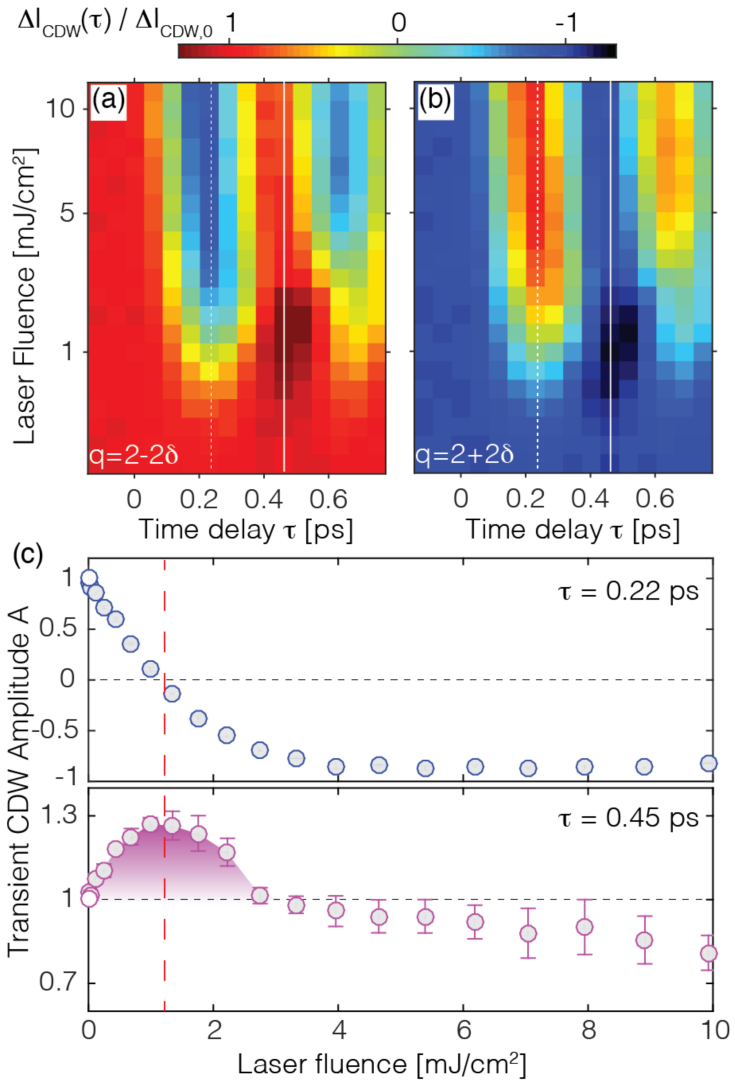

Figure 3.22: Enhancement of the charge density wave (CDW) amplitude in a 28 nm Cr film. (a),(b) The normalized intensity of the CDW satellite peak (see the caption of Fig. 3.19) as a function of the pump fluence and time delay for (a) $q = 2 - 2\delta$ and (b) $q = 2 + 2\delta$. (c) The transient amplitude of the CDW at 0.22 ps (top, first minimum of the oscillation in Fig. 3.19) and 0.45 ps (bottom, first maximum of the oscillation in Fig. 3.19) extracted as line scans along the white lines in (a) and (b).

where A_1 is the quasiequilibrium amplitude after excitation (see Fig. 3.24), and t_{ep} is the decay time for the shift of the quasiequilibrium towards A_F. The last term is indispensable to accurately reproduce the data. The fit results are presented in Fig. 3.23 and Table 3.23.

From the fits of the CDW amplitude, we are able to attribute the enhancement of the

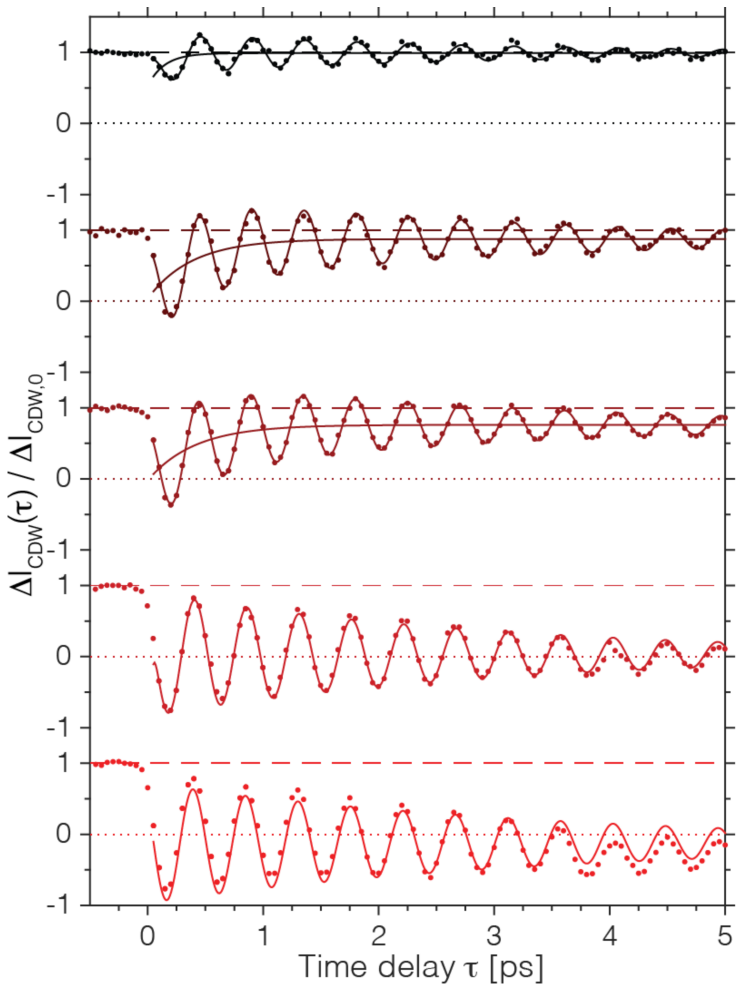

Figure 3.23: Fits of the charge density wave (CDW) amplitude to the data using the model described in Eq. 3.4 for $q = 2 - 2\delta$. Fluences from top to bottom: 1 mJ/cm^2, 2 mJ/cm^2, 4 mJ/cm^2, 11 mJ/cm2 mJ/cm^2, 16 mJ/cm^2. The fitting procedure for the highest fluence (16 mJ/cm^2) was compromised by the coherent phonon at the zone boundary.

CDW amplitude to dynamic electron-phonon interaction and present a model for the underlying physical processes in Fig. 3.24. We start with the low-temperature ground state ($\tau < 0$ ps), where the electronic order and electron-phonon coupling are responsible for the presence of the static CDW [33]. The schematic potential energy surface (blue curve) for the CDW amplitude, A, is centered at $A_0 > 0$, its value in the low-temperature ground state (see also Fig. 3.18(b)).

The photoexcitation creates hot charge carriers with temperatures well above T_N within less than 50 fs [134], the electronic order is partially suppressed, and the electronic and lattice

Table 3.1: Parameters determined from fits of the ultrafast dynamics of the charge density wave (CDW) amplitude following photoexcitation for time delays between 0 and 5 ps to the model described in Eq. 3.4. A_F is the final mean amplitude of the CDW, t_{ep} is the time scale of the shift of the oscillation (solid line in Fig. 3.23), and t_d is the damping time of the oscillation. The last column represents the ratio between the amplitude of the oscillation, B, and the initial suppression of the CDW amplitude $1-A_F+C$. The fitting procedure for the highest fluence (16 mJ/cm^2) was compromised by the coherent phonon at the zone boundary and the parameters are not shown. For a fluence of 11 mJ/cm^2, the system has heated to near T_N and there is no shift of the oscillation back to the initial state within the first few ps, so the fit for t_{ep} is not indicative of the electron-phonon coupling time.

q	Fluence [mJ/cm^2]	Oscillation period [ps]	A_F [arb. units]	t_{ep} [ps]	t_d [ps]	$\frac{B}{1-A_F+C}$
$2-2\delta$	1	0.453 ± 0.002	0.99 ± 0.01	0.14 ± 0.05	2.85 ± 0.5	0.64 ± 0.10
$2+2\delta$	1	0.454 ± 0.002	0.93 ± 0.01	0.23 ± 0.07	2.95 ± 0.4	0.73 ± 0.20
$2-2\delta$	2	0.454 ± 0.001	0.87 ± 0.01	0.38 ± 0.04	3.00 ± 0.2	0.68 ± 0.05
$2+2\delta$	2	0.454 ± 0.001	0.95 ± 0.01	0.34 ± 0.05	2.27 ± 0.2	0.69 ± 0.11
$2-2\delta$	4	0.453 ± 0.001	0.76 ± 0.01	0.41 ± 0.03	2.95 ± 0.2	0.66 ± 0.03
$2+2\delta$	4	0.452 ± 0.001	0.82 ± 0.01	0.48 ± 0.05	2.62 ± 0.2	0.73 ± 0.08
$2-2\delta$	11	0.453 ± 0.001	0.03 ± 0.01	0.02 ± 0.43	3.07 ± 0.3	0.86 ± 1.65
$2+2\delta$	11	0.452 ± 0.001	0.01 ± 0.01	0.05 ± 0.02	2.68 ± 0.1	0.67 ± 0.13

degrees of freedom are partially decoupled, shown at τ~0 ps in Fig. 3.24. The lattice distortion is still frozen; however, the potential energy surface has a new transient minimum at A_1 (red dashed curve) with a smaller or vanishing mean CDW amplitude due to the quenched electronic order. The lattice mode is thus released and starts oscillating. The frequency of this coherent lattice oscillation ($\nu = 2.21$ THz) is in agreement with the frequency of the longitudinal acoustic phonon at the corresponding wavelength measured in bulk chromium [141]. The initial drop of the CDW amplitude after 0.22 ps saturates at a fluence of 4 mJ/cm^2 (Fig. 3.22(c)), and A does not decrease below a value of -0.9. Therefore, the amplitude $A_1 = 0$ in Fig. 3.24 limits the initial displacement of the potential energy surface, indicating that only the preloaded energy due to the frozen phonon is released via quenching of the electronic order.

Surprisingly, for low fluences (smaller than 4 mJ/cm^2), we observe a dramatic deviation from the conventional model for displacive excitation of coherent phonons: here, the minimum

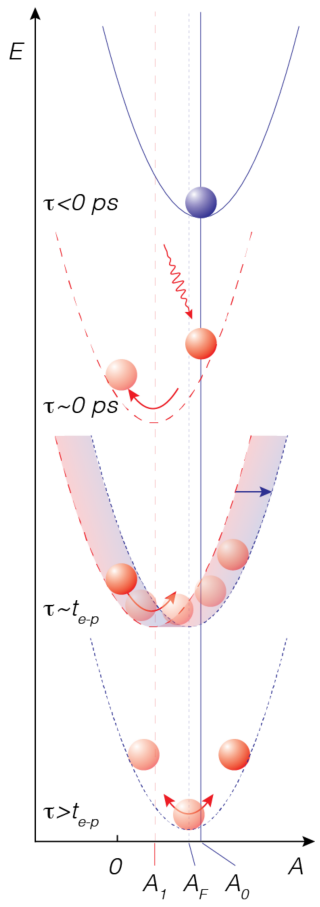

Figure 3.24: A schematic illustration of the mechanism behind the enhancement of the charge density wave (CDW) amplitude due to dynamic electron-phonon interaction. The potential energy surfaces are drawn for the dynamic CDW amplitude, shown on the horizontal axis. A_0 is the amplitude of the CDW in the ground state, A_1 is the quasiequilibrium position after the excitation, and A_F is its position after 10 ps. The transient amplitude $A(\tau)$ was fitted by the following equation $A(\tau) = A_F + B\cos(2\pi\tau'/\tau_P)\exp(-\tau'/\tau_D) - C\exp(-\tau'/t_{ep})$, where B is the amplitude, τ_P the period, τ_D the damping time of the oscillation, $\tau' = \tau - \tau_0$, τ_0 is the offset of the oscillation, $C = A_F - A_1$, and t_{ep} is the decay time for the shift of the quasiequilibrium towards A_F.

of the potential energy surface rapidly shifts back towards the initial ground state A_0, shown for $\tau \sim t_{ep}$ in Fig. 3.24. Note that the potential minimum does not reach its initial value A_0 because of the increase of the film temperature. To reproduce this essential feature of our data, we require superimposed exponential relaxation of the displacive component to the fit in Eq. 3.4. The time constant for this relaxation was determined to be 300 fs, in good agreement with the carrier-lattice

thermalization time measured by optical reflectivity [134]. Therefore, our analysis indicates that while the carriers cool down below T_N, the electronic ordering is reestablished and pulls the quasiequilibrium minimum of the potential energy surface towards higher values. In other words, the electronic and the lattice degrees of freedom recouple in less than 0.5 ps. This ultrafast backshift and the weak damping of the lattice oscillations about the dynamic quasiequilibrium are the essence of the transient enhancement of the CDW amplitude (see Fig. 3.24, $\tau > t_{\mathrm{ep}}$). The enhancement at 0.45 ps is maximized at a fluence of 1.2 mJ/cm^2 (see the vertical dashed line in Fig. 3.22(c)), which is coincident with the zero crossing of the CDW amplitude at 0.22 ps and indicates lattice-assisted recondensation of the electronic ordering.

The relaxation time slightly increases with pump fluence, which is qualitatively supported by calculations within the two-temperature model [133, 134, 142] (see Fig. 3.20); i.e., for increased fluences the carrier temperature stays above T_N longer. At even higher fluences (larger than 11 mJ/cm^2), when the quasiequilibrium temperature after carrier-lattice equilibration approaches or exceeds T_N, no shift of the potential energy surface occurs and the CDW amplitude oscillates around zero, the value it would assume in equilibrium above T_N (Fig. 3.19(b)). Since damping is also remarkably weak in the strong excitation regime, the CDW amplitude oscillations can persist above T_N. It is worth noting that the data measured at 1 mJ/cm^2 in Fig. 3.19(b) could be interpreted in terms of an impulsive excitation of the coherent phonon mode, i.e., excitation without displacement of the potential energy surface, whose characteristic signature is a sine-type oscillatory behavior [143]. The high fluence data (larger than 11 mJ/cm^2), however, clearly show that the coherent phonon is driven by a displacive excitation (cosine-type behavior). The correct interpretation relies on the dynamical picture introduced in Fig. 3.24, and the reforming of the electronic ordering is indispensable in explaining the CDW amplitude enhancement, because the amplitude of the lattice oscillation is always smaller than the initial suppression of the mean value (see Table 3.1).

The damping time constant of the coherent lattice oscillation is about 3 ps and independent

of the fluence. This surprisingly long time scale indicates anharmonic phonon-phonon interaction as the dominant decay channel. Electron-hole pair excitation, which typically leads to strong damping of order-parameter oscillations in strongly correlated electron systems [140, 144, 145], is expected to be ineffective here because of the SDW gap in the electronic spectrum [146]. Because of ultrafast carrier cooling and recondensation in the lattice distortion potential, this gap will quickly reopen, even after a complete quench of the electronic order [127]. Moreover, it is likely to persist above T_N in the form of a pseudogap due to incipient magnetic order [146]. Finally, the period of the lattice oscillation is much shorter than the damping time and also does not depend on fluence (see Table 3.1). Thus, the Cr system studied here essentially represents an effective converter of an electronic excitation into a well-defined, long-lived CDW amplitude oscillation: an oscillation that leads to a significant transient enhancement of the CDW amplitude and that can even persist above the equilibrium transition temperature. We anticipate that other sorts of excitation would lead to a similarly well-defined and persistent oscillation of the CDW amplitude in this system.

In summary, by using the unique capabilities possible with hard x-ray free-electron lasers, we directly observe a dramatic enhancement of the CDW amplitude in Cr following photoexcitation: 30% above its maximum value in equilibrium. We identify the ultrafast underlying physical processes by discerning multiple time scales and explain our results by three main processes, referred to as "dynamic electron-phonon interaction" throughout this work: (i) the photoinduced quench of the electronic order unfreezes a coherent lattice oscillation, (ii) the mean amplitude of this lattice oscillation is increased due to the ultrafast recondensation of the electronic order, and (iii) the reordering of electrons is assisted by the still present lattice distortion. The rapid electronic recondensation is evident from both the ultrafast backshift of the mean of the oscillation and the weak damping of the oscillation due to the reopening of the electronic gap. We demonstrate in [147] that the dynamic electron-phonon interaction can be combined with repeated photoexcitation to extend the coherent lattice oscillation and achieve an even higher enhancement

of the CDW amplitude. Our results also raise fundamental questions regarding the dynamics of the magnetic ordering and the electronic structure of the system. Finally, we anticipate that the enhancement of an order parameter via dynamic interaction of various degrees of freedom is a general phenomenon and can be observed and studied both theoretically and experimentally in a variety of systems.

3.4 Critical Slowing of Spin and Charge Density Wave Ordering Following Photoexcitation

In Section 3.3, we explored the ultrafast dynamics of the periodic lattice distortion and CDW in Cr within 10 ps following photoexcitation at different fluences, resulting in a dynamic coherent phonon. For higher fluences, we saw that once the phonon mode was damped out, the periodic lattice distortion in the system was reduced or disappeared by 10 ps. Here we explore how the periodic lattice distortion and CDW recover at time scales longer than 10 ps. We report on the slowing of the recovery of order when excited from a temperature near a hysteretic transition in thin film Cr. Using time-resolved x-ray diffraction, we track the distortion dynamically following photoexcitation by an optical laser pulse. When the system is initially at a temperature far below this region, the recovery of electronic order occurs on a time scale consistent with thermal recovery for a metallic film, around 20-30 ns. However, when the initial sample temperature approaches the transition region, we observe the recovery proceeding on time scales several orders of magnitude longer, which provides insight into the energy required to reorient the order into the initial ground state from the excited state. We reproduce this energetic behavior using a phenomenological Landau model extended to add boundary conditions necessary to describe the density wave ordering of Cr in confined geometry.

The Cr film that was measured was the same 28 nm film measured in Sections 3.2 and 3.3, which exhibits a half-integer number of CDW and periodic lattice distortion periods N_{CDW}

and pinning at the interfaces such that the N_{CDW} is 8.5 at low temperature and 7.5 between the hysteretic transition region (from about 210 K to 245 K). The previous sections have assumed a Néel temperature around 290 K, however we find evidence of CDW ordering at 300 K and some domains with $N_{CDW} = 6.5$ in this study, indicating a broad Néel transition that is difficult to measure due to the small amplitude of the ordering parameter at these temperatures [105]. Fig. 3.25 shows x-ray diffraction of the (002) Bragg peak and Laue oscillations measured at the APS at three temperatures, 296 K, 240 K, and 142 K, while cooling the film. The CDW satellite peaks are present at 142 K and 240 K and aligned on the 8th and 7th Laue fringes indicating 8.5 and 7.5 periods in the lattice distortion, respectively. At 296 K, there is little contribution from the CDW satellite peak: we primarily measure the Bragg peak and Laue fringes [148].

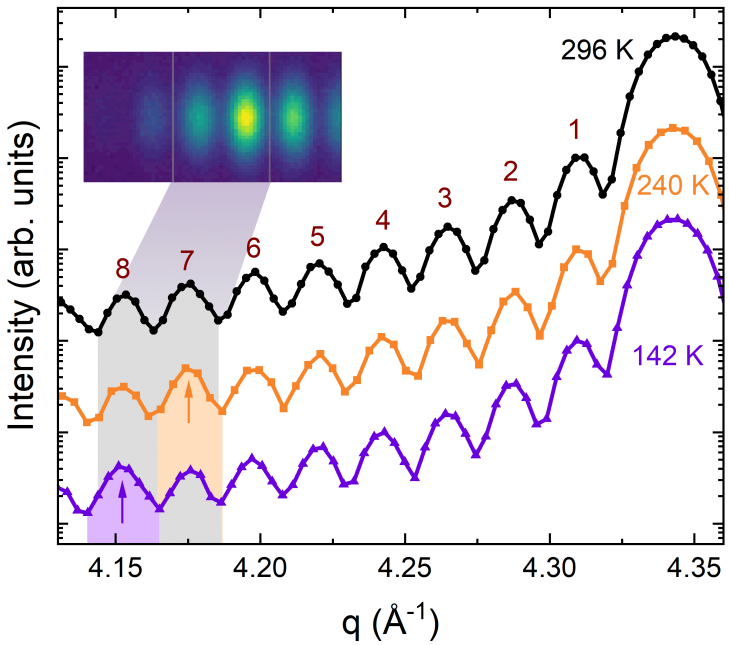

Figure 3.25: X-ray diffraction $\theta - 2\theta$ scans around the (002) Bragg peak of a 28 nm Cr thin film at 296 K (black circles), 240 K (orange squares), and 100 K (purple triangles). The Laue fringes are labeled, and arrows indicate the added intensity where the charge density wave satellite peaks appear on fringe 7 at 240 K and fringe 8 at 142 K. The inset shows a detector image from the experiment at the LCLS, with experimental geometry centered on fringe 7 at a sample temperature of 300 K.

In Fig. 3.8, we present the expected number of CDW and periodic lattice distortion periods in a 28 nm film given the bulk SDW wavevector if the pinning at the interfaces is ignored (green triangles, adapted from [3]) and the observed number of periods in this film between the film interfaces from x-ray diffraction data (see Section 3.2). The observed periodicity is either 7.5 or 8.5 periods, with a hysteretic change between these two states between 210 K and 245 K, indicating a mixed phase with each domain exhibiting one of the two orientations. Given the boundary pinning and quantization of the periodicity, the observed values align well to the expectation from bulk down to about 150 K. Below this, the bulk wavevector plateaus to almost reach 9.25 CDW periods in the film, so we might expect the presence of a lower temperature hysteretic transition between 8.5 and 9.5 CDW periods, mirroring the higher temperature one, but this is not observed. The expectation from bulk raises the possibility of a transition to 6.5 CDW periods (with a satellite peak expected on the 6^{th} Laue fringe), with transition region near 300 K, which is supported in this study, but can only be measured with the very high flux available at a free electron laser facility due to the decreasing amplitude of the satellite peaks as the sample temperature approaches T_N.

This study was conducted at the XPP instrument at the Linac Coherent Light Source (LCLS) x-ray free-electron laser, with 8.9 keV x-ray pulses of duration 15 fs. The sample was excited by 800 nm optical pulses with duration 45 fs and fluences 4.2 mJ/cm^2, 7.4 mJ/cm^2, and 9.2 mJ/cm^2 from initial sample temperatures of 130 K to 300 K. The inset in Fig.3.25 shows a detector image, where the experimental geometry is aligned to the fringe 7 and we are able to see neighboring peaks at lower intensity captured by the Ewald sphere. The time-dependent x-ray diffraction signal of several of the Laue fringes and interfering CDW satellite peaks was measured to a maximum of 400 ns to determine the dynamic charge ordering in the film.

Averaged detector images at times before photoexcitation, 10 ps after photoexcitation, and 400 ns after excitation are shown in Fig. 3.26 at an initial sample temperature 150 K for laser fluence 7.4 mJ/cm^2. The white dotted lines show the fringe 8 peak position. A shift in the Laue

fringes was observed following photoexcitation, consistent with the Bragg peak shift expected from lattice heating. Fig. 3.27 shows the time-resolved shift in the Bragg peak on the detector and the approximate increase in lattice temperature corresponding to that shift for the three laser fluences used in this study: 4.2 mJ/cm^2, 7.4 mJ/cm^2, and 9.2 mJ/cm^2. The maximum change in lattice temperature is an increase at 10 ps of approximately 75 K, 125 K, and 160 K, respectively. The cooling time of the film occurs as expected in a metallic film, fully recovered on the order of tens of ns.

Along with the shift in the fringe position, a change in the intensity of some of the fringes is also observed in Fig. 3.26. This change is dependent on the initial sample temperature and the fluence. Fig. 3.28 shows the fringe amplitudes normalized to their initial intensity before excitation with fluence 7.4 mJ/cm^2 at initial sample temperatures ranging from 130 K to 300 K. Fringe 9 has no satellite peak contribution at any temperature for this sample, and there is expected to be no response in the intensity to photoexcitation. Fig. 3.28(a) shows that there is a small

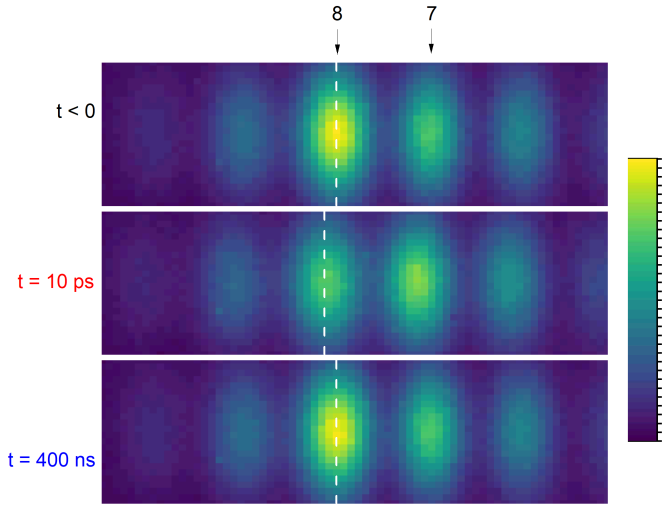

Figure 3.26: Averaged detector images before excitation, 10 ps after excitation, and 400 ns after excitation from an initial sample temperature of 150 K with laser fluence 7.4 mJ/cm^2. The sample and experiment geometry are aligned for diffraction from fringe 8. White dotted lines are shown at the fringe 8 peak position and fringes 7 and 8 are indicated with arrows.

decrease in intensity which recovers on the order of thermal recovery. This is also seen on other fringes, even when no satellite peak contribution is expected and could be attributed to some inhomogeneous structural change such as a gradient in heating that affects the Laue oscillations. There is a satellite peak contribution expected on fringe 8 which should disappear when heated and reappear as the film cools. This is confirmed in Fig. 3.28(b). At an initial sample temperature of 130 K (black data points), there is a dramatic initial drop in intensity at 10 ps when the film is heated to around 255 K followed by a recovery to the initial intensity by about 5 ns. At 150 K (purple data points), the initial satellite peak contribution to this fringe should be comparable to 130 K. The intensity following photoexcitation is similar, but there is a larger initial drop in intensity, reflecting that more loss of the 8.5 CDW orientation in the film and that some domains may have remained magnetized in this state with this fluence at 130 K. The time scales for

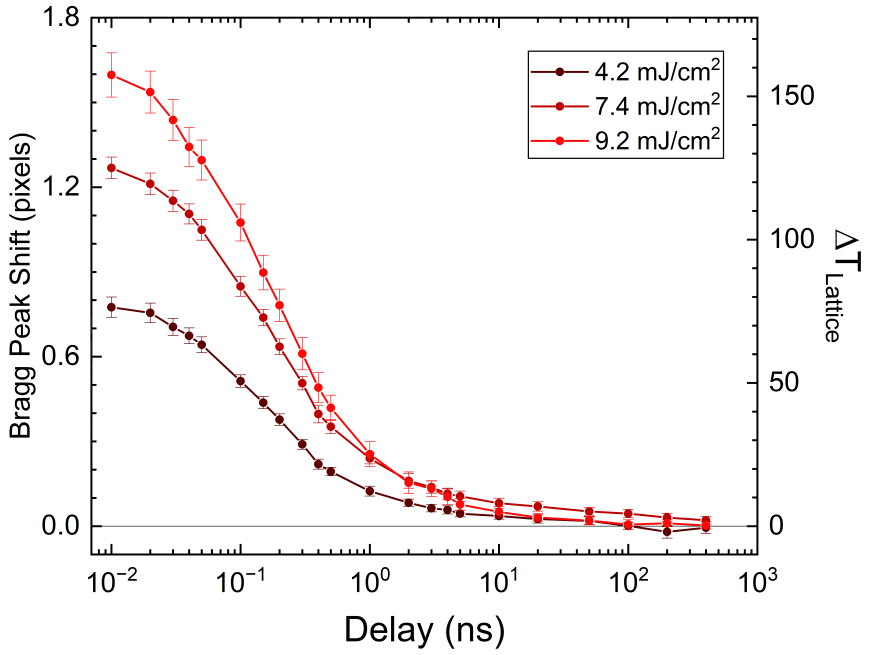

Figure 3.27: Bragg shift in pixels and approximate change in lattice temperature as a function of delay time following photoexcitation at all three fluences used in this study: 4.2 mJ/cm^2, 7.4 mJ/cm^2, and 9.2 mJ/cm^2.

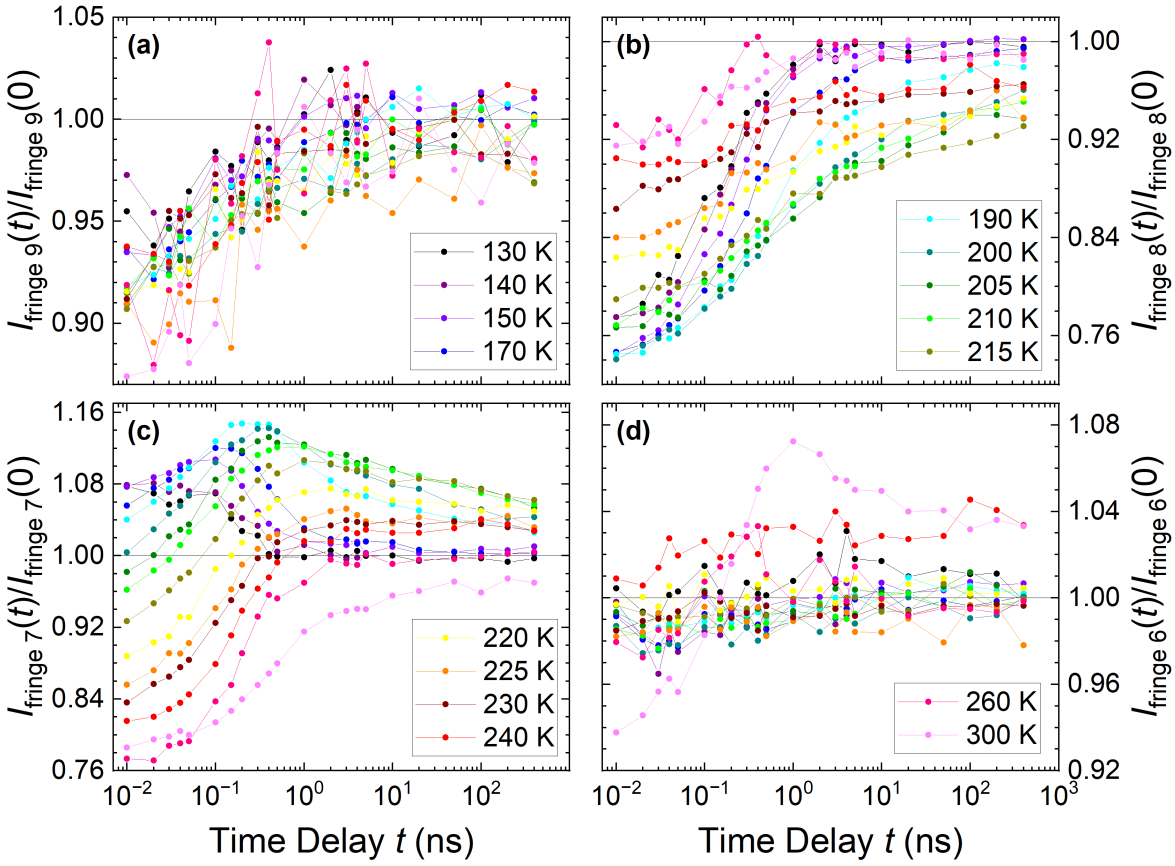

Figure 3.28: Normalized intensities of (a) fringe 9, (b) fringe 8, (c) fringe 7, and (d) fringe 6 following photoexcitation with laser fluence 7.4 mJ/cm^2 from initial temperatures ranging from 130 K to 300 K. Each data set is normalized to the fringe intensity before photoexcitation.

recovery at 150 K appear similar to the recovery at 130 K.

Looking next to the response at 190 K, in light blue, the drop in intensity is comparable to 150 K. Again, the initial satellite peak contribution and drop within 10 ps should be similar, and this indicates that the full satellite peak intensity has been lost for these scans. The recovery from 190 K, however, occurs much slower. By 10 ns, when the intensity at 130 K and 150 K have fully recovered back to the initial value, the total intensity of the 8$^{\text{th}}$ fringe is still depressed by about 4%. At 400 ns, two orders of magnitude longer than the full thermal recovery of the system, the intensity remains depressed by 2%. If we continue to higher temperatures and look at an initial sample temperature of 215 K (gold data points), the initial drop in intensity is less than for the

previously discussed scans. This is because we have entered the hysteretic mixed phase region where domains with 7.5 CDW periods and domains with 8.5 CDW periods coexist, so there is a satellite peak contribution to both fringe 7 and fringe 8, with the intensity of fringe 8 smaller than it would have been at 190 K. The initial drop in intensity is about 21% rather than the almost 26% at 150 K and 190 K. The recovery follows the pattern from lower temperatures, at 10 ns, the intensity is still depressed by over 10% and at 400 ns by 7%. As the initial temperature is increased further, the initial drop in intensity decreases as the satellite peak amplitude on this peak decreases, while the time scale of recovery increases until we reach 260 K, above the hysteretic region where there is no longer any satellite peak contribution to this fringe and we expect no change in intensity. We do observe a decrease in intensity here at both temperatures, but it is comparable to what was seen at all temperatures on fringe 9 and is an experimental artifact due to the peak shifts. So from fringe 8, we see a drop in intensity following photoexcitation consistent with the temperature change of the film and the amplitude of the satellite peak on that fringe at each temperature. However, the recovery of the intensity seems to occur on increasing time scales as the initial temperature increases.

Fig. 3.28(c) shows the normalized intensity of the 7^{th} fringe. At 130 K (black data points), there is an increase in the fringe intensity at 10 ps followed by a recovery back to the initial intensity within 500 ps. At 150 K (purple data points), there is a similar initial increase in the intensity at 10 ps and then a further increase until about 100 ps before the recovery occurs consistent with thermal time scales. At these temperatures, there is initially no satellite peak contribution to this fringe. With the laser pulse, the system has been excited into the higher temperature state where the satellite peak appears on the 7^{th} fringe. When starting at a ground state temperature of 130 K, the system is heated to just above the hysteretic transition and the satellite peak quickly disappears from the 7^{th} fringe back onto the 8^{th} fringe. From 150 K, the system is heated to around 275 K, where the satellite peak should be fully on the 7^{th} fringe. As the system cools, the peak amplitude increases on the 7^{th} fringe, as expected from the measurements

in Section 3.2, before disappearing and appearing on the 8th fringe. The behavior at these temperatures seems consistent with what might be expected from a model based purely on the temperature of the system at each moment in time.

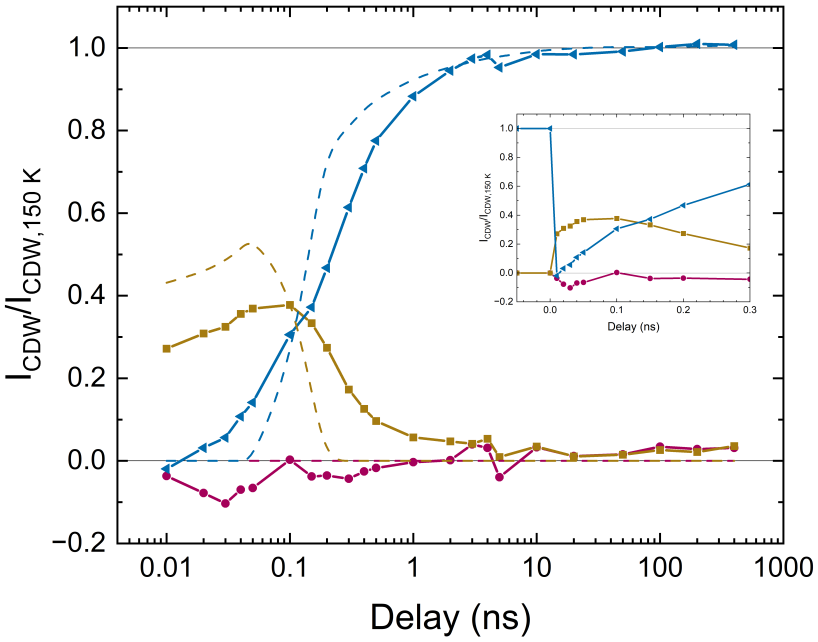

Figure 3.29: Normalized intensity of the charge density wave (CDW) satellite peak on fringe 7 (gold squares) and fringe 8 (blue triangles) following photoexcitation from 150 K with fluence 7.4 mJ/cm^2. The intensities are normalized to the initial charge density wave (CDW) amplitude, which appeared entirely on fringe 8. There was little change in amplitude observed on fringe 6 amplitude (pink circles). Dashed lines indicate the expected CDW amplitude assuming a quasi-static evolution of CDW ordering with the cooling of the lattice. Inset: CDW amplitudes of the three fringes on a linear scale in time for the first 300 ps.

Fig. 3.29 shows the satellite peak amplitude on the 6th (pink circles), 7th (gold squares), and 8th (blue triangles) fringes normalized to the initial amplitude on the 8th fringe, following photoexcitation with a laser fluence of 7.4 mJ/cm^2 from an initial sample temperature of 150 K. Here we assume that any change in intensity is a result of a change in the satellite peak intensity. The inset shows the first 300 ps on a linear scale in time. Initially, there are 8.5 CDW periods between the film interfaces and the full CDW satellite peak appears on the 8th fringe. Within

10 ps, the lattice temperature increases by about 125 K [109, 149] to 275 K, which heats the system to where the satellite peak has completely disappeared from the 8^{th} fringe. Interestingly, we see the satellite peak appear with smaller amplitude within 10 ps on the 7^{th} fringe, consistent with the preferred spin orientation at a temperature of 275 K. From here, the amplitude of the 8^{th} fringe increases and recovers back to its initial configuration by about 20 ns, a time scale that is consistent with the thermal recovery. The amplitude of the 7^{th} fringe initially increases until about 100 ps before decreasing back to its initial amplitude. If we consider that the system has been excited into the state that we would expect to see at a temperature of 275 K, this can be explained by the increase in amplitude of the CDW satellite peak as temperature decreases, as we observed in Section 3.2. At a lattice temperature of 275 K, the CDW peak would be expected to appear entirely on fringe 7, and as the system cools, the CDW peak amplitude will increase on this fringe before switching to fringe 8. We also include the amplitude of fringe 6 in this graph, expected to show no change. There is a small decrease, the artifact due to the shift in the peak, but this is small in comparison to what is observed from the satellite peaks. The dashed lines in Fig. 3.29 show the expected CDW amplitudes on each fringe modeled quasi-statically from the film temperature (which was determined by the Bragg peak shift from Fig. 3.27) and the CDW peak locations and amplitude (see Fig.3.15). The time scales and recovery follow this quasistatic model reasonably well at this temperature.

This quasi-static model breaks down at different ground state temperatures, however. In Fig. 3.28(c), the fringe 7 response at 215 K (gold data points) demonstrates this. There is an initial drop in intensity, indicating that there is an initial the satellite peak contribution that is reduced by the photoexcitation. As the system cools, the satellite peak reappears and is maximized at about 1 ns before beginning to decrease. However the recovery back to the initial intensity proceeds very slowly, with a 6% difference in fringe intensity at 400 ns compared to the intensity before the excitation. This slowing down of the recovery cannot be explained by a model that accounts only for evolution of the satellite peak with lattice temperature.

Moving to the response at higher temperatures, such as at 260 K (magenta data points). Here the fringe 7 response looks similar to the fringe 8 response at lower temperatures. There is an initial drop in intensity consistent with the full satellite peak intensity appearing on this fringe followed by a recovery consistent with thermal time scales. So it appears that above the transition region with the mixed phase, there is no slowing down and the system has reverted to thermal time scales. However, this slowing down begins to appear as we increase temperature again. At 300 K, it is expected that the system is above the Néel temperature and there should be no change in amplitude, however the transition is broad and we previously found evidence that there is a satellite peak contribution at 300 K in this film [150]. We see evidence of that in this work also, with the response shown with light pink data points. There is a significant initial drop in intensity followed by recovery, however once again, we see that the recovery to the initial intensity has not occurred by 400 ns. Fig. 3.28(d) includes the normalized intensity of fringe 6 for all the same initial temperatures. Mostly we see no response in the intensity to photoexcitation, however at 300 K, there is a clear decrease in intensity initially followed by an increase to more than the initial intensity and then a slow recovery, consistent with the slow recovery at 300 K for fringe 7. This suggests that at 300 K, there is some small satellite peak contribution to fringe 6 and following photoexcitation, some of the film orders into the 6.5 CDW orientation while cooling. At the initial temperature 300 K, we are in a hysteretic transition region where the preferred CDW periodicity switches between 7.5 and 6.5 CDWs in the film, and it appears that the recovery of the periodic lattice distortion in the film slows down on approach of these hysteretic transition regions.

Fig. 3.30 shows the normalized intensities for the fringes following a laser pulse with fluence of 4.2 mJ/cm^2, less than measured in Fig. 3.28. Here there is similar behavior, but consistent with a smaller initial increase in temperature from the photoexcitation. For example, for fringe 8 in Fig. 3.30(b), the drop in intensity from 150 K is significantly less than the drop in intensity from 170 K. At this fluence, the change in lattice temperature is about 75 K, so a pump

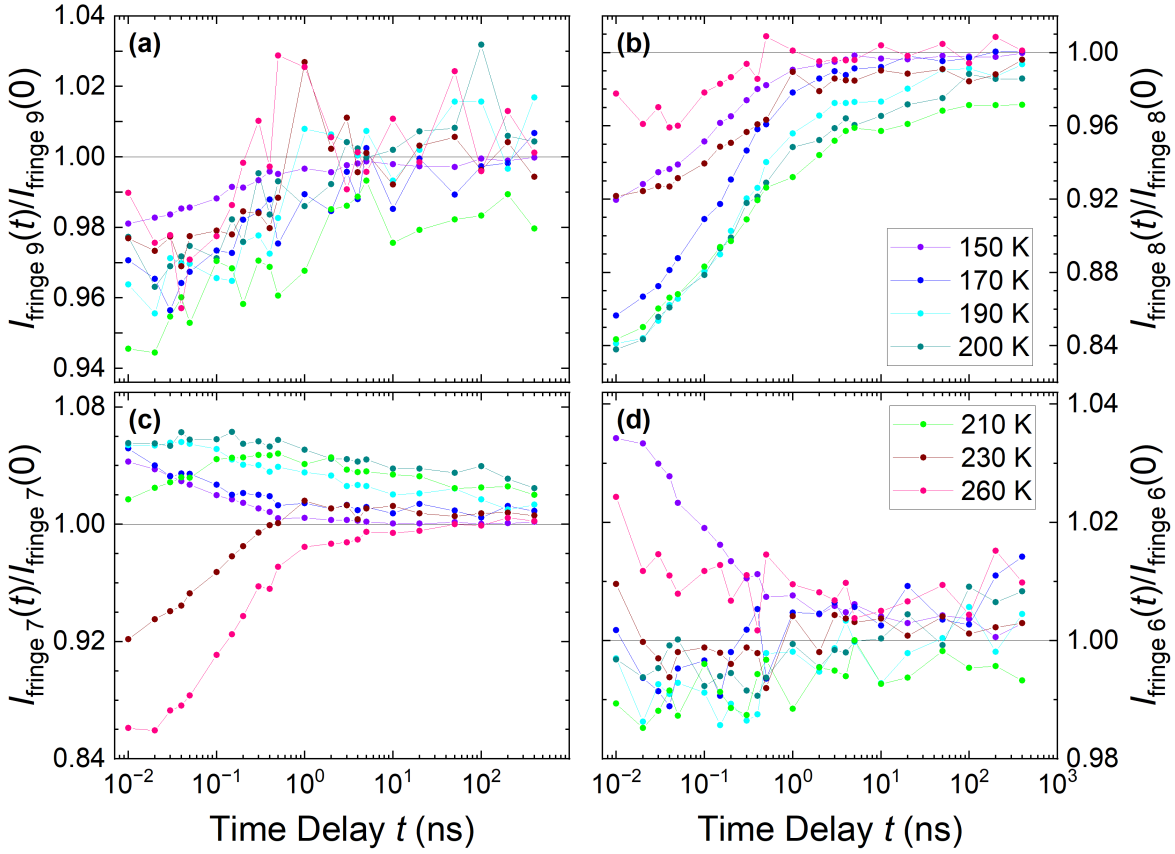

Figure 3.30: Normalized intensities of (a) fringe 9, (b) fringe 8, (c) fringe 7, and (d) fringe 6 following photoexcitation with laser fluence 4.2 mJ/cm^2 from initial temperatures ranging from 150 K to 260 K. Each data set is normalized to the fringe intensity before photoexcitation.

from 150 K will heat the lattice to about 225 K whereas a pump from 170 K will heat it to about 245 K. In the quasi-static model, there is a considerable difference. At 225 K, the satellite peak amplitude is still mostly on fringe 8 while at 245 K, the satellite peak is mostly on fringe 7. So the overall change in fringe intensity will be much greater from an initial sample temperature of 170 K than it will for an initial sample temperature of 150 K. It can also be seen in the fringe 8 data in Fig. 3.30(b) and fringe 7 data 3.30(c) that the time scales for recovery are comparable to the time scales for those temperatures in Fig. 3.28, meaning that as the initial sample temperature increases towards the hysteretic region, the recovery slows down considerably.

Fig. 3.31 shows the normalized intensities for the fringes at the higher laser fluence of

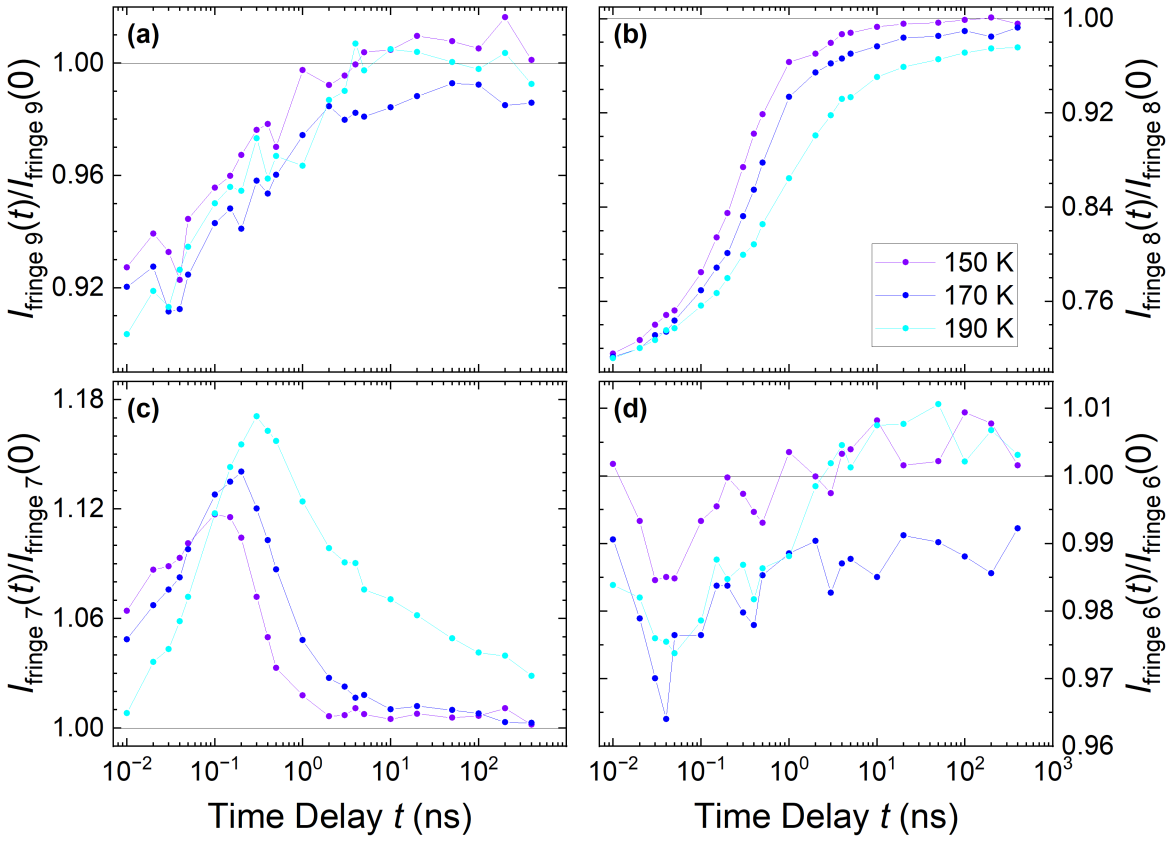

Figure 3.31: Normalized intensities of (a) fringe 9, (b) fringe 8, (c) fringe 7, and (d) fringe 6 following photoexcitation with laser fluence 9.2 mJ/cm^2 from initial temperatures of 150 K, 170 K, and 190 K. Each data set is normalized to the fringe intensity before photoexcitation.

9.2 mJ/cm^2 for three initial sample temperatures: 150 K, 170 K, and 190 K. For fringe 8 in Fig. 3.31(b), the drop in intensity is the same for all three initial temperatures, which is consistent since the initial peak amplitude should be nearly identical and the heating by about 160 K will move the system into the higher temperature state where there should be no satellite peak on this fringe. But we again see clearly for both fringe 8 in Fig. 3.31(b) and fringe 7 in Fig. 3.31(c) that the time scales for recovery lengthen as the temperature increases.

The fringe intensities in Figs. 3.28, 3.30, and 3.31 seem to indicate that the system evolution following photoexcitation is consistent with a quasi-static thermal model of recovery and an increase in length scales as temperature is increased to approach the hysteretic regions

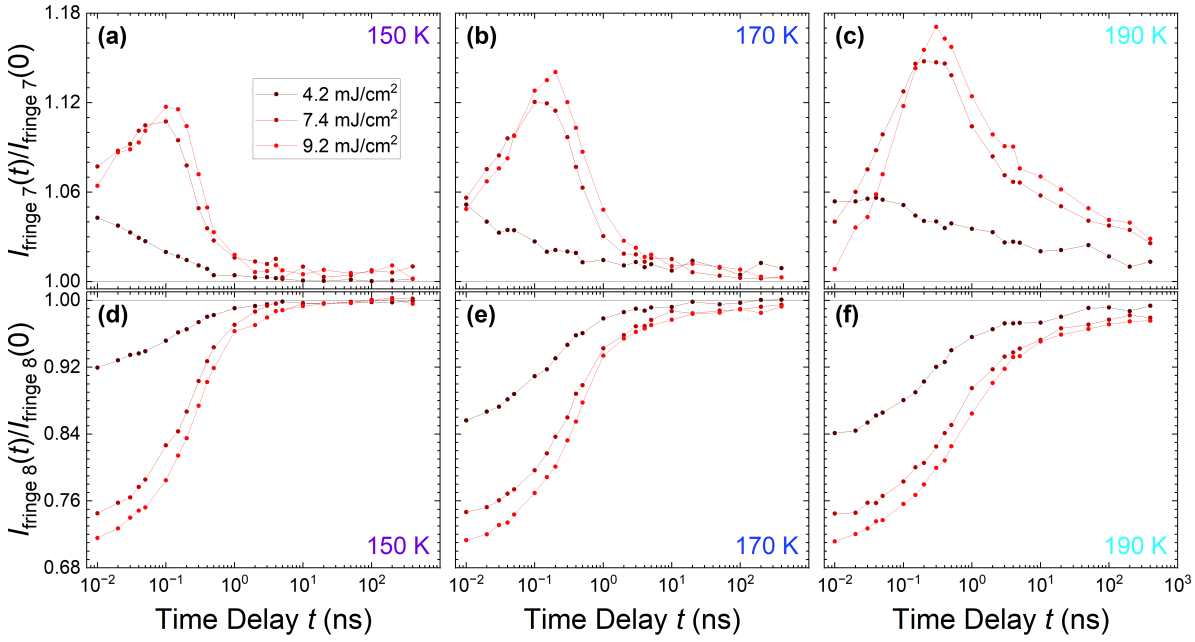

Figure 3.32: Normalized intensities of (a),(b),(c) fringe 7 and (d),(e),(f) fringe 8 following photoexcitation from (a),(d) 150 K, (b),(e) 170 K, and (c),(f) 190 K for three different fluences: 4.2 mJ/cm^2, 7.4 mJ/cm^2, and 9.2 mJ/cm^2.

of spin, charge, and lattice reorientation. Fig 3.32 reproduces some of the data to compare the response to the three laser fluences for fringe 7 (top) and fringe 8 (bottom) at 150 K (left), 170 K (middle), and 190 K (right). In each case, the initial system response is consistent with the expected temperature increases of 75 K, 125 K, and 160 K for 4.2 mJ/cm^2, 7.4 mJ/cm^2, and 9.2 mJ/cm^2, respectively. We can also see the slowing of the recovery as the initial temperature increases. At 150 K, full recovery occurs in 1-10 ns for all fluences. At 170 K, recovery is closer to 100 ns. At 190 K, the recovery for all fluences has not occurred by 400 ns.

The recovery of order in the system can be described with a double exponential decay with two time scales, t_{fast} and t_{slow}:

$$I(t) \sim A_1 e^{-\frac{t}{t_{\text{fast}}}} + A_2 e^{-\frac{t}{t_{\text{slow}}}} + C. \tag{3.5}$$

Example fits are shown in Fig. 3.33 for a pump fluence of 7.4 mJ/cm^2. At lower temperatures,

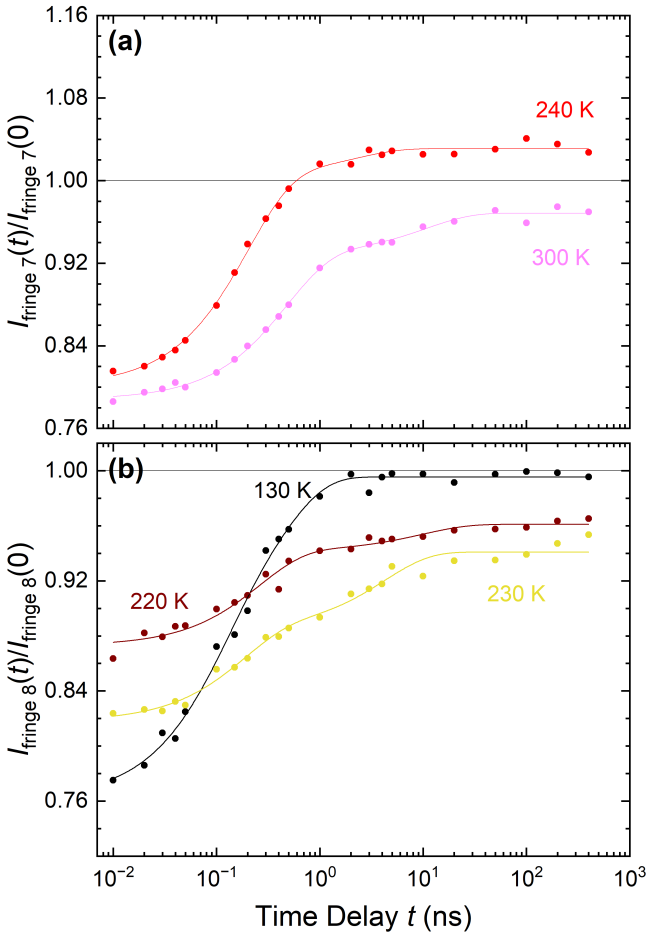

Figure 3.33: Examples of double exponential fits (solid lines) of the fringe recovery to Eq. 3.5 for (a) fringe 7 data at 240 K and 300 K and (b) fringe 8 data at 130 K, 220 K, and 230 K when photoexcited with a pump fluence of 7.4 mJ/cm^2.

130 K, 220 K, and 230 K, the fringe 8 intensities were fit, giving time scales for the reorientation of the system from 7.5 CDW periods to 8.5 CDW periods. At 240 K and 300 K, the fringe 7 intensities were fit, giving time scales for the reorientation of the system from 6.5 CDW periods to 7.5 CDW periods. The two time scales for recovery become clear at temperatures approaching the hysteretic region. The constant C here deviates from 1, especially within the hysteretic region. This reflects a metastable state reached in the recovery due to the hysteretic nature, that the recovery occurs to a different state while cooling from the initial state of the film that was

reached while warming from 130 K. We see good agreement of the fits to the observed data at low temperatures, however within the transition region, the fit suffers from a lack of data at delays greater than 400 ns, which is reflected in the large error bars and noisiness of t_{slow}.

Table 3.2: Parameters determined from fits of the recovery of the charge density wave amplitude following photoexcitation to Eq. 3.5. The initial sample temperature is T. Fitted fringe refers to which fringe amplitudes that was used for the fit. These amplitudes were the fringe intensities as a function of delay time normalized to their initial intensity prior to photoexcitation. E_b is the energy barrier calculated from t_{slow} assuming an attempt time of $\tau_0 = 250$ ps (see text for details).

T [K]	Fitted Fringe	Fluence [mJ/cm^2]	t_{fast} [ns]	t_{slow} [ns]	C	E_b [meV]
130	8	7.4	0.10 ± 0.04	0.43 ± 0.17	0.996 ± 0.002	6 ± 5
140	8	7.4	0.17 ± 0.04	0.76 ± 0.66	0.992 ± 0.004	14 ± 11
150	8	4.2	0.11 ± 0.02	0.80 ± 0.21	0.997 ± 0.001	15 ± 4
150	8	7.4	0.23 ± 0.02	1.8 ± 0.6	0.999 ± 0.002	25 ± 5
150	8	9.2	0.29 ± 0.01	3.7 ± 0.8	0.998 ± 0.001	35 ± 3
170	8	4.2	0.17 ± 0.02	2.2 ± 0.6	0.997 ± 0.001	32 ± 4
170	8	7.4	0.33 ± 0.02	3.8 ± 0.7	0.990 ± 0.001	40 ± 3
170	8	9.2	0.43 ± 0.02	7.4 ± 2.2	0.988 ± 0.002	50 ± 5
190	8	4.2	0.31 ± 0.02	17.1 ± 6.7	0.991 ± 0.002	69 ± 7
190	8	7.4	0.48 ± 0.04	9.0 ± 2.0	0.977 ± 0.002	59 ± 4
190	8	9.2	0.58 ± 0.06	10.5 ± 2.7	0.979 ± 0.003	61 ± 5
200	8	4.2	0.28 ± 0.03	22.8 ± 9.3	0.985 ± 0.003	78 ± 8
200	8	7.4	0.41 ± 0.05	9.5 ± 2.2	0.948 ± 0.003	63 ± 5
205	8	7.4	0.44 ± 0.06	16.0 ± 5.0	0.937 ± 0.004	73 ± 6
210	8	4.2	0.15 ± 0.03	2.7 ± 0.5	0.967 ± 0.002	43 ± 4
210	8	7.4	0.38 ± 0.04	18.3 ± 4.4	0.945 ± 0.003	78 ± 5
215	8	7.4	0.37 ± 0.04	20.5 ± 6.4	0.923 ± 0.003	82 ± 7
220	8	7.4	0.18 ± 0.05	4.2 ± 1.2	0.941 ± 0.003	54 ± 6
225	8	7.4	0.32 ± 0.06	58.0 ± 54.8	0.948 ± 0.007	106 ± 19
230	8	4.2	0.34 ± 0.06	7.2 ± 11.6	0.990 ± 0.002	67 ± 32
230	8	7.4	0.26 ± 0.05	9.7 ± 7.2	0.961 ± 0.003	73 ± 15
240	7	7.4	0.20 ± 0.02	2.1 ± 1.1	1.031 ± 0.002	44 ± 11
260	7	4.2	0.17 ± 0.02	4.1 ± 1.6	1.000 ± 0.002	63 ± 9
260	7	7.4	0.21 ± 0.03	2.2 ± 1.9	0.998 ± 0.003	48 ± 20
300	7	7.4	0.47 ± 0.03	10.6 ± 2.9	0.969 ± 0.002	8 ± 97

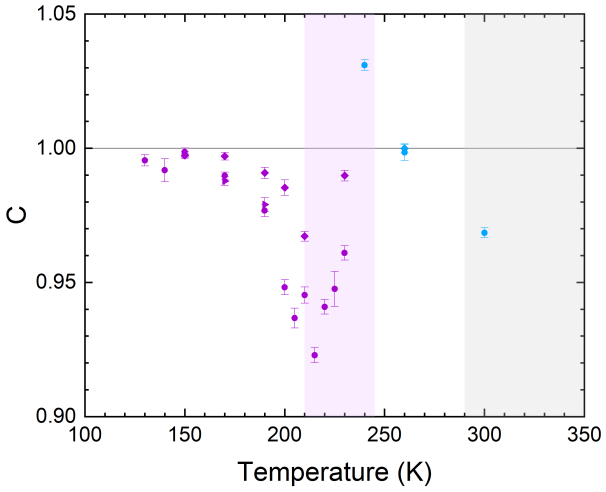

Figure 3.34: Constants C from the fits of the recovery of charge density wave (CDW) order to Eq. 3.5. Purple data points from fits to fringe 8 data and blue data points from fits to fringe 7 data. Constants found from data at 4.2 mJ/cm^2 (diamonds), 7.4 mJ/cm^2 (circles), and 9.2 mJ/cm^2 (triangles) are included. The purple shaded region indicates the hysteretic region of reorientation between $N_{\mathrm{CDW}} = 7.5$ and $N_{\mathrm{CDW}} = 8.5$. The gray shaded region begins at 290 K, which appears to be around the start of another hysteretic region and is near the Néel temperature.

The fitting parameters for all data sets are included in Table 3.2. The fitted data sets were the normalized fringe 8 intensities for initial sample temperatures of 130 K to 230 K and the normalized fringe 7 intensities for initial sample temperatures of 240 K to 300 K at all three fluences. The faster time scale t_{fast} ranges from 100 ps to 600 ps, consistent with the time scale for thermal recovery of a metallic film. The slower time scale t_{slow} ranges from 430 ps to nearly 60 ns. It is important to note that the uncertainty of the fits for t_{fast} within the hysteretic region, with error bars on the order of the fitting parameter. In this region, the simple model of two exponential decays may not fully account for the change in CDW amplitude with temperature or, more likely, the maximum achievable delay time of 400 ns was not sufficient to get a full picture of how the recovery proceeds.

The constants C are plotted in Fig. 3.34, which shows the deviation of the recovered mixed state from the initial state within the hysteretic regions. The time constants t_{fast} and t_{slow} are shown in Fig. 3.35(a). In these figures, the purple data points indicate parameters from fits

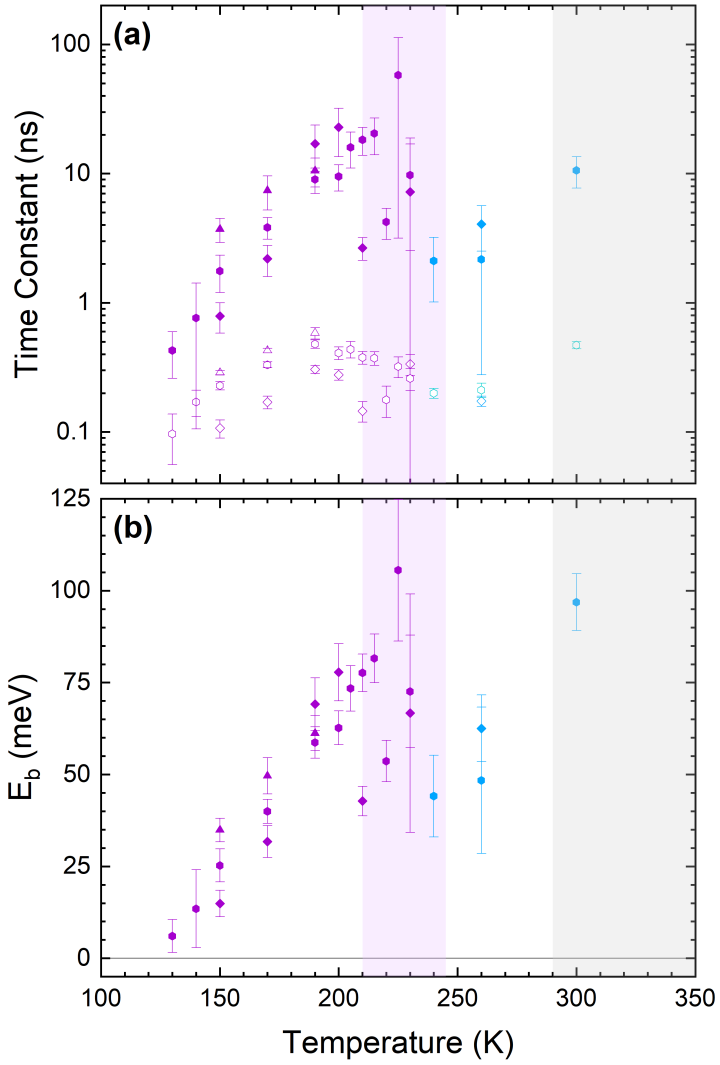

Figure 3.35: (a) Time constants on a log scale from the double exponential fits of the recovery of charge density wave (CDW) order to Eq. 3.5. Solid data points indicate τ_{slow} and open data points indicate τ_{fast}. Fits were made to the CDW amplitude on fringe 8 below the transition (purple data points) and fringe 7 above the transition (blue data points). (b) Energy barriers for the transitions from $N_{CDW} = 7.5$ to $N_{CDW} = 8.5$ (purple data points) and from $N_{CDW} = 6.5$ to $N_{CDW} = 7.5$ (blue data points) calculated from Eq. 3.6. Constants and barriers found from data at 4.2 mJ/cm^2 (diamonds), 7.4 mJ/cm^2 (circles), and 9.2 mJ/cm^2 (triangles) are included. The purple shaded region indicates the hysteretic region of reorientation between $N_{CDW} = 7.5$ and $N_{CDW} = 8.5$. The gray shaded region begins at 290 K, which appears to be around the start of another hysteretic region and is near the Néel temperature.

of fringe 8, indicating the process of reorientation from $N_{\mathrm{CDW}} = 7.5$ to $N_{\mathrm{CDW}} = 8.5$. The blue data points indicate parameters from fits of fringe 7, indicating the process of reorientation from $N_{\mathrm{CDW}} = 6.5$ to $N_{\mathrm{CDW}} = 7.5$. All three fluences are included, with diamonds for 4.2 mJ/cm^2, circles for 7.4 mJ/cm^2, and triangles for 9.2 mJ/cm^2. The time constant t_{slow} is shown with closed data points and t_{fast} with open data points in Fig. 3.35(a). For the measured temperatures, there is no obvious difference in the recovery times at a single temperature with different fluences. However, it does seem clear that there are two distinct time regimes: t_{fast}, which is a thermal recovery process and does not have a clear temperature dependence, and t_{slow}, which increases exponentially with temperature when approaching the transition region, by over two orders of magnitude. This is most clear for the 7.5 to 8.5 period reorientation, but also holds for the limited data available for the 6.5 to 7.5 period reorientation.

The slowing of the recovery can be explained by considering the confined geometry of a Cr thin film. In bulk, the SDW wavevector varies continuously with temperature so the recovery would more closely follow the thermal evolution. In films, however, the pinning of the interfaces and the discretized nature of the spin and charge order and of the lattice distortion results in potential minima at the wavevectors corresponding to half-integer numbers of CDW periods in the film. The recovery can then be thought of in a classical Arrhenius model as the activation energy required to reconfigure each domain back to its initial state. This energy barrier can be calculated from

$$\ln \frac{t_{\mathrm{slow}}}{\tau_0} = \frac{E_b}{k_B T}, \tag{3.6}$$

where τ_0 is the attempt time, k_B is the Boltzmann constant, and E_b is the energy barrier for the reorientation. The energy barriers were calculated from t_{slow} and are listed in Table 3.2. The attempt time for magnetic systems varies widely from 10^{-11} to 10^{-8} s [151] and is unknown for this system, so we take $\tau_0 = 250$ ps here. Fig. 3.35(b) shows the energy barrier as a function of initial sample temperature, with the energy barrier from the 7.5 to 8.5 CDW period reorientation in purple and from the 6.5 to 7.5 CDW period reorientation in blue. The energy barrier for the

lower temperature transition appears to depend linearly with temperature and go to zero at about 120 K. The higher temperature transition shows similar behavior, with the possibility that that barrier also extrapolates to zero near 200 K.

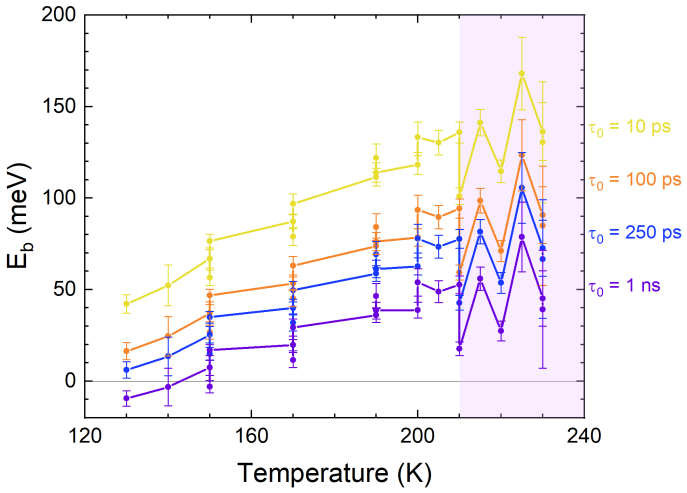

Figure 3.36: Energy barrier for the transition from $N_{CDW} = 7.5$ to $N_{CDW} = 8.5$ calculated from t_{slow} with attempt times τ_0 of 10 ps, 100 ps, 250 ps, and 1 ns for the measurements made with laser fluence 7.4 mJ/cm^2.

In Fig. 3.36, the calculated energy barrier is shown for the 7.5 to 8.5 CDW period reorientation for fluence 7.4 mJ/cm^2 for attempt times of 10 ps, 100 ps, 250 ps, and 1 ns. There is a small change in the temperature dependence associated with changing the attempt time, but the biggest difference we see in this range is a shift that changes the temperature at which the energy barrier goes to zero. For an attempt time of $\tau_0 = 1$ ns, a linear fit to the data shows the energy barrier goes to zero at about 135 K. For $\tau_0 = 250$ ps, the energy barrier would go to zero at 120 K, for $\tau_0 = 100$ ps at 100 K, and for $\tau_0 = 10$ ps at 80 K. We are unable to experimentally determine where the barrier goes to zero in this experiment because we cannot resolve a time constant smaller than the thermal time constant for recovery.

Phenomenological mean-field theory has been used to describe CDW and SDW systems. Landau theory was extended by McMillan to describe CDWs [152] and has been adapted for

bulk and thin film Cr in [149, 153, 154], The free energy density of the density wave system as a function of depth in the film x from these previous treatments is

$$F(x) = a_1\psi^2 + a_2\psi^4 + a_3\xi|\nabla\psi|^2 + a_4\psi^2|\nabla\phi - q_0|^2 + a_5\psi^4\cos(2\phi), \tag{3.7}$$

where $\psi e^{i\phi}$ is the SDW order parameter with amplitude ψ and phase $\phi = qx$, q_0 is the natural nesting wave vector in the band structure and assumed to be temperature-independent in this treatment, and a_1, a_2, a_3, a_4, a_5 are coefficients for each term. The first two terms in Eq. 3.7 follow from the Landau form for expansion of the free energy. The third term adds energy with spatial variation of the order parameter, which we assume to be zero here. The fourth term accounts for the energy cost to changing the SDW wavevector from the nesting wavevector q_0, which is determined from the Cr band structure and is temperature-independent. The fifth term reflects the SDW-lattice coupling, favoring a commensurate SDW and CDW. The free energy is found by integrating Eq. 3.7 over the film thickness L:

$$F(q) = L\left(a_1\psi^2 + a_2\psi^4 + a_3\xi|\nabla\psi|^2 + a_4\psi^2|q - q_0|^2\right) + a_5\psi^4\frac{\sin(2Lq)}{2q}. \tag{3.8}$$

The q-dependence in Eq. 3.8 lies in the fourth and fifth terms, which have a different temperature dependence (coming from the ψ^2 vs ψ^4). We can model this and minimize the energy get a temperature dependence of the SDW wavevector as a function of temperature, shown by the blue line in Fig. 3.37 with the measured bulk SDW wavevector from [33] is shown with the green data points. In this model, the temperature dependence of the wavevector is determined by the competition of the two terms, which reproduces the observed temperature dependence of the bulk SDW wavevector fairly well. There is an alternative explanation for the temperature dependence in which the temperature dependence of the natural wavevector q_0 arises from the thermal expansion of the lattice, but experiments and calculations of the expected wavevector from solely thermal expansion contradict this theory [153, 155].

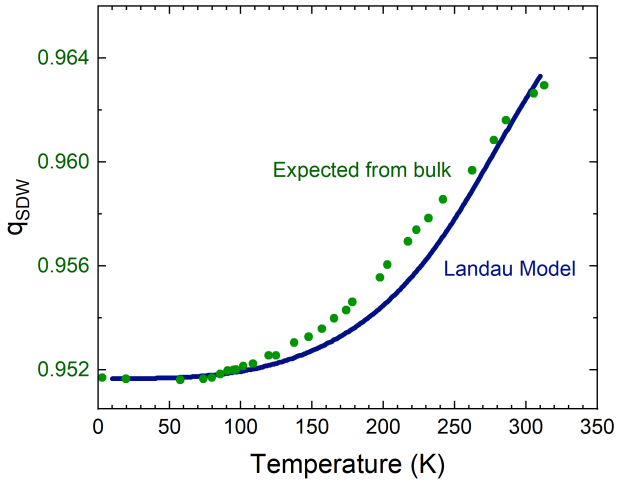

Figure 3.37: Temperature dependence of the Cr spin density wave wavevector predicted by the phenomenological Landau free energy model (blue line) and the observed bulk wavevector (green data points). Bulk data reproduced with permission from [33]. Copyright 1988 by the American Physical Society.

The free energy of Eq. 3.8 does not describe the strong boundary pinning and quantization of the wavevector that we see in thin films. To describe this behavior, we impose a constant phase at each interface, giving a phase φ_0 which is independent of temperature (and which we measured for this film, shown in Fig. 3.15). This condition is met when $\varphi_0 = Q_j L$ where Q_j are the allowed wavevectors corresponding to $N_{\mathrm{CDW}} = j$. The sixth term in the energy, then, adds a potential well $G(q)$ at each Q_j:

$$F_{\mathrm{pin}}(q) = a_6 G\left(1 - \frac{Q_j}{q}\right). \tag{3.9}$$

The origins of the boundary pinning are not well understood but we assume no T (or Ψ) dependence in the strength of the wells because the pinning remains strong as we approach T_N. The total free energy, then, can be expressed as the sum of Eq. 3.8 and Eq. 3.9:

$$F(q) = L\left(a_1\psi^2 + a_2\psi^4 + a_3\xi|\nabla\psi|^2 + a_4\psi^2|q-q_0|^2\right) + a_5\psi^4\frac{\sin(2Lq)}{2q} + a_6 G\left(1 - \frac{Q_j}{q}\right). \tag{3.10}$$

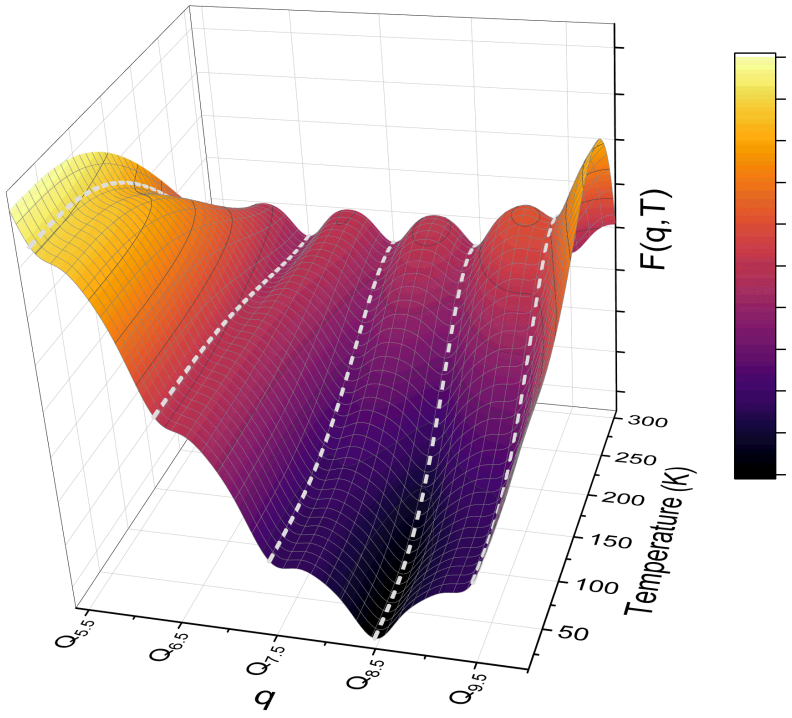

Figure 3.38: Landau free-energy surface modeled for a Cr film with an added boundary pinning term. Dashed lines show the potential for the wavevectors corresponding to 9.5, 8.5, 7.5, 6.5, and 5.5 charge density wave periods in the film. Note that terms with temperature dependence but no q-dependence have been omitted here.

Fig. 3.38 shows the resulting free-energy surface as a function of wavevector q and film temperature T, with dashed lines along the potentials at Q_j. The first two terms have no q dependence and have been neglected in this surface: they do have a temperature dependence, but that will not impact the magnitude of the energy barrier at a constant temperature or the location of the energy minimum in q at each temperature. The Néel temperature used in this model to find the amplitude of the ordering parameter ψ was the bulk value of 311 K, used because we continue to see evidence of low amplitude ordering at 300 K and have not precisely measured T_N for the film. There are local minima at $q = Q_j$ reflecting the strong pinning and quantization and the energy barriers between them reflect the ease of switching between spin and charge orientations.

The modeled SDW wavevector for the film, found from the Landau model as the wavevector at which the energy is a minimum, is shown in Fig. 3.39. This correctly reproduces what

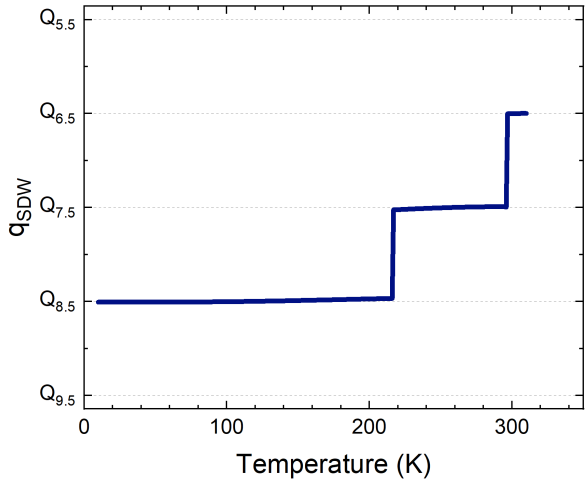

Figure 3.39: Temperature dependence of the spin density wave wavevector for the Cr film found from the minimum energy in the Landau free energy model with the added boundary pinning term.

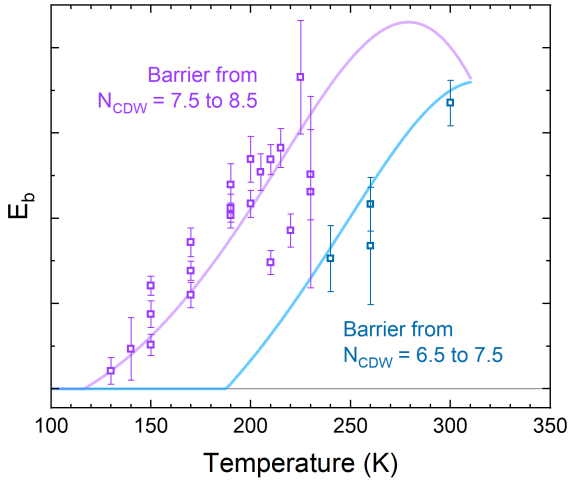

Figure 3.40: Energy barrier for the transitions between quantized spin density wave wavevectors from the Landau free energy model (solid lines) and shown with the data from Fig. 3.35(b) (data points). The transition from $N_{\mathrm{CDW}} = 7.5$ to $N_{\mathrm{CDW}} = 8.5$ is shown in purple and the transition from $N_{\mathrm{CDW}} = 6.5$ to $N_{\mathrm{CDW}} = 7.5$ is shown in blue.

we observe, with a $N_{\mathrm{CDW}} = 8.5$ ground state at low temperature, a transition to a $N_{\mathrm{CDW}} = 7.5$ ground state at about 220 K, and a transition to a $N_{\mathrm{CDW}} = 6.5$ around room temperature. The

temperature-dependence of the energy barriers for the transition from $N_{CDW} = 7.5$ to $N_{CDW} = 8.5$ and for the transition from $N_{CDW} = 6.5$ to $N_{CDW} = 7.5$ are shown in Fig. 3.40 in purple and blue, respectively. The modeled barriers (solid lines) reproduce the temperature dependence of the data (open squares), including the estimation of where the barrier extrapolates to zero.

Thus, we have measured the energy barrier for different SDW and CDW configurations in confined geometry through time-resolved x-ray diffraction. We measure the evolution of the periodic lattice distortion following photoexcitation from different temperatures, which can be described by two time scales, t_{fast} and t_{slow}. The first, t_{fast}, is on the order of 100 ps and consistent with the thermal evolution of the system when heated by the laser pulse and should be independent of the ground state temperature. The second, t_{slow}, shows a dramatic temperature dependence, demonstrating the slowing of the recovery of periodicity in the film by two orders of magnitude in the available temperature range. This is a reflection of an increasing activation energy required to achieve the spin, charge, and lattice reorientation in the film. This allows us to access the energy of the system through the time domain. We have been able to extend existing phenomenological Landau models for Cr with a term that reflects the strong pinning of the density waves and lattice distortion at the interfaces and creates a quantization of the allowable SDW wavevector in films. This model accurately reproduces the observed wavevector and temperature dependence of the energy barriers.

3.5 Conclusion

In this chapter, we have explored the magnetic and charge ordering and lattice distortion in a 28 nm Cr film through x-ray diffraction measurements of the satellite peak near the (002) Bragg peak. This requires the x-ray intensities available at synchrotron and free electron laser facilities like the APS and the LCLS. In Section 3.2, we characterized the CDW statically at different temperatures, giving insight into the boundary pinning and SDW and CDW amplitude

and wavevector as a function of temperature. In Section 3.3, we conducted an ultrafast time-resolved experiment to see the dynamics of the order in the first 10 ps following photoexcitation, demonstrating how the static periodic lattice distortion becomes a dynamic coherent phonon that is damped out by about 8 ps. We also measured how, for low excitation, we can transiently enhance the CDW by as much as 30%. And finally, in Section 3.4, we have measured the evolution of the order in the system on much longer time scales to 400 ns and separated the thermal contribution to the evolution from a second mechanism that slows the recovery of the ground state. This allows the energy barriers for the different SDW and CDW configurations in the confined geometry to be assessed through the time domain. Additional analyses have also been conducted on this film, published in [147, 149, 150].

The nature of the SDW and CDW in bulk Cr were quite thoroughly explored previously and the boundary pinning and quantization in thin films has been shown previously through different methods such as resistivity and neutron diffraction. But here we have shown a more complete analysis of the CDW in a thin film and used time-resolved measurements to explore interactions and energies in the system more closely. This opens avenues for measurements of other complex systems and gives insight into the dynamic behavior of spin and charge, which is of interest in developing devices with faster and more efficient spin transport.

Acknowledgements

Section 3.1.4 contains unpublished data coauthored by Sheena K. K. Patel and Eric E. Fullerton. The dissertation author was the primary investigator of this material. This work was performed in part at the San Diego Nanotechnology Infrastructure (SDNI) of UC San Diego, a member of the National Nanotechnology Coordinated Infrastructure, which is supported by the National Science Foundation (Grant ECCS-2025752).

Section 3.2, in full, contains a reprint of research published in Andrej Singer, Sheena K. K.

Patel, Vojtěch Uhlíř, Roopali Kukreja, Andrew Ulvestad, Eric M. Dufresne, Alec R. Sandy, Eric E. Fullerton, and Oleg G. Shpyrko, "Phase coexistence and pinning of charge density waves by interfaces in chromium," *Phys. Rev. B*, vol. 94, p. 174110, 2016. Copyright 2016 by the American Physical Society. The dissertation author was second author and made essential contributions to this work. This research used resources of the Advanced Photon Source, a U.S. Department of Energy (DOE) Office of Science user facility operated for the DOE Office of Science by Argonne National Laboratory under Contract No. DE-AC02-06CH11357.

Section 3.3, in full, contains a reprint of research published in Andrej Singer, Sheena K. K. Patel, Roopali Kukreja, Vojtěch Uhlíř, James Wingert, Sven Festersen, Diling Zhu, James M. Glownia, Henrik T. Lemke, Silke Nelson, Michael Kozina, Kai Rossnagel, Michael Bauer, Bridget Murphy, Olaf M. Magnussen, Eric E. Fullerton, and Oleg G. Shpyrko, "Photoinduced enhancement of the charge density wave amplitude," *Phys. Rev. Lett.*, vol. 117, p. 056401, 2016. Copyright 2016 by the American Physical Society. The dissertation author was second author and made essential contributions to this work. Use of the Linac Coherent Light Source (LCLS), SLAC National Accelerator Laboratory, is supported by the U.S. Department of Energy, Office of Science, Office of Basic Energy Sciences under Contract No. DE-AC02-76SF00515.

Section 3.4, in full, is currently being prepared for submission for publication of the material coauthored by Sheena K. K. Patel, Oleg Yu. Gorobtsov, Devin Cela, Stjepan B. Hrkac, Nelson Hua, Rajasekhar Medapalli, Anatoly G. Shabalin, James Wingert, James M. Glownia, Diling Zhu, Matthieu Chollet, Oleg G. Shpyrko, Andrej Singer, and Eric E. Fullerton. The dissertation author was the primary investigator and author of this material. Use of the Linac Coherent Light Source (LCLS), SLAC National Accelerator Laboratory, is supported by the U.S. Department of Energy, Office of Science, Office of Basic Energy Sciences under Contract No. DE-AC02-76SF00515.

Chapter 4

Thin Film Antiperovskite Manganese Nitrides (Mn_3AN)

4.1 Introduction

Antiperovskites are compounds with the formula M_3AX, where M and A are usually metals and X is an interstitial light element (hydrogen, oxygen, nitrogen, or carbon). This encompasses a very wide range of materials, but one group of antiperovskites of interest is the class where M is manganese (Mn) and X is nitrogen (N), referred to as antiperovskite manganese nitrides, or Mn_3AN. This group of materials exhibits many interesting phenomena that couple magnetic, electric, and structural order parameters. Of interest in this work are the compounds that exhibit negative thermal expansion through a magnetic phase transition.

This dissertation includes the fabrication and static characterization of two classes of thin films of Mn_3AN: $Mn_3Cu_{1-x}Ge_xN$ and $Mn_3Cu_{0.9}Ni_{0.1}N$. Both classes have regions of negative thermal expansion during a phase transition between a low temperature antiferromagnetic phase and a higher temperature paramagnetic phase. A second transition to a lower temperature phase that is either ferromagnetic or ferrimagnetic is seen in the $Mn_3Cu_{0.9}Ni_{0.1}N$ film. This is a first

order phase transition accompanied by a very large change in out-of-plane lattice parameter. Time-resolved pump-probe x-ray diffraction measurements were conducted at the Advanced Photon Source (APS) at the Argonne National Laboratory (ANL) to explore the lattice parameter dynamics following photoexcitation on ns time scales.

4.1.1 Thermal Expansion

Most materials expand when heated, a phenomenon which is explained by the asymmetry of the potential well for a chemical bond. The potential diverges as the distance between atoms approaches zero as a result of the Pauli exclusion principle, meaning that the magnitude of the slope of the potential is greater for a decrease in the distance between atoms than it is for an increase in that distance. As a material is heated, the vibrational energy added to the system will allow for movement of atoms, but the potential well asymmetry means the average interatomic distance at that temperature also increases. The resulting phononic thermal expansion with positive sign holds for most solids. The thermal expansion of a solid isotropic material can be quantified by the linear coefficient of thermal expansion:

$$\alpha_{\mathrm{L}} = \frac{1}{L}\left(\frac{\partial L}{\partial T}\right) \tag{4.1}$$

where L is the length or volume at a given temperature T. The linear coefficients of thermal expansion near room temperature for some common materials that exhibit positive thermal expansion are 16.6×10^{-6} K^{-1} for Cu, 6.2×10^{-6} K^{-1} for Cr, 12.0×10^{-6} K^{-1} for steel, 22×10^{-6} K^{-1}for Mn, 5.9×10^{-6} K^{-1} for Ge, 4.3×10^{-6} K^{-1} for Si_3N_4, and 10.8×10^{-6} K^{-1} for MgO [156].

A few materials have been found to exhibit negative thermal expansion, which cannot be explained by the potential well model above. Invar alloys, which are alloys with composition near $Fe_{0.64}Ni_{0.36}$, were the first materials found to exhibit negative thermal expansion (with a

very small coefficient of thermal expansion, so near-zero thermal expansion). This has been associated with magnetovolume effects of the ferromagnetic to paramagnetic transition. One popular model explains this property with two possible ordered states for an Fe-Ni alloy that are close in energy: a high-volume high-spin state and a low-volume low-spin state. Thermal excitation of the system in a high-spin ground state can partly increase the density of the low-spin state, resulting in a negative thermal expansion that closely compensates the phononic positive thermal expansion for certain compositions [157]. This model fails at low temperatures and has not found supporting experimental evidence [158]. More recent calculations have suggested that Invar experiences a continuous transition from a high-volume ferromagnetic to a low-volume paramagnetic state, which provides the competing negative contribution to the thermal expansion [159]. Another material that exhibits negative thermal expansion is ZrW_2O_8, which has a large negative coefficient of thermal expansion over the temperature range 0.3 K to 1050 K [160, 161]. This is one of the few systems where negative thermal expansion is well-understood, explained by the existence of rigid unit modes [162, 163], in which the structure is made up of rigid polyhedra which are linked together by O atoms. These atoms are able to vibrate in a way that will rotate and pull the polyhedra closer together, resulting in a contraction of the material.

However, the origin of negative thermal expansion varies between systems and remains a mystery for almost all of the materials that exhibit it. This includes some compounds of Mn_3AN, which we will introduce more in the subsequent sections. The negative thermal expansion in these compounds seems to be driven by the establishment of Γ^{5g} spin structure (which we will describe in the next section) as the material is cooled through the Néel transition, with an increase in lattice and bond length in order decrease the magnetic energy [164, 165]. This results in some of the largest measured magnetovolume effects, with tunable temperature ranges and linear coefficients of thermal expansion up to -30×10^{-6} K^{-1} [166]. Magnetovolume effects broadly are thought of as an increase in volume of a material resulting in a reduction of the overlap of electronic orbitals and a narrowing of the electron bandwidth, which increases the density of states at the

Fermi energy and favors magnetic ordering. But developing a more nuanced understanding of this in each system is often difficult.

For materials that exhibit a magnetovolume effect, the spontaneous volume magnetostriction ω_s is an estimate of the magnetic contribution to the volume. The observed thermal expansion of a system is a combination of the phononic thermal expansion $(\Delta L/L)_{\text{ph}}$ and the magnetic contribution. The phononic thermal expansion can be estimated as described in [167] and [168]. So the magnetic contribution to the thermal expansion is

$$(\Delta L/L)_{\text{magn}} = (\Delta L/L)_{\text{obs}} - (\Delta L/L)_{\text{ph}}$$

For a bulk cubic system, the spontaneous volume magnetostriction is $\omega_s \approx 3(\Delta L/L)_{\text{magn}}$, where we have assumed the thermal expansion is small.

In thin films, the in-plane lattice parameters are strained at the substrate interface and not free to expand or contract as a bulk sample. In this chapter, we assume that there is no in-plane magnetostriction of the films and the spontaneous volume magnetostriction is approximately

$$\omega_{\text{s,films}} \approx (\Delta L/L)_{\text{magn}}. \tag{4.2}$$

Phononic thermal expansion is generally linear down to around 100 K and is estimated in this work as a linear extrapolation of the thermal expansion above the magnetic ordering temperature to low temperatures.

4.1.2 Properties of Bulk Mn_3AN

Mn_3AN compounds are of interest because of the range of physical phenomena that have been observed: giant magnetoresistance [169–171], a near-zero temperature coefficient of resistivity [170, 172, 173], anomalous Hall effect [174–176], piezoelectric effects [177, 178],

anomalous Nernst effect [179], magnetocaloric effects [180], and magnetostructural effects including magnetostriction [181, 182], and giant magnetovolume effects [183, 184] including negative thermal expansion [169, 184].

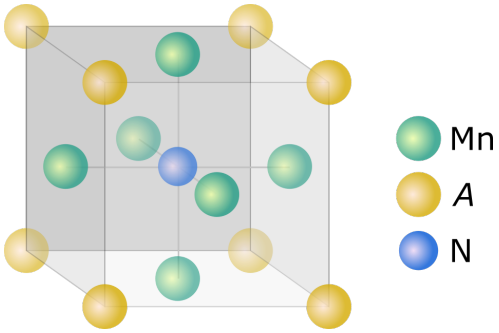

Figure 4.1: The cubic structure of Mn_3AN. Mn atoms are located on the faces of the cubic unit cell, N in the body, and A at the vertices.

The unit cell of Mn_3AN is generally the cubic structure shown in Fig. 4.1, with Mn atoms located on the face-centered positions of the cubic cell, N in the body-centered positions, and A at the vertices of the cubic cell. Different structural phases that have been observed include tetragonal distortions ($c/a < 1$ or $c/a > 1$) of this cubic cell and, less commonly, an orthorombic structure. Structural changes have been found to be associated with transitions between magnetic phases, most commonly a high temperature paramagnetic phase and lower temperature antiferromagnetic phase, but also including observed ferromagnetic and/or ferrimagnetic phases in some compounds [185, 186]. Many of the interesting phenomena reported in these materials occur during the phase transitions, such as the phase transition between antiferromagnetic and paramagnetic states also exhibiting a giant magnetoresistance and negative thermal expansion.

Neutron diffraction measurements first reported in [187] suggested the antiferromagnetic phase of Mn_3AN to be a combination of two possible spin configurations depending on the composition of A. These two spin configurations are Γ^{4g} and Γ^{5g}, shown in Fig. 4.2. In both configurations, the magnetic order can be characterized with three sublattices of Mn: Mn$'$ at $\frac{1}{2}\frac{1}{2}0$, Mn$''$ at $\frac{1}{2}0\frac{1}{2}$, and Mn$'''$ at $0\frac{1}{2}\frac{1}{2}$. All Mn moments are in the (111) plane and the three sublattices are nearest neighbors in this plane, with moments directed 120 deg with respect to one another so that

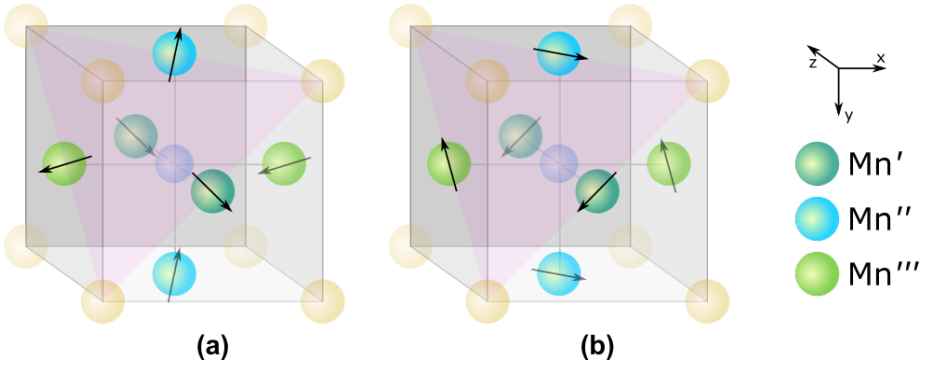

Figure 4.2: Possible spin configurations of antiferromagnetic Mn_3AN. Both configurations can be described with three sublattices: Mn′ at $\frac{1}{2}\frac{1}{2}0$, Mn″ at $\frac{1}{2}0\frac{1}{2}$, and Mn‴ at $0\frac{1}{2}\frac{1}{2}$. All moments are in the (111) plane shown in pink, but directed 120 deg with respect to moments in the other two sublattices so there is zero total moment. (a) The Γ^{4g} spin structure is characterized by Mn sublattice moments directed along $[11\bar{2}]$, $[1\bar{2}1]$, and $[\bar{2}11]$. (b) The Γ^{5g} spin structure is characterized by Mn sublattice moments directed along $[\bar{1}10]$, $[10\bar{1}]$, and $[0\bar{1}1]$.

the net magnetization of the material is zero. In the case of the Γ^{4g} spin structure in Fig. 4.2(a), the moments are perpendicular to the unit cell face diagonals in the (111) plane, directed along $[11\bar{2}]$, $[1\bar{2}1]$, and $[\bar{2}11]$. For the Γ^{5g} spin structure as shown in Fig. 4.2(b), the moments are along the face diagonals in the (111) plane, directed along $[\bar{1}10]$, $[10\bar{1}]$, and $[0\bar{1}1]$. In both cases, the Mn moments along $\langle 100 \rangle$ will be parallel to one another and the antiferromagnetic ordering wave vector is $\mathbf{q} = \frac{2\pi}{a}\left(\frac{1}{2}, \frac{1}{2}, \frac{1}{2}\right)$.

More recent neutron diffraction and nuclear magnetic resonance measurements in [188] have explored the presence of these two phases for two materials. For Mn_3NiN, it was found that the Γ^{5g} moment increases with decreasing temperature and the Γ^{4g} spin structure is absent. Measurements of $Mn_3Cu_{0.5}Ge_{0.5}N$ demonstrate a broad (around 100 K) Néel transition during which there is a linear combination of the two spin states, and below which the material exhibits only the Γ^{5g} structure. Calculations have proposed the existence of an intermediate phase, with spins rotated at some angle 0 deg $\leq \theta \leq$ 90 deg within the (111) plane (such that $\theta = 0$ deg would correspond to the Γ^{5g} structure and $\theta = 90$ deg to the Γ^{4g} structure), during the transition between the two states, meaning the transition would occur with a simultaneous rotation of the spins in the (111) plane [179, 189, 190].

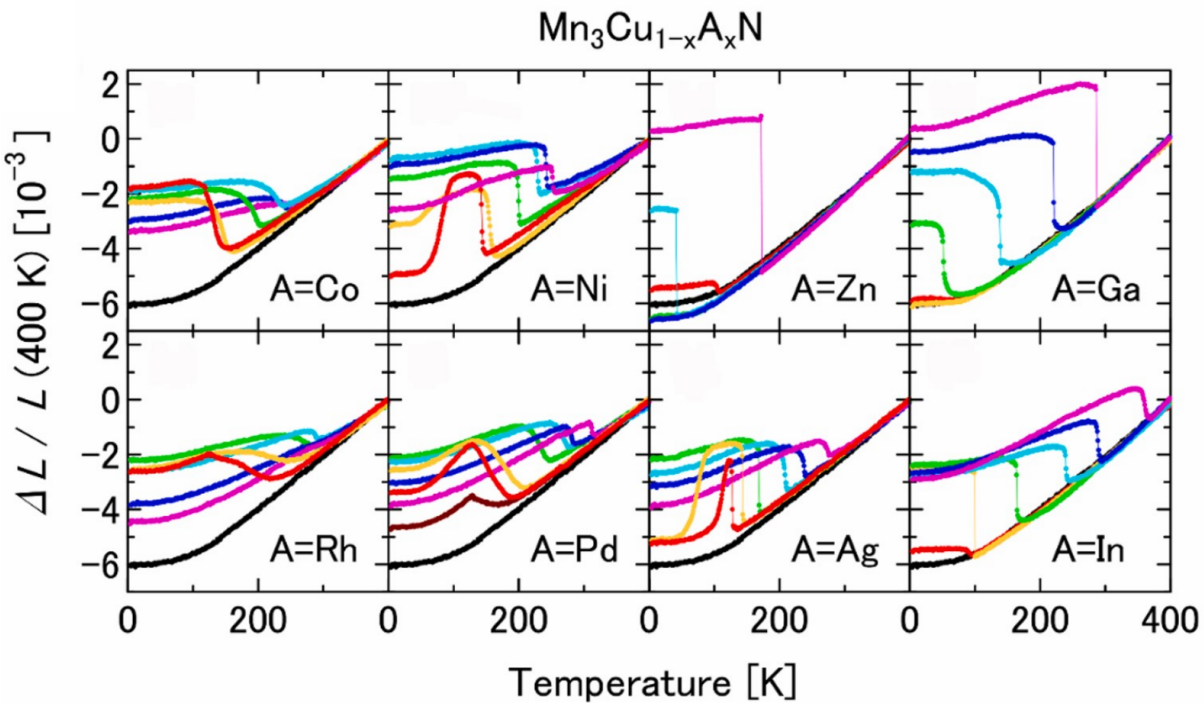

Figure 4.3: Thermal expansion of bulk $Mn_3Cu_{1-x}A_xN$ with $x = 0$ in black, $x = 0.1$ in red, $x = 0.15$ in orange, $x = 0.3$ in green, $x = 0.5$ in cyan, $x = 0.7$ in blue, and $x = 1$ in magenta. Figure reproduced from [167] under the terms of the CC BY-NC-SA 3.0 license.

Much of the work on Mn_3AN thus far has focused on the large magnetovolume effects. It has been suggested that these are a result of the geometrical frustration of the Mn spins in the antiperovskite structure, with negative thermal expansion observed during the antiferromagnetic-paramagnetic transition for compounds that exhibit a Γ^{5g} spin structure in the antiferromagnetic state [164, 165]. Fig. 4.3, reproduced here from [167], shows the change in lattice constant from 400 K in the paramagnetic phase for $Mn_3Cu_{1-x}A_xN$ where A = Co, Ni, Zn, Ga, Rh, Pd, Ag, In and $0 \leq x \leq 1$. Most of these compositions exhibit regions of negative thermal expansion. Some, such as Mn_3ZnN, exhibit a discontinuous decrease in lattice parameter of up to 0.5%. For other compounds, such as for A = Co, the width of the region of negative thermal expansion and the expansion coefficient are tunable with the ratio of Cu to A. Some compounds exhibit a second effect of interest at lower temperature where there is a large increase in lattice parameter, such as for $Mn_3Cu_{0.9}Ni_{0.1}N$, which shows a region of large positive thermal expansion of about 0.3%

near 100 K and then a region of negative thermal expansion of similar magnitude near 150 K. The lower temperature transition is not a continuous shift in the Bragg peak, but rather a split in the peak, indicating the coexistence of two cubic phases, one being the higher temperature antiferromagnetic phase with larger lattice parameter and one being the lower temperature phase, which exhibits positive magnetic moment and is believed to be ferromagnetic or ferrimagnetic [167].

The phase transitions in these materials are accompanied by varied effects in electric transport. Some compounds exhibit negative thermal expansion with an abrupt drop in resistivity at the antiferromagnetic-paramagnetic transition, as with $Mn_3Zn_{1-x}Ge_xN$ [169]. Compounds $Mn_3Cu_{0.6}Ag_xSn_{0.4-x}N$ exhibit negative thermal expansion and an increase in resistivity at this transition, along with nearly zero coefficient of resistivity (change in resistivity vs. temperature) in the paramagnetic phase [173].

In this work, we have focused on the compounds $Mn_3Cu_{1-x}Ge_xN$ and $Mn_3Cu_{0.9}Ni_{0.1}N$. Both systems have been shown in bulk to exhibit the antiferromagnetic-paramagnetic phase transition with negative thermal expansion and the latter has a lower temperature transition to a ferromagnetic or ferrimagnetic phase. The existence of these phases and complex charge-spin-lattice coupling makes this an interesting system in which to study the dynamic response to perturbations, potentially to gain knowledge for areas such as THz spintronics and particularly in applications where thermal expansion is of concern.

4.1.3 Existing Work in Thin Film Mn_3AN

There have been limited studies of thin film Mn_3AN in the past. It has been demonstrated that epitaxial growth of films is possible through sputtering, molecular beam epitaxy, and pulsed laser deposition on quartz substrates [191, 192], SiO_2 (001) substrates [193, 194], MgO (001) substrates [195–198], $SrTiO_3$ (001) substrates [199, 200], $(LaAlO_3)_{0.3}(Sr_2TaAlO_6)_{0.7}$ (001) substrates [199, 200], $BaTiO_3$ (001) substrates [199, 200], and YSZ (001) substrates [201].

Measurements of Mn_3CuN_x films have shown some significant differences from bulk Mn_3CuN. The antiferromagnetic-paramagnetic transition was observed in [191] at nearly the same temperature based off of the peak location in the susceptibility, however the peak was significantly broadened (over 150 K in width) compared to a bulk sample (around 25 K in width), indicating a very broad transition or poor quality of the film. Resistivity of the bulk sample showed metallic behavior, with resistivity increasing with temperature, and an anomaly with a nearly 25% decrease in resistivity during the antiferromagnetic-paramagnetic transition. In contrast, the resistivity of the film decreased monotonically with temperature up to 290 K. A second study in [193] found a ferrimagnetic-paramagnetic transition in a film rather than the expected antiferromagnetic-paramagnetic transition, which was attributed to a deficiency of N. This film did not find any obvious structural transitions, as the lattice constant varied linearly with temperature over the measured temperature range. The resistivity showed the same monotonically decreasing behavior as the film studied in [191].

Several studies have been conducted of Mn_3NiN films, demonstrating magnetoresistance and magnetization with spin-glass behavior [192], anomalous Hall effect [199], and giant piezomagnetism [200]. Exchange bias has been measured in $Mn_{3.6}Cu_{0.4}N$ films [195] and an initial study with bilayers of antiferromagnetic Mn_3GaN and ferromagnetic Co_3FeN demonstrated strong exchange coupling and AMR measurements that indicate this may be a possible system to study current-induced magnetization reversal and spin transfer torque [197]. No studies have yet demonstrated negative thermal expansion or significant magnetovolume effects in films. Demonstrating these effects and tunable properties in films can open avenues for technological applications and experimental techniques such as ultrafast x-ray diffraction to study the interaction of spin and lattice that drives these phenomena.

4.1.4 Growth of $Mn_3Cu_{1-x}A_xN$ Films

Several methods of thin film growth have been shown to achieve epitaxial Mn_3AN films, however sputtering is the process best suited for large-scale production. In this case, we are able to cosputter from pure Mn, Cu, and Ge or Ni targets to achieve the desired stoichiometric ratios of those materials. Films were sputtered with a mix of 2.5 mTorr Ar and 0.4 mTorr N_2 gas to achieve reactive sputtering as described in Section 2.2.3. As with the other materials grown in this work, crystallinity is best achieved with high temperature growth, however high temperatures will also increase diffusion of N out of the films, so optimal growth of Mn_3AN films was achieved at deposition temperatures of 600 °C with no post-anneal process on MgO (001) substrates. All samples were capped with Pt to protect from oxidation. Fig. 4.4 shows out-of-plane x-ray diffraction data for a 53 nm $Mn_3Cu_{0.5}Ge_{0.5}N$ film, indicating (001) out-of-plane preferred growth on these substrates.

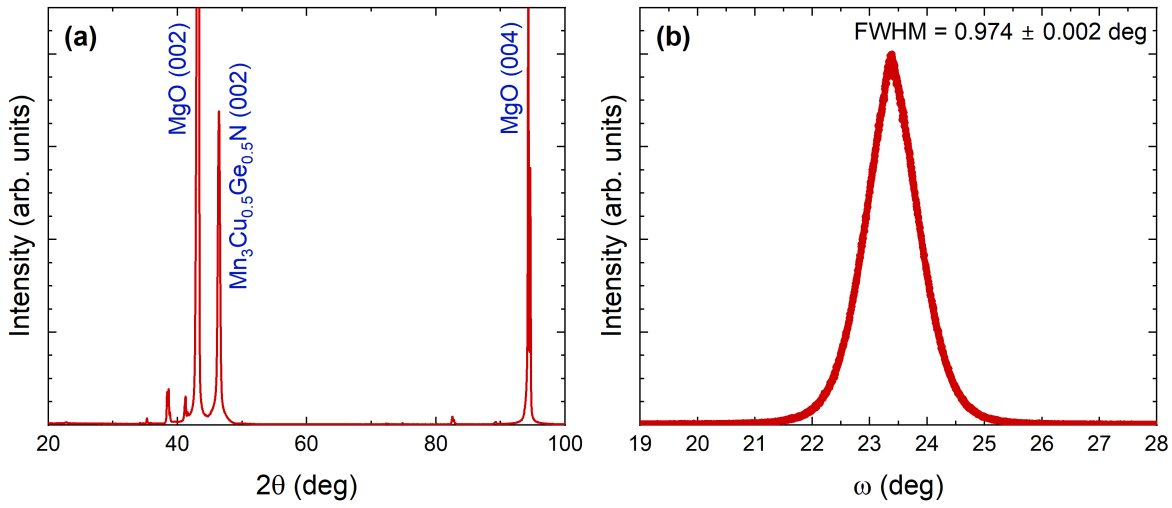

Figure 4.4: X-ray characterization of a 53 nm $Mn_3Cu_{0.5}Ge_{0.5}N$ film grown on MgO (001). (a) Out-of-plane x-ray diffraction showing the $Mn_3Cu_{0.5}Ge_{0.5}N$ (002) peak, the MgO (002) peak, and the MgO (004) peak. (b) X-ray diffraction rocking curve of the $Mn_3Cu_{0.5}Ge_{0.5}N$ (002) peak at $2\theta = 46.42$ deg. Measurements were made with Cu Kα radiation.

Fig. 4.5 shows out-of-plane and in-plane x-ray diffraction for a 29.7 nm $Mn_3Cu_{0.9}Ni_{0.1}N$ film. The out-of-plane (002) diffraction peak is seen at 46.58 deg, indicating an out-of-plane

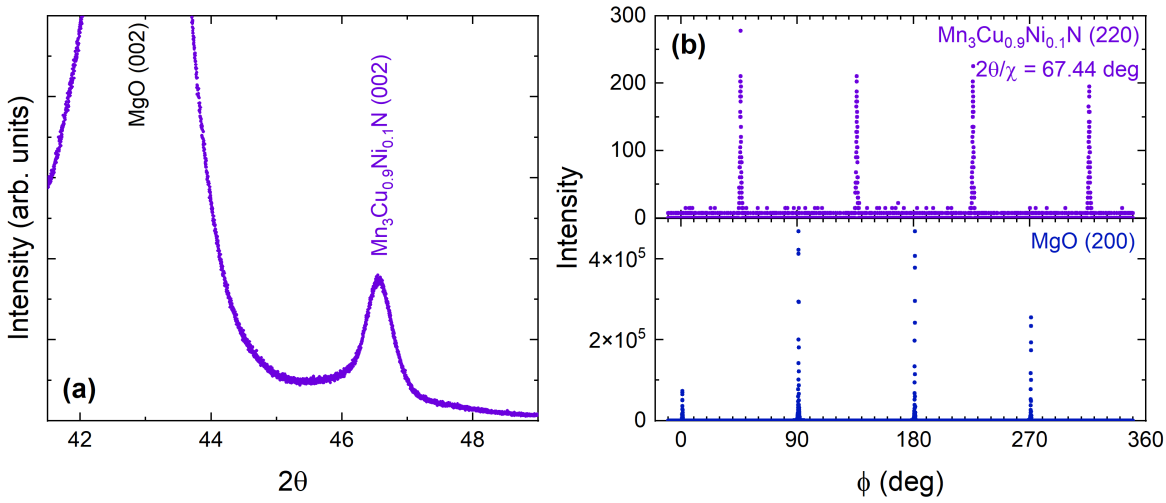

Figure 4.5: X-ray characterization of a 29.7 nm $Mn_3Cu_{0.9}Ni_{0.1}N$ film grown on MgO (001). (a) Out-of-plane x-ray diffraction showing the $Mn_3Cu_{0.9}Ni_{0.1}N$ (002) peak and the MgO (002) peak. (b) In-plane x-ray diffraction phi scans of the $Mn_3Cu_{0.9}Ni_{0.1}N$ (220) and MgO (200) peaks. The 45 deg rotation of these peaks indicates that the unit cell of the film is aligned with the unit cell of the MgO substrate. Measurements were made with Cu Kα radiation.

lattice parameter of $c = 0.390$ nm. In-plane phi scans of the (220) diffraction peak and the MgO (200) diffraction peak in Fig. 4.5(b) are shifted with respect to one another by 45 deg, indicating that the unit cell of the film grows in alignment with the MgO unit cell. The in-plane (220) diffraction peak indicates an in-plane lattice parameter of $a = 0.392$ nm. Since $a \approx c$, we find that the unit cell at room temperature (in the paramagnetic phase) is cubic.

The exact stoichiometric ratio for these films has not been measured. The ratio of Mn:Cu:*A* where *A* is Ge or Ni has been assumed based off of calibrated deposition rates of the three materials. The sputter pressure of N_2 gas was optimized for crystal quality (based off the rocking curve of the (002) peak) and film properties. The exact N content of these films is not known, but previous work, including in sputtered films [193], has shown that N deficiencies will alter film properties, so this maybe be a useful measurement to make moving forward. For the films studied here, we assume Mn:(Cu+Ge):N and Mn:(Cu+Ni):N ratios of 3:1:1.

4.2 Thin Film $Mn_3Cu_{1-x}Ge_xN$

The system $Mn_3Cu_{1-x}Ge_xN$ provides a good starting point for studying negative thermal expansion in Mn_3AN materials. Fig. 4.6, reproduced from [167], shows the change in lattice parameter for bulk samples with $x = 0$ (black), $x = 0.1$ (red), $x = 0.15$ (orange), $x = 0.3$ (green), $x = 0.4$ (mint), $x = 0.5$ (cyan), $x = 0.7$ (royal blue), and $x = 1$ (magenta). Positive thermal expansion is observed for much of the temperature range measured, however there are significant negative thermal expansion regions seen in most of the samples associated with the antiferromagnetic-paramagnetic transition. For $x = 0.15$, the transition region is near 100 K and very narrow, with an almost 0.4% decrease in lattice parameter. As the Cu:Ge ratio decreases, the transition shifts to higher temperature and broadens, and the magnitude of the coefficient of thermal expansion decreases. For $x = 0.7$, the coefficient is near zero and the transition is above room temperature, at approximately 400-450 K.

In this work, we fabricate a series of $Mn_3Cu_{1-x}Ge_xN$ films with $0.1 \leq x \leq 0.6$ which

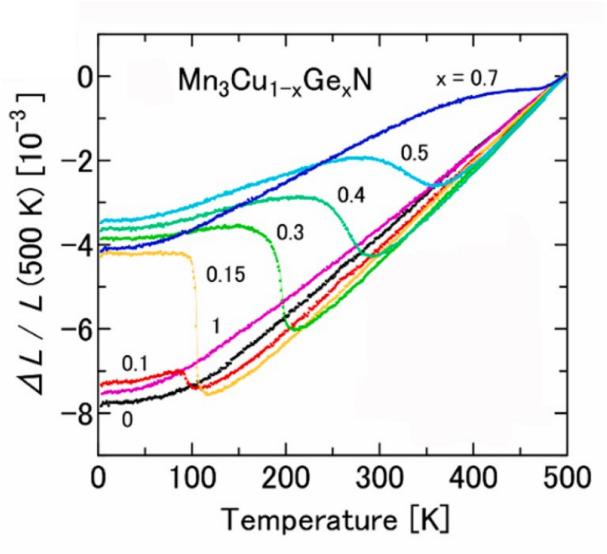

Figure 4.6: Thermal expansion of bulk $Mn_3Cu_{1-x}Ge_xN$. The samples include $x = 0$ (black), $x = 0.1$ (red), $x = 0.15$ (orange), $x = 0.3$ (green), $x = 0.4$ (mint), $x = 0.5$ (cyan), $x = 0.7$ (royal blue), and $x = 1$ (magenta). Figure reproduced from [167] under the terms of the CC BY-NC-SA 3.0 license.

exhibit negative thermal expansion. Temperature-dependent x-ray diffraction, magnetometry, and resistivity measurements have been conducted, as well as time-resolved x-ray diffraction measurements to measure the dynamic lattice response to laser pulses.

4.2.1 Film Characterization

Fig. 4.7 shows the room temperature (002) x-ray diffraction peak for the $Mn_3Cu_{1-x}Ge_xN$ films, corresponding out out-of-plane lattice parameter c between 0.390 nm and 0.392 nm. The shift to lower angle (higher lattice parameter for $x = 0.5$ and $x = 0.6$ is consistent with measurements in bulk that suggest these two films could be in the larger volume antiferromagnetic phase at room temperature while the others would be in the paramagnetic phase.

The (002) diffraction peak was measured for five of these films as a function of temperature

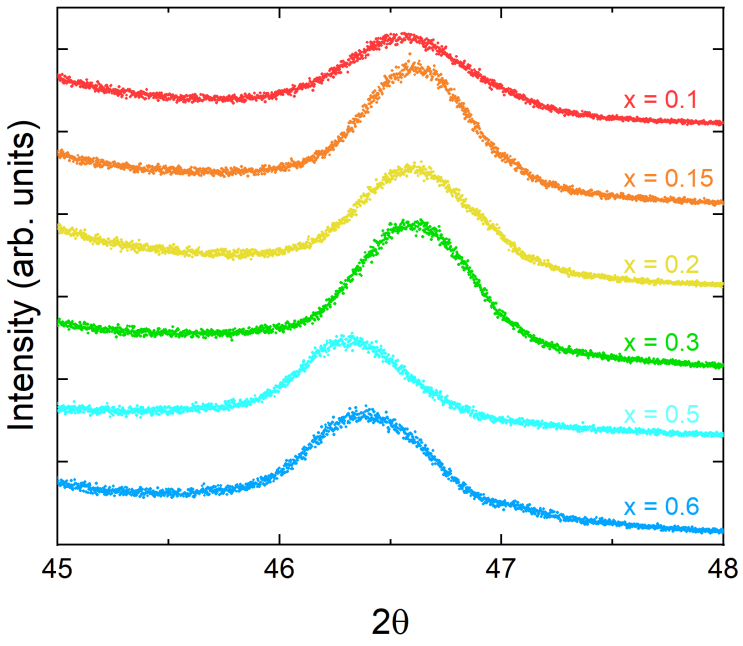

Figure 4.7: X-ray diffraction (002) peak of 30 nm $Mn_3Cu_{1-x}Ge_xN$ films measured at room temperature, for $x = 0.1$ (red), $x = 0.15$ (orange), $x = 0.2$ (yellow), $x = 0.3$ (green), $x = 0.5$ (cyan), and $x = 0.6$ (blue). Measurements were made with Cu Kα radiation.

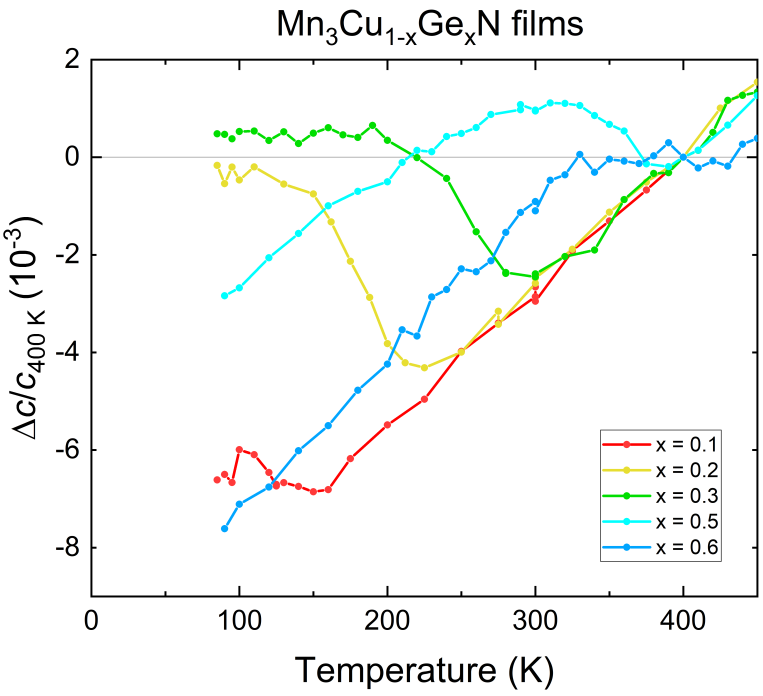

Figure 4.8: Out-of-plane thermal expansion of 30 nm $Mn_3Cu_{1-x}Ge_xN$ films, for $x = 0.1$ (red), $x = 0.2$ (yellow), $x = 0.3$ (green), $x = 0.5$ (cyan), and $x = 0.6$ (blue). The data points are calculated from the (002) peak position fit to a Voigt profile.

and fit with a Voigt profile to determine the peak position and out-of-plane lattice parameter. The normalized change in out-of-plane lattice parameter from the 400 K value is shown in Fig. 4.8. This result is remarkably similar to what was observed in bulk, reproduced from [167] in Fig. 4.6. For increasing x, the transition shifts to higher temperature and the coefficient of thermal expansion decreases to near zero for $x = 0.6$. The exception is $x = 0.1$, which has a smaller drop in lattice parameter, also consistent with bulk. In bulk, the transition clearly broadens with increasing Ge fraction, however in the films, the width of the transition is broader for smaller Ge fraction and does not have a clear correlation with Ge fraction. Overall, the regions of negative thermal expansion (the Néel transition region) are comparable to or a little broader than in bulk. We have demonstrated the existence of negative thermal expansion in films and tunability of the negative thermal expansion region with Ge substitution of Cu. Table 4.1 summarizes the results for these

Table 4.1: Properties of negative thermal expansion in $Mn_3Cu_{1-x}Ge_xN$ films determined from x-ray diffraction data. The spontaneous volume magnetostriction ω_s is found at temperatures just below the transition for each film. The thermal expansion coefficients in the antiferromagnetic (AF), transition, and paramagnetic (PM) regions were determined by linear fits of the lattice parameter within each region.

x	Néel Transition Region		ω_s (10^{-3})	Thermal Expansion Coefficient (10^{-6}/K)		
	T_N (K)	Width (K)		AF	Transition	PM
0.1	155	55	2.4		-15.4 ± 3.5	28.0 ± 0.5
0.2	225	80	7.7		-57.9 ± 2.1	27.7 ± 0.1
0.3	300	95	6.1	0.6 ± 0.8	-34.0 ± 4.6	26.4 ± 1.1
0.5	390	65	3.0	19.4 ± 0.8	-24.5 ± 0.8	25.8 ± 1.8
0.6	430	100	3.0	31.7 ± 0.5	-0.2 ± 1.7	

films. The Néel temperature T_N is taken to be the high temperature endpoint of the transition region. The spontaneous volume magnetostriction ω_s is found as described in Section 4.1.1, at a temperature just below the transition region. The lattice expansion out-of-plane in the films is comparable to the lattice expansion in bulk in each dimension, so ω_s in these films is believed to be about $1/3$ of what is seen in bulk in [167]. The thermal expansion coefficient was found with linear fits in the three regions (where possible given the temperature range of measurements). In the paramagnetic phase, the coefficients are very similar. In the antiferromagnetic phase and the transition regions, we see significant differences between the films and the maximum negative thermal expansion coefficient observed was for $x = 0.2$ with $\alpha = -57.9 \pm 2.1$ $(10^{-6})/\text{K}$. For $x = 0.5$, the observed coefficient in the film was $\alpha = -24.5 \pm 0.8$ $(10^{-6})/\text{K}$, compared to $\alpha = -12$ $(10^{-6})/\text{K}$ for bulk from [202]. There were two regions of near-zero thermal expansion observed: for $x = 0.3$ in the antiferromagnetic phase and for $x = 0.6$ in the transition region.

Bulk measurements have revealed giant magnetoresistance and other electric transport effects, as discussed in Section 4.1.3. Three 30 nm $Mn_3Cu_{0.9}Ni_{0.1}N$ films with $x = 0.1$ (red), $x = 0.2$ (yellow), and $x = 0.3$ (green) were patterned by UV photolithography into a wire along the (100) axis. Resistivity vs. temperature measurements were made, shown in Fig. 4.9(a).

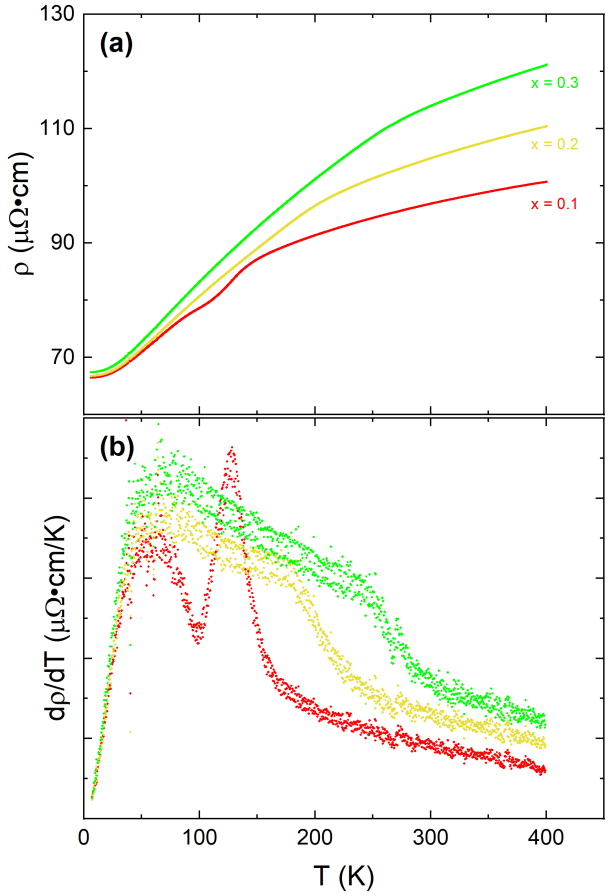

Figure 4.9: Resistivity vs. temperature of 30 nm $Mn_3Cu_{0.9}Ni_{0.1}N$ films for $x = 0.1$ (red), $x = 0.2$ (yellow), and $x = 0.3$ (green) with no applied magnetic field. (a) Resistivity vs. temperature shows metallic behavior with slight anomalies during the magnetic transition. (b) Peaks are observed in the derivative of the resistivity with respect to temperature in the transition region.

Overall, the resistivity shows metallic behavior, increasing with temperature. For $x = 0.1$, there is a clearly visible region with greater coefficient of resistivity which aligns to the negative thermal expansion region from Fig. 4.8. This effect is more subtle for $x = 0.2$ and $x = 0.3$ but is also present. Fig. 4.9(b) shows the derivative of the resistivity measurement with respect to temperature for each of the three films, which shows peaks for each of the samples that align with the negative thermal expansion region. These results are in contrast to the measurements of bulk Mn_3CuN in [191], which shows a much larger decrease in resistivity at the transition, and

of a Mn_3CuN film in [191], which exhibits semiconductor resistivity behavior with no obvious magnetoresistance effects, and in [201], which shows metallic behavior with a 1-2% drop in resistivity at the transition.

We have demonstrated negative thermal expansion in Mn_3AN films grown by sputtering on MgO (001) substrates. A series of $Mn_3Cu_{1-x}Ge_xN$ films shows the tunability of the transition temperature and the coefficients of thermal expansion. The magnetic ordering has not been confirmed in these films, however the similarity to bulk suggests that these films exhibit a low temperature antiferromagnetic phase and the transition between the antiferromagnetic phase and paramagnetic phase is a region of significant interest. Next, we will present some dynamic measurements of the lattice parameter following photoexcitation in a $Mn_3Cu_{0.7}Ge_{0.3}N$ film.

4.2.2 Laser-Pump X-Ray-Probe Experiment of a $Mn_3Cu_{0.7}Ge_{0.3}N$ film

Static measurements of structural and magnetic properties of $Mn_3Cu_{1-x}Ge_xN$ provide some insight into the mechanisms driving behavior such as negative thermal expansion, however time-resolved measurements are of increasing interest for some applications. For example, the dynamics of magnetic ordering in antiferromagnetic materials is studied because of the potential for THz spintronics. One method of probing in this way is through time-resolved pump-probe diffraction, where a system is excited with a laser pulse and the structural response is probed with x-ray diffraction. Considering the limited penetration depth of optical wavelengths, the capability to grow 20-40 nm films of these materials is necessary as it allows for uniform optical excitation of the material.

For this experiment, a 21.5 nm $Mn_3Cu_{0.7}Ge_{0.3}N$ film was grown by sputtering. Fig. 4.10 shows the lattice parameter for this film as a function of temperature. The purple data points are from x-ray diffraction measurements taken on a Rigaku SmartLab X-ray Diffractometer at UC San Diego and the blue data points are from x-ray diffraction measurements made at the APS. The negative thermal expansion region ranges from 220 K to 300 K with a thermal expansion

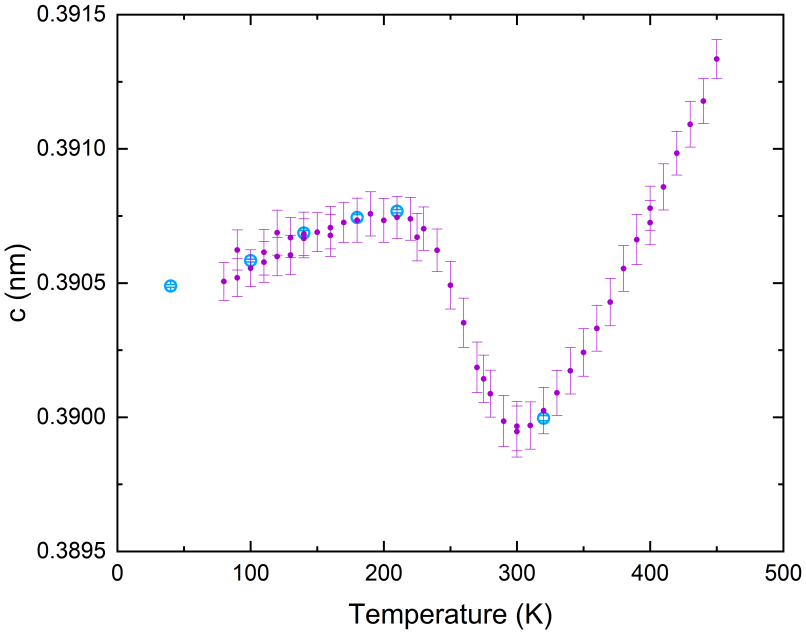

Figure 4.10: Out-of-plane lattice parameter c as a function of temperature for a 21.5 nm $Mn_3Cu_{0.7}Ge_{0.3}N$ film. The purple data points are calculated from x-ray diffraction measurements made on a Rigaku diffractometer at UC San Diego. The blue data points are calculated from x-ray diffraction measurements at the Advanced Photon Source. The error bars indicate a 99% confidence interval.

coefficient of $-32.4 \pm 1.1(10^{-6})/\text{K}$. Above this region, the thermal expansion coefficient in the paramagnetic phase is comparable to those found for the films in Table 4.1. The spontaneous volume magnetostriction ω_s at 210 K found by extrapolating the thermal expansion in the paramagnetic phase is 4.7×10^{-3}. Table 4.2 reflects the properties found from the static x-ray diffraction measurements. The differences between this film and the film with $x = 0.3$ in Table 4.1 can be explained by small differences in composition.

Time-resolved x-ray diffraction measurements were performed at beamline 7ID-C at the APS (see Section 2.6.2) following photoexcitation by an 800 nm Ti:Sapphire laser delivered in 100 fs pulses with a spot size of 0.27 mm by 0.34 mm. The x-ray energy was 11.0 keV, with a pulse width of about 100 ps and spatial resolution on the μm scale. Fig. 4.11 shows measurements

Table 4.2: Properties of negative thermal expansion in a $Mn_3Cu_{0.7}Ge_{0.3}N$ film determined from x-ray diffraction data taken while cooling temperature. The thermal expansion coefficients in the antiferromagnetic (AF), transition, and paramagnetic (PM) regions were determined by linear fits of the lattice parameter within each region.

Néel Transition Region		ω_s (10^{-3})	Thermal Expansion Coefficient (10^{-6}/K)		
T_N (K)	Width (K)	210 K	AF	Transition	PM
300	80	4.7	5.0 ± 0.6	-32.4 ± 1.1	25.4 ± 0.6

of the lattice parameter as a function of time following photoexcitation at four temperatures: 40 K and 100 K (which are within the antiferromagnetic region for this film), 210 K (which is at the start of the transition to the paramagnetic phase), and 320 K (which is above the Néel transition). Measurements were made at several laser fluences ranging from 6.7 mJ/cm^2 to 52.1 mJ/cm^2. At 320 K, the response to the laser pump is consistent with what would be expected from a material with positive thermal expansion: the laser pulse excites charges in the system, which transfer energy to the lattice within 100 ps. The system relaxes back to the initial temperature ground state on time scales consistent with heating in a metallic film (about 10 ns), with the lattice parameter following an exponential decay curve with time constant of about 370-400 ps. At 40 K, there is similar behavior of an increase in lattice parameter withing the first 100 ps, however the magnitude of the change in lattice parameter is considerably lower. This is consistent with a thermal expansion coefficient in the antiferromagnetic phase that is much smaller than in the paramagnetic phase.

The measurements at 210 K, at the start of the antiferromagnetic-paramagnetic transition which exhibits negative thermal expansion, reflect the difference between this material and others that exhibit positive thermal expansion. For the lowest fluence (6.7 mJ/cm^2), we see an immediate decrease in lattice parameter following photoexcitation and then relaxation back to the initial state, consistent with heating within the negative thermal expansion region. At 19.6 mJ/cm^2 there is similarly a decrease in lattice parameter, however the minimum value is not reached

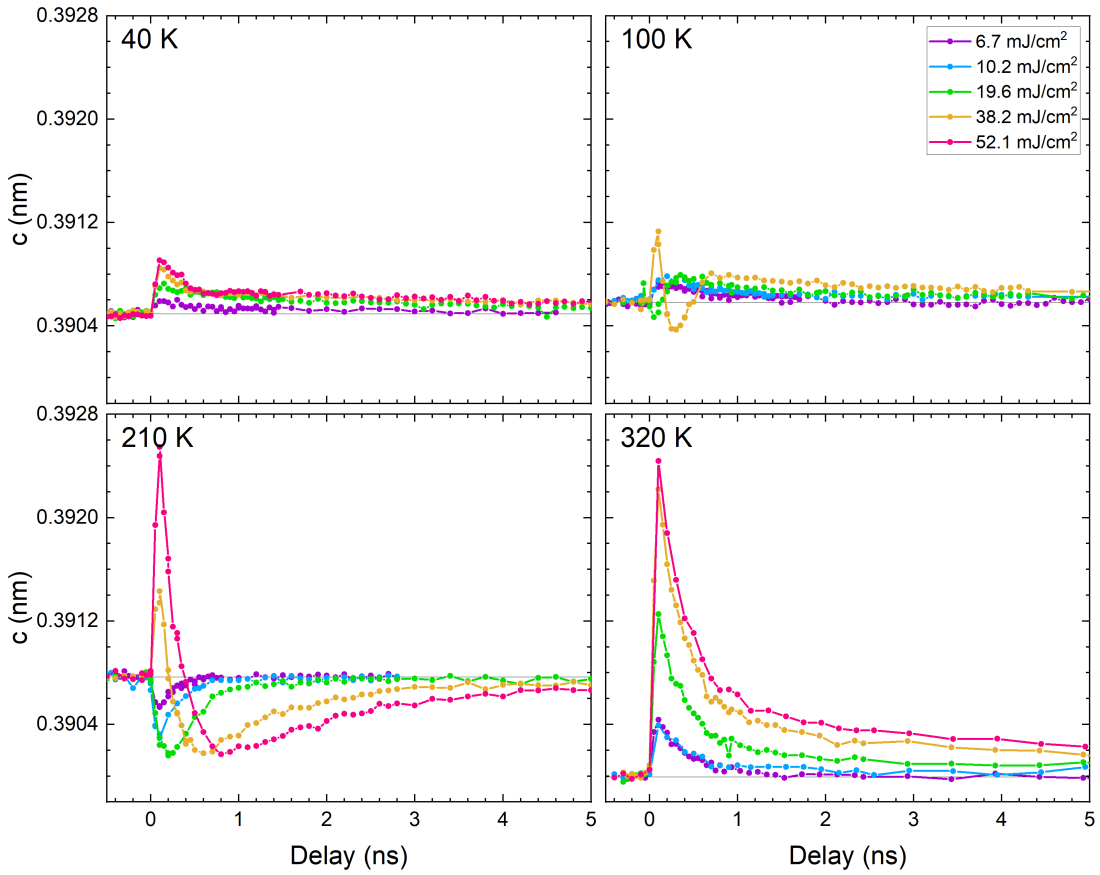

Figure 4.11: Out-of-plane lattice parameter for a 21.5 nm $Mn_3Cu_{0.7}Ge_{0.3}N$ film following photoexcitation at different temperatures and laser fluences, found from time-resolved x-ray diffraction measurements of the (002) Bragg peak. Horizontal black lines for each temperature indicate the ground state lattice parameter, found by an average of the peak positions before time zero (photoexcitation) at that temperature. The lattice parameter was calculated from the (002) peak position fit to a Voigt profile.

until about 200 ps following photoexcitation, suggesting that the laser has heated the system to just above the ordering temperature and as it cools, there is an initial contraction following by expansion. At 38.2 mJ/cm^2 and 52.1 mJ/cm^2, there is an increase in lattice parameter within the first 100 ps followed by a quick decrease to smaller lattice parameter than the initial value until the minimum is reached at 600 ps and 800 ps respectively before relaxing back to the ground state. For these higher fluences, we can explain this as heating the lattice to temperatures above

the Néel transition where the lattice parameter is larger than the initial value. On these time scales, following photoexcitation, the lattice response can be qualitatively considered as a quasi-static measurement of lattice temperature. If the laser fluence was high enough to heat the lattice above 300 K, there is an initial decrease in lattice parameter followed by an increase as the system cools from 300 K to 210 K.

At 100 K, low fluences that do not increase the system temperature into the negative thermal expansion region look similar to the measurements made at 40 K. At 19.6 mJ/cm^2, there is an initial decrease in lattice parameter followed by an increase, indicating that the lattice temperature at 100 ps is within the negative thermal expansion region and the recovery proceeds as an increase in lattice parameter followed by a decrease. At 38.2 mJ/cm^2, the lattice temperature reaches temperatures in the paramagnetic phase with lattice parameter greater than the initial,

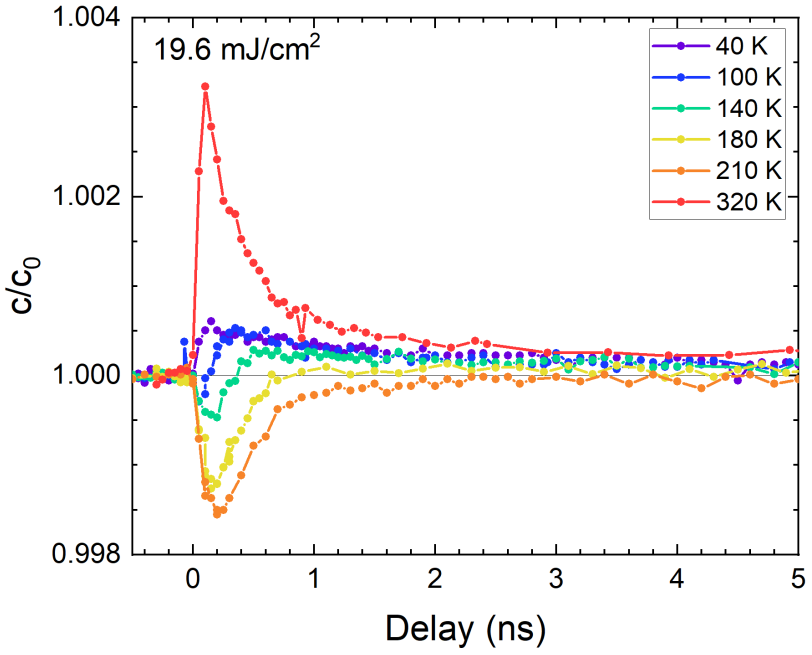

Figure 4.12: Normalized out-of-plane lattice parameter for a 21.5 nm $Mn_3Cu_{0.7}Ge_{0.3}N$ film following photoexcitation at different temperatures for a single laser fluence 19.6 mJ/cm^2, found from time-resolved x-ray diffraction measurements. Data are normalized to the lattice parameter in the static ground state temperature for each scan.

so the recovery proceeds with a decrease, then increase, then decrease. Fig. 4.12 shows the out-of-plane lattice parameter normalized to the initial ground state for six temperatures at a single laser fluence of 19.6 mJ/cm^2.

Quantitatively, it is more difficult to directly map a lattice temperature to the lattice parameter. In the initial ground state (prior to photoexcitation), the lattice parameter is consistent with the static measurements, as we see with the blue data points in Fig. 4.10. In the static measurements, the local minimum in lattice parameter just above the Néel transition at around 300 K is at about 0.38995 nm and the local maximum just below the Néel transition at around 210 K is at about 0.39076 nm. The lattice parameter in three of the fluences at 210 K should reach this minimum, however the observed minimum reach in all three fluences is about 0.39016 nm. For the highest measured fluence at 100 K, we would also expect to reach the same minimum, but instead the minimum reached is about 0.39036 nm. That same data set has a local maximum at about 700 ps which is about 0.39081 nm, higher than the value expected of 0.39076 nm. So while the quasi-static model explains the lattice response qualitatively, the lattice parameters cannot directly map onto the static curve. One explanation for this is the likelihood that we are also heating the substrate below the film with the laser pulse, which results in an increase in the substrate lattice parameter. This would likely strain the film, resulting in an increase in lattice parameter from what we might expect. We have not measured how strain in the film influences the transition, but it is possible to see shifts in the temperature ranges and different coefficients of thermal expansion.

4.3 Thin Film $Mn_3Cu_{0.9}Ni_{0.1}N$

Another compound of interest in this work is $Mn_3Cu_{0.9}Ni_{0.1}N$. Fig. 4.3 shows the bulk behavior from [167], with two regions of magnetovolume effects. One region is just below 100 K with significant positive thermal expansion: an increase of almost 0.4% in lattice parameter. The

second region at about 150 K is a negative thermal expansion region or around 0.35%. This suggests three different magnetic phases in the material. In that work, the lower temperature transition is shown to be a coexistence of two cubic phases with different lattice parameters rather than a gradual shift in the lattice parameter, which suggests that the lower temperature transition is a first-order transition. There is evidence in bulk of similar compounds of this being a magnetic transition with an increase in magnetization, suggesting that the transition is one to a ferrimagnetic or ferrimagnetic state at low temperature [164, 195, 201, 203].

4.3.1 Film Characterization

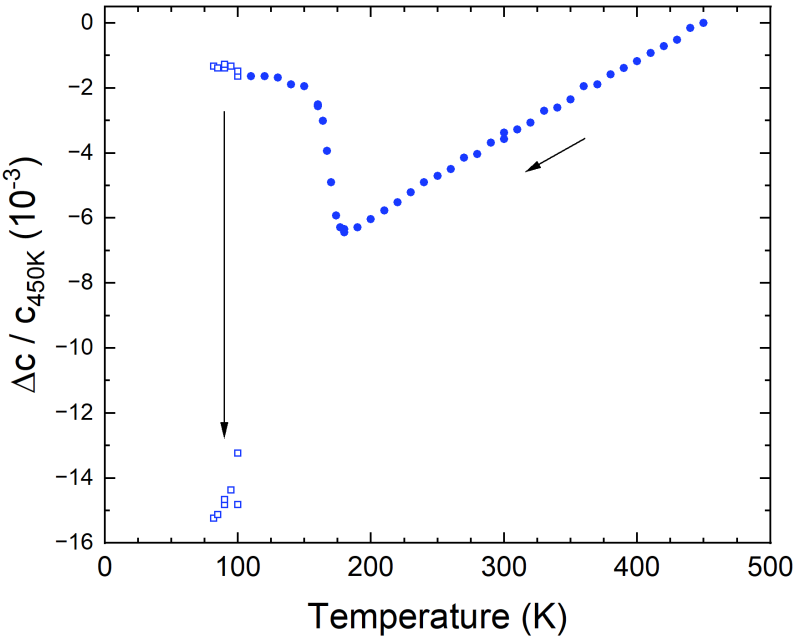

Figure 4.13: Out-of-plane thermal expansion of a 30 nm $Mn_3Cu_{0.9}Ni_{0.1}N$ film measured during cooling. Closed circular data points are calculated from the (002) peak position fit to a Voigt profile. The open square data points are calculated from a weighted average of the peak positions for a fit to two Voigt profiles.

Fig. 4.13 shows the measured out-of-plane lattice parameter normalized to the 450 K value for a 30 nm $Mn_3Cu_{0.9}Ni_{0.1}N$ film deposited by sputtering on a MgO (001) substrate.

Qualitatively, this is very similar to what was observed in bulk. The transition exhibiting negative thermal expansion is centered at about 167 K and occurs over a temperature range of about 25 K. The lattice parameter decreases by about 0.5% over this transition. A second transition is observed at lower temperature, at about 90 K over a temperature range of about 30 K (the limits of temperature ranges available prevent a more exact measurement of the transition temperature). The normalized lattice parameters shown are Voigt profile fits for temperatures above 110 K. Below this temperature, the diffraction was fit to two Voigt profiles and the lattice parameters corresponding to both are plotted.

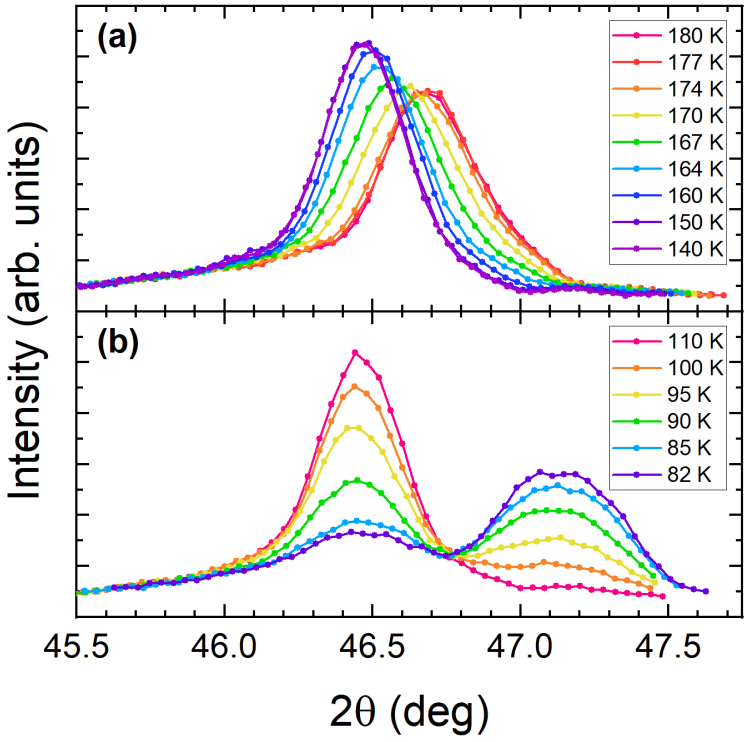

Figure 4.14: X-ray diffraction of the (002) peaks of a 30 nm $Mn_3Cu_{0.9}Ni_{0.1}N$ film through both transitions while cooling. (a) The higher temperature transition exhibits negative thermal expansion, with a shift in the Bragg peak to higher angle as temperature is increased. (b) The lower temperature transition shows the coexistence of two cubic or tetragonal phases with different lattice parameters.

Fig. 4.14 shows the (002) x-ray diffraction peaks for these two transitions. Each transition

is similar to what is seen in bulk, with a shift in the Bragg peak during the higher temperature transition and two distinct peaks during the lower temperature transition. This lower temperature transition exhibits a much larger change in out-of-plane lattice parameter: an increase of almost 1.5% when warming through the transition. Since the film is strained in-plane and cannot expand or contract in the same way, this suggests the total volume change across this transition is consistent with bulk, however the change in volume is entirely in the out-of-plane direction rather than equally in all three dimensions.

Table 4.3: Properties of negative thermal expansion in a $Mn_3Cu_{0.9}Ni_{0.1}N$ film determined from x-ray diffraction data taken while cooling temperature. The FiM-AF Transition refers to the lower temperature transition between the ferrimagnetic and antiferromagnetic phases. The thermal expansion coefficients in the antiferromagnetic (AF), transition, and paramagnetic (PM) regions were determined by linear fits of the lattice parameter within each region.

FiM-AF Transition		ω_s (10^{-3})	Néel Transition		ω_s (10^{-3})
T_{FiM} (K)	Width (K)	80 K	T_N (K)	Width (K)	150 K
~90	~30	~ -6.5	181	24	5.2

Thermal Expansion Coefficient (10^{-6}/K)		
AF	Néel Transition	PM
-7.5 ± 1.5	-245 ± 18	24.0 ± 0.2

Table 4.3 summarizes the parameters determined from this film. The lower temperature transition properties are less well studied due to the limits of temperature available on the x-ray diffractometer. We assume this to be a transition between ferrimagnetic and antiferromagnetic states due to the expectation from bulk and magnetometry measurements that will be discussed later and are shown in Fig. 4.16 and refer to the low temperature phase as ferrimagnetic, however it is not clear whether the low temperature phase is ferromagnetic or ferrimagnetic. Note that the spontaneous volume magnetostriction for the two transitions have the opposite sign, as the lattice parameter at low temperature is smaller than would be expected from phononic thermal

expansion and in the antiferromagnetic phase is larger than would be expected from phononic thermal expansion. These values were determined again by extrapolating the thermal expansion from the paramagnetic phase above the magnetic ordering temperature, which is less linear below 100 K, so the estimation of ω_s at 80 K is likely slightly larger in magnitude than the real value for this film.

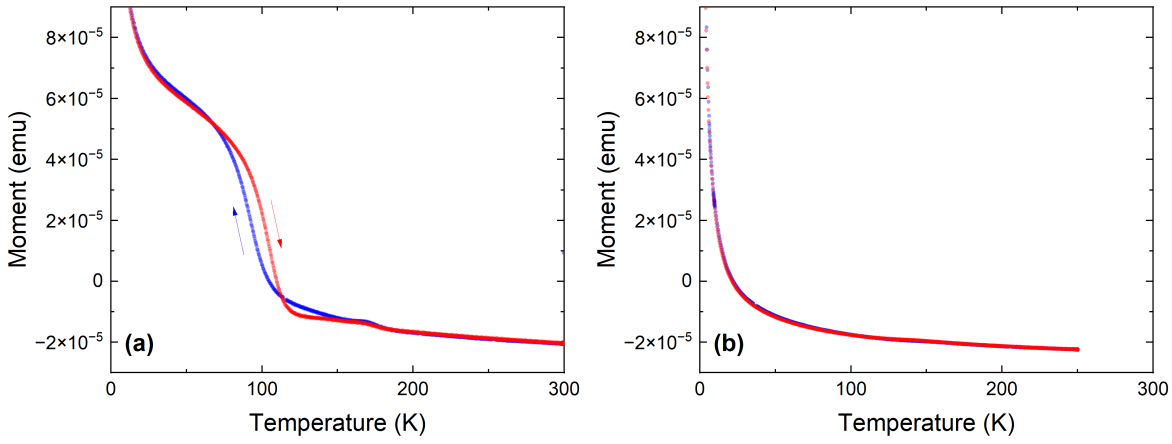

Figure 4.15: SQUID VSM measurements of (a) a 30 nm $Mn_3Cu_{0.9}Ni_{0.1}N$ film grown on MgO (001) and of (b) a MgO (001) substrate. Blue data points were measured during cooling and red during warming.

Fig. 4.15(a) shows the SQUID VSM measurement of moment vs. temperature for the 30 nm $Mn_3Cu_{0.9}Ni_{0.1}N$ film grown on a MgO (001) substrate in the presence of a 0.2 T in-plane field. This measurement includes contributions from the film, the substrate, and the sample holder, so a measurement of a MgO (001) substrate in the sample holder in the same field is included in Fig. 4.15(b). The MgO substrate exhibits a significant increase in moment at low temperature and a diamagnetic response at higher temperature which can be seen in the overall measurement. Because this measurement is a different substrate, it is not the exact background of the sample measurement in Fig. 4.15(a), however the magnetization for just the film is approximated in Fig. 4.16 by subtracting the substrate measurement from the total measurement. The two transitions seen in thermal expansion are visible in the magnetization measurement. The lower temperature transition can be seen here as a hysteretic transition between

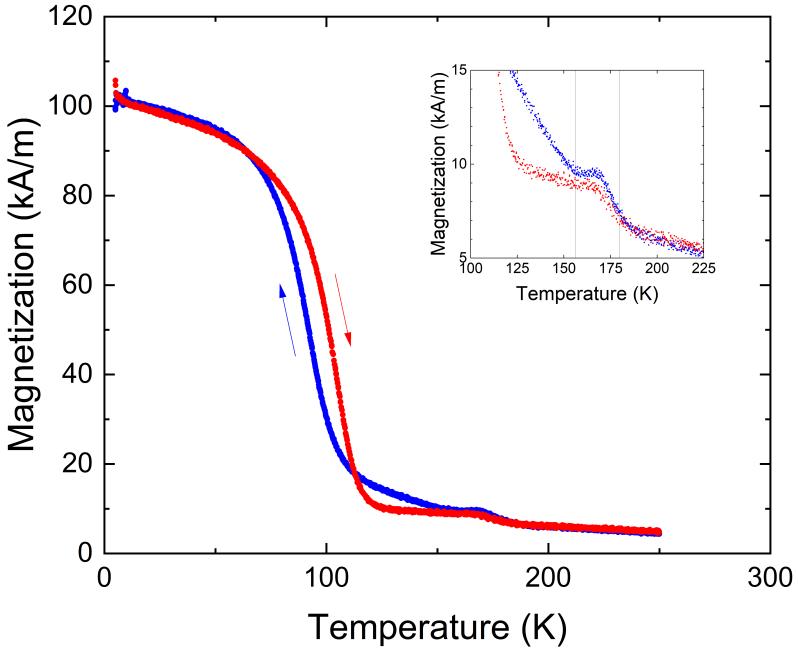

Figure 4.16: Magnetization measurement of a 30 nm $Mn_3Cu_{0.9}Ni_{0.1}N$ film with substrate and background subtracted in the presence of a 0.2 T in-plane field. The inset shows the magnetization near the antiferromagnetic-paramagnetic transition with vertical lines at 156 K and 180 K, the boundaries of the antiferromagnetic-paramagnetic transition. Blue data points were measured during cooling and red during warming.

a low temperature high moment phase and a moderate temperature low moment phase. The transition temperatures, found by taking the derivative with respect to temperature across and fitting the peaks, are $T_{\text{FiM-AF,cool}} = 97$ K and $T_{\text{FiM-AF,warm}} = 110$ K, giving a hysteresis width of approximately 13 K. The second transition between the antiferromagnetic and paramagnetic phases can be seen as a peak in the magnetization. The inset of Fig. 4.16 shows this more clearly, with vertical lines at 156 K and 180 K, the boundaries of the antiferromagnetic-paramagnetic transition as determined from thermal expansion data in Fig. 4.13.

A second 30 nm $Mn_3Cu_{0.9}Ni_{0.1}N$ film was patterned into a Hall cross by UV lithography and resistivity measurements along the (100) film direction with no applied field were made, shown in Fig. 4.17. This measurement is similar to the resistivity measurement for a 30 nm

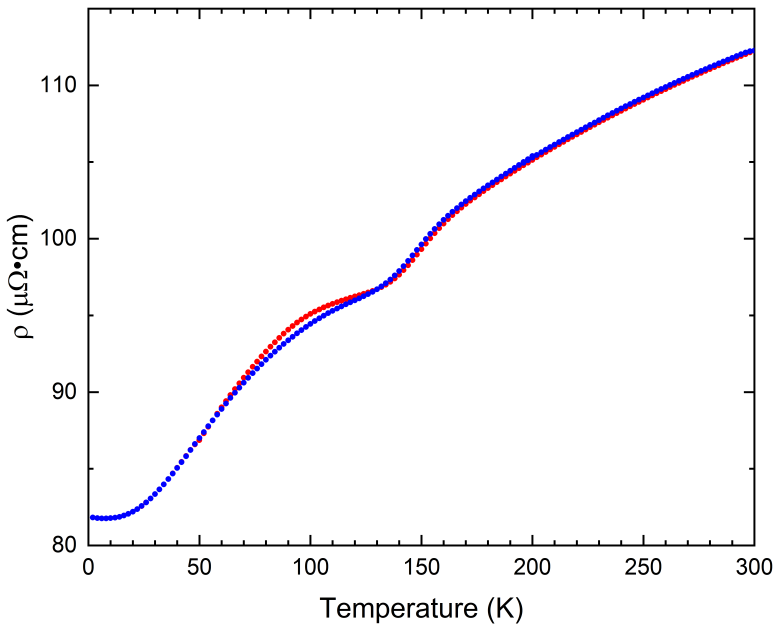

Figure 4.17: Resistivity measurement of a 30 nm $Mn_3Cu_{0.9}Ni_{0.1}N$ film with no applied field. Current and voltage were measured along the (100) film direction. Blue data points were measured during cooling and red during warming.

$Mn_3Cu_{0.9}Ge_{0.1}N$ from Fig. 4.9(a). There is an increase in resistivity at the antiferromagnetic-paramagnetic transition, but no large drop as could be expected from bulk measurements. There is also a small hysteresis seen where the lower temperature transition is expected.

We have presented the thermal expansion, magnetization, and resistivity of a 30 nm $Mn_3Cu_{0.9}Ni_{0.1}N$ film here. As with bulk, this film exhibits two magnetostructural transitions: a lower temperature first-order hysteretic transition between a ferrimagnetic (or ferromagnetic) phase and an antiferromagnetic phase and a higher temperature transition that exhibits negative thermal expansion between the antiferromagnetic phase and a paramagnetic phase. The ferrimagnetic-antiferromagnetic transition exhibits a magnetovolume change comparable to bulk, but entirely in the out-of-plane direction. The antiferromagnetic-paramagnetic transition exhibits a change in lattice parameter comparable to the bulk change in lattice parameter, meaning a

smaller overall change in the volume of the unit cell. This negative thermal expansion has a very large negative coefficient of thermal expansion of -245 ± 18 (10^{-6}/K) over a narrow temperature range of 24 K (between 156 K and 180 K). In the next section, we will present some dynamic measurements of the lattice parameter following photoexcitation in a $Mn_3Cu_{0.9}Ni_{0.1}N$ film.

4.3.2 Laser-Pump X-Ray-Probe Experiment of a $Mn_3Cu_{0.91}Ni_{0.09}N$ film

Static measurements of structural and magnetic properties of a $Mn_3Cu_{0.9}Ni_{0.1}N$ film have shown the presence of three magnetic phases: ferrimagnetic (or ferromagnetic), antiferromagnetic, and paramagnetic. The transitions between the phases are quite different: The ferrimagnetic-antiferromagnetic transition is a first-order hysteretic transition with the coexistence of two cubic or tetragonal phases while the antiferromagnetic-paramagnetic transition is non-hysteretic and a more gradual shift in the lattice parameter exhibiting negative thermal expansion. The out-of-plane lattice parameter for the film exhibits a similar magnitude change across as in measurements of the cubic lattice parameter in bulk, but in-plane directions are strained so the overall volume magnetostriction is about 1/3 of the bulk volume magnetostriction. In contrast, during the ferrimagnetic-antiferromagnetic transition, the out-of-plane lattice parameter changes by significantly more than the bulk lattice parameter, so that the volume magnetostriction across this transition is about equal in the film and in bulk. This presents another interesting system in which to study the dynamics of magnetic ordering with time-resolved x-ray diffraction following photoexcitation. These dynamics can be studied within each of the ferrimagnetic, antiferromagnetic, and paramagnetic phases as well as during the transitions between them.

Fig. 4.18 shows the static out-of-plane thermal expansion for a 32.8 nm film of composition $Mn_3Cu_{0.91}Ni_{0.09}N$, determined by Voigt profile fits to x-ray diffraction data. For the ferrimagnetic to antiferromagnetic transition where there is a coexistence of two tetragonal phases and therefore two peaks, the data was fit to two Voigt peaks and the lattice parameters of both peaks were included with open triangular data points. The closed triangular data points reflect averages

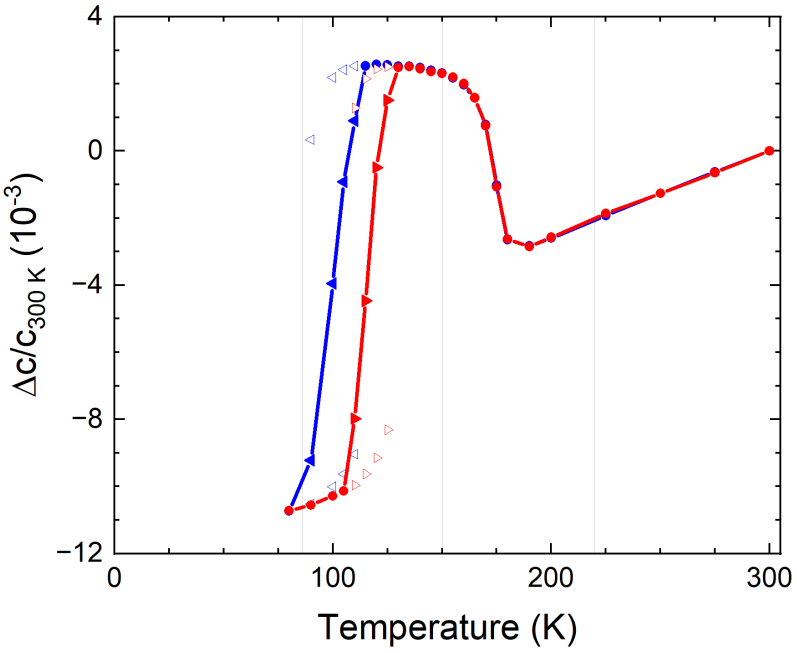

Figure 4.18: Out-of-plane thermal expansion of a 32.8 nm $Mn_3Cu_{0.91}Ni_{0.09}N$ film. Blue data points are measured during cooling and red during warming. Circular data points are calculated from the (002) peak position fit to a Voigt profile. At the low temperature transition, x-ray diffraction data was fit to two Voigt profiles and the lattice parameter from each peak is shown with open triangular data points. The closed triangular data points at those temperatures are a weighted average of the two peak positions. The gray vertical lines in the graph are at 86 K, 150 K and 220 K.

of the two lattice parameters weighted by the amplitude of the peak fits. For this film, we see both phase transitions. The negative thermal expansion region that marks the antiferromagnetic-paramagnetic transition occurs in a temperature range of about 160 K to 180 K. We also see the lower temperature hysteretic ferrimagnetic to antiferromagnetic transition with the two coexisting tetragonal phases. During cooling, this transition temperature is about 100 K, and during warming, it is about 116 K. Table 4.4 summarizes the parameters determined from this thermal expansion data. For the ferrimagnetic-antiferromagnetic transition, the transition temperature and width reflect the region down to 80 K during cooling and up to 130 K during warming in which double peaks were observed. The transition temperature when roughly half the film is in each

phase is about 100 K during cooling and 116 K during warming, giving a hysteresis width of 16 K. The Néel transition is narrower in this film, resulting in a larger magnitude thermal expansion coefficient over the transition when compared to the $Mn_3Cu_{0.9}Ni_{0.1}N$ film in the previous section. However the thermal expansion in the antiferromagnetic and paramagnetic phases and the calculated magnetostriction is comparable.

Table 4.4: Properties of negative thermal expansion in a $Mn_3Cu_{0.91}Ni_{0.09}N$ film determined from x-ray diffraction data. The FiM-AF Transition refers to the lower temperature transition between the ferrimagnetic and antiferromagnetic phases. The thermal expansion coefficients in the antiferromagnetic (AF), transition, and paramagnetic (PM) regions were determined by linear fits of the lattice parameter within each region.

FiM-AF Transition		ω_s (10^{-3})	Néel Transition		ω_s (10^{-3})
T_{FiM} (K)	Width (K)	80 K	T_N (K)	Width (K)	150 K
105	50	-5.1	185	23	6.2

Thermal Expansion Coefficient (10^{-6}/K)		
AF	Néel Transition	PM
-7.6 ± 1.2	-289 ± 17	25.8 ± 0.2

Time-resolved x-ray diffraction measurements were performed at beamline 7ID-C at the APS (see Section 2.6.2) following photoexcitation with an 800 nm Ti:Sapphire laser delivered in 100 fs pulses with a spot size of 0.27 mm by 0.34 mm. The x-ray energy was 11.0 keV, with a pulse width of about 100 ps and spatial resolution on the μm scale. Fig. 4.19 shows measurements of the lattice parameter as a function of time following photoexcitation at three temperatures (with data from 86 K below both transitions shown on two time scales). The lattice parameter was found by Voigt profile fits of the film (002) peak. For an initial ground state at 86 K, some scans after photoexcitation exhibited the double peak expected from the lower temperature transition, so the lattice parameter was found by fitting to two Voigt profiles and averaging the peak positions weighted by their amplitudes.

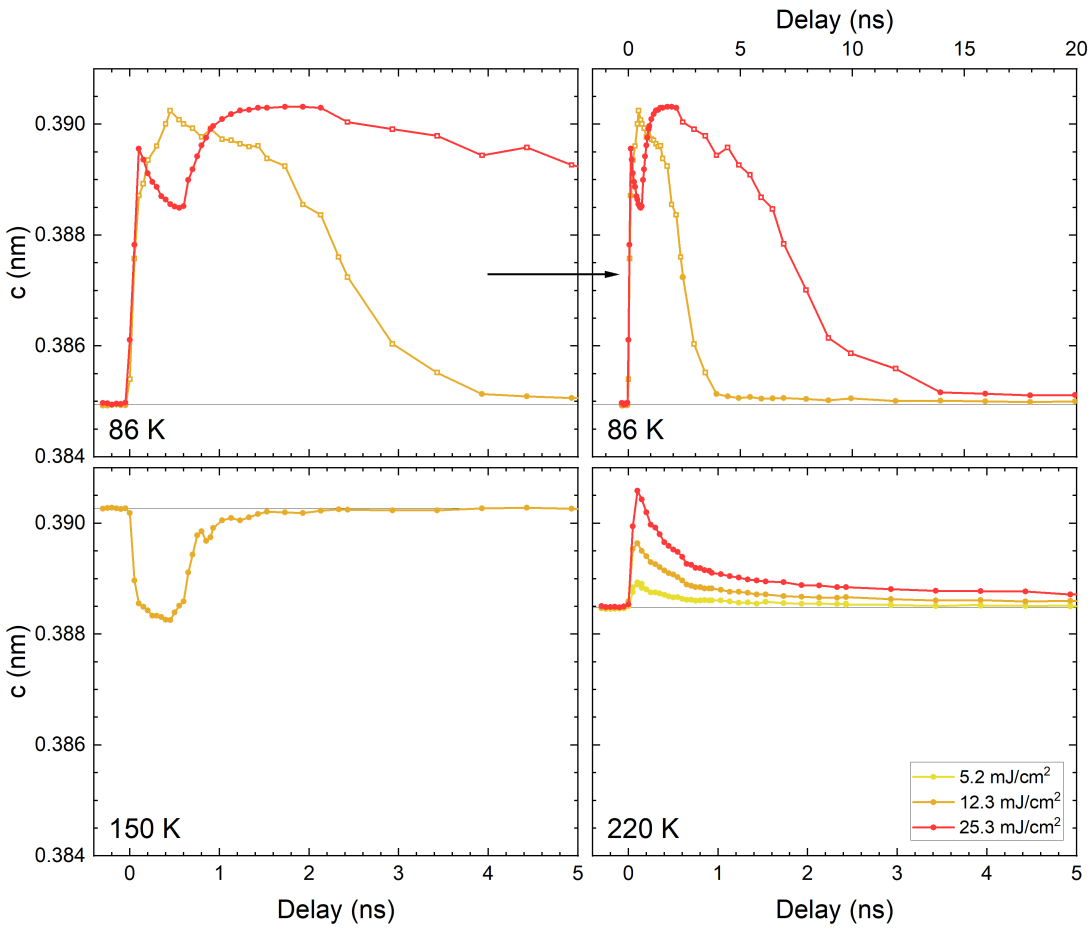

Figure 4.19: Out-of-plane lattice parameter for a 32.8 nm $Mn_3Cu_{0.91}Ni_{0.09}N$ film following photoexcitation at different temperatures and laser fluences, found from time-resolved x-ray diffraction measurements of the (002) Bragg peak. The top right graph is a duplicate of the top left at 86 K with lattice response shown on a longer time scale. Horizontal black lines for each temperature indicate the ground state lattice parameter, found by an average of the peak positions before time zero (photoexcitation) at that temperature. The lattice parameter was calculated from the (002) peak position fit to a Voigt profile. The open square data points following photoexcitation from 86 K are calculated from a weighted average of the peak positions for a fit to two Voigt profiles.

At 220 K, the lattice response is consistent with what we would expect from most materials with positive thermal expansion and consistent with the $Mn_3Cu_{0.7}Ge_{0.3}N$ film measured earlier. The laser pump transfers heat to the system which increases the lattice temperature and the lattice spacing increases before relaxing back to the initial ground state. At 150 K, the lattice response is consistent with an increase in lattice temperature to about 220 K within 100 ps. As the system

cools, the lattice parameter initially contracts and then quickly expands, presumably as the system goes through the Néel transition and magnetic order is reestablished.

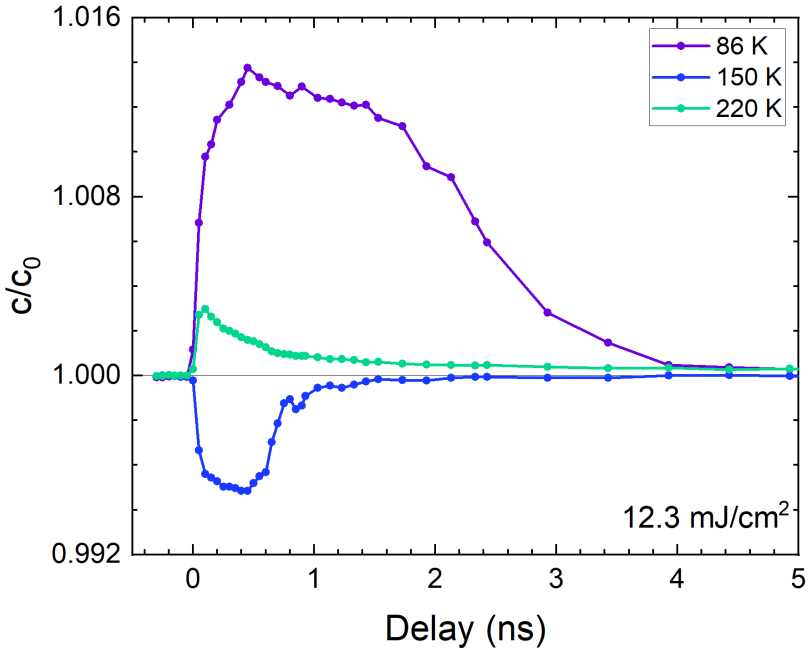

Figure 4.20: Normalized out-of-plane lattice parameter for a 32.8 nm $Mn_3Cu_{0.91}Ni_{0.09}N$ film following photoexcitation at different temperatures for a single laser fluence 12.3 mJ/cm^2, found from time-resolved x-ray diffraction measurements. Data are normalized to the lattice parameter in the static ground state temperature for each scan.

At 86 K, the film is in the low temperature ferrimagnetic state. The photoexcitation of 12.3 mJ/cm^2 is enough to excite the film into the Néel transition region within 100 ps, followed by cooling with an initial increase in lattice parameter until 450 ps and then decrease. The system cools through the ferrimagnetic-antiferromagnetic transition from about 1.5 ns to 4 ns. The photoexcitation of 25.3 mJ/cm^2 excites the film above the Néel transition to around room temperature within 100 ps. From here, the lattice responds by contracting until the Néel transition is reached and it expands from about 600 ps to 1.2 ns. The ferrimagnetic-antiferromagnetic transition occurs from about 2.5 ns to 14 ns, which interestingly is longer than the recovery for the lower fluence. It is interesting to note that when excited into the paramagnetic phase from this

ferrimagnetic phase, the lattice response shows that as the film cools, it does fully reorient into the antiferromagnetic phase prior to cooling into the low temperature ferrimagnetic phase.

Fig. 4.20 presents the out-of-plane lattice parameter at all three initial temperatures normalized to the initial lattice parameter at that temperature for a pump fluence of 12.3 mJ/cm^2. Reflected here is the 0.5% decrease in lattice parameter for the Néel transition and about 1.2% increase in lattice parameter for the low temperature transition. This experiment required repeated and extended photoexcitation of the film through these phases. Materials with large structural changes often will degrade with repeated cycling, as was seen in bulk Mn_3ZnN with a 1.5% change in lattice parameter, where microcracks appeared and the transition shifted to higher temperature with each successive cycle [183]. For this experiment, repeated and extended cycling occurred with the photoexcitation from 86 K, but there appears to be no shift in the transition temperatures and no degradation in the film quality measured by x-ray diffraction.

4.4 Conclusion

We have successfully fabricated thin films of $Mn_3Cu_{1-x}Ge_xN$ and $Mn_3Cu_{0.9}Ni_{0.1}N$ which exhibit magnetovolume effects including negative thermal expansion by sputtering. X-ray diffraction measurements of $Mn_3Cu_{1-x}Ge_xN$ films demonstrate out-of-plane thermal expansion coefficients in the negative thermal expansion regions up to -57.9 ± 2.1 (10^{-6})/K over temperature ranges of over 100 K. A much larger effect is seen for the $Mn_3Cu_{0.9}Ni_{0.1}N$ films, though this is over a smaller range of temperature. In addition, we see a lower temperature hysteretic transition in $Mn_3Cu_{0.9}Ni_{0.1}N$ which exhibits an almost 1.5% increase in lattice parameter with warming. Resistivity and magnetization measurements were made which support the existence of the expected ferrimagnetic and antiferromagnetic magnetic phases expected in these materials in bulk. Laser-induced dynamics measurements probed with x-ray diffraction were conducted on two films, $Mn_3Cu_{0.7}Ge_{0.3}N$ and $Mn_3Cu_{0.91}Ni_{0.09}N$, on ns time scales, which demonstrate a

lattice response to photoexcitation within the first 100 ps followed by a quasi-static progression of lattice parameter consistent with cooling of the lattice. The large structural changes withstood repeated cycling during this experiment without changes to the observed material properties.

There are several avenues for future work on these films. One would be to fabricate films on different substrates and substrate orientations to determine the effects of strain on the transition and magnetic ordering and how that influences the negative thermal expansion. This is one way of providing more insight into the coupling of structural and magnetic degrees of freedom possible with thin films. Temperature-dependent in-plane measurements would be useful to confirm the difference in total volume magnetostriction in each transition in films vs. bulk. Neutron diffraction measurements can confirm the existence of the Γ^{5g} spin structure and how it is influenced by the strain and shape anisotropy in films as well as determine the spin structure in the low temperature ferromagnetic or ferrimagnetic phase. And the most interesting prospect for future work would be ultrafast pump-probe measurements on 100 fs to ps time scales. On these time scales, the laser pulse would induce a quick demagnetization before the lattice could respond and we would be able to observe nonequilibrium behavior and transient states as the lattice is allowed to evolve without the influence of the spins. The evolution and recoupling of the degrees of freedom would proceed on different time scales which could be measured and separated.

Acknowledgements

Chapter 4, in part, is currently being prepared for submission for publication of the material coauthored by Sheena K. K. Patel, Stjepan B. Hrkac, Jeffrey A. Brock, Nelson Hua, Haidan Wen, Donald Walko, Oleg G. Shpyrko, and Eric E. Fullerton. The dissertation author was the primary investigator and author of this material. This research used resources of the Advanced Photon Source, a U.S. Department of Energy (DOE) Office of Science user facility operated for the DOE Office of Science by Argonne National Laboratory under Contract No.

DE-AC02-06CH11357. This work was performed in part at the San Diego Nanotechnology Infrastructure (SDNI) of UC San Diego, a member of the National Nanotechnology Coordinated Infrastructure, which is supported by the National Science Foundation (Grant ECCS-2025752).

Chapter 5

Thin Film Iron Rhodium (FeRh)

5.1 Introduction

FeRh is a material that has been of increasing interest in the past few decades, primarily because it exhibits a first-order phase transition between a low temperature antiferromagnetic state and a higher temperature ferromagnetic state, which couples magnetic, electric, and structural degrees of freedom. There are other systems that exhibit both antiferromagnetic and ferromagnetic phases and interesting transitions for potential study [204–206], however these systems usually contain rare earth materials or are rare earth-doped, with transitions at cryogenic temperatures. The phase transition in FeRh is near or a little above room temperature and highly tunable with composition, which makes it both easier to study and more useful for applications. This potential for use ranges anywhere from implementation in magnetic hard drives [207, 208] to use as high-contrast labels inside the human body in MRIs [11, 12]. Current areas of research usually focus on FeRh properties in confined geometries, as technological applications often require nanoscale features. The work in this chapter includes measurements made at UC San Diego, at the High Flux Isotope Reactor (HFIR) at the Oak Ridge National Laboratory (ORNL), the High Field Magnet Laboratory (HFML), the European Synchrotron Radiation Facility (ESRF), and

the Spallation Neutron Source (SNS) at the ORNL . The first of the two primary experiments involves resistivity measurements, x-ray magnetic circular dichroism (XMCD) measurements, and simulations of the phase transition to understand the magnetic phase diagram of FeRh, and the other includes polarized neutron reflectometry measurements of FeRh films and stripes to understand how strain and disorder affects the magnetism.

5.1.1 Properties of Bulk FeRh

The first reported measurements in roughly equiatomic bulk FeRh of an abrupt magnetic phase transition which was hysteretic with temperature and accompanied by a structural change were described by Fallot and Hocart in 1939 [209]. The structural change was determined by x-ray diffraction to be a uniform expansion of the CsCl crystal structure upon warming through this first-order transition, with a total volume expansion of 1-2% [210, 211]. Neutron diffraction, magnetization, and Mössbauer spectroscopy studies showed the low temperature phase to be G-type antiferromagnetic, meaning antiferromagnetic in all three cubic directions (see Fig. 1.8(g)), and the higher temperature phase to be ferromagnetic [211–213]. In the ferromagnetic phase, all spins are aligned, with Fe atom moment measured to be approximately 3.2 μ_B (where $\mu_B = \frac{e\hbar}{2m_e} = 9.274 \times 10^{-24}$ J/T is the Bohr magneton) and Rh atom moment approximately 0.9 μ_B. Early work found that in the antiferromagnetic phase, Fe atoms have moment of approximately 3.3 μ_B aligned collinearly, alternating in sign, while Rh atoms have no net moment [213, 214]. More recent calculations have suggested Fe to have moment 3.12 μ_B in the antiferromagnetic phase and 3.17 μ_B in the ferromagnetic phase while Rh has no moment in the antiferromagnetic phase and a moment of 1.05 μ_B in the ferromagnetic phase [215]. The magnetic phase transition is accompanied by a significant drop in electrical resistivity in the ferromagnetic state [211]. This is shown in Fig. 5.1, where the magnetization upon cooling (open data points) below the Curie temperature increases in the ferromagnetic phase until a transition to the antiferromagnetic phase near 350 K results in a near-zero magnetization. Resistivity measurements increase during

this transition from ferromagnetic to antiferromagnetic phase. This transition is hysteretic, so a shift in the transition to higher temperatures while warming is observed. This suggests that the phase transition in FeRh is first-order and exhibits a coupling of magnetic, electric, and structural degrees of freedom.

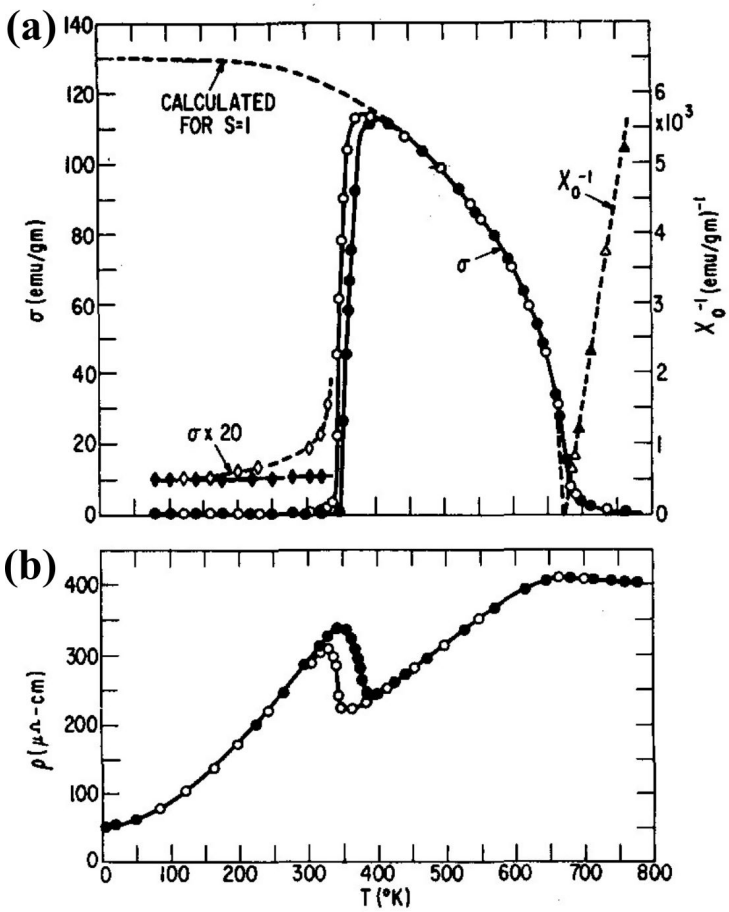

Figure 5.1: (a) Magnetization and susceptibility in a 0.5 T applied field and (b) electrical resistivity of bulk $Fe_{0.48}Rh_{0.52}$. Closed data points are taken during warming and open data points during cooling. Figure reproduced from [211] with the permission of AIP Publishing.

Fig. 5.2 shows a part of the magnetic phase diagram for bulk Fe_xRh_{1-x} as a function of temperature and x. The magnetic phase transition that is of interest in this work occurs between the antiferromagnetic phase α" and the ferromagnetic phase α'. This exists in the compositional range of approximately 48% to around 56% Fe. With increasing Fe content, the transition shifts

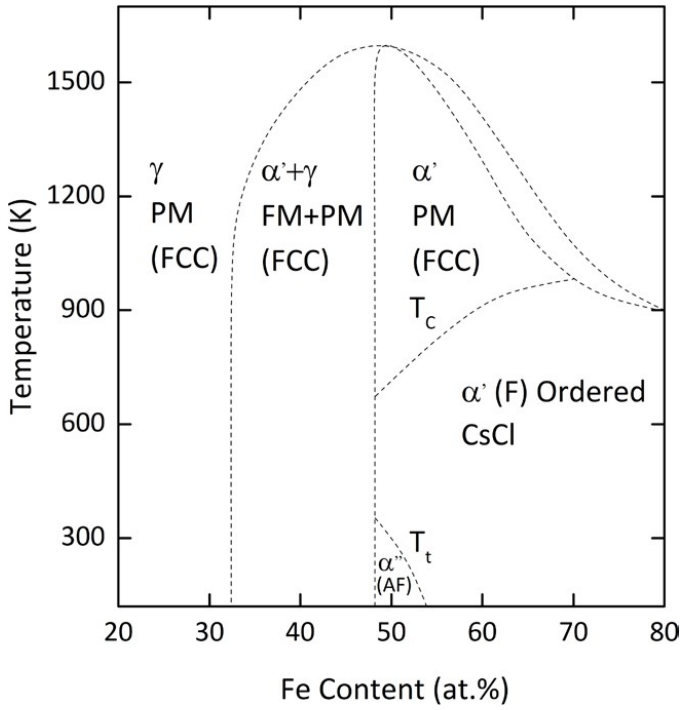

Figure 5.2: Phase diagram of bulk Fe_xRh_{1-x}. The transition of interest in this work is between the antiferromagnetic α" and ferromagnetic α' phases, seen here in the compositional range of $48\% \leq x < 53\%$. Figure reproduced with permission from [216]. Copyright 2016 by IOP Publishing Ltd.

to lower temperature, from approaching 400 K for $Fe_{0.48}Rh_{0.52}$ to 150 K at about $Fe_{0.54}Rh_{0.46}$. There is some variation on the exact range of composition and transition temperatures [216–219], but this is the accepted composition range of interest.

5.1.2 Properties of Thin Film FeRh

Since many potential implementations of FeRh into technology require confinement to much smaller length scales, we focus on studies in thin films in this work. Thin film FeRh can be grown epitaxially, including by sputtering, and exhibits the antiferromagnetic-ferromagnetic transition seen in bulk. The magnetization for one such film, a 21 nm FeRh film grown on MgO (001) and capped with 1.2 nm Pt, is shown in Fig. 5.3(a) with red and blue data for warming and cooling in a 1 T field. The transition exhibits a 20 K wide hysteresis between the low

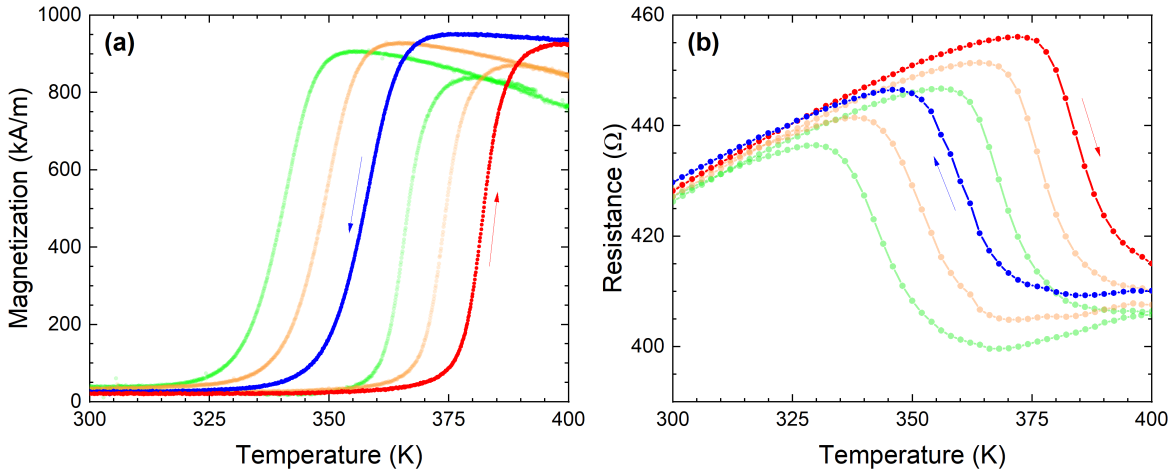

Figure 5.3: Magnetization of a 21 nm FeRh film and resistivity measured after patterning into a 50 μm wide wire of the phase transition in a 21 nm FeRh film with magnetic field applied in-plane. (a) Magnetization measurements show a hysteretic phase transition with a low-moment phase at low temperature and a high-moment phase at high temperature. (b) Electrical resistivity measurements show a high-resistance phase at low temperature and a lower-resistance phase at high temperature, with the same transition temperatures as in the magnetization data. Red data is for warming at 1 T and blue data for cooling at 1 T. Also included in orange and green are measurements at 2 T and 3 T, respectively, demonstrating a shift in the transition with applied field of about -8.5 K/T.

magnetization and high magnetization states. The hysteresis in films is broader (20 K or more) than in bulk (10 K or less [209, 220]). It is also often more of a continuous transition in films compared to the abrupt transition in bulk, especially as the film thickness is decreased. For the 21 nm thick film shown here, the width of the hysteresis is about 25 K. During both warming and cooling, most of the film transitions in a 15 K range, however the full transition is more like 40 K. This is attributed to differences in composition, structural properties, and defects affecting the quality of the films and will result in some variability in the transition properties even between two films that are grown simultaneously. Another difference is in the low but non-zero moment in the low temperature phase. In bulk, this moment was essentially zero, consistent with the entire sample reaching an antiferromagnetic phase. In films, however, there is almost always a small positive moment remaining. This is not a result of any background signal, as that is diamagnetic and has been subtracted that out as laid out in Section 2.4.3. This is attributed to an interfacial

layer of FeRh that remains ferromagnetic rather than becoming antiferromagnetic. This will be discussed further in Section 5.1.4 and Section 5.3.

Fig. 5.3(a) also includes magnetization curves for the same sample at 2 T and 3 T applied field. We see that application of a magnetic field tends to stabilize the ferromagnetic phase and shift the transition to lower temperature, shifting by 9 or 10 K per 1 T field applied. This raises the question of what happens at higher field how the energy landscape changes with temperature and applied field. The magnetic phase diagram of a film will be measured in higher fields and lower temperatures in Section 5.2.

As with bulk, the transition in thin films can also be observed in the electrical resistivity [221, 222]. Fig. 5.3(b) shows resistivity vs. temperature for the same FeRh film after patterning into a 50 μm-wide wire by UV photolithography. The drop in resistivity in a 1 T applied field occurs during warming in red in the same temperature ranges as the increase in magnetization in

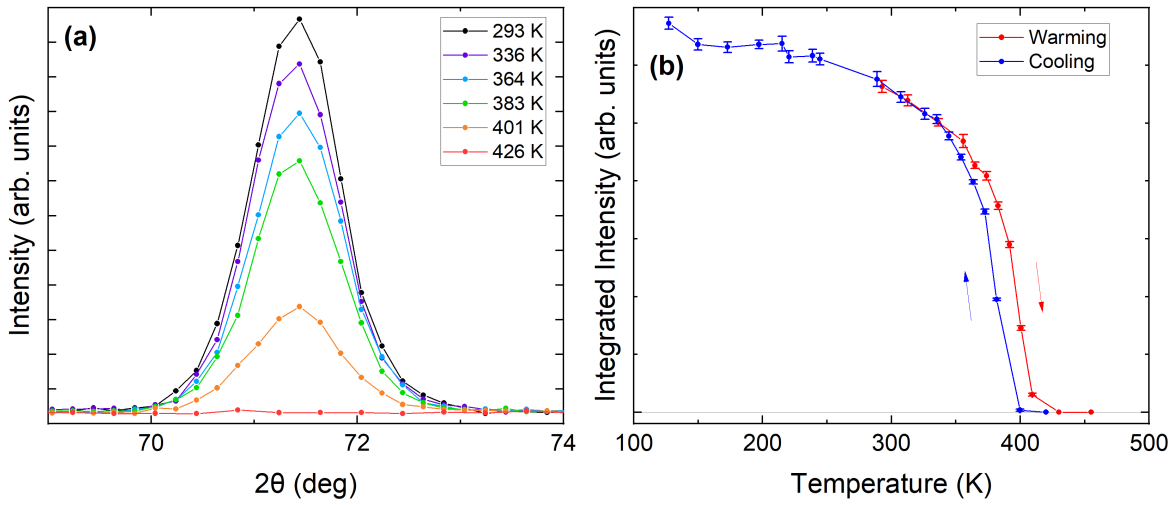

Figure 5.4: Neutron diffraction measurements of the FeRh (½ ½ ½) peak at different temperatures for a 100 nm film, measured at the High Flux Isotope Reactor (HFIR). (a) At 426 K, when the film is ferromagnetic, there is no scattering intensity observed at this location. The peak appears as the film is cooled through its transition. (b) The integrated signal intensity of the peak as a function of temperature is shown during cooling (blue data points) and warming (red data points), demonstrating the existence of the expected G-type antiferromagnetic order in the film below this hysteretic transition.

the full film. During cooling in blue, we see the increase in resistivity where the magnetization drops. The resistivity at 2 T and 3 T applied field show the same shift in the transition as was observed in the magnetization.

Fig. 5.4 presents neutron diffraction of the (½ ½ ½) peak at different temperatures for a 100 nm film taken at the CG-4C CTAX (Cold Neutron Triple-Axis Spectrometer) at the HFIR. This peak will appear for G-type antiferromagnetic materials, as discussed in Section 2.7.1, but is a forbidden peak for a ferromagnetic film, so we would expect to see it appear in the lower temperature phase when the magnetization of the film is near zero. In Fig. 5.4(a), we see that above the transition at 426 K, there is no (½ ½ ½) peak, but then it appears as the film is cooled, consistent with G-type antiferromagnetic order appearing below the hysteretic transition. Fig. 5.4(b) shows the integrated intensity of the peaks fit to a Gaussian curve, demonstrating the hysteretic nature of the transition.

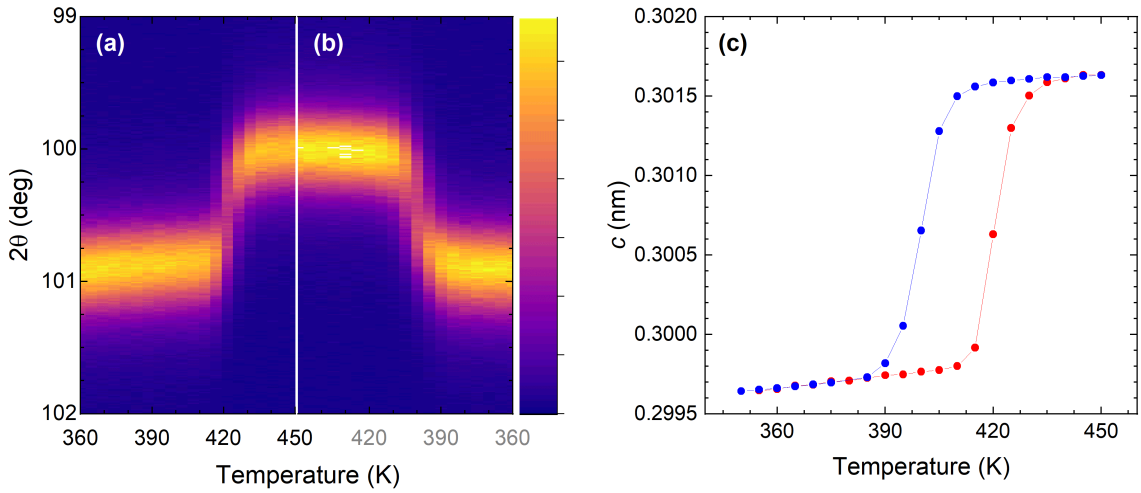

Figure 5.5: X-ray diffraction measurements of the FeRh (003) peak demonstrating a structural phase transition for a 46 nm FeRh film grown on MgO (001) during (a) warming from 360 K to 450 K and (b) cooling from 450 K to 360 K. Measurements were made with Cu Kα radiation. (c) The out-of-plane lattice parameter *c* during the phase transition during warming (red) and cooling (blue), calculated from the peak location of Gaussian fits to the x-ray diffraction peaks in (a) and (b).

In bulk FeRh, the phase transition is also seen structurally, with a 1-2% change in the

unit cell volume, equally in all three cubic directions. In thin films, the film is constrained in the in-plane directions and the unit cell has a tetragonal distortion, which will be discussed more in Section 5.1.4. The in-plane strain prevents the kind of isotropic structural transition that we see in bulk, however the phase transition can be seen out-of-plane. For an FeRh film grown on MgO (001), there is a significant expansion observed in the *c*-axis lattice parameter when warming through the transition. Fig. 5.5 shows this for a 46 nm FeRh film grown on MgO (001). In Fig. 5.5(a)-(b), we see the evolution of the FeRh (003) peak with x-ray diffraction measurements while warming from 360 K to 450 K and then cooling from 450 K to 360 K (right). The peak can be fit with a Gaussian curve at each temperature to determine the peak intensity and calculate the determine the out-of-plane lattice parameter, shown in Fig. 5.5(c). The hysteretic phase transition is clearly observed in this unconstrained dimension.

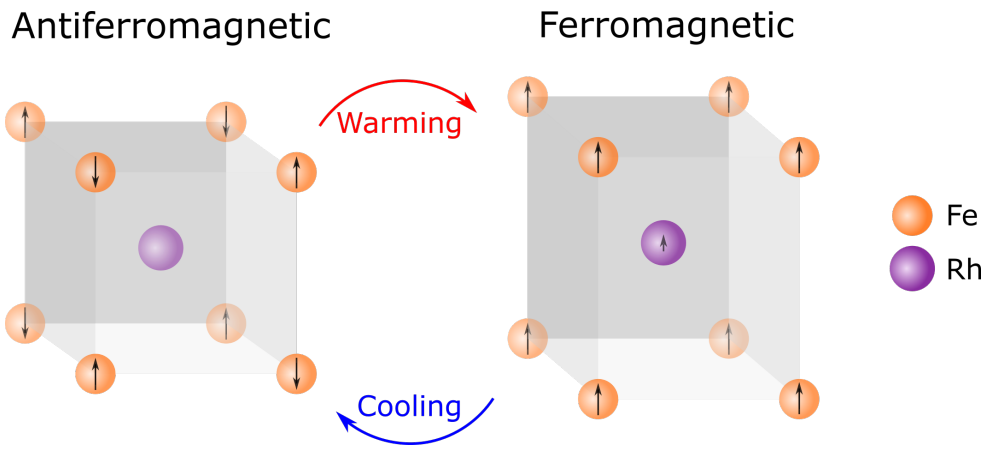

Figure 5.6: Structure and magnetic configuration of the FeRh unit cell in a thin film in the antiferromagnetic and ferromagnetic phases. In the antiferromagnetic phase, adjacent Fe moments are oriented antiparallel and Rh is non-magnetic. In the higher temperature ferromagnetic phase, the Fe and Rh atoms are all magnetic and aligned with one another. During the transition from antiferromagnetic to ferromagnetic, there is an expansion in the c-axis lattice parameter (not to scale).

Fig. 5.6 shows a summary of the phase transition in the FeRh unit cell for thin film grown in the (001) orientation. In the antiferromagnetic state, Rh is non-magnetic and Fe atoms exhibit G-type antiferromagnetic ordering, with antiferromagnetic ordering in all three cubic directions.

After the transition to the ferromagnetic state, Rh and Fe atoms are magnetic and aligned. There is also an expansion in the out-of-plane lattice parameter (not to scale) but little change in-plane due to strain upon warming into the ferromagnetic state. And as observed in magnetoresistance measurements, the antiferromagnetic state is a state of higher electrical resistance than the ferromagnetic state, resulting in a drop in resistance during the antiferromagnetic-to-ferromagnetic transition and increase during the ferromagnetic-to-antiferromagnetic transition.

5.1.3 Growth of FeRh Films

In order to observe the desired phases in an FeRh film, it must be grown with crystalline ordering. This can be achieved through many different deposition methods, including by sputtering at high temperature and post-annealing. Fig. 5.7 shows the out-of-plane x-ray characterization of a 21 nm FeRh film grown on MgO (001), the same film measured in Fig. 5.3. The θ-2θ scan in Fig. 5.7(a) shows that the film has grown in the (001) out-of-plane orientation with the FeRh (001) peak centered at 29.80 deg and the FeRh (002) peak centered at 61.88 deg. From this, we find the out-of-plane lattice parameter at room temperature to be $c = 0.2995$ nm. Rocking curves of these peaks are shown in Fig. 5.7(b). A phi scan of the MgO (200) and FeRh (100) peaks are shown in Fig. 5.8, demonstrating a 45 deg rotation of crystal orientation in-plane for FeRh atop the MgO substrate. While bulk FeRh is cubic, FeRh films grown on MgO (001) exhibit a tetragonal distortion, with in-plane compression $a_{\text{film}} < a_{\text{bulk}}$ and out-of-plane expansion $c_{\text{film}} > c_{\text{bulk}} = a_{\text{bulk}}$.

Epitaxial growth of films is best achieved with close lattice-matching to substrates, as discussed in Section 2.2.4. The most common substrates used for FeRh are MgO (001) and Al_2O_3 (0001) (c-axis sapphire). FeRh grown on Al_2O_3 (0001) grows in the (111) orientation and experiences a rhombohedral distortion [57]. Less commonly used substrates include glass/quartz [220], IBAD-MgO (MgO deposited by ion-beam assisted deposition) [223, 224], W (001) on MgO (001) [57, 225], Ge [226], $SrTiO_3$ [223], $KTaO_3$ [223], $BaTiO_3$ [227], and more. The

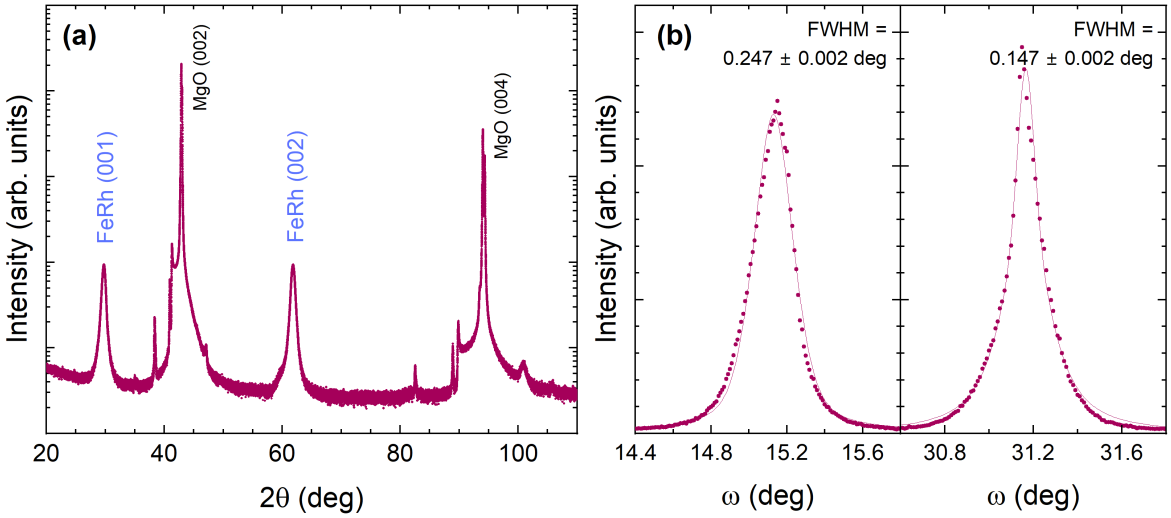

Figure 5.7: Out-of-plane x-ray diffraction characterization of a 21 nm FeRh film grown on MgO (001). (a) Out-of-plane θ-2θ scan of FeRh, showing the (001) and (002) diffraction peaks of FeRh and the (002) and (004) diffraction peaks of MgO. (b) X-ray diffraction rocking curves of the (left) (100) peak and (right) (200) peak of FeRh. Measurements were made with Cu Kα radiation.

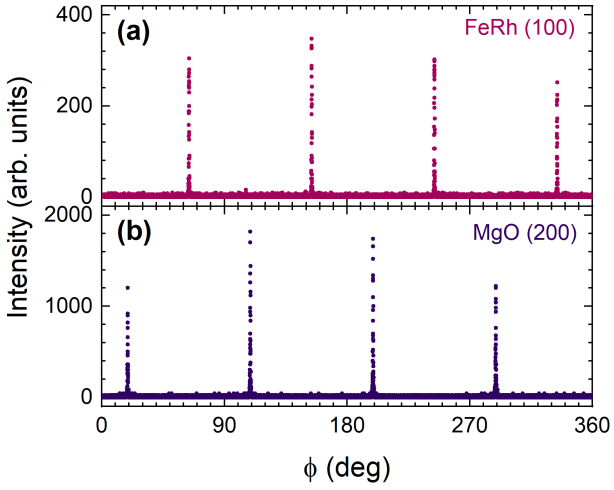

Figure 5.8: X-ray diffraction phi scans of the (a) FeRh (100) peak and (b) MgO (200) peak for a 21 nm FeRh film grown on MgO (001), showing four-fold symmetry and the 45 deg in-plane rotation of the FeRh cubic cell with respect to the MgO cubic cell. Measurements were made with Cu Kα radiation.

lattice mismatch between substrate and FeRh leads to lattice distortions and strain in the films, especially near the interface [57, 223, 228]. We will discuss how this impacts the phase transition in the next section.

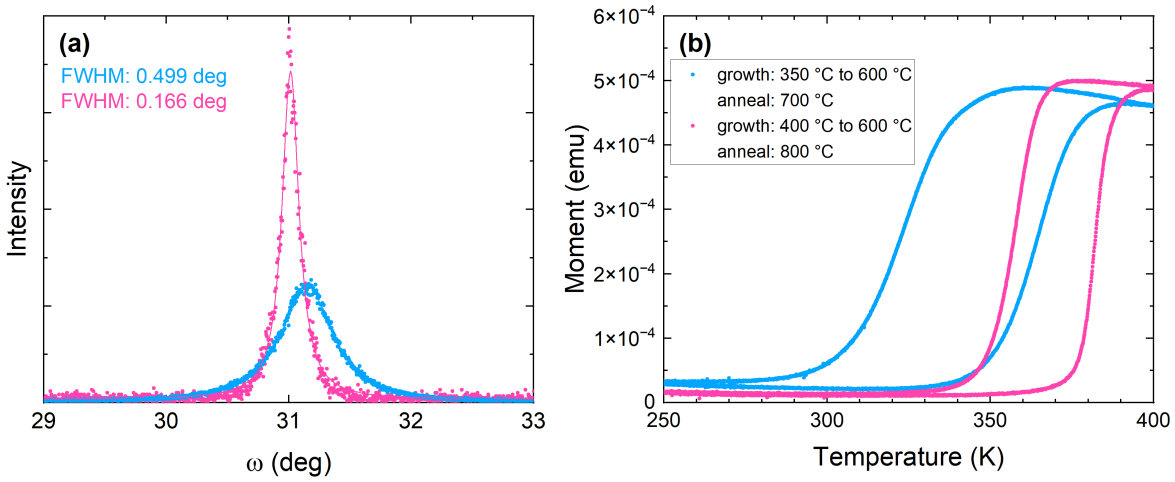

Figure 5.9: Comparison of the structural and magnetic characterization of two 21 nm FeRh films grown at different temperatures. The blue data shows measurements for a film grown starting at 350 °C and increasing to 600 °C during growth, followed by a post-anneal process at 800 °C. The pink data shows measurements for a film grown starting at 400 °C and increasing to 600 °C during growth, followed by a post-anneal process at 800 °C. All other process parameters were kept the same. (a) X-ray diffraction rocking curve of the FeRh (002) peak in both films shows a sharper narrower peak for the film grown and annealed at higher temperature, indicating better crystallinity and fewer defects. The lines are Lorentz fits to the peaks, used to determine the FWHM of each curve. Measurements were made with Cu Kα radiation. (b) VSM measurements of the phase transition show a sharper transition and narrower hysteresis for the film grown and annealed at higher temperature, suggesting more homogeneity and better crystalline quality of the film.

In Section 2.2.4, we discussed how heating a substrate during growth and post-annealing helps achieve better epitaxial growth. Fig. 5.9 demonstrates this for two films, one grown starting at 350 °C and increasing to 600 °C during the growth followed by post-annealing at 700 °C (blue data), and another grown starting at 400 °C and increasing to 600 °C during the growth followed by post-annealing at 800 °C (pink data). Fig. 5.9(a) shows rocking curves of the FeRh (002) peaks. The sharper narrower peak for the film grown and annealed at higher temperature demonstrates the higher crystal quality of the film. The broadening of the peak for the other film indicates

the presence of more defects. In Fig. 5.9(b), we see from magnetometry measurements that the film with higher crystal quality has a sharper transition and a narrower hysteresis, indicating more homogeneity and fewer defects within the film. Small changes in temperature during the growth process can make a significant difference, so there can be variability in the properties of different samples if there is a difference in the thermal contact of the substrates to the sample holder (a sample that is not clamped as well may experience a thermal gradient or achieve a lower temperature and have poorer crystalline quality).

Another consideration in the growth of FeRh films is the composition of the films. As discussed in Section 2.2.2 and in [55], the concentrations of Fe and Rh in a film grown from an alloy target, as done in this work, will not be the same as the concentrations of Fe and Rh in the target, and the temperature and Ar pressure during growth will impact the relative concentrations by changing the relative odds of Fe atoms and Rh atoms to reach the sample surface from the target surface and by altering the likelihood of the atoms to remain on the sample surface rather than bouncing off (the sticking probability). In [55], there emerges a clear change in the relative concentrations of the two materials in Ar sputter pressures of 5 mTorr to 30 mTorr. FeRh films in this work were usually grown in pressures lower pressures than this, somewhere around 2.7 to 3.3 mTorr, but we can expect the pressure at which an alloy is grown to have an impact on the film composition and therefore on the nature of the transition. [229] suggests there is a 2% change in Fe concentration when the Ar sputter pressure is increased from 0.3 Pa (2.3 mTorr) to 0.5 Pa (3.8 mTorr). And we saw from the bulk phase diagram (Fig. 5.2) that a 1% change in Fe concentration will result in an over 40 K change in transition temperature, so we can expect changes in Ar sputter pressure to also have a significant impact on film properties. In this work, we will assume that FeRh refers to a sample composition near the $Fe_{0.5}Rh_{0.5}$ composition where the antiferromagnetic-ferromagnetic phase transition occurs, with the understanding that the true composition of each film will vary.

Additional factors will also impact the film properties. The sticking probabilities are

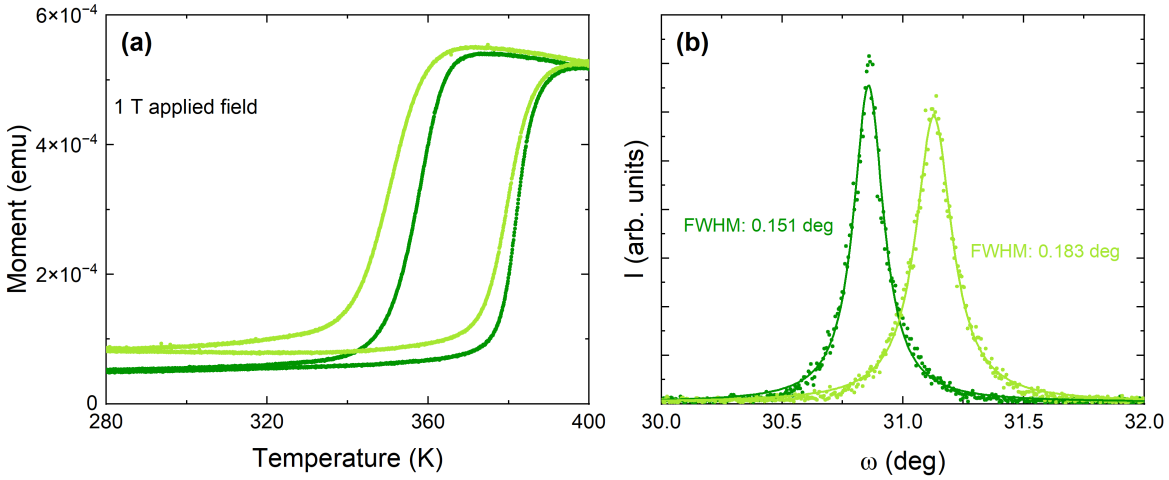

Figure 5.10: Comparison of the magnetic and structural characterization of two 21 nm films of FeRh grown simultaneously. (a) VSM measurements of the phase transition find that one sample (dark green) has a narrower transition and hysteresis and lower residual moment in the low temperature phase than the other sample (light green). (b) Rocking curves of the FeRh (002) peak of both samples show a broader peak (larger FWHM) for the film with the broader transition (light green), indicating more defects and lower crystalline quality. X-ray measurements were made with Cu Kα radiation. The solid lines in (b) are Lorentzian fits to the peaks. The difference in epitaxy is attributed to slightly different thermal contact between the substrate and sample holder during film growth.

unknown, but will likely depend on the Ar pressure, the temperature of the substrate, and the substrate material. Compositional differences and crystal quality will impact the strain in the film [229]. Strain becomes important because of the in-plane confinement that occurs in thin films and because it tends to stabilize one of the phases preferentially, as discussed in the next section. The imperfect lattice-matching between film and substrate can result in different quality of epitaxial growth for different composition and strain, potentially resulting in more or less defects, which will alter the width and shape of the hysteresis (broadening for films with more defects). Changes in the temperature during growth or post-anneal time and temperature similarly alters the epitaxy and transition [229], which makes the thermal contact of a substrate to a substrate holder a very important parameter in the growth process for ensuring uniform and reproducible heating of substrates. An improperly clamped substrate will experience lower growth temperature

and annealing temperature and be of poorer quality. Fig. 5.10(a) shows the magnetization vs. temperature in a 1 T applied field for two 21 nm FeRh films grown on MgO (001) at the same time at the same radial distance from the center of the sample holder. The expectation is that the composition, strain, and phase transition will be essentially identical for both, however we see that one film has a narrower and sharper transition and lower moment in the antiferromagnetic phase compared to the other. This film also has a sharper narrower rocking curve, seen in Fig. 5.10(b), indicating that it has better crystalline quality. One explanation for this is differences in the thermal contact between the substrate and sample holder.

So while FeRh films can be grown to exhibit the phase transition, there are many complications to achieving and tuning the transition and difficulty in reliably reproducing samples with the same transition. But the nature of the transition makes this a very interesting material fundamentally as well as in applications, so it is an area of continuing work. One area of study is how strain impacts the phase transition and can be used to manipulate the transition. This is discussed further in the next section.

5.1.4 The Impact of Strain

As stated previously, thin films must be grown on a substrate. Ideally, the crystal structure of the substrate forms a pattern for the crystalline growth of the film with minimal defects, which requires close matching of lattice parameters. For FeRh, a few examples of this are shown in Fig. 2.5. MgO has a face-centered cubic crystal structure with a lattice parameter of 0.4212 nm. This means the diagonal distance between like atoms is 0.2978 nm, which closely matches the FeRh lattice parameter of about 0.2987 nm. We observed in Fig. 5.8 that FeRh (001) grows at a 45 deg angle in-plane with respect to the MgO (001) substrate. In a film with good crystal quality, the Fe and Rh atoms will align as shown in Fig. 2.5(a) to form ordered FeRh. But the in-plane lattice directions will be compressively strained by 0.3%, so that $a_{film} < a_{bulk}$. FeRh will also grow on top of an Al_2O_3 substrate, shown in Fig. 2.5(c). Here, Fe atoms, which in bulk would be

spaced 0.4224 nm apart, are aligned on O atoms spaced 0.4759 nm apart, resulting in a tensile strain of -11.3% [57].

The most immediate consequence of the in-plane strain is a distortion in the unit cell of FeRh. On MgO, with a compressive strain in the (100) and (010) directions, the FeRh unit cell will exhibit a tetragonal distortion: in-plane directions are compressed with respect to bulk while the out-of-plane direction is expanded ($c_{film} > c_{bulk}$). On Al_2O_3, there is a tensile rhombohedral distortion in-plane and the out-of-plane (111) direction is compressed.

Increased strain in a film will also tend to increase dislocations in the structure, so the film starts to look more polycrystalline rather than single-crystal. This will broaden the transition, with different domains having slightly different transition temperatures, so there is a wider range of temperature through which there is a coexistence of antiferromagnetic and ferromagnetic domains [222, 228]. It may also create regions of the film near the interface that do not transition at all. The choice of substrate, therefore, can affect the magnetic properties considerably.

Since the transition in FeRh is also a structural transition, strain in the film may favor one of the states over the other. Bulk measurements have shown that FeRh experiences a volume expansion of 1-2% upon transition from the antiferromagnetic to the ferromagnetic state. For a film on MgO (001), we saw in Fig. 5.5 that there is an out-of-plane expansion of the unit cell. For a film, the in-plane directions are prevented from undergoing a change because the strain at the substrate interface opposes any significant expansion or compression. So we tend to see an out-of-plane expansion to the ferromagnetic state. But the strength of the in-plane confinement can stabilize one of the two states, either antiferromagnetic or ferromagnetic. For in-plane compression, such as for FeRh on MgO (001), the compressive strain stabilizes the antiferromagnetic phase that prefers a smaller lattice parameter and shifts the phase transition to higher temperature. Tensile strain stabilizes the ferromagnetic phase and shifts the transition to lower temperature [228, 230, 231].

The effect the of the strain will be highest at the substrate-film interface. For thicker films,

FeRh will relax away from this interface and the overall in-plane strain may lessen [57, 229]. So for films around 100 nm or more, the transition temperature and behavior may approach bulk properties. But for thinner films, the interfacial strain has a significant impact [232, 233]. The top interface with a capping layer can also provide some strain and alter the magnetic properties. Within a film, the magnetic properties near the interfaces will differ from the properties further away, which contributes to a broadening of the magnetic transition, as different layers through the film will have different transition temperatures. This can be measured by polarized neutron reflectometry [234–236]. When strain at an interface is significant, we sometimes will not observe the phase transition at all there. This is one explanation for the observed interfacial layer that remains ferromagnetic in these films. This is the motivation for the work presented in Section 5.3, which looks into the magnetization profile in thin film FeRh as a function of depth through polarized neutron reflectometry.

The residual ferromagnetic layer at one or more interfaces results in a small but positive net moment at low temperatures when measuring magnetometry. This explains the non-zero magnetization in the antiferromagnetic state in Fig. 5.3(a). Assuming this is entirely at the substrate interface for an FeRh film grown on MgO (001) and capped with Pt, the percentage of the residual moment in the antiferromagnetic state as compared to the ferromagnetic state gives a measure of the thickness of the layer that does not exhibit a phase transition due to strain.

5.2 Magnetic Phase Diagram of the Antiferromagnetic to Ferromagnetic Transition in FeRh

While there has been great interest in understanding the nature of the antiferromagnetic-ferromagnetic transition in FeRh through various types of measurements, there has been limited work thoroughly exploring the magnetic phase diagram experimentally and theoretically in high fields and at low temperatures. The transition has been measured in fields up to 9 T through

magnetization and resistivity measurements, which show that the ferromagnetic phase is stabilized by a magnetic field and the transition shifts to lower temperatures as the field is increased or that the field required to achieve the ferromagnetic state in measurements made as a function of applied field decreases as the temperature is increased. The observed shifts are around -8 K/T for films grown on MgO (001) and -9 K/T for films grown on Al_2O_3 (0001), which is in agreement with an Ising spin model calculation of -10 K/T to a maximum field of about 5.5 T [228]. There have been limited measurements of the transition for higher fields. Modeling of the phase diagram and transition, especially at high field and low temperature, has also not been thoroughly explored. Mean-field calculations have been used to predict the phase diagram in [237], but the nature of the transition and properties such as whether a canted antiferromagnetic state exists for FeRh remain unknown. In this work, we measure the magnetic phase diagram of FeRh through electrical resistivity measurements in fields up to 33.2 T. We use this data and mean-field modeling to propose possible phase diagrams. We are able to narrow the range of possible phase diagrams through x-ray magnetic circular dichroism (XMCD) measurements in fields up to 17 T.

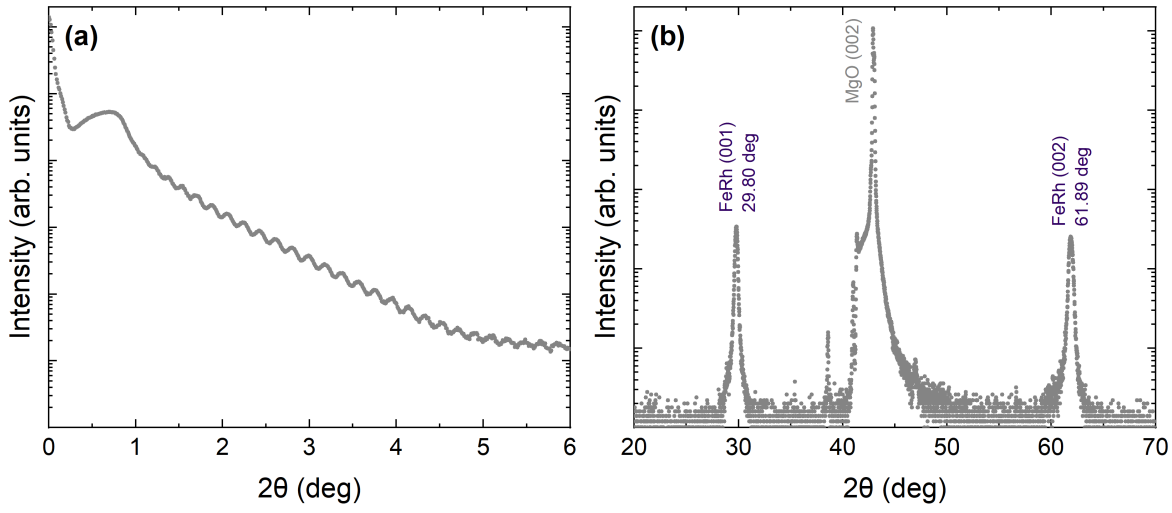

Figure 5.11: X-ray characterization of a 43 nm FeRh film. (a) X-ray reflectometry is used to determine the film thickness and smoothness of the interfaces. (b) X-ray diffraction shows the (001) and (002) diffraction peaks of FeRh, with lattice parameter determined to be 0.2995 nm. Measurements were made with Cu Kα radiation.

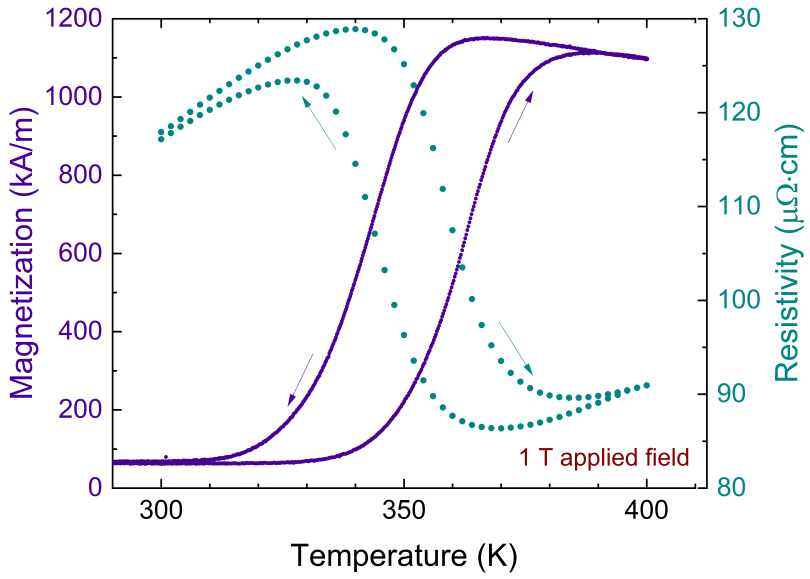

Figure 5.12: Magnetization and resistivity as a function of temperature for a 43 nm FeRh film in a 1 T applied field. Magnetization (purple) was measured for the full film and resistivity (teal) was measured after patterning into a 50 μm wide wire.

A thin film of FeRh was grown on a MgO (001) substrate by sputtering from a single material target composed of an alloy of 50% Fe and 50% Rh. The deposition began at 500 °C and continued while temperature was increased to 550 °C. The film was then annealed for 1 hr at 700 °C, cooled to room temperature, and capped with a 2 nm layer of Pt. The Ar pressure during deposition of the FeRh layer was 2.7 mTorr and during deposition of the Pt layer was 2.5 mTorr. The FeRh layer thickness was determined to be 43 nm from the x-ray reflectivity measurement in Fig. 5.11(a). X-ray diffraction measurements in Fig. 5.11(b) show the (001) and (002) diffraction peaks of FeRh at 29.80 deg and 61.89 deg respectively, giving a room temperature lattice parameter of 0.2995 nm. The moment of the sample in a 1 T applied field was measured using the VSM option in the VersaLab. The diamagnetic signal from the substrate and sample holder in the VSM were subtracted out so the magnetization of the FeRh film could be determined, as shown with the hysteretic transition between the low temperature low magnetization antiferromagnetic state and high temperature high magnetization ferromagnetic

state in purple in Fig. 5.12. The non-zero magnetization at low temperature suggests an interfacial layer of FeRh at the substrate of thickness 2.6 nm that does not transition with the rest of the film, but remains ferromagnetic.

The film was subsequently patterned by UV lithography into a Hall cross with a 50 μm width wire oriented along the FeRh (110) crystallographic axis. A resistivity measurement of the film was taken in-house at UC San Diego in a PPMS at 1 T, as shown in blue in Fig. 5.12, demonstrating good agreement of the transition with the magnetization measurement made before patterning. When warming from the antiferromagnetic state, the onset of ferromagnetic order is seen by a drop in the resistance while the magnetization increases. Conversely, while cooling from the ferromagnetic state, we see a jump in resistance as the magnetization decreases and the antiferromagnetic state is established.

Measurements of the phase transition were made through electrical resistivity measurements at the HFML and in-house at UC San Diego in a PPMS with magnetic field oriented parallel to the wire and applied current. Voltage was measured along an 800 μm segment of the wire. Measurements at the HFML in this work were made in Cell 5, with a Bitter magnet that can produce fields up to $\pm$33.2 T. The temperature of the sample was stabilized at several points between 4.6 K and room temperature, and the resistance was measured using a lock-in amplifier with an AC current of 275 nA for a field sweep from 0 T to 33.2 T to 0 T, as shown in Fig. 5.13. Additional measurements were taken on a PPMS with AC current 50 μA at 310 K, 330 K, and 340 K from 0 T to 9 T and at 0 T, 1 T, and 3 T from 250 K to 400 K in a PPMS. The transition is smooth and quite broad, indicating a high level of local structural variations and heterogeneity in the wire.

Transition temperatures were determined from peaks in the derivative of the resistance vs. temperature. The resulting phase diagram observed experimentally for this FeRh wire is presented in Fig. 5.14. The blue circular data points represent the transition to the antiferromagnetic state from high field or high temperature. The red triangular data points are from the transition to the

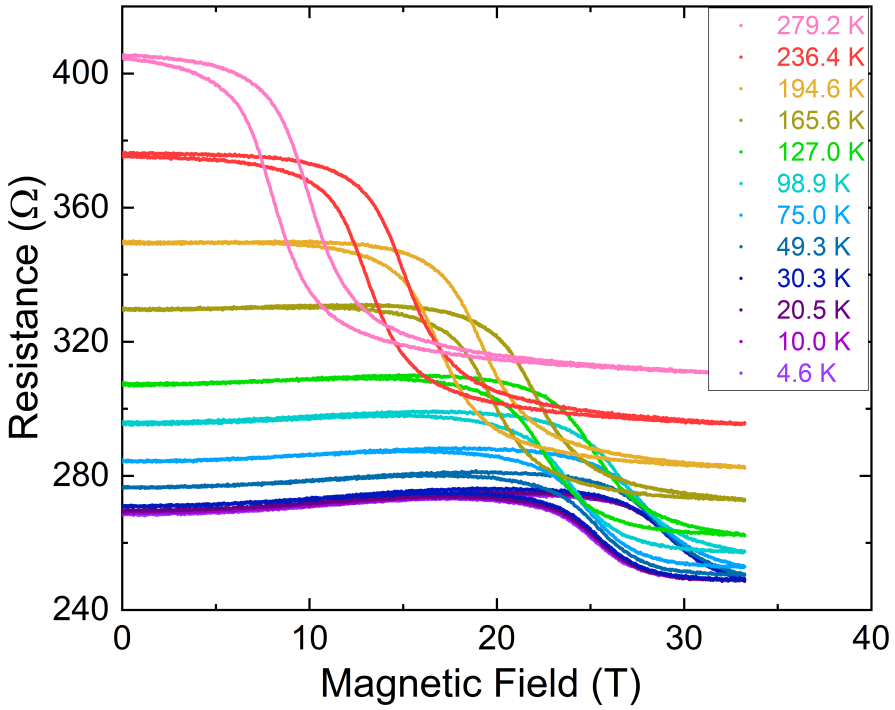

Figure 5.13: Resistance vs. magnetic field of a 50 μm wide FeRh wire patterned from a 43 nm thick film at various temperatures measured at the High Field Magnet Laboratory (HFML) with an AC current of 275 nA.

ferromagnetic state from low field or low temperature. Open data points are measurements made on a PPMS, while closed data points are measurements made at the HFML. The gray points are the average of the transition temperatures measured in each scan of resistance vs. temperature or resistance vs. field.

Linear fits of the data points at temperatures greater than 194 K give a transition temperature shift of -9.4 $\pm$ 0.1 K/T for the antiferromagnetic transition and -8.9 $\pm$ 0.1 K/T for the ferromagnetic transition. This is in agreement with previous work [228] and the mean-field model of the phase diagram to high field and low temperature in [237, 238]. That work correctly predicts the linear shift in the transition temperature to slow below around 150 K and approach 0 below about 100 K. The average transition temperature, shown as gray data points in Fig. 5.14

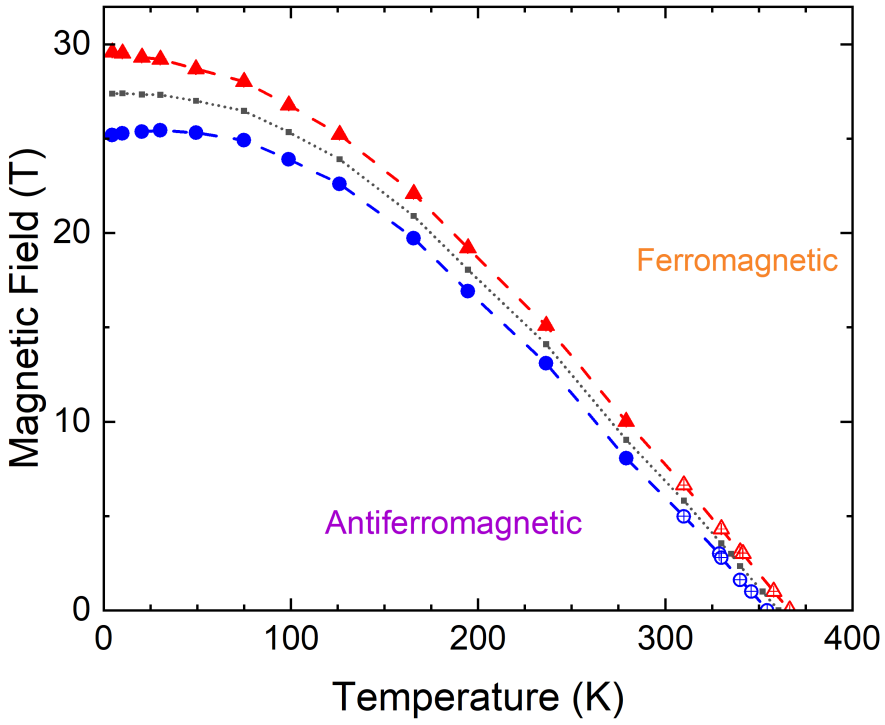

Figure 5.14: Magnetic phase diagram of a 50 μm wide FeRh wire patterned from a 43 nm thick film measured by magnetotransport measurements. Blue circular data points indicate the temperature of the transition from the ferromagnetic phase to the antiferromagnetic phase while decreasing temperature. Red triangular data points indicate the temperature of the transition from the antiferromagnetic phase to the ferromagnetic phase while increasing temperature. Solid data points were taken from measurements at the High Field Magnet Laboratory (HFML) and open data points are from in-house PPMS measurements. The gray data points represent the average of the transition temperatures measured from each scan (resistance vs. temperature or resistance vs. field.

agrees with this modeling remarkably well. The different zero-field transition temperature or zero-temperature transition field can be explained by small differences in alloy concentration of Fe and Rh between films, which results in significant shifts in the transition temperature and field.

We can use mean-field theory to understand and model the phase diagram. The magnetic structure of FeRh in the antiferromagnetic phase can be described in terms of the magnetizations of three sublattices: $\mathbf{M}_1$ and $\mathbf{M}_2$, which describe the antiferromagnetically-coupled Fe sublattices,

and $\mathbf{M}_{\text{Rh}}$, which describes the Rh sublattice. The exchange interaction between Rh ions can be neglected, so they can be modeled as a PM in the presence of an effective magnetic field generated by the net magnetization of the Fe ions $\mathbf{M} = \mathbf{M}_1 + \mathbf{M}_2$ and an external magnetic field. The free energy $\mathcal{F}$ is given by

$$\mathcal{F} = W_{\text{Fe-Fe}} + W_{\text{Rh}} - (\mathbf{M}_1 + \mathbf{M}_2) \cdot \mathbf{H} + W_{\text{ani}} + W_{\text{MS}}, \tag{5.1}$$

where $W_{\text{Fe-Fe}}$ is the exchange interaction between the Fe sublattices, W_{Rh} is the interaction between Rh spins and the effective field acting on them, $(\mathbf{M}_1 + \mathbf{M}_2) \cdot \mathbf{H}$ is the interaction of Fe spins with the external magnetic field, W_{ani} is due to the magnetic anisotropy, and W_{MS} is a magnetostrictive term that accounts for the magnetostructural effects seen in the transition.

Following the approach in [239], the first two terms of Eq. 5.1 can be defined as

$$W_{\text{Fe-Fe}} = \frac{1}{\chi_{\text{Fe}}}(\mathbf{M}_1 \cdot \mathbf{M}_2)$$

and

$$W_{\text{Rh}} = -\frac{1}{2}\chi_{\text{Rh}}(\lambda(\mathbf{M}_1 + \mathbf{M}_2) + \mathbf{H})^2$$

where χ_{Fe} is inversely proportional to the Fe-Fe exchange interaction constant, χ_{Rh} is the paramagnetic (PM) susceptibility of Rh, and λ is the coupling constant of Fe and Rh.

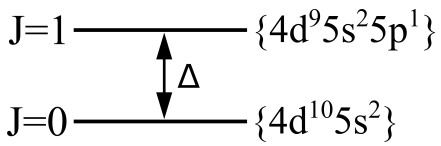

Figure 5.15: Schematically represented Rh ion energy levels.

In our model, the temperature dependence of the PM susceptibility of Rh plays a decisive role for the phase transition of FeRh. During the phase transition from the antiferromagnetic to the ferromagnetic state, Rh acquires a magnetic moment and the electronic conductivity of FeRh

increases dramatically. These changes can be understood by analyzing the corresponding changes in the electronic structure of Rh ions in FeRh. For temperatures below the phase transition, the Rh ion has an electronic configuration of $4d^{10}5s^2$, which implies no net magnetic moment and total angular momentum quantum number $J = 0$. At the phase transition Rh acquires a magnetic moment and the best candidate for the corresponding electronic structure is the $4d^9 5s^2 5p^1$ configuration with $J = 1$. So in the low temperature antiferromagnetic phase, Rh contributes to the electric conductivity with its two $5s$ electrons, but in the high temperature ferromagnetic phase, the conductivity is enhanced by an additional $5p$ electron. This electronic structure can be modeled as a two-level system, shown in Fig. 5.15, in which all electrons occupy the non-magnetic ground state with $J = 0$ at low temperature. At the transition temperature, an electron is excited into the state with $J = 1$. The energy difference between the ground state and this excited state is Δ. This model is analogous to that of Eu^{3+} in Eu_2O_3 [240], which allows us to similarly model the temperature dependence of χ_{Rh} using Gibbs statistics. We find the susceptibility to be dependent on the Van Vleck susceptibility χ_{vv} and the paramagnetic susceptibility χ_p. To a first approximation, χ_p is constant since $\chi_p \sim \frac{c_h(T)}{k_b T}$ where $c_h(T) \sim k_B T$ is the concentration of $4d$ holes. The paramagnetic susceptibility is then found to be

$$\chi_{\mathrm{Rh}}(T) = \frac{\chi_{vv}}{1 + e^{-\Delta/k_b T}} + \frac{e^{-\Delta/k_b T}\chi_p}{1 + e^{-\Delta/k_b T}}.$$

We assume uniaxial magnetic anisotropy in the system, so the anisotropy term W_{ani} in Eq. 5.1 becomes

$$W_{\mathrm{ani}} = -\frac{1}{2}K(\alpha_{\mathrm{M}_1}^2 + \alpha_{\mathrm{M}_2}^2),$$

where K is the anisotropy constant and α_{M_1} and α_{M_2} are the direction cosines between the anisotropy axis and $\mathbf{M}_1$, $\mathbf{M}_2$. The coordinate system used in this model is shown in Fig. 5.16. We can consider the cases when the external field $\mathbf{H}$ is applied parallel or perpendicular to the easy axis $\mathbf{L}$ where $\mathbf{L} = \mathbf{M}_1 - \mathbf{M}_2$. For $\mathbf{H} \parallel \mathbf{L}$, we use $\alpha_{\mathrm{M}_1} = \cos(\pi/2 - \xi - \theta)$ and $\alpha_{\mathrm{M}_2} = \cos(\pi/2 + \xi - \theta)$.

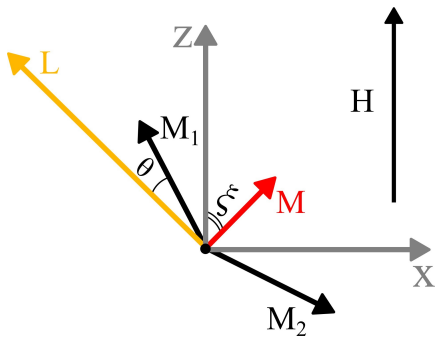

Figure 5.16: Schematic coordinate system used in the model of the FeRh magnetic phase diagram, where $\mathbf{M}_1$ and $\mathbf{M}_2$ are the magnetizations of the Fe sublattices, $\mathbf{M} = \mathbf{M}_1 + \mathbf{M}_2$, $\mathbf{H}$ is the applied field in the $\hat{z}$ direction, and $\mathbf{L}$ is the easy axis.

For $\mathbf{H} \perp \mathbf{L}$, the direction cosines become $\alpha_{M_1} = \alpha_{M_2} = \cos\theta$.

The magnetostrictive term W_{MS} in Eq. 5.1 models the volume changes seen during the magnetic transition. Following [241], the energy of the Fe-Fe exchange interaction in the simplest approximation is a linear function of applied strain u, and

$$W_{MS} = -\beta(\mathbf{M}_1 \cdot \mathbf{M}_2)u + \frac{Eu^2}{2},$$

where β is the partial derivative of the Fe-Fe exchange with respect to the strain u and E is Young's modulus. Minimization of the free energy with respect to the strain gives that in thermodynamic equilibrium,

$$u = \frac{\beta}{E}\mathbf{M}_1 \cdot \mathbf{M}_2,$$

which gives

$$W_{MS} = -\frac{\beta^2}{2E}(\mathbf{M}_1 \cdot \mathbf{M}_2)^2,$$

To minimize the number of free parameters in the model, we have made the following assumptions. In agreement with *ab initio* simulations from [242], we assume that the magnetic susceptibility of Fe in FeRh is $\chi_{Fe} = 1.5 \times 10^{-4}$ emu/cm^3 and the partial derivative of the Fe-Fe exchange interaction with respect to the strain u is β ~10^4 Oe^2·cm^3/erg. Although the Van Vleck

susceptibility of the Rh ion is not known, here we rely on the similarities between the roles of Rh and Eu^{3+} for magnetic changes in FeRh and Eu_2O_3 [240], respectively, so we assume $\chi_{vv} = 10^{-4}$ emu/cm^3. Young's modulus is taken from [243] to be $E = 15 \times 10^{11}$ dyne/cm^2. The coupling constant λ, energy gap Δ, and PM susceptibility χ_p are fit parameters in the model. These parameters are summarized in Table 5.1.

Table 5.1: Parameters used in the mean-field model of the FeRh phase diagram. Parameters marked *free* are fit parameters in the model.

Parameter	Symbol	Value	Units	Reference
Magnetic susceptibility of Fe	χ_{Fe}	1.5×10^{-4}	emu/cm^3	[242]
Partial derivatives of the Fe-Fe exchange	β	10^4	Oe^2·cm^3/erg	[242]
Van Vleck susceptibility of Rh	χ_{vv}	10^{-4}	emu/cm^3	[240]
Young's modulus	E	15×10^{11}	dyne/cm^2	[243]
Coupling constant	λ	*free*	Oe·cm^3/emu	
Energy gap	Δ	*free*	erg	
Paramagnetic susceptibility	χ_p	*free*	emu/cm^3	

Fig. 5.17 shows two possible phase diagrams for the case $\mathbf{H} \perp \mathbf{L}$, where θ reflects the antiferromagnetic canting of the Fe sublattices. The ratio $\beta^2 M^2/2E$, which determines the height of the barrier that separates the antiferromagnetic and ferromagnetic phases, is critical in determining the order of the transition. For $\beta^2 M^2/2E \gtrsim 5 \times 10^7$ erg/cm^3, the transition is first order everywhere when the critical field does not exceed 30 T. For $\beta^2 M^2/2E < 5 \times 10^7$ erg/cm^3, second order transitions are possible. This is shown for $\beta^2 M^2/2E = 10^8$ erg/cm^3 in Fig. 5.17(a), where the transition is first order everywhere, and $\beta^2 M^2/2E = 10^6$ erg/cm^3 in Fig. 5.17(b), where the transition is first order only at 0 T. The black data points in both figures show the observed average transition temperature measured for the 46 nm FeRh film (the gray data points in Fig. 5.14). The model shows fits to this data to obtain the free parameters of $\lambda = 3.1 \times 10^3$ Oe·cm^3/emu, $\chi_p = 4.3 \times 10^4$ emu/cm^3, and $\Delta = 600 \cdot k_b$ erg in in Fig. 5.17(a) and $\lambda = 3.58 \times 10^3$ Oe·cm^3/emu, $\chi_p = 2.9 \times 10^4$ emu/cm^3, and $\Delta = 600 \cdot k_b$ erg in in Fig. 5.17(b). It is possible to tune the

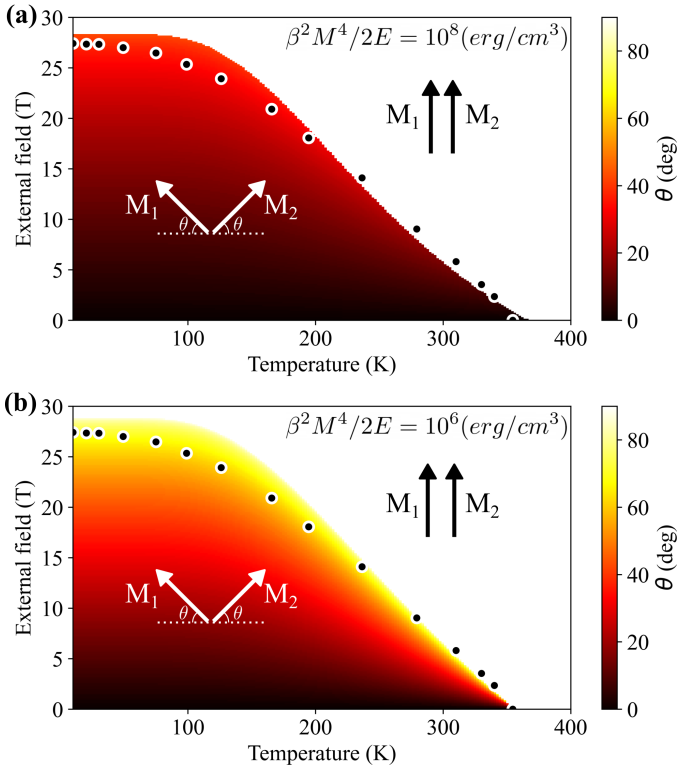

Figure 5.17: Possible FeRh phase diagrams for two different values of $\beta^2 M^2/2E$ with experimental data (black dots). (a) Parameters $\beta^2 M^2/2E = 10^8$ erg/cm^3, $\lambda = 3.1 \times 10^3$ Oe·cm^3/emu, $\chi_p = 4.3 \times 10^4$ emu/cm^3, and $\Delta = 600 \cdot k_b$ erg result in a phase diagram with some canting of the spins in the antiferromagnetic phase and a first-order transition everywhere between the antiferromagnetic and ferromagnetic phases. (b) Parameters $\beta^2 M^2/2E = 10^6$ erg/cm^3 result in a phase diagram with significant canting of the spins in the antiferromagnetic phase and a first-order transition only at 0 T.

parameters and achieve a simulated phase diagram with a critical point where the phase transition changes from first order to second order. However, the observed transition is first order down to 4.6 K (see Fig. 5.13), which suggests that the model in Fig. 5.17(a), with a first order transition everywhere, is the more accurate model of the two.

The strength of the magnetic anisotropy can play a role in the nature of the antiferromagnetic state. With weak magnetic anisotropy, the spins will cant in the direction of the applied field by angle θ, represented in these phase diagrams by the color map in Fig. 5.17. For stronger magnetic anisotropy, the spins may orient in a collinear antiferromagnetic orientation parallel to the field axis. In Fig. 5.18, we show the phase diagram with **H** ∥ **L** and

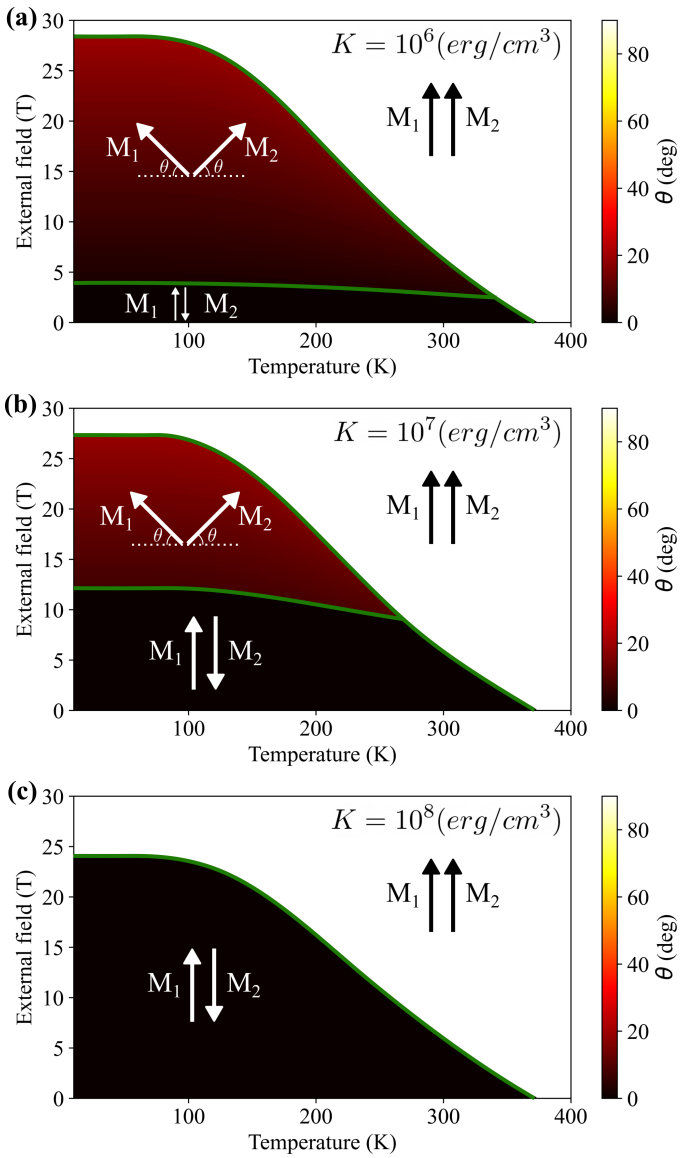

Figure 5.18: Possible FeRh phase diagrams for three different values of the anisotropy constant K that demonstrate a possible spin-flop transition between collinear and canted antiferromagnetic phases. Parameters used are $\beta^2 M^2/2E = 10^8$ erg/cm^3, $\lambda = 3.1 \times 10^3$ Oe·cm^3/emu, $\chi_p = 4.3 \times 10^4$ emu/cm^3, and $\Delta = 600 \cdot k_b$ erg. The anisotropy constant is (a) $K = 10^6$ erg/cm^3, (b) $K = 10^7$ erg/cm^3, and (c) $K = 10^8$ erg/cm^3. The green solid lines indicate a first order phase transition.

free parameters $\beta^2 M^2/2E = 10^8$ erg/cm^3, $\lambda = 3.1 \times 10^3$ Oe·cm^3/emu, $\chi_p = 4.3 \times 10^4$ emu/cm^3, and $\Delta = 600 \cdot k_b$ erg, equivalent to what was used in Fig. 5.17(a), for anisotropy constants $K = 10^6$ erg/cm^3, $K = 10^7$ erg/cm^3, and $K = 10^8$ erg/cm^3. This demonstrates the possibility of a

first order spin-flop transition in the phase diagram with three possible magnetic phases: collinear antiferromagnetic, canted antiferromagnetic, and ferromagnetic. As the magnetic anisotropy increases, the spin-flop transition shifts to higher field until the canted antiferromagnetic phase disappears.

XMCD measurements can be used to gain insight into the nature of the antiferromagnetic phase. A 40 nm film of FeRh was grown on a MgO (001) substrate by sputtering. The deposition began at 450 °C and continued while the temperature was increased to 780 °C. The film was

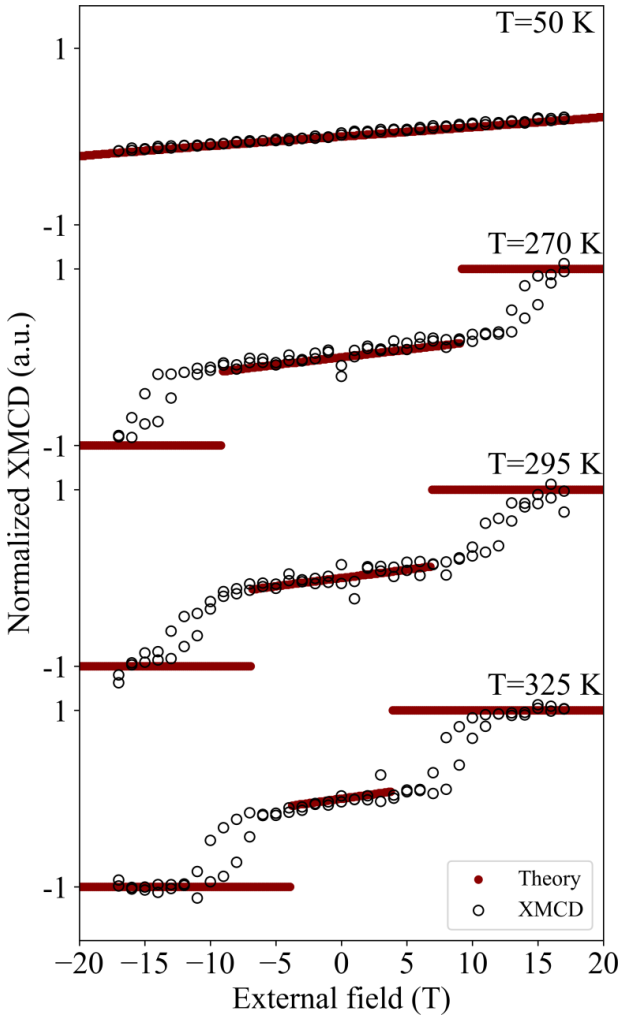

Figure 5.19: X-ray magnetic circular dichroism (XMCD) signal of the Rh L_2 and L_3 edge normalized to the maximum signal at 325 K and 17 T from a 40 nm FeRh film. Open circles show measured data points. Lines show theoretical calculations with parameters $\beta^2 M^2/2E = 3\times10^8$ erg/cm^3, $\lambda = 2.3\times10^3$ Oe·cm^3/emu, $\chi_p = 7.5\times10^4$ emu/cm^3, and $\Delta = 600\cdot k_b$ erg.

annealed for 45 min at 800 °C and then cooled to room temperature and capped with a 5 nm layer of Pt. The Ar pressure during deposition of the FeRh layer was 2.9 mTorr and during deposition of the Pt layer was 2.5 mTorr. XMCD was measured as a function of field at various temperatures at the ID12 beamline at the ESRF using the differential absorption of left- and right-circularly polarized x-rays at the L_2 an L_3 edges of Rh. The field was applied along the beam direction and measurements were made at normal and grazing incidence.

Fig. 5.19 shows the XMCD measurements with open circle data points at four temperatures, normalized to the maximum XMCD signal obtained at 325 K at 17 T. This signal shows the field dependence of the Rh moment induced by the magnetization of Fe. We expect a net moment at high field and temperature when FeRh is ferromagnetic. At low field and temperature, the FeRh state can be either collinear antiferromagnetic or canted antiferromagnetic. In the collinear antiferromagnetic state, the we would expect zero Rh moment and zero XMCD signal. In the canted antiferromagnetic state, the Rh moment would increase as the canting angle θ increases, giving a non-zero slope to the XMCD signal as a function of external field. In this case, we see a small positive slope to the XMCD signal in the antiferromagnetic phase which corresponds to a canting angle no greater than 10 deg. At high field at 325 K, the normalized XMCD signal has a net zero slope, consistent with a saturated ferromagnetic state.

The model shown in Fig. 5.17(a) was tuned slightly to fit the XMCD data for this film, as shown with the red lines in Fig. 5.19 for parameters $\beta^2 M^2/2E = 3 \times 10^8$ erg/cm^3, $\lambda = 2.3 \times 10^3$ Oe·cm^3/emu, $\chi_p = 7.5 \times 10^4$ emu/cm^3, and $\Delta = 600 \cdot k_b$ erg. This model is not unique in reproducing the observations, however. Another model that reproduces this behavior is the one in Fig. 5.18(a) with slightly tuned parameters but field parallel to the easy axis ($\mathbf{H} \parallel \mathbf{L}$). So we are unable to determine further characteristics of the magnetic anisotropy.

However, we have used mean-field theory to model the phase transition of FeRh here. Experimental resistivity measurements suggest that the transition is of first order everywhere and is in good agreement with a mean-field model of the phase transition. Experimental XMCD

measurements show the existence of a canted antiferromagnetic phase and a ferromagnetic phase, which allows us to conclude that the anisotropy in FeRh is not high enough to suppress a spin-canted phase. The models most closely aligned with the experimental data are those shown in Fig. 5.17(a) and Fig. 5.18(a).

5.3 Polarized Neutron Reflectometry Measurements of the Magnetic Depth Profile of an FeRh Film and Stripes

An FeRh film is expected to have a high temperature high magnetization ferromagnetic state and a low temperature antiferromagnetic state with no net magnetization. However we previously discussed that with magnetometry measurements of FeRh thin films, there is a small positive moment that remains in the antiferromagnetic state. We also discussed how strain can have an impact on the transition temperature in FeRh, with a higher transition temperature for films grown on MgO, which imparts a compressive in-plane strain that prefers the antiferromagnetic phase (as compared to films grown on Al_2O_3, which imparts a tensile strain and stabilizes the ferromagnetic phase, lowering the transition temperature). One way to observe the influence of strain on the magnetism is through polarized neutron reflectometry measurements, which measures the depth dependence of the in-plane magnetization in a film. In this case, we compare measurements in the antiferromagnetic state (at 300 K) and the ferromagnetic state (at 450 K), which should help identify if strain at the substrate interface results in a ferromagnetic layer that does not switch or if defects and disorder throughout the film contribute to the small ferromagnetic signal at low temperature. Measurements in saturation with 1 T field applied in-plane will give the magnetization depth profile through the film. Measurements in remanence at 5 mT can be compared to the saturation measurements, with spin-flip scattering indicating a perpendicular in-plane component to the magnetization. Further, we can explore the question of how patterning the films into stripes and restricting the lateral dimension will influence the magnetization depth

profile and preferred orientation.

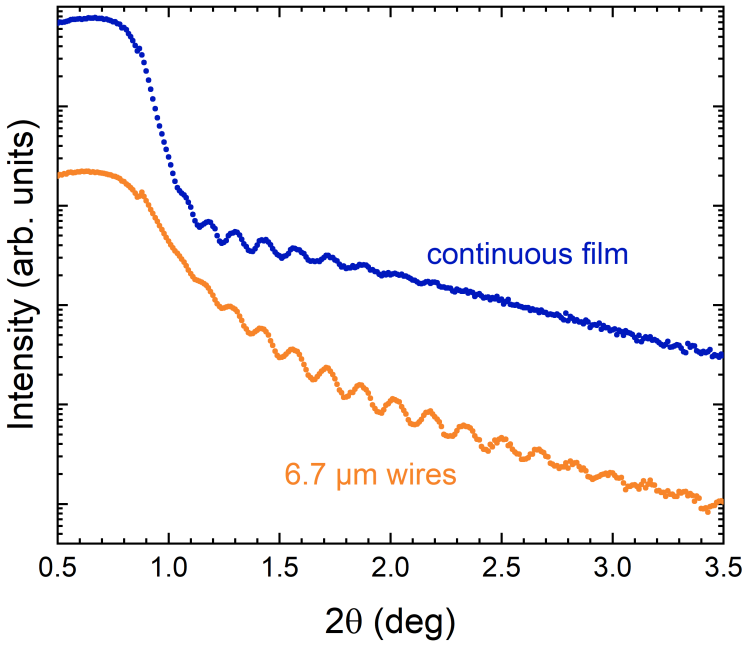

Figure 5.20: X-ray reflectivity of a 46 nm FeRh film grown on MgO (001) and a 46 nm FeRh film grown on MgO (001) that was patterned into stripes of width 6.7 μm and periodicity 10 μm. Measurements were made with Cu Kα radiation.

Two thin films of FeRh were grown on MgO (001) substrates by sputtering from a single material target alloy of 50% Fe and 50% Rh. The deposition started at 450 °C and increased to 800 °C during the growth. The films were then annealed for 45 min at 800 °C, cooled to room temperature, and capped with a 2 nm layer of Pt. The Ar pressure during deposition of the FeRh layer was 2.9 mTorr and during deposition of the Pt layer was 2.5 mTorr. One of the films was patterned by UV photolithography into stripes that were 6.7 μm thick with 3.3 μm space in between. The thickness of both samples was 46 nm, determined from x-ray reflectivity measurements shown in Fig. 5.20. FeRh grows with the (001) orientation out-of-plane on top of MgO (001), as confirmed by out-of-plane x-ray diffraction measurements in Fig. 5.21. Measurements at 300 K (blue lines) and 420 K or 430 K (pink lines) are shown, with very little

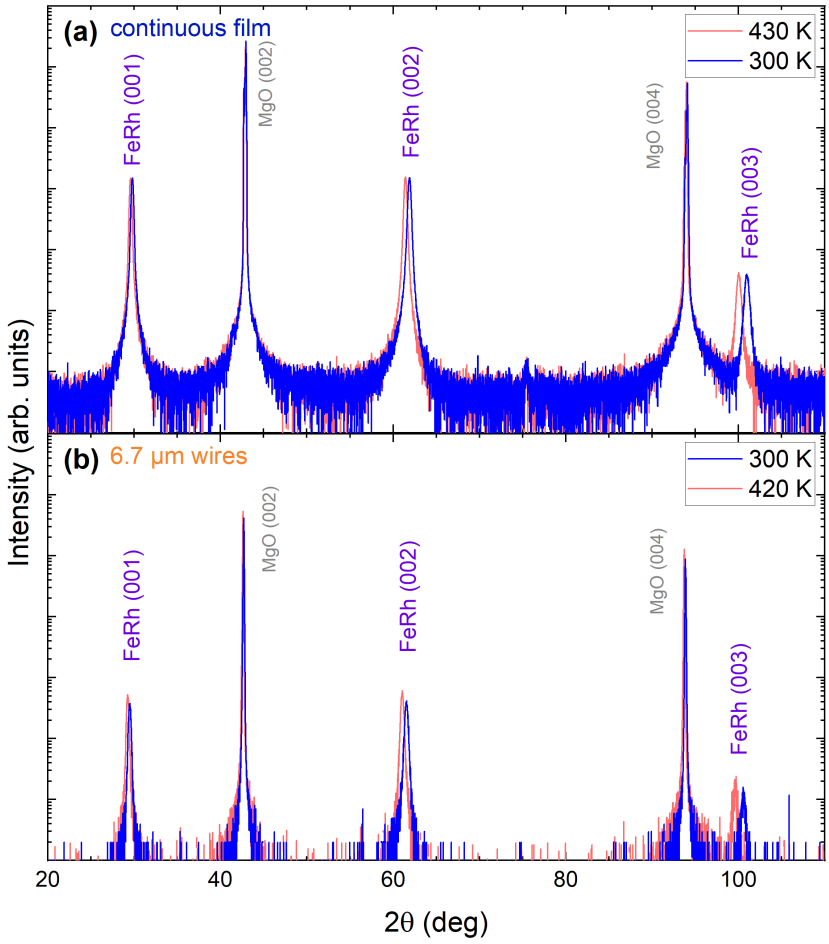

Figure 5.21: Out-of-plane x-ray diffraction measurements of (a) a 46 nm FeRh film grown on MgO (001) and (b) a 46 nm FeRh film grown on MgO (001) that was patterned into stripes of width 6.7 μm and periodicity 10 μm at 300 K (blue lines) and 420 K or 430 K (pink lines). The substrate MgO (002) and MgO (004) peaks and the film FeRh (001), FeRh (002), and FeRh (003) peaks are identified. Measurements were made with Cu Kα radiation.

shift in the substrate peaks but significant shift to lower angle for the film peaks, consistent with the large out-of-plane lattice expansion seen in FeRh films between the room temperature antiferromagnetic state and the high temperature ferromagnetic state.

The x-ray diffraction intensity near the FeRh (003) peak is shown for the two samples as a function of angle 2θ and temperature during warming in Fig. 5.5(a) and Fig. 5.22(a) and cooling in Fig. 5.5(b) and Fig. 5.22(b). These measurements were made with on a Rigaku diffractometer

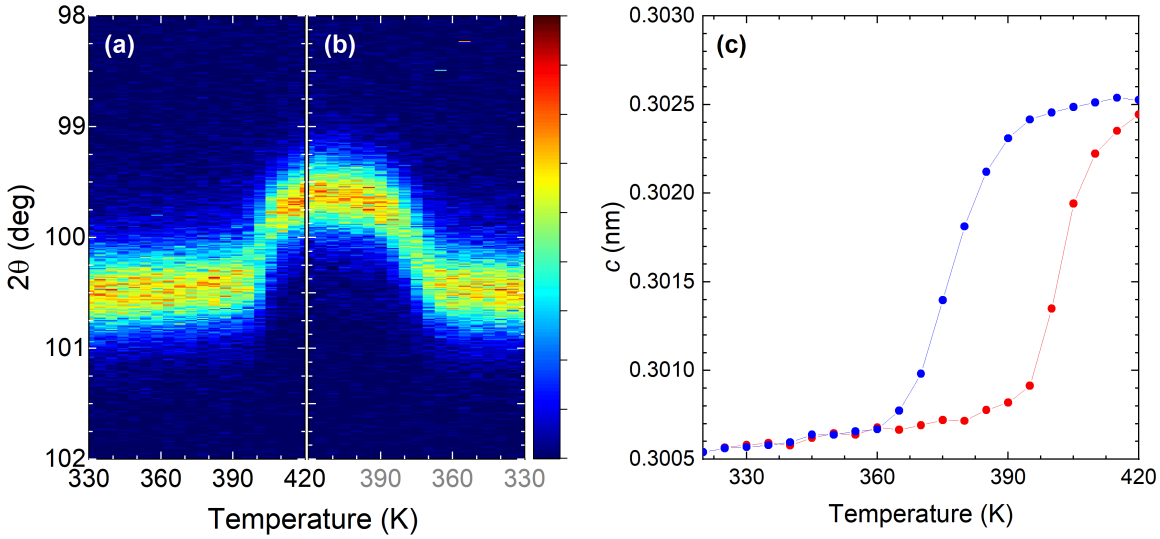

Figure 5.22: X-ray diffraction measurements of the FeRh (003) peak showing a structural phase transition for a 46 nm FeRh film patterned into stripes of width 6.7 μm and periodicity 10 μm grown on MgO (001) during (a) warming from 330 K to 420 K and (b) cooling from 420 K to 330 K. Measurements were made with Cu Kα radiation. (c) The out-of-plane lattice parameter *c* during the phase transition during warming (red) and cooling (blue), calculated from the peak location of Gaussian fits to the x-ray diffraction peaks in (a) and (b).

with Cu Kα radiation. There is a clear shift in the peak position at different temperatures during warming and cooling, confirming the hysteretic structural transition. The out-of-plane lattice parameter *c* was found from Gaussian fits to the x-ray diffraction peaks and plotted in Fig. 5.5(c) and Fig. 5.22(c). In both samples, an out-of-plane lattice expansion of over 0.5% is seen during the antiferromagnetic-ferromagnetic transition.

Polarized neutron reflectometry measurements of this film were conducted at the BL-4A MAGREF instrument at the SNS at sample temperatures of 450 K and at 300 K, with applied fields of 5 mT (remanence) and 1 T (saturation). For a perfect film, we could expect a fully-saturated uniform depth profile for the magnetization at 450 K and no magnetization at any depth at 300 K. Deviations from this will result from strain or disorder. Fig. 1.23 shows a diagram of the experiment. Incident neutrons that are spin-up or spin-down are scattered from the film with an applied field in-plane and parallel to the neutron spin axis. The scattered neutrons' spin can

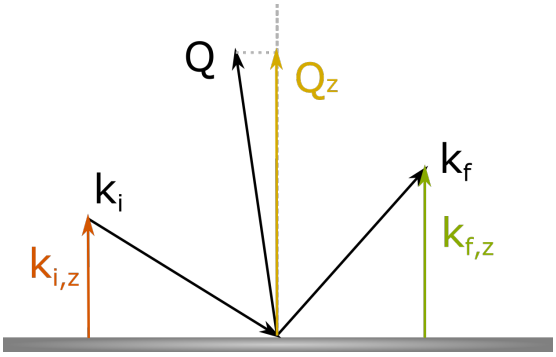

Figure 5.23: Schematic of the neutron scattering wavevector geometry for polarized neutron reflectometry, where $\mathbf{Q}$ is the scattering wavevector, $\mathbf{k}_i$ is the incident neutron wavevector, $\mathbf{k}_f$ is the reflected neutron wavevector, and Q_z, $k_{i,z}$, and $k_{f,z}$ are the projection of $\mathbf{Q}$, $\mathbf{k}_i$, and $\mathbf{k}_f$ on the axis normal to the film plane.

either remain unchanged or flip. Fig. 5.23 shows the scattering wavevector $\mathbf{Q}$, which is related to the incident neutron wavevector $\mathbf{k}_i$ and reflected neutron wavevector $\mathbf{k}_f$ by $\mathbf{Q} = \mathbf{k}_f - \mathbf{k}_i$. Specular reflection, or reflectivity, occurs when the angle of incidence equals the angle of reflection and $\mathbf{Q} = Q_z\hat{z}$ and can be used to determine the magnetization depth profile [244, 245]. For a homogeneously magnetized sample with magnetization $\mathbf{M}$ at an angle γ with respect to the neutron polarization axis, the non-spin-flip reflectivities are defined by

$$\begin{aligned} \mathscr{R}^{++} &= \frac{1}{4}|\,(r_+ + r_-) + (r_+ - r_-)\cos\gamma\,|^2 \\ \mathscr{R}^{--} &= \frac{1}{4}|\,(r_+ + r_-) - (r_+ - r_-)\cos\gamma\,|^2 \end{aligned} \tag{5.2}$$

and the spin-flip reflectivities are defined by

$$\mathscr{R}^{\pm\mp} = \frac{1}{4}|r_+ - r_-|^2 \sin^2\gamma\,, \tag{5.3}$$

where $r_\pm$ are complex reflection amplitudes that are related to the the sum or difference of the nuclear scattering length density (nSLD) and magnetic scattering length density (mSLD). From this, we see that in the case of a film with no in-plane perpendicular magnetization, $\mathscr{R}^{\pm\mp} = 0$ and there is no spin-flip reflectivity [245].

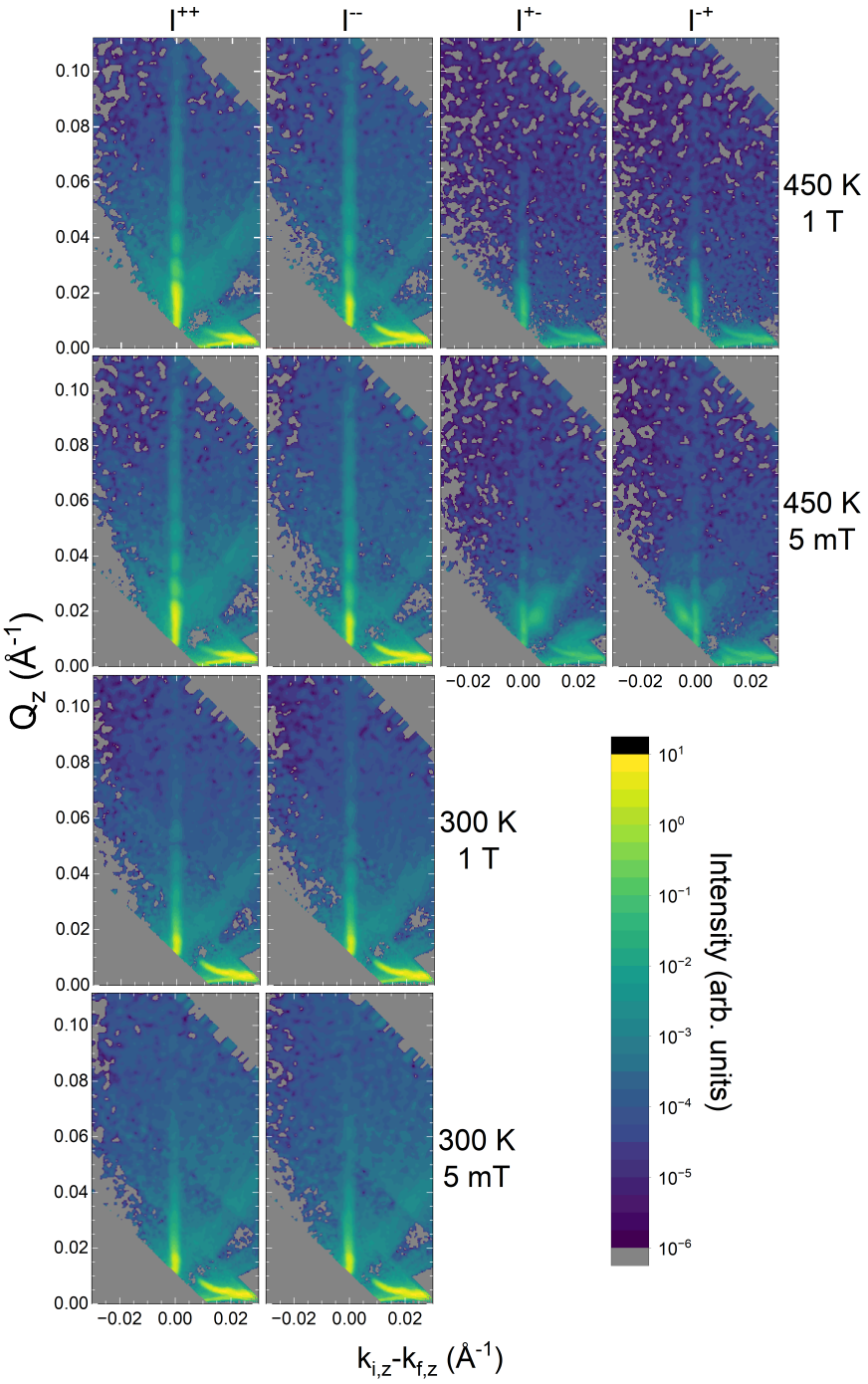

Figure 5.24: Polarized neutron reflectometry intensity maps of specular reflection and off-specular scattering for a 46 nm FeRh film. Measurements were made at 300 K and 450 K for applied fields 5 mT and 1 T.

There can also be off-specular scattering as a result of periodic inhomogeneities in the films, which can be structural, such as for patterned periodic structures or interfacial roughness, or magnetic, such as in the presence of magnetic domains. These defects break the translational symmetry and impart an in-plane momentum transfer [246]. We expect to see obvious off-specular scattering at specific angles from the film patterned into stripes of width 6.7 μm and spacing 3.3 μm giving a 10 μm periodicity. Off-specular scattering of magnetic origin is suspected by differences when probing with differently polarized neutrons or when the sample environment is changed so that measurements are made in different magnetic states. This scattering can be analyzed for information in the domain state of the system [247, 248].

The intensity maps of specular reflection and off-specular scattering for the continuous film at the four combinations of temperature and field are shown in Fig. 5.24. The first two columns show non-spin-flip scattering and the second two show spin-flip scattering. There was very little spin-flip scattering at 300 K, so those conditions have not been measured. The reflectivity measurements can be extracted from the maps at $k_{i,z} - k_{f,z} = 0$. The high intensity direct beam and refracted beam are present near $Q_z = 0$. We also see off-specular scattering in each case. The diffuse scattering is likely due to sample roughness, but there is a clear increase in off-specular scattering in the spin-flip channels at specific angles in remanence at 450 K as compared to saturation, indicating a magnetic origin of the scattering, and indicative of a domain state. Further analysis of the off-specular scattering is required.

The reflectivity measurements extracted from Fig. 5.24 are shown in Fig. 5.25 along with fits that have been made using the reflectivity fitting software *GenX* [45]. At 450 K, we see very obvious differences in $\mathscr{R}^{++}$ and $\mathscr{R}^{--}$ at for both saturation and remanence, indicating a non-zero mSLD in the films. There is also some spin-flip scattering, which tells us that the magnetization even at 1 T has not fully aligned to the polarization axis. In contrast, at 300 K, there is much less difference in $\mathscr{R}^{++}$ and $\mathscr{R}^{--}$ at saturation and virtually no difference in remanence. There are a few possible conditions that would result in $\mathscr{R}^{++} = \mathscr{R}^{--}$: the average magnetization in

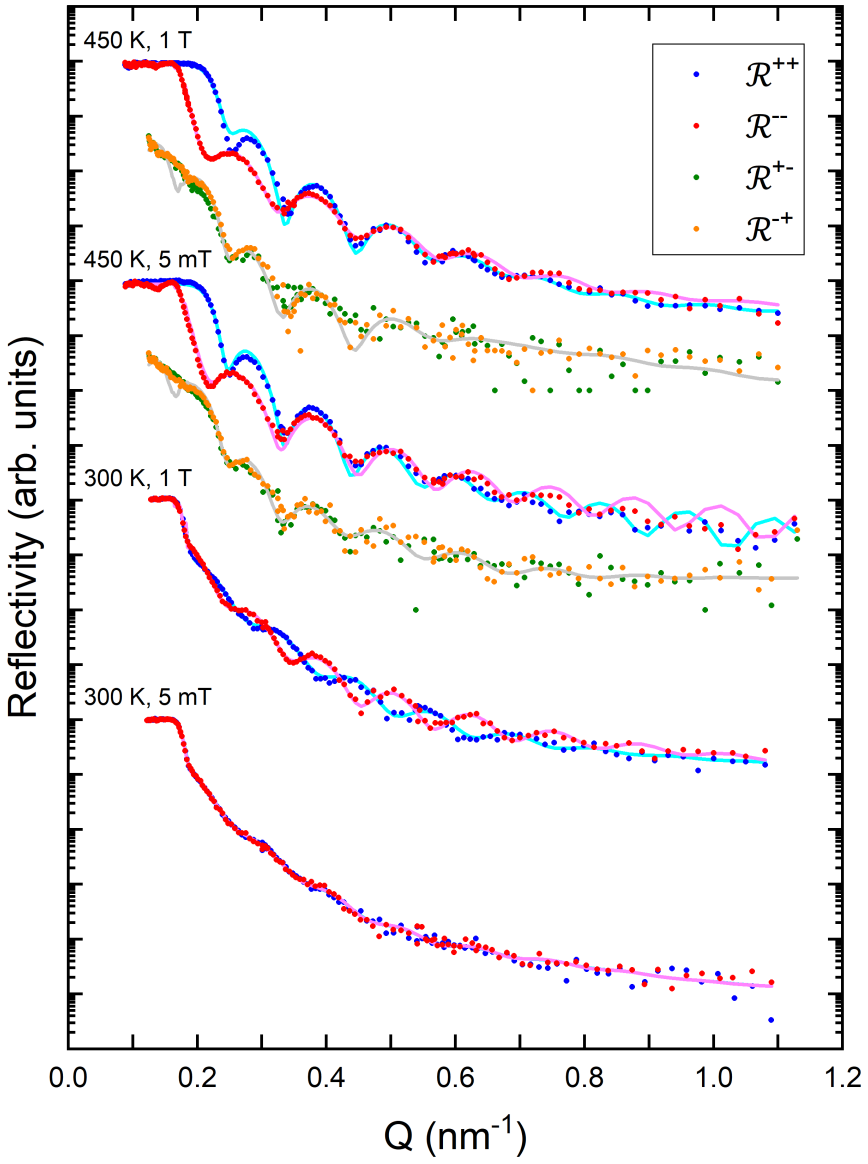

Figure 5.25: Neutron reflectivity data and fits for a 46 nm FeRh film. Data was taken at temperatures of 450 K and 300 K with applied fields of 1 T and 5 mT. Blue data points and cyan lines indicate data and fits for spin-up incident and reflected neutrons. Red data points and pink lines indicate data and fits for spin-down incident and reflected neutrons. Green and orange data points and gray lines indicate data and fits for spin-flip scattering. Fits were made using the reflectivity fitting software *GenX* [45].

the sample is zero (meaning it is either non-magnetic or demagnetized), the magnetization is oriented in-plane perpendicular to the polarization axis in the plane of the film (which would give

significant spin-flip scattering), or the magnetization is oriented normal to the film surface. Since we expect to be in an antiferromagnetic state, it makes sense that there is low net magnetization from the film at this temperature, however we can see from the 300 K saturation field condition that there is still some residual net magnetization in the film.

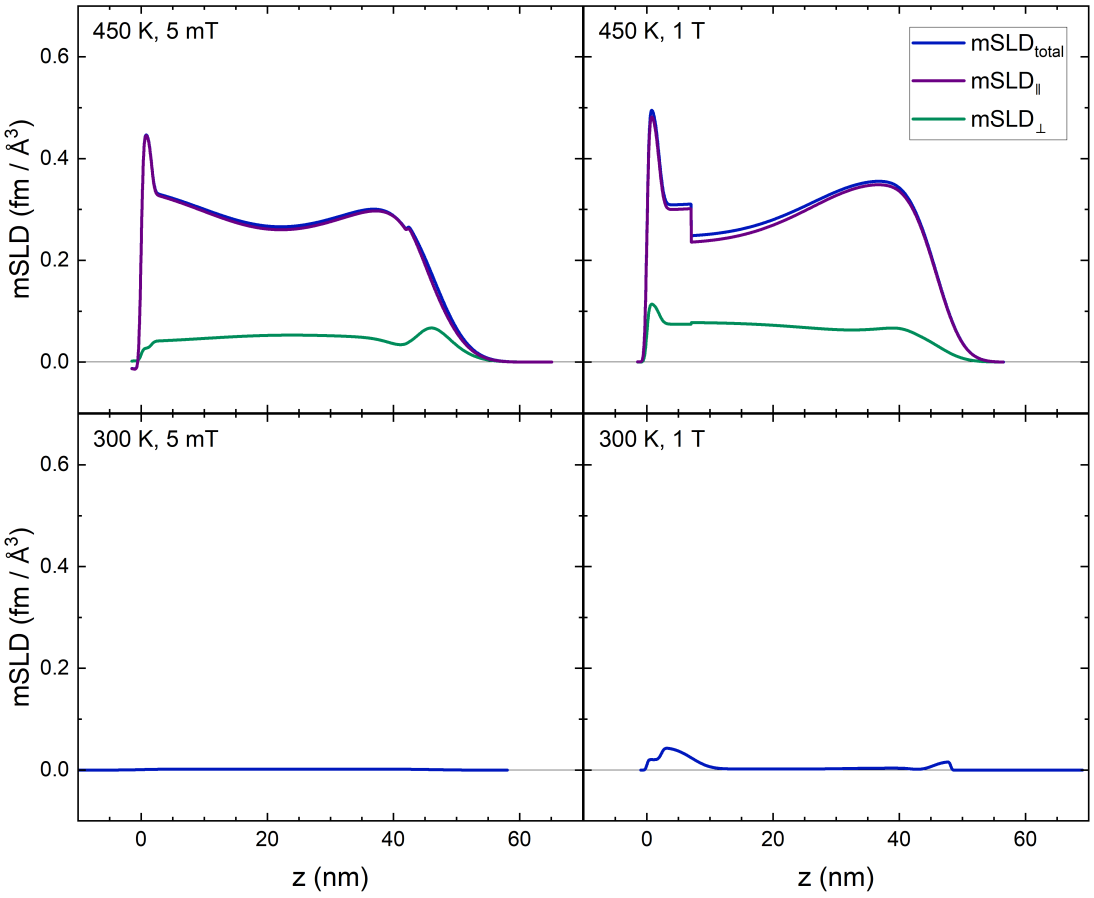

Figure 5.26: Depth profile of the magnetic scattering length density (mSLD) at 300 K and 450 K in remanence and saturation for a 46 nm FeRh film. These profiles were calculated from fits to the reflectivity data in Fig. 5.25 using the reflectivity fitting software *GenX* [45]. At 450 K, the in-plane components parallel (purple lines) and perpendicular (green lines) to the polarization axis and the total in-plane mSLD (blue lines) are shown. At 300 K, almost no spin-flip scattering was observed so the perpendicular component is essentially zero and the parallel component is assumed to be the total in-plane mSLD (blue lines).

Fig. 5.26 shows the mSLD calculated in each condition for the fits in Fig. 5.25. As

expected, the total mSLD in blue is much greater at 450 K than at 300 K, consistent with a ferromagnetic phase at 450 K and an antiferromagnetic phase at 300 K. At 300 K in saturation, the fit suggests that there is some mSLD at both the substrate interface and the surface, confirming that there exists some ferromagnetic phase near both interfaces, possibly a result of strain or disorder. In remanence at this temperature, the mSLD is essentially zero and the reflectivity is dominated by nuclear scattering, so those ferromagnetic regions near the interfaces at 1 T were demagnetized. At 450 K, we again see a slightly larger mSLD at the interfaces compared to the rest of the film. This again may be a reflection of strain and disorder at the interface preventing a uniform ordered FeRh phase. The magnitude of the mSLD in saturation and in remanence is similar through most of the film. Interestingly, there is a non-zero perpendicular component of the mSLD shown in green (which comes from the component $M_{\perp}$ in Fig. 1.23), indicating the ferromagnetic spins are not completely aligning to the axis of applied field, (which is directed along FeRh (110) in this experimental geometry), even for the saturation condition.

The second sample, which was patterned into stripes along the FeRh (110) axis, was oriented so the stripes were parallel to the polarization axis for the reflectometry measurement. The intensity maps of specular reflection and off-specular scattering for this sample at the same four temperature and field combinations are shown in Fig. 5.27. In this case, both non-spin-flip scattering (left two columns) and spin-flip scattering (right two columns) were measured for all conditions, since it was non-negligible even at 300 K. An immediate difference in the scattering for the stripes as compared to the continuous film is seen with significant off-specular scattering at specific angles in all four conditions, as expected for the periodic structural features. Overall, there is significantly more off-specular scattering everywhere at 300 K compared to at 450 K, and we also see significant off-specular scattering in the spin-flip channels at specific angles, especially at remanence at 450 K and a little at remanence at 300 K. This is indicative of magnetic origins of the off-specular scattering and potentially useful in studying magnetic domains in these films.

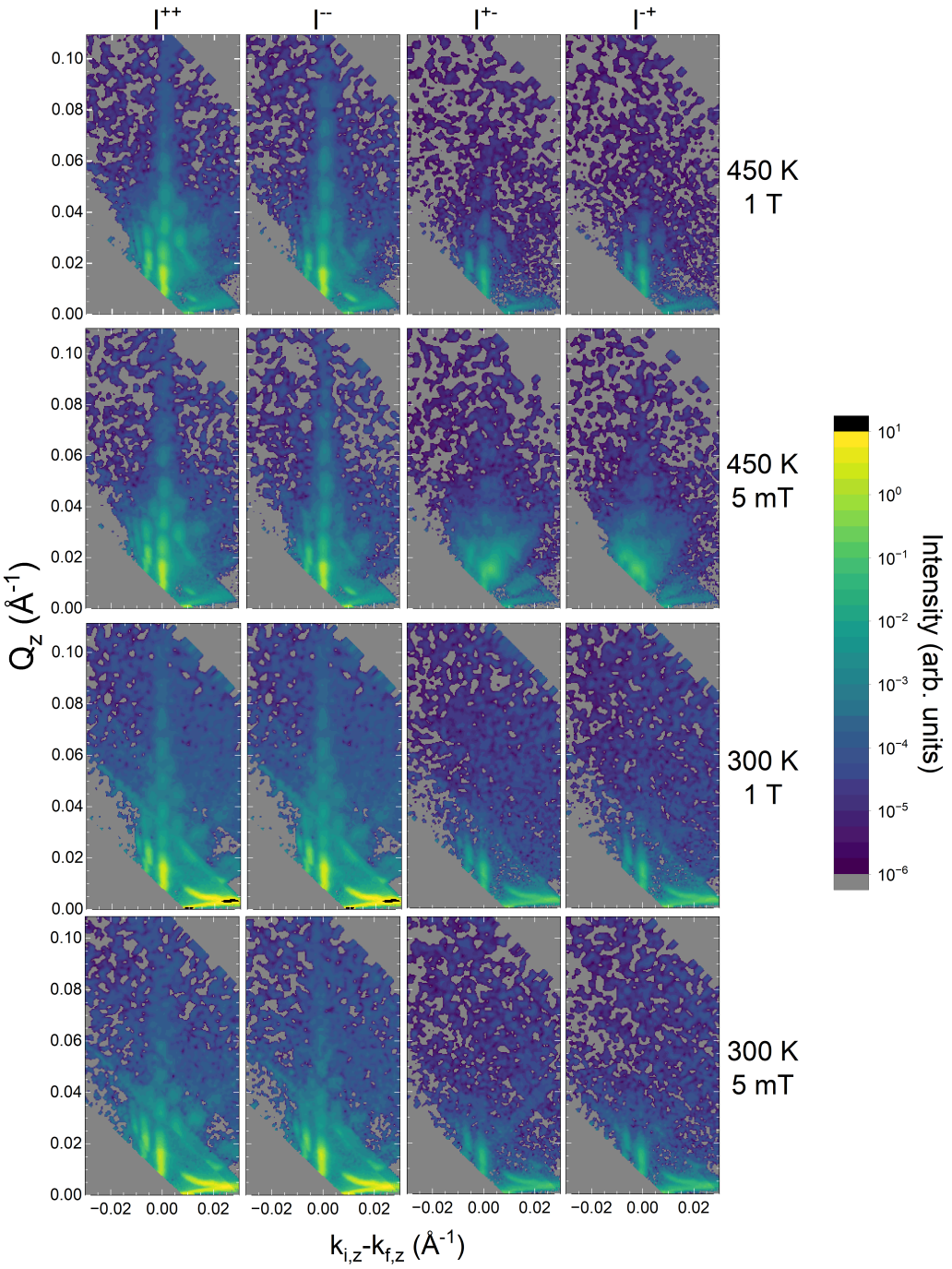

Figure 5.27: Polarized neutron reflectometry intensity maps of specular reflection and off-specular scattering for FeRh stripes of width 6.7 µm and periodicity 10 µm patterned from a 46 nm film. Measurements were made at 300 K and 450 K for applied fields 5 mT and 1 T.

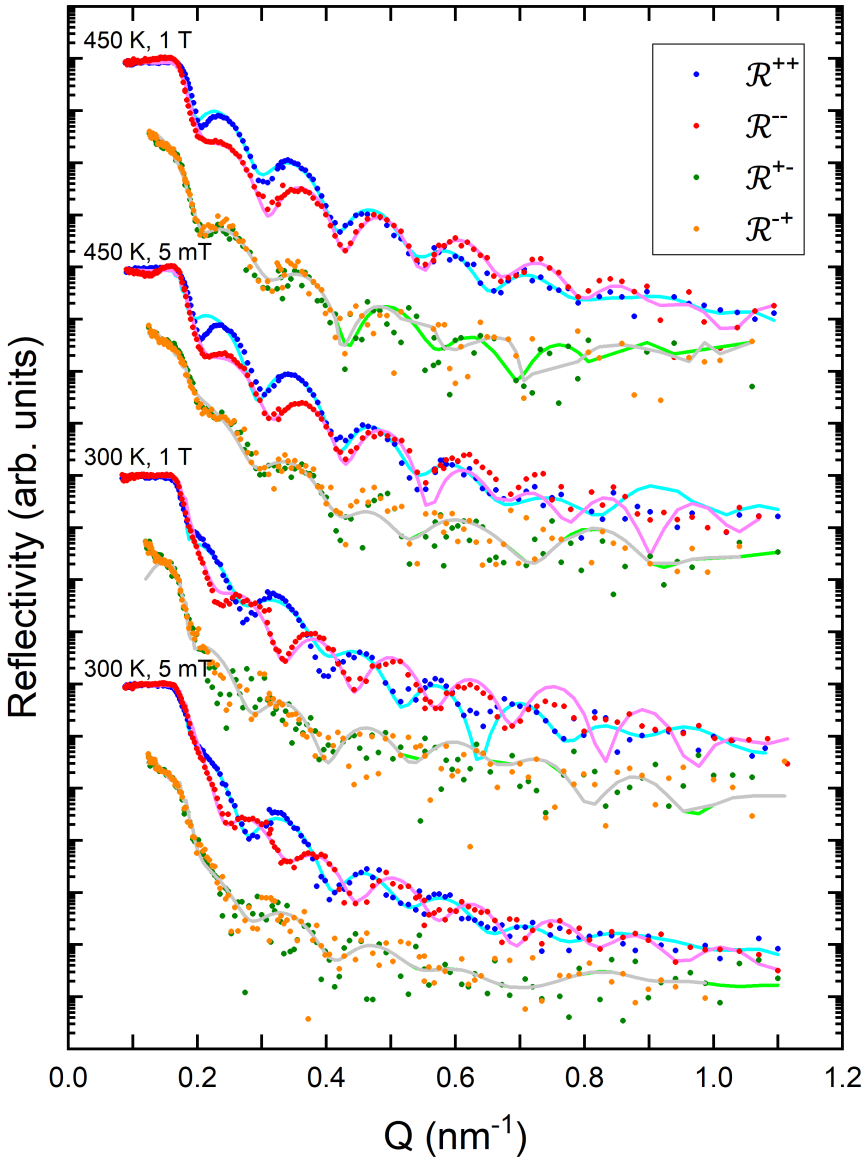

Figure 5.28: Neutron reflectivity data and fits for FeRh stripes of width 6.7 µm and periodicity 10 µm patterned from a 46 nm thick film. Data was taken at temperatures of 450 K and 300 K with applied fields of 1 T and 5 mT. Blue data points and cyan lines indicate data and fits for spin-up incident and reflected neutrons. Red data points and pink lines indicate data and fits for spin-down incident and reflected neutrons. Orange and green data points and gray lines and light green lines indicate data and fits for spin-flip scattering. Fits were made using the reflectivity fitting software *GenX* [45].

Domain characteristics have been studied previously in [222] by electrical resistivity measurements of very thin wires (sub μm width) that are on the order of the characteristic domain size in FeRh. This showed that the electrical transition occurs with discrete jumps for different domains and there was a fundamental difference observed between the transition during warming and cooling. When cooling from the ferromagnetic state, there was a collective single change in resistance. When warming from the antiferromagnetic state, the transition occurred in many discrete steps, indicating a transition governed by local nucleation and a fundamental difference in domain nucleation and motion in the two states. Future analysis of the off-specular scattering here may provide more insight into domain size and distribution in both the continuous film and the patterned stripes.

The reflectivity measurements extracted from Fig. 5.27 and the fits made using *GenX* [45] are shown in Fig. 5.28. In comparison to the reflectivities of the continuous film in Fig. 5.25, the non-spin-flip scattering here shows less magnetic signal parallel to the polarization axis at 450 K and more magnetic signal at 300 K. There is also significant spin-flip scattering for all conditions, meaning there is a significant perpendicular in-plane component to the magnetization. Fig. 5.29 shows the mSLD for these fits for all four conditions. For three of the cases, 450 K remanence and saturation and 300 K saturation, there does appear to be the thin strained ferromagnetic layer at the substrate interface that may not be switching to an antiferromagnetic phase and increased magnetization at the Pt interface. However, the fits contain FeRh layers near the substrate interface that are thinner than the length scale for roughness, resulting in anomalies in the mSLD data which are not physically possible for the film, suggesting that additional work needs to be done in understanding the intermixing or disorder at the interface. At 450 K, the film is in the ferromagnetic phase and fits with what we expect, larger magnetization near the interfaces and large positive moment throughout. This is consistent with what was seen in the continuous film, with a reduced magnetic scattering length density consistent with the missing material in the patterned regions. At saturation at 300 K, the mSLD is reduced some from 450 K except at the

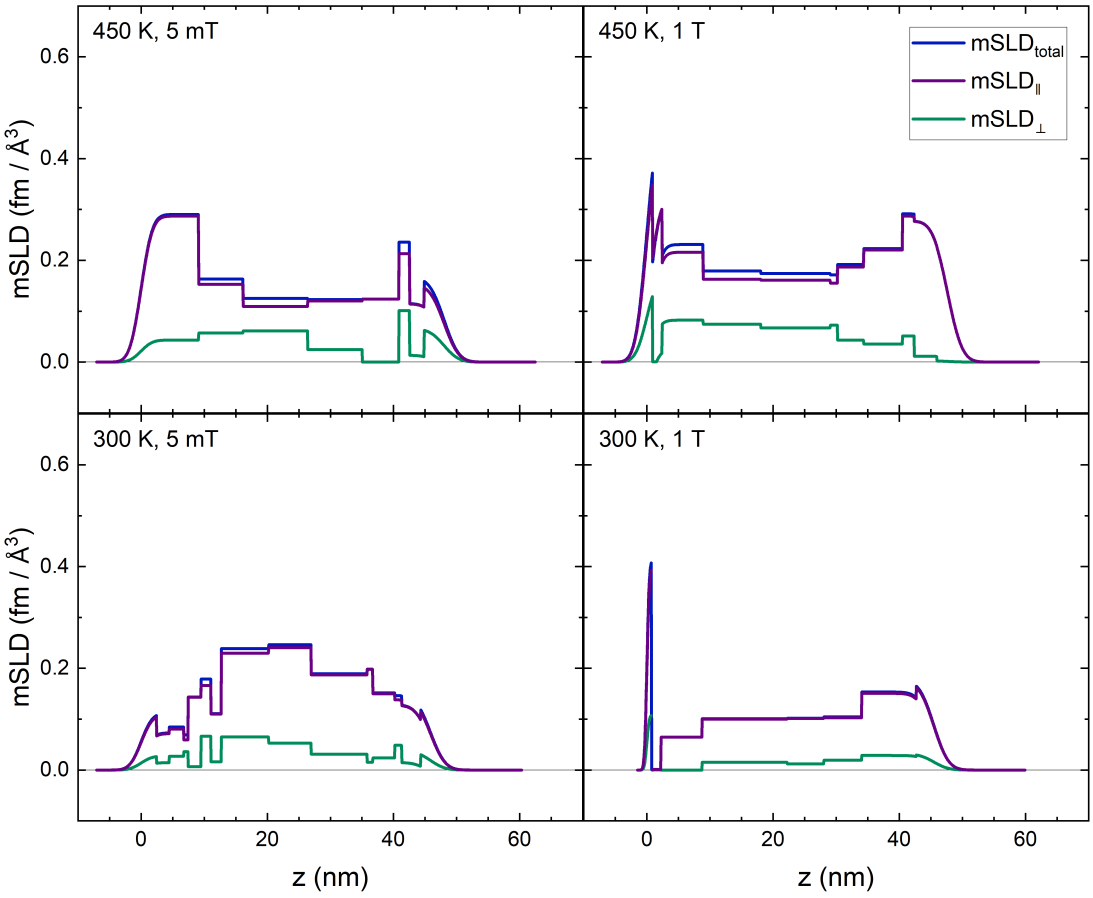

Figure 5.29: Depth profile of the magnetic scattering length density (mSLD) at 300 K and 450 K in remanence and saturation for FeRh stripes of width 6.7 µm and periodicity 10 µm patterned from a 46 nm thick film. These profiles were calculated from fits to the reflectivity data in Fig. 5.28 using the reflectivity fitting software *GenX* [45]. The in-plane components parallel (purple lines) and perpendicular (green lines) to the polarization axis and the total in-plane mSLD (blue lines) are shown.

interfaces, however there is significant magnetic scattering throughout the profile that was not seen for the continuous film. This suggests that patterning, perhaps during the dry etching step, has introduced defects which influence the FeRh phase. At remanence at 300 K, the model does not fit with what is expected or seen in the other conditions, with a greater magnetization implied in the center of the film and reduced at the interfaces. It has been shown that very different mSLD profiles can result in similar reflectivities [48], so additional work must be done to determine if

there are additional models that are consistent with this reflectivity and find the model that is most reasonable for this system and consistent with the rest of the data. However the reflectivities overall suggest that there is significant consequence to the FeRh phase with patterning, either because of defects introduced during the fabrication process or as a consequence of confining length scales further.

In summary, we have measured polarized neutron reflectometry for a continuous FeRh film and FeRh stripes patterned from a continuous film. We have confirmed the suggestion that the residual positive moment in thin films in the antiferromagnetic phase originates from the interfaces, probably a result of strain and disorder. In the stripes, fits of the reflectivity suggest similar behavior to the continuous film but with the addition of defects throughout the film depth, likely at the wire edges, which influence the FeRh phase and transition. Future analysis will look into the off-specular scattering for both samples, which demonstrates some magnetic origin with differences between the phases and fields and holds promise for understanding the nature of domains in the material when confined to different length scales.

5.4 Conclusion

In this work, we have conducted two main experiments to understand the magnetism of FeRh. The first area of research was an exploration of the magnetic phase diagram of FeRh to gain insight into the nature of the transition and the magnetic anisotropy. We measured resistivity measurements of a patterned film as a function of field to 33.2 T at various temperatures down to 4.6 K, demonstrating that the transition remains first order likely at all temperatures. XMCD measurements of a continuous film were used to determine that the antiferromagnetic state is a canted state with canting angles up to 10 deg and not collinear. Mean-field modeling was use to suggest several possible models of the phase transition consistent with these experiments.

The second experiment aimed to determine the influence of strain and disorder at the

interfaces of FeRh in confined dimensions (thin film and wires). Polarized neutron reflectometry measurements were used to suggest depth profiles of the magnetization which confirm that there is an interfacial dead layer which remains ferromagnetic rather than becoming antiferromagnetic at low temperature. Patterning a film into stripes further induced ferromagnetic signal at lower temperatures, demonstrating that interfaces and edges are important features for consideration in achieving the transition in FeRh. We also see the presence of off-specular scattering of magnetic origin in the films and stripes, which is an area for future analysis that can give some insight into the nature of domains and differences in films and stripes.

FeRh continues to be a very interesting material due to the transition between the low temperature antiferromagnetic state and the high temperature ferromagnetic state that occurs near room temperature. Understanding the nature of the transition will allow for tuning and manipulation of the transition for application in technology. Further work can allow us to further understand the domain structure, phase diagram, and magnetic anisotropy. This work can also include and influence the study of other materials, such as MnRh, which show similar transitions with useful characteristics.

Acknowledgements

Section 5.1.2 contains unpublished data coauthored by Sheena K. K. Patel, Timothy R. Charlton, Michael R. Fitzsimmons, Tao Zou, Tao Hong, and Eric E. Fullerton. The dissertation author was the primary investigator of this material. Neutron diffraction was conducted as part of a user project at the High Flux Isotope Reactor (HFIR), which is a US Department of Energy, Office of Science User Facility at Oak Ridge National Laboratory.

Section 5.2, in part, is currently being prepared for submission for publication of the material coauthored by Aleksandr Buzdakov, Irina Dolgikh, Sheena K. K. Patel, Rajasekhar Medapalli, Km Rubi, Elvina Dilmieva, Uli Zeitler, Theo Rasing, Eric E. Fullerton, Peter C. M.

Christianen, Konstantin A. Zvezdin, Anatoly K. Zvezdin, and Alexey V. Kimel. The dissertation author was the primary investigator of a portion of this material and a contributing author to the paper. High field transport measurements were conducted as part of a user project supported by the High Field Magnet Laboratory and the Foundation for Dutch Scientific Research Institutes (HFML-RU/NWO-I), members of the European Magnetic Field Laboratory (EMFL). We acknowledge the European Synchrotron Radiation Facility (ESRF) for provision of synchrotron radiation facilities and we would like to thank Elvina Dilmieva for assistance and support in using beamline ID12 for measurements of x-ray magnetic circular dichroism. This work was performed in part at the San Diego Nanotechnology Infrastructure (SDNI) of UC San Diego, a member of the National Nanotechnology Coordinated Infrastructure, which is supported by the National Science Foundation (Grant ECCS-2025752).

Section 5.3 contains unpublished data coauthored by Sheena K. K. Patel, Jon Ander Arregi, Sunil K. Sinha, Valeria Lauter, Vojtěch Uhlíř, and Eric E. Fullerton. The dissertation author was the primary investigator of this material. Polarized neutron reflectometry was conducted as part of a user project at the Spallation Neutron Source (SNS), which is a US Department of Energy, Office of Science User Facility at Oak Ridge National Laboratory. This work was performed in part at the San Diego Nanotechnology Infrastructure (SDNI) of UC San Diego, a member of the National Nanotechnology Coordinated Infrastructure, which is supported by the National Science Foundation (Grant ECCS-2025752).

Chapter 6

Conclusion

In this dissertation, we sought to examine some magnetic systems that exhibit complex ordering with many different experimental techniques in order to understand or exploit the coupling of degrees of freedom, primarily of charge, spin, and lattice. The three materials that were studied were chromium (Cr), antiperovskite manganese nitrides (Mn_3AN), and iron rhodium (FeRh). The goal was specifically to conduct experiments in confined geometries, in which the magnetic behavior may diverge from bulk behavior and in which certain experimental techniques can be implemented that are not possible in bulk, to provide insight into the nature of the behavior and, hopefully, into its origins.

In thin film Cr that has coupled spin density wave, charge density wave, and periodic lattice distortion, we conducted x-ray diffraction measurements to directly probe structural order of the system and, through the coupling of the structure and magnetism, to indirectly understand the magnetic order of the system. This was performed statically and then dynamically with laser-induced dynamics on two time scales of evolution, requiring a thin film geometry and the brilliance available at modern x-ray sources. In the ultrafast regime, we probed the nonequilibrium behavior and observed the ultrafast uncoupling and recoupling of degrees of freedom. On longer time scales, we observed the evolution of the system and assess the energetic contributions to

the magnetic ordering through the time domain. This enables an extension of phenomenological Landau modeling of spin and charge density wave systems to a thin film system with boundary conditions and a new way of measuring the competition between two energetic terms (one which prefers for the spin density wave wavevector to equal the natural nesting wavevector and another which prefers for the spin density wave to be commensurate with the lattice).

The second system studied was thin film Mn_3AN exhibiting magnetovolume effects including negative thermal expansion. These compounds have an interaction of magnetism and structure resulting in magnetostriction and magnetovolume effects which are not well-understood, but by fabricating thin films and measuring laser-induced dynamics, we have opened up the opportunity to study them in new ways to understand the competing effects on the thermal expansion. The goal moving forward is to measure ultrafast laser-induced dynamics through x-ray diffraction to uncouple the charge, spin, and lattice degrees of freedom to watch their evolution on different time scales and how they recouple to gain an understanding of the competition of phononic and magnetic effects on the structure.

The final system included in this work was thin film FeRh, which is of great interest for numerous applications due to its magnetic transition near room temperature. One experiment focused on a fundamental exploration of its magnetic phase transition, which had not previously been measured thoroughly in high fields and low temperatures, and which is used to better model the material behavior through mean-field theory. The second experiment explored how miniaturization impacts the magnetism and the transition through polarized neutron reflectometry measurements, which must be understood and optimized for potential application.

We will simply end here with this: the fundamental problem in condensed matter physics is how particles interact to give rise to collective behavior. Understanding rooted in first principles is rare given the complexity of these systems and the interactions and range of ordering that are observed. But studying the problem in individual systems with a wide range of techniques and in different conditions is important in both arriving at an understanding of the origins of

emergent phenomena and in eventually engineering and manipulating the systems and materials we need to continue technological advancement. This work aims to contribute to that body of knowledge and demonstrate some of the techniques that are useful and necessary to garner a deeper understanding of our world.

Bibliography

[1] Y. Tokura, M. Kawasaki, and N. Nagaosa, "Emergent functions of quantum materials," *Nat. Phys.*, vol. 13, no. 11, pp. 1056–1068, 2017.

[2] E. Dagotto and Y. Tokura, "Strongly correlated electronic materials: Present and future," *MRS Bull.*, vol. 33, no. 11, p. 1037–1045, 2008.

[3] G. R. Stewart, "Unconventional superconductivity," *Adv. Phys.*, vol. 66, no. 2, pp. 75–196, 2017.

[4] H. Gu, X. Zhang, H. Wei, Y. Huang, S. Wei, and Z. Guo, "An overview of the magnetoresistance phenomenon in molecular systems," *Chem. Soc. Rev.*, vol. 42, no. 13, pp. 5907–5943, 2013.

[5] L. Xiang, Y. Shi, W. Chao, H. Zhang, Q. Li, W. Hu, W. Wang, H. Guo, C. Zheng, J. Etheridge, L. Yin, Y. Zhu, X. Zhou, and J. Shen, "Uncovering the path to low-field colossal magnetoresistance: A microscopic view of field driven percolative insulator-to-metal transition in manganites," *Appl. Phys. Lett.*, vol. 122, no. 11, 2023.

[6] A. P. Ramirez, "Colossal magnetoresistance," *J. Phys.: Condens. Matter*, vol. 9, no. 39, p. 8171, 1997.

[7] Y. Tokura and N. Kanazawa, "Magnetic skyrmion materials," *Chem. Rev.*, vol. 121, no. 5, pp. 2857–2897, 2020.

[8] T. Li, A. Patz, L. Mouchliadis, J. Yan, T. A. Lograsso, I. E. Perakis, and J. Wang, "Femtosecond switching of magnetism via strongly correlated spin–charge quantum excitations," *Nature*, vol. 496, no. 7443, pp. 69–73, 2013.

[9] M. Fiebig, N. P. Duong, T. Satoh, B. B. Van Aken, K. Miyano, Y. Tomioka, and Y. Tokura, "Ultrafast magnetization dynamics of antiferromagnetic compounds," *J. Phys. D: Appl. Phys.*, vol. 41, no. 16, p. 164005, 2008.

[10] T. Kampfrath, A. Sell, G. Klatt, A. Pashkin, S. Mährlein, T. Dekorsy, M. Wolf, M. Fiebig, A. Leitenstorfer, and R. Huber, "Coherent terahertz control of antiferromagnetic spin waves," *Nat. Photonics*, vol. 5, no. 1, pp. 31–34, 2011.

[11] M. Barbic, S. J. Dodd, H. ElBidweihy, N. R. Dilley, B. Marcheschi, A. L. Huston, H. D.

Morris, and A. P. Koretsky, "Multifield and inverse-contrast switching of magnetocaloric high contrast ratio MRI labels," *Magn Reson Med.*, vol. 85, pp. 506–517, 2020.

[12] M. Barbic, S. J. Dodd, H. D. Morris, N. Dilley, B. Marcheschi, A. Huston, T. D. Harris, and A. P. Koretsky, "Magnetocaloric materials as switchable high contrast ratio MRI labels," *Magn Reson Med.*, vol. 81, pp. 2238–2246, 2018.

[13] J. Finley and L. Liu, "Spintronics with compensated ferrimagnets," *Appl. Phys. Lett.*, vol. 116, no. 11, p. 110501, 2020.

[14] J. Han, R. Cheng, L. Liu, H. Ohno, and S. Fukami, "Coherent antiferromagnetic spintronics," *Nat. Mater.*, pp. 1–12, 2023.

[15] T. Jungwirth, X. Marti, P. Wadley, and J. Wunderlich, "Antiferromagnetic spintronics," *Nat. Nanotechnol.*, vol. 11, no. 3, pp. 231–241, 2016.

[16] J. B. Kramer, "The early history of magnetism," *Trans. Newcomen Soc.*, vol. 14, no. 1, pp. 183–200, 1933.

[17] D. C. Mattis, *The Theory Of Magnetism Made Simple: An Introduction to Physical Concepts and to Some Useful Mathematical Methods*. World Scientific Publishing Company, 2006.

[18] J. M. D. Coey, *Magnetism and Magnetic Materials*. Cambridge University Press, 2011.

[19] P. van Alem. (2005) Hydrogen orbitals. MATLAB Central File Exchange. Accessed: 2023-06-01. [Online]. Available: https://www.mathworks.com/matlabcentral/fileexchange/64274-hydrogen-orbitals

[20] B. Odom, D. Hanneke, B. D'Urso, and G. Gabrielse, "New measurement of the electron magnetic moment using a one-electron quantum cyclotron," *Phys. Rev. Lett.*, vol. 97, p. 030801, 2006.

[21] A. Landé, "Über den anomalen zeemaneffekt (teil i)," *Z. Phys*, vol. 5, no. 4, pp. 231–241, 1921.

[22] K. M. Krishnan, *Fundamentals and Applications of Magnetic Materials*. Oxford University Press, 2016.

[23] C. Kittel, *Introduction to Solid State Physics*. New York: John Wiley & Sons, 2005.

[24] P. Langevin, "Sur la théorie du magnétisme," *J. Phys. Theor. Appl.*, vol. 4, no. 1, pp. 678–693, 1905.

[25] P. Weiss, "L'hypothèse du champ moléculaire et la propriété ferromagnétique," *J. Phys. Theor. Appl.*, vol. 6, no. 1, pp. 661–690, 1907.

[26] F. Tyler, "The magnetization-temperature curves of iron, cobalt, and nickel," *Lond. Edinb. Dublin Philos. Mag. J. Sci.*, vol. 11, no. 70, pp. 596–602, 1931.

[27] J. C. Slater, "The ferromagnetism of nickel. ii. temperature effects," *Phys. Rev.*, vol. 49, pp. 931–937, 1936.

[28] L. Pauling, "The nature of the interatomic forces in metals," *Phys. Rev.*, vol. 54, pp. 899–904, 1938.

[29] P. A. Fedders and P. C. Martin, "Itinerant antiferromagnetism," *Phys. Rev.*, vol. 143, pp. 245–259, 1966.

[30] U. Brandt, "Theory of itinerant antiferromagnets in magnetic fields," *Z. Phys.*, vol. 257, no. 4, pp. 320–335, 1972.

[31] A. Shibatani, K. Motizuki, and T. Nagamiya, "Spin density wave in chromium and its alloys," *Phys. Rev.*, vol. 177, no. 2, p. 984, 1969.

[32] E. Fawcett, "Spin-density-wave antiferromagnetism in the chromium system I: Magnetic phase diagrams, impurity states, magnetic excitations and structure in the sdw phase," *Mat.-Fys. Medd.*, pp. 325–344, 1997.

[33] E. Fawcett, "Spin-density-wave antiferromagnetism in chromium," *Rev. Mod. Phys.*, vol. 60, no. 1, p. 209, 1988.

[34] M. Mori and Y. Tsunoda, "Searching for charge density waves in chromium," *J. Phys.: Condens. Matter*, vol. 5, no. 7, p. L77, 1993.

[35] C. Li and A. J. Freeman, "Giant monolayer magnetization of Fe on MgO: A nearly ideal two-dimensional magnetic system," *Phys. Rev. B*, vol. 43, pp. 780–787, 1991.

[36] M. Sicot, S. Andrieu, F. Bertran, and F. Fortuna, "Electronic properties of Fe, Co, and Mn ultrathin films at the interface with MgO (001)," *Phys. Rev. B*, vol. 72, no. 14, p. 144414, 2005.

[37] K. Miyokawa, S. Saito, T. Katayama, T. Saito, T. Kamino, K. Hanashima, Y. Suzuki, K. Mamiya, T. Koide, and S. Yuasa, "X-ray absorption and x-ray magnetic circular dichroism studies of a monatomic Fe (001) layer facing a single-crystalline MgO (001) tunnel barrier," *Jpn. J. Appl. Phys.*, vol. 44, no. 1L, p. L9, 2004.

[38] C. L. Fu, A. J. Freeman, and T. Oguchi, "Prediction of strongly enhanced two-dimensional ferromagnetic moments on metallic overlayers, interfaces, and superlattices," *Phys. Rev. Lett.*, vol. 54, pp. 2700–2703, 1985.

[39] C. Turtur and G. Bayreuther, "Magnetic moments in ultrathin cr films on fe(100)," *Phys. Rev. Lett.*, vol. 72, pp. 1557–1560, 1994.

[40] P. W. Bridgman, "Compressibilities and pressure coefficients of resistance of elements, compounds, and alloys, many of them anomalous," *CR Acad. Sci. Paris*, vol. 68, pp. 27–93, 1932.

[41] L. Néel, "Theory of constant paramagnetism. Application to manganese," *CR Acad. Sci. Paris*, vol. 203, pp. 304–306, 1936.

[42] V. N. Bykov, V. S. Golovkin, N. V. Ageev, V. A. Levdik, and S. I. Vinogradov, "Neutron diffraction study in CrV dilute alloys," *Dokl. Akad. Nauk SSSR*, vol. 128, p. 1153, 1959.

[43] L. M. Corliss, J. M. Hastings, and R. J. Weiss, "Antiphase antiferromagnetic structure of chromium," *Phys. Rev. Lett.*, vol. 3, pp. 211–212, 1959.

[44] W. C. Röntgen, "On a new kind of rays," *Science*, vol. 3, no. 59, pp. 227–231, 1896.

[45] A. Glavic and M. Björck, "*GenX 3*: the latest generation of an established tool," *Journal of Applied Crystallography*, vol. 55, no. 4, pp. 1063–1071, 2022.

[46] H. Kiessig, "Studies on the total reflection of x-rays," *Ann. Phys.*, vol. 10, p. 715, 1931.

[47] M. Blume, "Magnetic scattering of x rays," *J. Appl. Phys.*, vol. 57, no. 8, pp. 3615–3618, 1985.

[48] D. S. Sivia, W. A. Hamilton, G. S. Smith, T. P. Rieker, and R. Pynn, "A novel experimental procedure for removing ambiguity from the interpretation of neutron and x-ray reflectivity measurements: 'speckle holography'," *Journal of Applied Physics*, vol. 70, no. 2, pp. 732–738, 1991.

[49] E. Beaurepaire, J.-C. Merle, A. Daunois, and J.-Y. Bigot, "Ultrafast spin dynamics in ferromagnetic nickel," *Phys. Rev. Lett.*, vol. 76, pp. 4250–4253, May 1996.

[50] M. B. Agranat, S. I. Ashitkov, A. B. Granovskii, and G. I. Rukman, "Interaction of picosecond laser pulses with the electron, spin, and phonon subsystems of nickel," *Zh. Eksp. Teor. Fiz*, vol. 86, no. 10, pp. 1376–1379, 1984.

[51] A. Kirilyuk, A. V. Kimel, and T. Rasing, "Ultrafast optical manipulation of magnetic order," *Rev. Mod. Phys.*, vol. 82, pp. 2731–2784, 2010.

[52] D. L. Rode, V. R. Gaddam, and J. H. Yi, "Subnanometer surface roughness of dc magnetron sputtered Al films," *J. Appl. Phys.*, vol. 102, p. 024303, 2007.

[53] D. Song, A. G. Aberle, and J. Xia, "Optimisation of ZnO: Al films by change of sputter gas pressure for solar cell application," *Appl. Surf. Sci.*, vol. 195, pp. 291–296, 2002.

[54] K. Srinivas, M. M. Raja, D. S. Rao, and S. V. Kamat, "Effect of sputtering pressure and power on composition, surface roughness, microstructure and magnetic properties of as-deposited Co_2FeSi thin films," *Thin Solid Films*, vol. 558, pp. 349–355, 2014.

[55] S. M. Rossnagel, I. Yang, and J. J. Cuomo, "Compositional changes during magnetron sputtering of alloys," *Thin Solid Films*, vol. 199, pp. 59–69, 1991.

[56] S. M. Rossnagel, "Deposition and redeposition in magnetrons," *J. Vac. Sci. Technol., A*, vol. 6, p. 3049, 1988.

[57] J. Arregi, O. Caha, and V. Uhlíř, "Evolution of strain across the magnetostructural phase transition in epitaxial FeRh films on different substrates," *Phys. Rev. B*, vol. 101, p. 174413, 2020.

[58] A. E. Grigorescu, M. C. Van der Krogt, C. W. Hagen, and P. Kruit, "10 nm lines and spaces written in HSQ, using electron beam lithography," *Microelectron. Eng.*, vol. 84, pp. 822–824, 2007.

[59] H. Yang, A. Jin, Q. Luo, J. Li, C. Gu, and Z. Cui, "Electron beam lithography of HSQ/PMMA bilayer resists for negative tone lift-off process," *Microelectron. Eng.*, vol. 85, pp. 814–817, 2008.

[60] S. Foner, "Versatile and sensitive vibrating-sample magnetometer," *Rev. Sci. Instrum.*, vol. 30, pp. 548–557, 1959.

[61] S. Foner, "Magnetic test apparatus," U.S. Patent 2 946 948, 1960.

[62] S. Foner, "Vibrating Sample Magnetometers," U.S. Patent 3 496 459, 1967.

[63] B. D. Cullity and C. D. Graham, *Introduction to Magnetic Materials*. John Wiley & Sons, 2009.

[64] Vibrating Sample Magetometer (VSM). Quantum Design. Accessed: 2022-10-24. [Online]. Available: https://qdusa.com/siteDocs/productBrochures/1084-500_PPMS_VSM.pdf

[65] Large Bore Coil Set (VSM). Quantum Design. Accessed: 2022-10-24. [Online]. Available: https://qdusa.com/siteDocs/productBrochures/1084-500_PPMS_LBCS_VSM.pdf

[66] Quantum Design PPMS. Quantum Design. Accessed: 2022-10-24. [Online]. Available: https://www.qdusa.com/products/ppms.html

[67] Quantum Design PPMS VersaLab. Quantum Design. Accessed: 2022-10-24. [Online]. Available: https://www.qdusa.com/products/versalab.html

[68] Vibrating Sample Magetometer Oven. Quantum Design. Accessed: 2022-10-24. [Online]. Available: https://qdusa.com/siteDocs/productBrochures/1084-500_PPMS_VSM_Oven.pdf

[69] MPMS3. Quantum Design. Accessed: 2022-10-24. [Online]. Available: https://qdusa.com/siteDocs/productBrochures/1500-102.pdf

[70] O. Schmidt, E. Benda, D. Capatina, T. Clute, J. Collins, M. Erdmann, T. Graber, D. Haeffner, Y. Jaski, J. Knopp, G. Navrotski, and R. Winarski, "Beamline engineering overview for the APS upgrade," in *Mech. Eng. Design of Synchrotron Radiat. Equip. and Instrum (MEDSI'18)*, Paris, France, June 2018, pp. 324–326.

[71] About The APS. Argonne National Laboratory. Accessed: 2023-05-26. [Online]. Available: https://www.aps.anl.gov/About/Overview

[72] Beamline 7-ID-B,C,D: Time Resolved Scattering and Spectroscopy. Argonne National Laboratory. Accessed: 2023-05-26. [Online]. Available: https://www.aps.anl.gov/Beamlines/Directory/Details?beamline_id=11

[73] Beamline 8-ID-E: GIXS, GISAXS, GIWAXS, and XPCS. Argonne National Laboratory. Accessed: 2023-05-26. [Online]. Available: https://www.aps.anl.gov/Beamlines/Directory/Details?beamline_id=109

[74] About Us. The European Synchrotron Radiation Facility. Accessed: 2023-06-02. [Online]. Available: https://www.esrf.fr/about

[75] ID12 - Circular Polarisation Beamine. The European Synchrotron Radiation Facility. Accessed: 2023-06-02. [Online]. Available: https://www.esrf.fr/UsersAndScience/Experiments/EMD/ID12

[76] LCLS Overview. SLAC National Accelerator Laboratory. Accessed: 2023-05-27. [Online]. Available: https://lcls.slac.stanford.edu/overview

[77] XPP - X-ray Pump Probe. SLAC National Accelerator Laboratory. Accessed: 2023-05-27. [Online]. Available: https://lcls.slac.stanford.edu/instruments/xpp

[78] High Flux Isotope Reactor technical parameters. Oak Ridge National Laboratory. Accessed: 2023-01-19. [Online]. Available: https://neutrons.ornl.gov/hfir/parameters

[79] How SNS works. Oak Ridge National Laboratory. Accessed: 2023-01-19. [Online]. Available: https://neutrons.ornl.gov/content/how-sns-works

[80] Magnetism Reflectometer. Oak Ridge National Laboratory. Accessed: 2023-02-01. [Online]. Available: https://neutrons.ornl.gov/mr

[81] J. Han, R. Cheng, L. Liu, H. Ohno, and S. Fukami, "Coherent antiferromagnetic spintronics," *Nat. Mater.*, pp. 1–12, 2023.

[82] T. Jungwirth, X. Marti, P. Wadley, and J. Wunderlich, "Antiferromagnetic spintronics," *Nature nanotechnology*, vol. 11, no. 3, pp. 231–241, 2016.

[83] V. Baltz, A. Manchon, M. Tsoi, T. Moriyama, T. Ono, and Y. Tserkovnyak, "Antiferromagnetic spintronics," *Rev. Mod. Phys.*, vol. 90, p. 015005, 2018.

[84] J. J. Heitz, L. Nádvorník, V. Balos, Y. Behovits, A. L. Chekhov, T. S. Seifert, K. Olejník, Z. Kašpar, K. Geishendorf, V. Novák *et al.*, "Optically gated terahertz-field-driven switching of antiferromagnetic CuMnAs," *Physical Review Applied*, vol. 16, no. 6, p. 064047, 2021.

[85] R. K. Kummamuru and Y.-A. Soh, "Electrical effects of spin density wave quantization and magnetic domain walls in chromium," *Nature*, vol. 452, no. 7189, pp. 859–863, 2008.

[86] Y.-A. Soh and R. K. Kummamuru, "Spintronics in antiferromagnets," *Philos. Trans. R. Soc. London, Ser. A*, vol. 369, no. 1951, pp. 3646–3657, 2011.

[87] O. G. Shpyrko, E. D. Isaacs, J. M. Logan, Y. Feng, G. Aeppli, R. Jaramillo, H. C. Kim, T. F. Rosenbaum, P. Zschack, M. Sprung, S. Narayanan, and A. R. Sandy, "Direct measurement of antiferromagnetic domain fluctuations," *Nature*, vol. 447, no. 7140, pp. 68–71, 2007.

[88] G. Grüner, "The dynamics of charge-density waves," *Rev. Mod. Phys.*, vol. 60, pp. 1129–1181, 1988.

[89] G. Shirane and W. J. Takei, "Neutron diffraction study of chromium single crystals," *J. Phys. Soc. Japan*, vol. 17, 1962.

[90] P. G. Evans, E. D. Isaacs, G. Aeppli, Z. Cai, and B. Lai, "X-ray microdiffraction images of antiferromagnetic domain evolution in chromium," *Science*, vol. 295, no. 5557, pp. 1042–1045, 2002.

[91] E. E. Fullerton, J. L. Robertson, A. R. E. Prinsloo, H. L. Alberts, and S. D. Bader, "Hysteretic spin-density-wave ordering in confined geometries," *Phys. Rev. Lett.*, vol. 91, p. 237201, 2003.

[92] E. E. Fullerton, S. Adenwalla, G. P. Felcher, K. T. Riggs, C. H. Sowers, S. D. Bader, and J. L. Robertson, "Neutron diffraction and reflectivity studies of the cr néel transition in fe/cr (001) superlattices," *Physica B: Condens. Matter*, vol. 221, no. 1-4, pp. 370–376, 1996.

[93] J. Unguris, R. J. Celotta, and D. T. Pierce, "Magnetism in cr thin films on fe(100)," *Phys. Rev. Lett.*, vol. 69, pp. 1125–1128, 1992.

[94] E. E. Fullerton, S. D. Bader, and J. L. Robertson, "Spin-density-wave antiferromagnetism of Cr in Fe/Cr(001) superlattices," *Phys. Rev. Lett.*, vol. 77, pp. 1382–1385, 1996.

[95] Z.-P. Shi and R. S. Fishman, "Interplay between spin-density wave and proximity magnetic layers," *Phys. Rev. Lett.*, vol. 78, pp. 1351–1354, 1997.

[96] R. S. Fishman, "Magnetic phase diagram of interfacially rough fe/cr multilayers," *Phys. Rev. B*, vol. 57, pp. 10 284–10 286, 1998.

[97] K. Hirai, "Spin-density wave in fe/cr superlattices: A first-principles study," *Phys. Rev. B*,

vol. 59, pp. R6612–R6615, 1999.

[98] P. A. Lee and T. M. Rice, "Electric field depinning of charge density waves," *Phys. Rev. B*, vol. 19, pp. 3970–3980, 1979.

[99] P. B. Littlewood and T. M. Rice, "Metastability of the q vector of pinned charge- and spin-density waves," *Phys. Rev. Lett.*, vol. 48, pp. 44–47, 1982.

[100] G. Teisseron, J. Berthier, P. Peretto, C. Benski, M. Robin, and S. Choulet, "The spin density waves in chromium detected by hyperfine field measurements," *J. Magn. Magn. Mater.*, vol. 8, no. 2, pp. 157–163, 1978.

[101] A. M. N. Niklasson, "Magnetism in layered materials," Ph.D. dissertation, Uppsala Universiteit, 1998.

[102] H. Zabel, "Magnetism of chromium at surfaces, at interfaces and in thin films," *J. Phys. Condens. Matter*, vol. 11, no. 48, p. 9303, 1999.

[103] T. Asada, G. Bihlmayer, S. Handschuh, S. Heinze, P. Kurz, and S. Blügel, "First-principles theory of ultrathin magnetic films," *J. Phys.: Condens. Matter*, vol. 11, no. 48, p. 9347, 1999.

[104] A. M. N. Niklasson, J. M. Wills, and L. Nordström, "Spin density waves in Cr/Mo films," *Phys. Rev. B*, vol. 63, p. 104417, 2001.

[105] A. Singer, M. J. Marsh, S. H. Dietze, V. Uhlíř, Y. Li, D. A. Walko, E. M. Dufresne, G. Srajer, M. P. Cosgriff, P. G. Evans, E. E. Fullerton, and O. G. Shpyrko, "Condensation of collective charge ordering in chromium," *Phys. Rev. B*, vol. 91, p. 115134, 2015.

[106] A. L. Trego and A. R. Mackintosh, "Antiferromagnetism in chromium alloys. ii. transport properties," *Phys. Rev.*, vol. 166, pp. 495–506, 1968.

[107] E. E. Fullerton, K. T. Riggs, C. H. Sowers, S. D. Bader, and A. Berger, "Suppression of biquadratic coupling in fe /cr(001) superlattices below the néel transition of cr," *Phys. Rev. Lett.*, vol. 75, pp. 330–333, 1995.

[108] P. Sonntag, P. Bödeker, T. Thurston, and H. Zabel, "Charge-density waves and strain waves in thin epitaxial Cr(001) films on Nb," *Phys. Rev. B*, vol. 52, pp. 7363–7368, 1995.

[109] A. Singer, S. K. K. Patel, R. Kukreja, V. Uhlíř, J. Wingert, S. Festersen, D. Zhu, J. M. Glownia, H. T. Lemke, S. Nelson, M. Kozina, K. Rossnagel, M. Bauer, B. M. Murphy, O. M. Magnussen, E. E. Fullerton, and O. G. Shpyrko, "Photoinduced enhancement of the charge density wave amplitude," *Phys. Rev. Lett.*, vol. 117, p. 056401, 2016.

[110] B. E. Warren, *X-Ray Diffraction*. New York: Courier Dover Publications, 1990.

[111] E. E. Fullerton, I. K. Schuller, H. Vanderstraeten, and Y. Bruynseraede, "Structural re-

finement of superlattices from x-ray diffraction," *Phys. Rev. B*, vol. 45, pp. 9292–9310, 1992.

[112] E. E. Fullerton, D. Stoeffler, K. Ounadjela, B. Heinrich, Z. Celinski, and J. A. C. Bland, "Structure and magnetism of epitaxially strained Pd(001) films on Fe(001): Experiment and theory," *Phys. Rev. B*, vol. 51, pp. 6364–6378, 1995.

[113] S. K. Sinha, E. B. Sirota, S. Garoff, and H. B. Stanley, "X-ray and neutron scattering from rough surfaces," *Phys. Rev. B*, vol. 38, pp. 2297–2311, 1988.

[114] G. White, R. Roberts, and E. Fawcett, "Thermal expansion of Cr and CrV alloys. i. experiment," *J. Phys. F: Met. Phys.*, vol. 16, no. 4, p. 449, 1986.

[115] J. Bardeen, L. N. Cooper, and J. R. Schrieffer, "Theory of superconductivity," *Phys. Rev.*, vol. 108, pp. 1175–1204, 1957.

[116] A. W. Overhauser, "Spin density waves in an electron gas," *Phys. Rev.*, vol. 128, pp. 1437–1452, 1962.

[117] K. W. Kim, A. Pashkin, H. Schäfer, M. Beyer, M. Porer, T. Wolf, C. Bernhard, J. Demsar, R. Huber, and A. Leitenstorfer, "Ultrafast transient generation of spin-density-wave order in the normal state of $BaFe_2As_2$ driven by coherent lattice vibrations," *Nature materials*, vol. 11, no. 6, pp. 497–501, 2012.

[118] T. Ishikawa, Y. Sagae, Y. Naitoh, Y. Kawakami, H. Itoh, K. Yamamoto, K. Yakushi, H. Kishida, T. Sasaki, S. Ishihara, Y. Tanaka, K. Yonemitsu, and S. Iwai, "Optical freezing of charge motion in an organic conductor," *Nat. Commun.*, vol. 5, no. 1, p. 5528, 2014.

[119] D. Fausti, R. Tobey, N. Dean, S. Kaiser, A. Dienst, M. C. Hoffmann, S. Pyon, T. Takayama, H. Takagi, and A. Cavalleri, "Light-induced superconductivity in a stripe-ordered cuprate," *Science*, vol. 331, no. 6014, pp. 189–191, 2011.

[120] R. Mankowsky, A. Subedi, M. Först, S. O. Mariager, M. Chollet, H. Lemke, J. S. Robinson, J. M. Glownia, M. P. Minitti, A. Frano *et al.*, "Nonlinear lattice dynamics as a basis for enhanced superconductivity in $YBa_2Cu_3O_{6.5}$," *Nature*, vol. 516, no. 7529, pp. 71–73, 2014.

[121] W. Hu, S. Kaiser, D. Nicoletti, C. R. Hunt, I. Gierz, M. C. Hoffmann, M. Le Tacon, T. Loew, B. Keimer, and A. Cavalleri, "Optically enhanced coherent transport in $YBa_2Cu_3O_{6.5}$ by ultrafast redistribution of interlayer coupling," *Nat. Mat.*, vol. 13, no. 7, pp. 705–711, 2014.

[122] K. Onda, S. Ogihara, K. Yonemitsu, N. Maeshima, T. Ishikawa, Y. Okimoto, X. Shao, Y. Nakano, H. Yamochi, G. Saito, and S.-Y. Koshihara, "Photoinduced change in the charge order pattern in the quarter-filled organic conductor $(EDO{-}TTF)_2PF_6$ with a strong electron-phonon interaction," *Phys. Rev. Lett.*, vol. 101, p. 067403, 2008.

[123] H. Ichikawa, S. Nozawa, T. Sato, A. Tomita, K. Ichiyanagi, M. Chollet, L. Guerin, N. Dean, A. Cavalleri, S.-i. Adachi, T.-H. Arima, H. Sawa, Y. Ogimoto, M. Nakamura, R. Tamaki, K. Miyano, and S.-Y. Koshihara, "Transient photoinduced 'hidden' phase in a manganite," *Nat. Mat.*, vol. 10, no. 2, pp. 101–105, 2011.

[124] L. Stojchevska, I. Vaskivskyi, T. Mertelj, P. Kusar, D. Svetin, S. Brazovskii, and D. Mihailovic, "Ultrafast switching to a stable hidden quantum state in an electronic crystal," *Science*, vol. 344, no. 6180, pp. 177–180, 2014.

[125] V. R. Morrison, R. P. Chatelain, K. L. Tiwari, A. Hendaoui, A. Bruhács, M. Chaker, and B. J. Siwick, "A photoinduced metal-like phase of monoclinic VO_2 revealed by ultrafast electron diffraction," *Science*, vol. 346, no. 6208, pp. 445–448, 2014.

[126] F. Schmitt, P. S. Kirchmann, U. Bovensiepen, R. G. Moore, L. Rettig, M. Krenz, J.-H. Chu, N. Ru, L. Perfetti, D. Lu, M. Wolf, I. R. Fisher, and Z.-X. Shen, "Transient electronic structure and melting of a charge density wave in $TbTe_3$," *Science*, vol. 321, no. 5896, pp. 1649–1652, 2008.

[127] A. Tomeljak, H. Schäfer, D. Städter, M. Beyer, K. Biljakovic, and J. Demsar, "Dynamics of photoinduced charge-density-wave to metal phase transition in $K_{0.3}MoO_3$," *Phys. Rev. Lett.*, vol. 102, p. 066404, 2009.

[128] M. Eichberger, H. Schäfer, M. Krumova, M. Beyer, J. Demsar, H. Berger, G. Moriena, G. Sciaini, and R. D. Miller, "Snapshots of cooperative atomic motions in the optical suppression of charge density waves," *Nature*, vol. 468, no. 7325, pp. 799–802, 2010.

[129] P. Beaud, A. Caviezel, S. Mariager, L. Rettig, G. Ingold, C. Dornes, S. Huang, J. Johnson, M. Radovic, T. Huber, T. Kubacka, A. Ferrer, H. T. Lemke, M. Chollet, D. Zhu, J. M. Glownia, M. Sikorski, A. Robert, H. Wadati, M. Nakamura, M. Kawasaki, Y. Tokura, S. L. Johnson, and U. Staub, "A time-dependent order parameter for ultrafast photoinduced phase transitions," *Nat. Mat.*, vol. 13, no. 10, pp. 923–927, 2014.

[130] S. A. Friedberg, I. Estermann, and J. E. Goldman, "The electronic specific heat in chromium and magnesium," *Phys. Rev.*, vol. 85, pp. 375–376, 1952.

[131] P. Emma, R. Akre, J. Arthur, R. Bionta, C. Bostedt, J. Bozek, A. Brachmann, P. Bucksbaum, R. Coffee, F.-J. Decker, Y. Ding, D. Dowell, S. Edstrom, A. Fisher, J. Frisch, S. Gilevich, J. Hastings, G. Hays, P. Hering, Z. Huang, R. Iverson, H. Loos, M. Messerschmidt, A. Miahnahri, S. Moeller, H.-D. Nuhn, G. Pile, D. Ratner, J. Rzepiela, D. Schultz, T. Smith, P. Stefan, H. Tompkins, J. Turner, J. Welch, W. White, J. Wu, G. Yocky, and J. Galayda, "First lasing and operation of an ångstrom-wavelength free-electron laser," *Nat. Photonics*, vol. 4, no. 9, pp. 641–647, 2010.

[132] D. Zhu, Y. Feng, S. Stoupin, S. A. Terentyev, H. T. Lemke, D. M. Fritz, M. Chollet, J. Glownia, R. Alonso-Mori, M. Sikorski, S. Song, T. B. van Driel1, G. J. Williams, M. Messerschmidt, S. Boutet, V. D. Blank, Y. V. Shvyd'ko, and A. Robert, "Performance

of a beam-multiplexing diamond crystal monochromator at the linac coherent light source," *Rev. Sci. Instrum.*, vol. 85, no. 6, p. 063106, 2014.

[133] S. I. Anisimov, B. L. Kapeliovich, and T. L. Perel'man, "Electron emission from metal surfaces exposed to ultrashort laser pulses," *Zh. Eksp. Teor. Fiz*, vol. 66, no. 2, pp. 375–377, 1974.

[134] S. D. Brorson, A. Kazeroonian, J. S. Moodera, D. W. Face, T. K. Cheng, E. P. Ippen, M. S. Dresselhaus, and G. Dresselhaus, "Femtosecond room-temperature measurement of the electron-phonon coupling constant γ in metallic superconductors," *Phys. Rev. Lett.*, vol. 64, pp. 2172–2175, 1990.

[135] I. Estermann, S. A. Friedberg, and J. E. Goldman, "The specific heats of several metals between 1.8° and 4.2°K," *Phys. Rev.*, vol. 87, pp. 582–588, 1952.

[136] M. Trigo, M. Fuchs, J. Chen, M. P. Jiang, M. Cammarata, S. Fahy, D. M. Fritz, K. Gaffney, S. Ghimire, A. Higginbotham, S. L. Johnson, M. E. Kozina, J. Larsson, H. Lemke, A. M. Lindenberg, G. Ndabashimiye, F. Quirin, K. Sokolowski-Tinten, C. Uher, G. Wang, J. S. Wark, D. Zhu, and D. A. Reis, "Fourier-transform inelastic x-ray scattering from time- and momentum-dependent phonon–phonon correlations," *Nat. Phys.*, vol. 9, no. 12, pp. 790–794, 2013.

[137] D. Zhu, A. Robert, T. Henighan, H. T. Lemke, M. Chollet, J. M. Glownia, D. A. Reis, and M. Trigo, "Phonon spectroscopy with sub-meV resolution by femtosecond x-ray diffuse scattering," *Phys. Rev. B*, vol. 92, p. 054303, 2015.

[138] H. J. Zeiger, J. Vidal, T. K. Cheng, E. P. Ippen, G. Dresselhaus, and M. S. Dresselhaus, "Theory for displacive excitation of coherent phonons," *Phys. Rev. B*, vol. 45, pp. 768–778, 1992.

[139] A. Melnikov, I. Radu, A. Povolotskiy, T. Wehling, A. Lichtenstein, and U. Bovensiepen, "Ultrafast dynamics at lanthanide surfaces: microscopic interaction of the charge, lattice and spin subsystems," *J. Phys. D: Appl. Phys.*, vol. 41, no. 16, p. 164004, 2008.

[140] T. Huber, S. O. Mariager, A. Ferrer, H. Schäfer, J. A. Johnson, S. Grübel, A. Lübcke, L. Huber, T. Kubacka, C. Dornes, C. Laulhe, S. Ravy, G. Ingold, P. Beaud, J. Demsar, and S. L. Johnson, "Coherent structural dynamics of a prototypical charge-density-wave-to-metal transition," *Phys. Rev. Lett.*, vol. 113, p. 026401, 2014.

[141] W. M. Shaw and L. D. Muhlestein, "Investigation of the phonon dispersion relations of chromium by inelastic neutron scattering," *Phys. Rev. B*, vol. 4, pp. 969–973, 1971.

[142] R. H. M. Groeneveld, R. Sprik, and A. Lagendijk, "Femtosecond spectroscopy of electron-electron and electron-phonon energy relaxation in Ag and Au," *Phys. Rev. B*, vol. 51, pp. 11 433–11 445, 1995.

[143] K. Ishioka and O. Misochko, "Progress in ultrafast intense laser science," *Springer Ser. Chem. Phys.*, pp. 23–64, 2010.

[144] P. Beaud, S. L. Johnson, A. Streun, R. Abela, D. Abramsohn, D. Grolimund, F. Krasniqi, T. Schmidt, V. Schlott, and G. Ingold, "Spatiotemporal stability of a femtosecond hard–x-ray undulator source studied by control of coherent optical phonons," *Phys. Rev. Lett.*, vol. 99, p. 174801, 2007.

[145] H. Schaefer, V. V. Kabanov, and J. Demsar, "Collective modes in quasi-one-dimensional charge-density wave systems probed by femtosecond time-resolved optical studies," *Phys. Rev. B*, vol. 89, p. 045106, 2014.

[146] R. Jaramillo, Y. Feng, J. C. Lang, Z. Islam, G. Srajer, H. M. Rønnow, P. B. Littlewood, and T. F. Rosenbaum, "Chromium at high pressures: Weak coupling and strong fluctuations in an itinerant antiferromagnet," *Phys. Rev. B*, vol. 77, p. 184418, 2008.

[147] O. Y. Gorobtsov, L. Ponet, S. K. K. Patel, N. Hua, A. Shabalin, S. Hrkac, J. Wingert, D. Cela, J. Glownia, D. Zhu, R. Medapalli, M. Chollet, E. E. Fullerton, S. Artyukhin, O. G. Shpyrko, and A. Singer, "Femtosecond control of phonon dynamics near a magnetic order critical point," *Nat. Commun.*, vol. 12, p. 2865, 2021.

[148] A. Singer, S. K. K. Patel, V. Uhlíř, R. Kukreja, A. Ulvestad, E. M. Dufresne, A. R. Sandy, E. E. Fullerton, and O. G. Shpyrko, "Phase coexistence and pinning of charge density waves by interfaces in chromium," *Phys. Rev. B*, vol. 94, p. 174110, 2016.

[149] J. Li, O. Y. Gorobtsov, S. K. K. Patel, N. Hua, B. Gregory, A. G. Shabalin, S. Hrkac, J. Wingert, D. Cela, J. M. Glownia, M. Chollet, D. Zhu, R. Medapalli, E. E. Fullerton, O. G. Shpyrko, and A. Singer, "Phonon-assisted formation of an itinerant electronic density wave," *Commun. Phys.*, vol. 5, no. 1, p. 125, 2022.

[150] J. Wingert, A. Singer, S. K. K. Patel, R. Kukreja, M. J. Verstraete, A. H. Romero, V. Uhlíř, S. Festersen, D. Zhu, J. M. Glownia, H. T. Lemke, S. Nelson, M. Kozina, K. Rossnagel, B. M. Murphy, O. M. Magnussen, E. E. Fullerton, and O. G. Shpyrko, "Direct time-domain determination of electron-phonon coupling strengths in chromium," *Phys. Rev. B*, vol. 102, p. 041101, 2020.

[151] T. Berndt, A. R. Muxworthy, and G. A. Paterson, "Determining the magnetic attempt time τ_0, its temperature dependence, and the grain size distribution from magnetic viscosity measurements," *J. Geophys. Res.: Solid Earth*, vol. 120, no. 11, pp. 7322–7336, 2015.

[152] W. L. McMillan, "Microscopic model of charge-density waves in $2h - \mathrm{Tase}_2$," *Phys. Rev. B*, vol. 16, pp. 643–650, 1977.

[153] R. Jaramillo, Y. Feng, J. C. Lang, Z. Islam, G. Srajer, P. B. Littlewood, D. B. McWhan, and T. F. Rosenbaum, "Breakdown of the bardeen–cooper–schrieffer ground state at a quantum phase transition," *Nature*, vol. 459, no. 7245, pp. 405–409, 2009.

[154] Y. Feng, J. Van Wezel, J. Wang, F. Flicker, D. M. Silevitch, P. B. Littlewood, and T. F. Rosenbaum, "Itinerant density wave instabilities at classical and quantum critical points," *Nat. Phys.*, vol. 11, no. 10, pp. 865–871, 2015.

[155] W. J. Venema, R. Griessen, and W. Ruesink, "Volume dependence of the fermi surface and of the spin-density-wave q vector in antiferromagnetic chromium," *J. Phys. F: Met. Phys.*, vol. 10, no. 12, p. 2841, 1980.

[156] List of thermal expansion coefficients (CTE) for natural and engineered materials. MSE Supplies. Accessed: 2023-03-06. [Online]. Available: https://www.msesupplies.com/pages/list-of-thermal-expansion-coefficients-cte-for-natural-and-engineered-materials

[157] R. J. Weiss, "The origin of the Invar effect," *Proc. Phys. Soc.*, vol. 82, no. 2, p. 281, 1963.

[158] S. Khmelevskyi, I. Turek, and P. Mohn, "Large negative magnetic contribution to the thermal expansion in iron-platinum alloys: Quantitative theory of the Invar effect," *Phys. Rev. Lett.*, vol. 91, p. 037201, 2003.

[159] M. van Schilfgaarde, I. A. Abrikosov, and B. Johansson, "Origin of the Invar effect in iron–nickel alloys," *Nature*, vol. 400, no. 6739, pp. 46–49, 1999.

[160] J. S. O. Evans, T. A. Mary, T. Vogt, M. A. Subramanian, and A. W. Sleight, "Negative thermal expansion in ZrW_2O_8 and HfW_2O_8," *Chem. Mater.*, vol. 8, no. 12, pp. 2809–2823, 1996.

[161] J. S. O. Evans, W. I. F. David, and A. W. Sleight, "Structural investigation of the negative-thermal-expansion material ZrW_2O_8," *Acta Crystallogr., Sect. B: Struct. Sci*, vol. 55, no. 3, pp. 333–340, 1999.

[162] A. K. A. Pryde, K. D. Hammonds, M. T. Dove, V. Heine, J. D. Gale, and M. C. Warren, "Origin of the negative thermal expansion in ZrW_2O_8 and ZrV_2O_7," *J. Phys.: Condens. Matter*, vol. 8, no. 50, p. 10973, 1996.

[163] M. G. Tucker, A. L. Goodwin, M. T. Dove, D. A. Keen, S. A. Wells, and J. S. O. Evans, "Negative thermal expansion in ZrW_2O_8: Mechanisms, rigid unit modes, and neutron total scattering," *Phys. Rev. Lett.*, vol. 95, p. 255501, 2005.

[164] S. Iikubo, K. Kodama, K. Takenaka, H. Takagi, and S. Shamoto, "Magnetovolume effect in $Mn_3Cu_{1-x}Ge_xN$ related to the magnetic structure: neutron powder diffraction measurements," *Phys. Rev. B*, vol. 77, p. 020409, 2008.

[165] B. Y. Qu and B. C. Pan, "Nature of the negative thermal expansion in antiperovskite compound Mn_3ZnN," *J. Appl. Phys.*, vol. 108, p. 113920, 2010.

[166] K. Takenaka, "Negative thermal expansion materials: technological key for control of thermal expansion," *Sci. Technol. Adv. Mater.*, vol. 13, p. 013001, 2012.

[167] K. Takenaka, M. Ichigo, T. Hamada, A. Ozawa, T. Shibayama, T. Inagaki, and K. Asano, "Magnetovolume effects in manganese nitrides with antiperovskite structure," *Sci. Technol. Adv. Mater.*, vol. 15, p. 015009, 2014.

[168] F. Sayetat, P. Fertey, , and M. Kessler, "An easy method for the determination of debye temperature from thermal expansion analyses," *J. Appl. Crystallogr.*, vol. 31, pp. 121–127, 1998.

[169] Y. Sun, C. Wang, Y. Wen, K. Zhu, and J. Zhao, "Lattice contraction and magnetic and electronic transport properties of $Mn_3Zn_{1-x}Ge_xN$," *Appl. Phys. Lett.*, vol. 91, p. 231913, 2007.

[170] E. O. Chi, W. S. Kim, and N. H. Hur, "Nearly zero temperature coefficient of resistivity in antiperovskite compound $CuNMn_3$," *Solid State Commun.*, vol. 120, pp. 307–310, 2001.

[171] K. Kamishima, T. Goto, H. Nakagawa, N. Miura, M. Ohashi, N. Mori, T. Sasaki, and T. Kanomata, "Giant magnetoresistance in the intermetallic compound Mn_3GaC," *Phys. Rev. B*, vol. 63, p. 024426, 2000.

[172] Y. Sun, C. Wang, L. Chu, Y. Wen, M. Nie, and F. Liu, "Low temperature coefficient of resistivity induced by magnetic transition and lattice contraction in Mn_3NiN compound," *Scr. Mater.*, vol. 62, p. 686–689, 2010.

[173] Z. Chen, R. Huang, X. Chu, Z. Wu, Z. Liu, Y. Zhou, and L. Li, "Negative thermal expansion and nearly zero temperature coefficient of resistivity in anti-perovskite manganese nitride Mn_3CuN co-doped with Ag and Sn," *Cryogenics*, vol. 52, pp. 629–631, 2012.

[174] G. Gurung, D.-F. Shao, T. R. Paudel, and E. Y. Tsymbal, "Anomalous Hall conductivity of noncollinear magnetic antiperovskites," *Phys. Rev. Mater.*, vol. 3, p. 044409, 2019.

[175] D. Boldrin, I. Samathrakis, J. Zemen, A. Mihai, B. Zou, F. Johnson, B. D. Esser, D. W. McComb, P. K. Petrov, H. Zhang, and L. F. Cohen, "Anomalous Hall effect in noncollinear antiferromagnetic Mn_3NiN thin films," *Phys. Rev. Mater.*, vol. 3, p. 094409, 2019.

[176] I. Samathrakis and H. Zhang, "Tailoring the anomalous Hall effect in the noncollinear antiperovskite Mn_3GaN," *Phys. Rev. B*, vol. 101, p. 214423, 2020.

[177] P. Lukashev, R. F. Sabirianov, and K. Belashchenko, "Theory of the piezomagnetic effect in Mn-based antiperovskites," *Phys. Rev. B*, vol. 78, p. 184414, 2008.

[178] J. Zemen, Z. Gercsi, and K. G. Sandeman, "Piezomagnetism as a counterpart of the magnetovolume effect in magnetically frustrated Mn-based antiperovskite nitrides," *Phys. Rev. B*, vol. 96, p. 024451, 2017.

[179] X. Zhou, J.-P. Hanke, W. Feng, S. Blügel, Y. Mokrousov, and Y. Yao, "Giant anomalous Nernst effect in noncollinear antiferromagnetic Mn-based antiperovskite nitrides," *Phys.*

Rev. Mat., vol. 4, p. 024408, 2020.

[180] K. Takenaka, T. Sugiura, Y. Kadowaki, M. Ozeki, Y. Okamoto, and A. Fujita, "Giant magneto-volume and magneto-caloric effects of frustrated antiferromagnet Mn_3GaN under hydrostatic pressure," *J. Phys. Soc. Jpn.*, vol. 90, p. 044601, 2021.

[181] K. Asano, K. Koyama, and K. Takenaka, "Magnetostriction in Mn_3CuN," *Appl. Phys. Lett.*, vol. 92, p. 161909, 2008.

[182] M. R. Fruchart, R. Madar, M. Barberon, M. E. Fruchart, , and M. G. Lorthioir, "Transitions magnétiques et déformations cristallographiques associées dans les nitrures du type perowskite $ZnMn_3N$ et $SnMn_3N$," *Le Journal de Physique Colloques*, vol. 32, pp. C1–982, 1971.

[183] W. S. Kim, E. O. Chi, J. C. Kim, N. H. Hur, K. W. Lee, and Y. N. Choi, "Cracks induced by magnetic ordering in the antiperovskite $ZnNMn_3$," *Phys. Rev. B*, vol. 68, p. 172402, 2003.

[184] T. Hamada and K. Takenaka, "Phase instability of magnetic ground state in antiperovskite Mn_3ZnN: giant magnetovolume effects related to magnetic structure," *J. Appl. Phys.*, vol. 111, p. 07A904, 2012.

[185] D. Fruchart and E. F. Bertaut, "Magnetic studies of the metallic perovskite-type compounds of manganese," *J. Phys. Soc. Jpn.*, vol. 44, pp. 781–791, 1978.

[186] P. l'Heritier, D. Boursier, R. Fruchart, and D. Fruchart, "Structures magnetiques et transitions du premier ordre dans les perovskites metalliques $GaMn_3(C_{1-x}N_x)$. relation avec les composes de terres rares a changement de valence." *Mat. Res. Bull.*, vol. 14, pp. 1203–1212, 1979.

[187] E. F. Bertaut, D. Fruchart, J. P. Bouchaud, and R. Fruchart, "Diffraction neutronique de Mn_3GaN," *Phys. Rev. B*, vol. 6, pp. 251–256, 1968.

[188] K. Kodama, S. Iikubo, K. Takenaka, M. Takigawa, H. Takagi, and S. Shamoto, "Gradual development of Γ^{5g} antiferromagnetic moment in the giant negative thermal expansion material $Mn_3Cu_{1-x}Ge_xN$ (x~0.5)," *Phys. Rev. B*, vol. 81, p. 224419, 2010.

[189] X. Zhou, J.-P. Hanke, W. Feng, F. Li, G.-Y. Guo, Y. Yao, S. Blügel, , and Y. Mokrousov, "Spin-order dependent anomalous hall effect and magneto-optical effect in the noncollinear antiferromagnets Mn_3XN with X = Ga, Zn, Ag, or Ni," *Phys. Rev. B*, vol. 99, p. 104428, 2019.

[190] E. V. Gomonaj, "Mangetostriction and piezomagnetism of noncollinear antiferromagnet Mn_3NiN," *Phase Transitions*, vol. 18, pp. 93–101, 1989.

[191] Y. Sun, C. Wang, Y. Na, L. Chu, Y. Wen, and M. Nie, "Investigation of antiperovskite Mn_3CuN_x film prepared by dc reactive magnetron sputtering," *Mater. Res. Bull.*, vol. 45, p.

1230–1233, 2010.

[192] Y. Na, C. Wang, L. Chu, L. Ding, J. Yan, Y. Xue, W. Xie, and X. Chen, "Preparation and properties of antiperovskite Mn_3NiN thin film," *Mater. Lett.*, vol. 65, pp. 3447–3449, 2011.

[193] Y. Na, C. Wang, Y. Sun, L. Chu, M. Nie, N. Ji, and J.-P. Wang, "Structure and properties of ternary manganese nitride Mn_3CuN_y thin films fabricated by facing target magnetron sputtering," *Mater. Res. Bull.*, vol. 46, pp. 1022–1027, 2011.

[194] Y. Na, C. Wang, E. Tomasella, J. Cellier, and J. Xiang, "Effect of Cu doping on structural and magnetic properties of antiperovskite $Mn_3Ni(Cu)N$ thin films," *J. Alloys Compd.*, vol. 647, pp. 35–40, 2015.

[195] F. Yu, L. Ren, M. Meng, Y. Wang, M. Yang, S. Wu, and S. Li, "Growth and magnetic property of antiperovskite manganese nitride films doped with Cu by molecular beam epitaxy," *J. Appl. Phys.*, vol. 115, p. 133911, 2014.

[196] Y. Na, C. Wang, and J. Xiang, "Structural and magnetic properties of antiperovskite Mn_3NiN_x thin films," *Mater. Lett.*, vol. 152, pp. 213–216, 2015.

[197] H. Sakakibara, H. Ando, Y. Kuroki, S. Kawai, K. Ueda, and H. Asano, "Magnetic properties and anisotropic magnetoresistance of antiperovskite nitride Mn_3GaN/Co_3FeN exchange-coupled bilayers," *J. Appl. Phys.*, vol. 117, p. 17D725, 2015.

[198] H. Lee, H. Sukegawa, J. Liu, T. Ohkubo, S. Kasai, S. Mitani, and K. Hono, "Ferromagnetic MnGaN thin films with perpendicular magnetic anisotropy for spintronics applications," *Appl. Phys. Lett.*, vol. 107, p. 032403, 2015.

[199] D. Boldrin, I. Samathrakis, J. Zemen, A. Mihai, B. Zou, F. Johnson, B. D. Esser, D. W. McComb, P. K. Petrov, H. Zhang, and L. F. Cohen, "Anomalous Hall effect in noncollinear antiferromagnetic Mn_3NiN thin films," *Phys. Rev. Mater.*, vol. 3, p. 294409, 2019.

[200] D. Boldrin, A. P. Mihai, B. Zou, J. Zemen, R. Thompson, E. Ware, B. V. Neamtu, L. Ghivelder, B. Esser, D. W. McComb, P. Petrov, and L. F. Cohen, "Giant piezomagnetism in Mn_3NiN," *ACS Appl. Mater. Interfaces*, vol. 10, pp. 18 863–18 868, 2018.

[201] M. Aoyama, K. Takenaka, and H. Ikuta, "Sputter deposition and characterization of Mn_3CuN thin films," *J. Alloys Compd.*, vol. 577S, pp. S314–S317, 2013.

[202] K. Takenaka and H. Takagi, "Giant negative thermal expansion in Ge-doped anti-perovskite manganese nitrides," *Appl. Phys. Lett.*, vol. 87, p. 261902, 2005.

[203] Y. Na, C. Wang, E. Tomasella, J. Cellier, and J. Xiang, "Effect of Cu doping on structural and magnetic properties of antiperovskite $Mn_3Ni(Cu)N$ thin films," *J. Alloys Compd.*, vol. 647, pp. 35–40, 2015.

[204] E. Duman, M. Acet, I. Dincer, A. Elmali, and Y. Elerman, "Competing magnetic interac-

tions in rare-earth manganese silicides and germanides," *J. Magn. Magn. Mater.*, vol. 309, pp. 40–53, 2007.

[205] S. Chaudhary, P. Garg, and S. Rajput, "Investigations of the first order magnetic phase transition in dysprosium," *Solid State Commun.*, vol. 132, pp. 293–297, 2004.

[206] M. K. Chattopadhyay, M. A. Manekar, and S. B. Roy, "Magnetocaloric effect in $CeFe_2$ and Ru-doped $CeFe_2$ alloys," *J. Phys. D: Appl. Phys.*, vol. 39, p. 1006, 2006.

[207] X. Marti, I. Fina, C. Frontera, J. Liu, P. Wadley, Q. He, R. J. Paull, J. D. Clarkson, J. Kudrnovský, I. Turek, J. Kuneš, D. Yi, J.-H. Chu, C. T. Nelson, L. You, E. Arenholz, S. Salahuddin, J. Fontcuberta, T. Jungwirth, and R. Ramesh, "Room-temperature antiferromagnetic memory resistor," *Nat. Mater.*, vol. 13, pp. 367–374, 2014.

[208] T. Moriyama, N. Matsuzaki, K.-J. Kim, I. Suzuki, T. Taniyama, and T. Ono, "Sequential write-read operations in FeRh antiferromagnetic memory," *: Appl. Phys. Lett.*, vol. 107, p. 122403, 2015.

[209] M. Fallot and R. Hocart, "Sur l'apparition du ferromagnétisme par élévation de température dans des alliages de fer et de rhodium," *Rev. Sci.*, vol. 77, p. 498, 1939.

[210] F. de Bergevin and L. Muldawer, "Étude cristallographique de certains alliages fer-rhodium," *Compt. Rend.*, vol. 252, p. 1347, 1961.

[211] J. S. Kouvel and C. C. Hartelius, "Anomalous magnetic moments and transformations in the ordered alloy FeRh," *J. Appl. Phys.*, vol. 33, pp. 1343–1344, 1962.

[212] F. de Bergevin and L. Muldawer, *Bull. Am. Phys. Soc.*, vol. 6, p. 159, 1961.

[213] G. Shirane, C. W. Chen, P. A. Flinn, and R. Nathans, "Mössbauer study of hyperfine fields and isomer shifts in the Fe-Rh alloys," *Phys. Rev.*, vol. 131, p. 183, 1963.

[214] G. Shirane, R. Nathans, and C. W. Chen, "Magnetic moments and unpaired spin densities in the Fe-Rh alloys," *Phys. Rev.*, vol. 131, p. A1547, 1964.

[215] M. P. Belov, A. B. Syzdykova, and I. A. Abrikosov, "Temperature-dependent lattice dynamics of antiferromagnetic and ferromagnetic phases of FeRh," *Phys. Rev. B*, vol. 101, p. 134303, 2020.

[216] L. H. Lewis, C. H. Marrows, and S. Langridge, "Coupled magnetic, structural, and electronic phase transitions in FeRh," *J. Phys. D: Appl. Phys.*, vol. 49, p. 323002, 2016.

[217] M. Takahashi and R. Oshima, "Annealing effect on phase transition of equiatomic FeRh alloy," *Mater. Trans., JIM*, vol. 36, pp. 735–742, 1995.

[218] L. J. Swartzendruber, "The Fe-Rh (Iron-Rhodium) system," *Bull. Alloy Phase Diagrams*, vol. 5, pp. 456–462, 1984.

[219] H. Kumar, D. R. Cornejo, S. L. Morelhao, S. Kycia, I. M. Montellano, N. R. Álvarez, G. Alejandro, and A. Buter, "Strain effects on the magnetic order of epitaxial FeRh thin films," *J. Appl. Phys.*, vol. 124, p. 085306, 2018.

[220] J. M. Lommel, "Magnetic and electrical properties of FeRh thin films," *J. Appl. Phys.*, vol. 37, p. 1483, 1966.

[221] M. Sharma, H. M. Aarbogh, J.-U. Thiele, S. Maat, E. E. Fullerton, and C. Leighton, "Magnetotransport properties of epitaxial MgO(001)/FeRh films across the antiferromagnet to ferromagnet transition," *J. Appl. Phys.*, vol. 109, p. 083913, 2011.

[222] V. Uhlíř, J. A. Arregi, and E. E. Fullerton, "Colossal magnetic phase transition asymmetry in mesoscale FeRh stripes," *Nat. Commun.*, vol. 7, pp. 1–7, 2016.

[223] A. Ceballos, Z. Chen, O. Schneider, C. Bordel, L.-W. Wang, and F. Hellman, "Effect of strain and thickness on the transition temperature of epitaxial FeRh thin-films," *Appl. Phys. Lett.*, vol. 111, p. 172401, 2017.

[224] C. Bordel, J. Juraszek, D. W. Cooke, C. Baldasseroni, S. Mankovsky, J. Minár, H. Ebert, S. Moyerman, E. E. Fullerton, , and F. Hellman, "Fe spin reorientation across the metamagnetic transition in strained FeRh thin films," *Phys. Rev. Lett.*, vol. 109, p. 117201, 2012.

[225] Y. Ohtani and I. Hatakeyama, "Tailoring magnetic frustration in strained epitaxial ferh films," *Phys. Rev. B*, vol. 93, p. 104416, 2016.

[226] S. Yamada, K. Tanikawa, J. Hirayama, T. Kanashima, T. Taniyama, and K. Hamaya, "Low-temperature b2 ordering and magnetic properties of $Fe_{100-x}Rh_x$ films on bcc alloys," *Phys. Rev. B*, vol. 93, p. 094416, 2015.

[227] R. O. Cherifi, V. Ivanovskaya, L. C. Phillips, A. Zobelli, I. C. Infante, E. Jacquet, V. Garcia, S. Fusil, P. R. Briddon, N. Guiblin, A. Mougin, A. A. Ünal, F. Kronast, S. Valencia, B. Dkhil, A. Barthélémy, and M. Bibes, "Electric-field control of magnetic order above room temperature," *Nat. Mater.*, vol. 13, p. 345–351, 2014.

[228] S. Maat, J.-U. Thiele, and E. E. Fullerton, "Temperature and field hysteresis of the antiferromagnetic-to-ferromagnetic phase transition in epitaxial FeRh films," *Phys. Rev. B*, vol. 72, p. 214432, 2005.

[229] M. Jiang, X. Z. Chen, X. J. Zhou, Y. Y. Wang, F. Pan, and C.Song, "Influence of film composition on the transition temperature of FeRh films," *J. Cryst. Growth*, vol. 438, pp. 19–24, 2016.

[230] J. Cao, N. T. Nam, S. Inoue, H. Y. Y. Ko, N. N. Phuoc, and T. Suzuki, "Magnetization behaviors for FeRh single crystal thin films," *J. Appl. Phys.*, vol. 103, p. 07F501, 2008.

[231] C. W. Barton, T. A. Ostler, D. Huskisson, C. J. Kinane, S. J. Haigh, G. Hrkac, and T. Thomson, "Substrate induced strain field in FeRh epilayers grown on single crystal MgO (001) substrates," *Sci. Rep.*, vol. 7, p. 44397, 2017.

[232] C. Q. Yu, H. Li, Y. M. Luo, L. Y. Zhu, Z. H. Qian, and T. J. Zhou, "Thickness-dependent magnetic order and phase-transition dynamics in epitaxial Fe-rich FeRh thin films," *Phys. Lett. A*, vol. 383, pp. 2424–2428, 2019.

[233] G. C. Han, J. J. Qiu, Q. J. Yap, P. Luo, D. E. Laughlin, J. G. Zhu, T. Kanbe, and T. Shige, "Magnetic stability of ultrathin FeRh films," *J. Appl. Phys.*, vol. 113, p. 17C107, 2013.

[234] R. Fan, C. J. Kinane, T. R. Charlton, R. Dorner, M. Ali, M. A. de Vries, R. M. D. Brydson, C. H. Marrows, B. J. Hickey, D. A. Arena, B. K. Tanner, G. Nisbet, and S. Langridge, "Ferromagnetism at the interfaces of antiferromagnetic FeRh epilayers," *Phys. Rev. B*, vol. 82, p. 184418, 2010.

[235] C. Bull, C. W. Barton, W. Griggs, A. Caruana, C. J. Kinane, P. W. Nutter, and b. T. Thomson1, "PNR study of the phase transition in FeRh thin films," *APL Mater.*, vol. 7, p. 101117, 2019.

[236] C. Baldasseroni, G. K. Palsson, C. Bordel, S. Valencia, A. A. Unal, F. Kronast, S. Nemsak, C. S. Fadley, J. A. Borchers, B. B. Maranville, , and F. Hellman, "Effect of capping material on interfacial ferromagnetism in FeRh thin films," *J. Appl. Phys.*, vol. 115, p. 043919, 2014.

[237] E. Stern-Taulats, T. Castán, A. Planes, L. H. Lewis, R. Barua, S. Pramanick, S. Majumdar, and L. Mañosa, "Giant multicaloric response of bulk $Fe_{49}Rh_{51}$," *Phys. Rev. B*, vol. 95, p. 104424, 2017.

[238] E. Stern-Taulats, A. Planes, P. Lloveras, M. Barrio, J.-L. Tamarit, S. Pramanick, S. Majumdar, C. Frontera, and L. Mañosa, "Barocaloric and magnetocaloric effects in $Fe_{49}Rh_{51}$," *Phys. Rev. B*, vol. 89, p. 214105, 2014.

[239] A. C. Botterman, "Magnetization and susceptibility studies on some antiferromagnetic linear chains," Ph.D. dissertation, Technische Hogeschool Eindhoven, 1976.

[240] Y. Takikawa, S. Ebisu, and S. Nagata, "Van Vleck paramagnetism of the trivalent Eu ions," *J. Phys. Chem. Solids*, vol. 71, no. 11, pp. 1592–1598, 2010.

[241] C. Kittel, "Model of exchange-inversion magnetization," *Phys. Rev.*, vol. 120, pp. 335–342, 1960.

[242] M. E. Gruner, E. Hoffmann, and P. Entel, "Instability of the rhodium magnetic moment as the origin of the metamagnetic phase transition in $\alpha - FeRh$," *Phys. Rev. B*, vol. 67, p. 064415, 2003.

[243] W. He, H. Huang, and X. Ma, "First-principles calculations on elastic and entropy properties in FeRh alloys," *Materials Letters*, vol. 195, pp. 156–158, 2017.

[244] F. Ott and S. Kozhevnikov, "Off-specular data representations in neutron reflectivity," *Journal of Applied Crystallography*, vol. 44, no. 2, pp. 359–369, 2011.

[245] D. Gorkov, B. P. Toperverg, and H. Zabel, "Artificial magnetic pattern arrays probed by polarized neutron reflectivity," *Nanomaterials*, vol. 10, no. 5, 2020.

[246] T. Saerbeck, N. Loh, D. Lott, B. P. Toperverg, A. M. Mulders, M. Ali, B. J. Hickey, A. P. J. Stampfl, F. Klose, and R. L. Stamps, "Specular and off-specular polarized neutron reflectometry of canted magnetic domains in loose spin coupled cumn/co multilayers," *Phys. Rev. B*, vol. 85, p. 014411, 2012.

[247] T. Saerbeck, N. Loh, D. Lott, B. P. Toperverg, A. M. Mulders, A. F. Rodríguez, J. W. Freeland, M. Ali, B. J. Hickey, A. P. J. Stampfl, F. Klose, and R. L. Stamps, "Spatial fluctuations of loose spin coupling in CuMn/Co multilayers," *Phys. Rev. Lett.*, vol. 107, p. 127201, 2011.

[248] C. D. Cress, O. van 't Erve, J. Prestigiacomo, S. W. LaGasse, A. Glavic, V. Lauter, and S. P. Bennett, "Domain state exchange bias in a single layer ferh thin film formed via low energy ion implantation," *Journal of Materials Chemistry C*, vol. 11, no. 3, pp. 903–909, 2023.